The synthesis of novel precursors for the CVD of antimony sulphide and antimony sulpho-iodide thin films

Rodriguez Castro, Jorge

Award date:
2006

Awarding institution:
University of Bath

THE SYNTHESIS OF NOVEL PRECURSORS FOR THE CVD OF ANTIMONY SULPHIDE AND ANTIMONY SULPHO-IODIDE THIN FILMS

Submitted by Jorge Rodriguez Castro
For the degree of Doctor of Philosophy
University of Bath
November 2006

COPYRIGHT

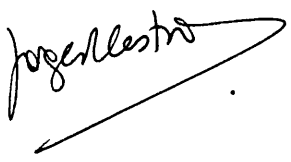

ProQuest LLC
789 East Eisenhower Parkway
P.O. Box 1346
Ann Arbor, MI 48106-1346

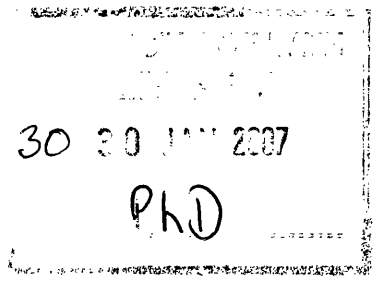
30 JAN 2007
PhD

ABSTRACT

The research described in this thesis has been concern with the synthesis and characterisation of a range of novel single-source precursors for the CVD of antimony sulphide and antimony sulpho-iodide thin films. Four classes of antimony(III) complexes have been investigated such as dithiocarbamates, xanthates, thiolates and iodo-thiolates.

Chapter One - Introduction - provides information regarding the applications of sulphide materials in general and of antimony sulphide and antimony sulpho-iodide in particular. Chemical Vapour Deposition (CVD) is also discussed, followed by the chemistry of antimony to provide basic information regarding the chemistry of the compounds discussed in subsequent chapters. It is also included a survey of the current precursors for the CVD of metal sulphide thin films.

Chapter Two - Antimony(III) Dithiocarbamates - details the synthesis and characterisation of a series of asymmetrically substituted antimony(III) dithiocarbamates containing a variety of alkyl groups. Compounds have been characterised by NMR spectroscopy and by single X-ray diffraction. Subsequently, the compounds are tested as CVD precursors where conditions used for the deposition experiments are described together with the analysis to identify the composition of the deposited species.

Chapter Three - Antimony(III) Xanthates - describes the synthesis and characterisation of a range of antimony(III) xanthates containing a variety of alkyl groups. Compounds have been characterised by NMR spectroscopy and elemental analysis and subsequently tested as CVD precursors. Details of the CVD methodology employed the film analysis and the influence of the substrate used is also included.

Chapter Four - Antimony(III) Thiolates - describes the synthesis and characterisation of a range of antimony(III) thiolates containing a variety of alkyl groups, including fluorinated groups. Complexes have been characterised by NMR spectroscopy

and the ones obtained as solids also characterised by X-ray diffraction. Subsequently, the compounds are tested as CVD precursors where conditions used for the deposition experiments, film analysis and influence of the substrate employed for the deposition are examined.

Chapter Five - Antimony(III) Iodo-thiolates - details the synthesis and characterisation of two novel antimony(III) iodo-thiolates. Compounds have been characterised by NMR spectroscopy and by single X-ray diffraction. Subsequently, the compounds are tested as CVD precursors where conditions used for the deposition and decomposition experiments are described together with the analysis to identify the composition of the species formed.

Finally, a brief conclusion follows comparing the different classes of precursors investigated and highlighting the main discoveries. Appendices regarding details of instrumentation, deposition methodology, and numerical list of all the compounds prepared are provided. Crystallographic data and details of the CVD equipment are also included.

ACKNOWLEDGEMENTS

Firstly, I would like to thank my supervisor, Prof. Kieran C. Molloy for his guidance throughout the last three years and for giving me the opportunity to enjoy and learn from this project and for helping me to be a better chemist.

I would also like to thank Dr. Mike Whittlesey, my internal supervisor, and Dr. Andy Johnson, for their help, support and advices during my PhD and also to Dr. Mary Mahon and Dr. Gabi Kociok-Köhn for the assistance with the crystallography. A big thanks also goes for the technical staff from the Chemistry Department: Robert, Alan, Sheila, Sarah... for their help and co-operation during the laboratory work and Hugh Perrot for his help at the Optics Department.

To my colleagues from Lab. 1.35, Nathan, Doug, Hamid... for the enjoyable time, their help and patience with me. Especially to Purvi, who was not only a *great-super-lab-mate* but has proved to be a better friend.

To the entire Spanish bunch (and other international friends), the PhD students and all the Erasmus that come and go so quickly! All of them made this time much easier and made me feel closer to home. To Edu, Luisa, Lorena, Diego, Walter, Cris, Margarida, Sonia, Paqui, Laura... (I'm sure I will forget someone now, but I do remember each one of you guys!). To my friends in Spain, Javi, Cris, Silvia, Guada, people from the UAM and also to my friends from Bristol: Edmundo, Paquito, Ana, etc, thanks for your unconditional friendship!

My eternal gratitude goes to Narad, my main support here. Thanks for being there every time I needed you. Your constant support and devotion, through the thick and the thicker, makes everything worth it. And that is why... *love you always in all ways.*

And last but not least, to my Family, especially Mamá, Papá and David, the nucleus of my life, which their underestimated strength towards adversity has been an invaluable lesson for me. This work could not have been possible without their unconditional support and faith in me. *Pienso en vosotros todos los dias. Os quiero mucho.*

ABBREVIATIONS

AACVD : Aerosol-Assisted Chemical Vapour Deposition

APCVD : Atmospheric-Pressure Chemical Vapour Deposition

b.p. : Boiling Point

^{n}Bu : n-Butyl

^{t}Bu : Tertiary Butyl

Bz : Benzyl

CVD : Chemical Vapour Deposition

DCM : Dichloromethane

Dtc : Dithiocarbamate

Et : Ethyl

EDAX : Energy Dispersive X-ray Analysis

Hex : Hexyl

IR : Infra-red

L : Ligand

LPCVD : Low-Pressure Chemical Vapour Deposition

m : multiplet

Me : Methyl

m.p. : Melting Point

MOCVD : Metal-Organic Chemical Vapour Deposition

NMR : Nuclear Magnetic Resonance

Ph : Phenyl

^{i}Pr : Isopropyl

^{n}Pr : n-Propyl

PVT : Physical Vapour Transport

r.t. : Room Temperature

R_f : Fluorinated alkyl group

s : singlet

SEM : Scanning Electron Microscopy

t : triplet

TGA : Thermogravimetric Analysis

THF : Tetrahydrofuran

Tol : Toluene

VSEPR : Valence Shell Electron Pair Repulsion

WDS : Wavelength Dispersive Spectroscopy

Xan : Xanthate

XRD : X-ray Diffraction

CONTENTS

To Eva y Félix

Chapter One

Introduction

1.1 TARGETS

This thesis describes attempts to synthesise novel single-source precursors for the Chemical Vapour Deposition (CVD) of antimony(III) sulphide, Sb_2S_3 and, ultimately, antimony (III) sulpho-iodide thin films, both of which are potential ferroelectric materials. There are no references up to date of the deposition of antimony sulphide by CVD and hence the first chapters of this thesis will not only involve the full characterisation of novel single-source precursors for this material but also the study of the films produce by both Low-Pressure CVD (LPCVD) and Aerosol-Assisted CVD (AACVD).

The second part of this thesis will describe the synthesis of new iodo-antimony complexes which also incorporate sulphur-based ligands. These kinds of compounds have been reported in the literature but only relatively few had been structurally characterised. Hence, the synthesised precursors will be tested for their suitability as CVD precursors and the films produced analysed in order to determine their composition and to tailor their decomposition pathway.

1.2 CHEMICAL VAPOUR DEPOSITION (CVD)

There are a large number of deposition techniques available to produce thin films[1] and each one of these present advantages and disadvantages, however due to the nature of this thesis only Chemical Vapour Deposition (CVD) will be discussed in detail.

1.2.1. Introduction

Chemical Vapour Deposition (CVD) consists of a reaction involving one or more gaseous species at the surface of a substrate leading to the deposition of a solid species. Metal Organic Chemical Vapour Deposition (MOCVD) is a related term, implying the use of a metal complex in the experimental process. Other terms, like Metal-Organic Vapour Phase Epitaxy (MOVPE), are less general and imply specific features of the system, e.g. an organometallic precursor (direct metal-to-carbon bonds in at least one of the species) and epitaxy which is the growth of the crystals of one mineral on the crystal face of another mineral, such that the crystalline substrates of both minerals have the same structural orientation.

Some aspects of CVD area cross the interface between materials science and conventional chemistry. An optimal deposition system will involve a precursor (chemistry), which decompose at a solid-vapour phase interface (surface science), to generate a solid phase with useful properties (materials science), using a properly-engineered reactor. [2]

For several decades the formation of metal-containing thin films has been an area of great interest and research. These materials have widespread uses, from traditional applications such as hard coatings for cutting tools, to more technological ones such as electronic materials, optoelectronic devices, superconducting materials, device interconnects, aerospace components, high energy optical systems, high temperature devices and new magnetic materials.[3]

The growth of thin films by CVD has become one of the most important methods of film formation. The reason for the rapidly growing importance of CVD in the past decade lies primarily in its versatility for depositing a very large variety of elements at relatively low temperatures with high purity and the ability to coat large areas.

CVD technology provides considerable advantages over other traditional deposition methods including: [4]

(a) *Kinetic deposition control.*

(b) *Selective area and pattern deposition with sharp boundary features.*

(c) *Lower deposition temperatures with clean and controllable stoichiometric deposition processes (resultant films are often only dependent on the choice of precursor material and easily controlled deposition conditions).*

(d) *Superior thin film uniformity.*

(e) *Superior step coverage.*

(f) *Monolayer interfacial control.*

(g) *Formation of high purity materials.*

(h) *Significant migration reduction at film-substrate interfaces.*

(i) *Experimental ease of deposition from starting precursor materials.*

(j) *Facility for larger scale production processes.*

(k) *Low cost.*

1.2.2 Basic Principles

CVD is a process where one or more volatile inorganic, metal-organic or organometallic precursors are transported in the vapour phase, often in a carrier gas, to the reactor chamber where they decompose on a heated substrate and consequently deposit a solid film.

The decomposition results in elimination of volatile by-products. An inert carrier gas such as Ar or N_2 is often used to enhance the rate of transport of solid or liquid phase precursors to the reactor chamber. However, other reactive carrier gases such as H_2, NH_3, H_2S and O_2 are also used which participate in the chemistry of film deposition by acting as reducing or oxidising agents. Epitaxial, polycrystalline and amorphous films can be deposited, dependent upon the deposition conditions and the material to be deposited.[3]

The CVD process involves several fundamental steps. Absorption of the species on the substrate generating the deposited solid film and the consequent desorption of the by-products (and then elimination from the reaction chamber) are the two main steps of the process.

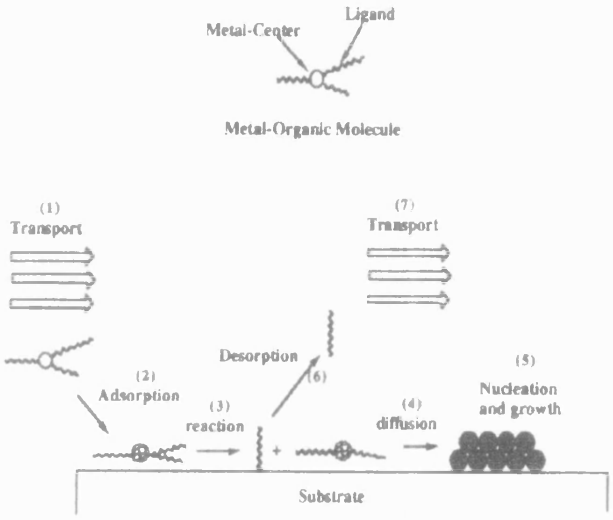

Figure 1.1 Fundamental steps involved in CVD process.

These steps are ruled by the velocity of the gas flows, temperature of the substrate and concentration of the species. The relative rates of these various processes are crucial over the overall deposition rate.

Basically, the CVD process consists of a series of steps (Figure 1.1):

(i) *Mass transport of the precursor from the reactor inlet to the deposition site.*

(ii) *Gas-phase reactions, leading to the formation of film precursors and by-products.*

(iii) *Mass transport of the precursor to the substrate.*

(iv) *Adsorption of the precursor on the substrate surface.*

(v) *Surface diffusion of the precursor to the growth site.*

(vi) *Surface reactions and incorporation of the film constituents into the growing film.*

(vii) *Desorption of by-products.*

(viii) *Mass transport of by-products from the reactor.*

Gas-phase transport rates and surface reaction rates are important for CVD and any of them can be rate limiting.[3, 5]

(a) *If the surface is at a sufficiently high temperature the reaction can proceed much more rapidly than the rate at which reactant gases are supplied to the substrate. This results in a mass-transport limited process.*

(b) *If the mass-transport is sufficiently fast, the deposition rate may then be limited by the feed-rate of the reactants to the chamber. In such case, the deposition is feed-rate limited.*

1.2.3 Chemical Vapour Deposition Techniques

During the last decades, several CVD techniques have been developed in order to grow new varieties of materials. Some of the most important ones are:

- Atmospheric Pressure Chemical Vapour Deposition (APCVD).
- Low Pressure Chemical Vapour Deposition (LPCVD).
- Aerosol-Assisted Chemical Vapour Deposition (AACVD).
- Plasma Chemical Vapour Deposition (PCVD).
- Photochemical Vapour Deposition (PVD).

Other less common techniques include chlorine vapour phase epitaxy (ClVPE), hydride vapour phase epitaxy (HVPE) and organometallic vapour phase epitaxy (OMVPE).

Since AACVD, APCVD and LPCVD have been the techniques utilised during this work they will be discussed in greater depth below.

1.2.3.1 Atmospheric and Low Pressure Chemical Vapour Deposition

In APCVD and LPCVD, pressure rules the deposition on an underlying substrate, controlling both uniformity and varying the coating. While APCVD is a simplest technique, LPCVD requires more complex engineering systems but allows the use of less volatile precursors.

During the 1970s, APCVD was the most common method used, however its applications were limited and was not useful for precursors with low volatility or with high decomposition temperatures. When the first LPCVD equipment was introduced it rapidly became a widely used method for CVD of thin films mainly because it could solve the limitations of APCVD by being able to produce thin film deposition from precursors with low volatility and hence widening the range of precursors that could be used. LPCVD provides superior quality films, a reduced processing cost and increased throughput. The main advantage over APCVD is the rate of mass transfer of the gaseous reactant and by-product species relative to their surface reaction rate to produce the deposited film.[5]

A comparison of LPCVD over APCVD reveals that the low pressure films produce better thickness uniformity, superior structural integrity with fewer pinholes, fewer particulate contaminants, better conformability and finer surface texture. [6] While in APCVD process gas-phase reactions are promoted producing particulates that create defects on the film, in LPCVD those gas-phase reactions are inhibited minimising the substrate contamination.

Due to the low pressure at which LPCVD takes place, the formation of hazardous or toxic vapour phase by-products are minimised providing a more effective process from a safety perspective. Nonetheless, due to the set-up of a LPCVD apparatus, it is only suitable for small scale coatings.

1.2.3.2 Aerosol-Assisted Chemical Vapour Deposition

This method is one of the most important CVD processes, primarily for compounds with low volatility and thermal stability that cannot be used for either AP- or LPCVD but that are soluble in most (or some) of the common organic solvents. The precursor is dissolved in a solvent and the solution is atomised or vaporised into a gas carrier stream. Ultrasonic techniques are perhaps the simplest and most commonly used route to produce an aerosol.[7] Ultrasonic droplet generators consist of a piezoelectric transducer which vibrates underneath the solution containing the dissolved precursor and will generate the aerosol that can then be transported to the reactor in an inert gas such as nitrogen or helium.

Aerosol delivery presents several advantages over bubblers and liquid delivery systems; precursors are held outside the reactor, therefore they do not suffer thermal degradation. The precursors are in a solution, so the delivery rates are constant and do not change in time. This helps to produce reproducible deposition of multicomponent films with consistent deposition. Also, higher deposition rates can be obtained performing at higher temperatures due to vapourisation occurring without contact with hot surfaces.

The main disadvantage of this method is that requires total pressures near atmospheric or high enough so that the droplets do not settle in the reactor before evaporating. Also, the decomposition of the solvent increases the possibility of the incorporation of contaminants.

1.2.4 Decomposition Pathways

There are two main decomposition pathways generally observed in CVD processes, α and β-eliminations. Both of them have been found to compete with one another. It is also believed that many other gas-phase reactions may take place under CVD conditions, such as radical and fragment coupling reactions.[4]

(a) β-Elimination: A metal alkyl is converted into a metal hydride and either a co-ordinated or free alkene. The proposed mechanism is illustrated below by Figure 1.2.

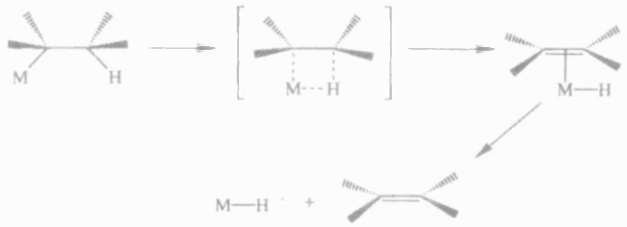

Figure 1.2 β-Hydrogen elimination pathway.

Is believed the reaction proceeds through a planar, four co-ordinate metal-alkene hydride intermediate. The hydrogen atom on a β-carbon of a co-ordinated alkyl group is then transferred to the metal centre, forming a hydrido-metal alkene complex. This elimination can only occur when a complex has β-hydrogens available for transfer; a co-planar intermediate can be formed and has a vacant *cis* co-ordination site on the metal centre.

(b) α-Elimination: A hydrogen atom in the α position to the metal centre is transferred to a second alkyl group via a four-centred planar intermediate. The alkane formed is then eliminated to generate a metal alkylidene. The proposed mechanism is shown in Figure 1.3.

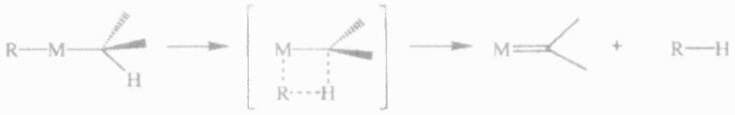

Figure 1.3 α-Hydrogen elimination pathway.

Usually in CVD reactions, the α-elimination process typically leads to large amounts of carbon incorporation into the films due to the formation of surface bound alkylidene species.

1.2.5 Film Growth Mechanisms

In the CVD process the rate-limiting step is the gas-phase transport and adsorption of the precursor to the substrate. After the precursor is absorbed on the surface, it may diffuse to a growth site. The growth mechanism depends on the interactions between the developing film and the substrate, the thermodynamics of absorption, kinetics of crystal growth and the temperature of the substrate.

There are three classical mechanisms of film growth (Figure 1.4):[4]

(a) Layer or Franck-var der Merwe growth: In this model, the deposited atoms are more strongly bound to the substrate than each other. Commonly, this growth process is referred to as "simultaneous multilayer growth" and its presence depends on the relative rates of nucleation and growth during deposition.

(b) Layer Plus Island or Stranski-Krastanov growth: A layer type growth takes place at the beginning of the process, then due to the unfavourable deposition of further layers, islands are formed on the previously deposited layers.

(c) Island or Volmer-Webber growth: Small droplets or clusters initially nucleate on the surface forming island sites. Growth occurs on these island sites. This mechanism prevails when the depositing atoms bind to each other more strongly than to the substrate.

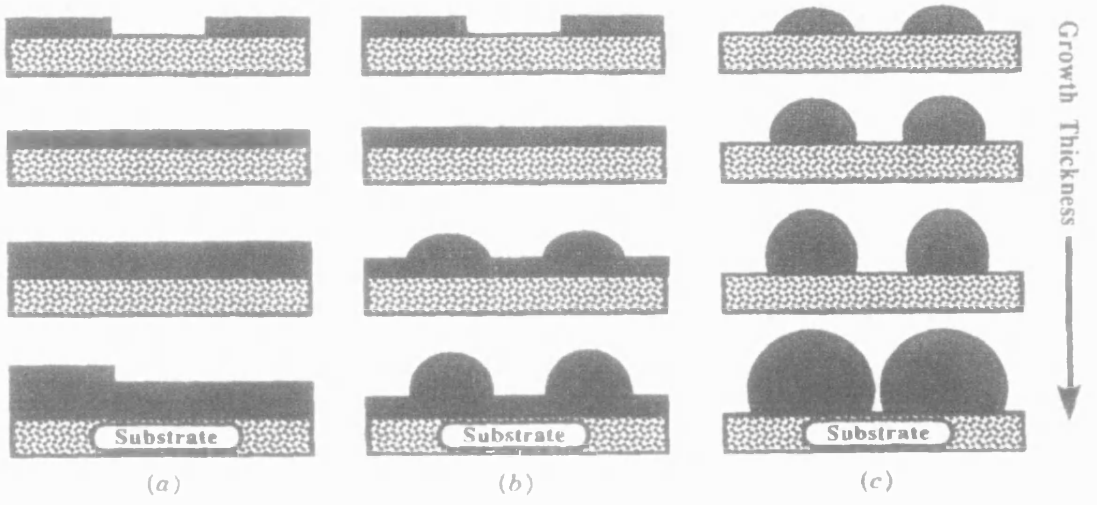

Figure 1.4 CVD film growth mechanisms.

1.2.6 Reactor Design

The CVD experiments have been carried out in many types of reactors and the choice of reactor can have an effect on the nature and the quality of the material deposited. However, CVD reactors can be grouped in two main categories, hot-walled and cold-walled reactors, and the difference between them is quite self explanatory. Hot-walled reactors

contain an external heat source surrounding the reaction chamber and cold-wall systems keep the temperature around the reactor walls fairly low.

Despite the broader use of hot-walled reactors on laboratory scale they do present some significant disadvantages:

(i) *Deposition and decomposition of the precursors can not only take place on the substrate but also on the reactor walls. The deposits accumulated over the different runs can fall off over the substrate surface contaminating the films.*

(ii) *Due to the large area coated, including both substrate and reactor walls, the consumption of the precursors is higher.*

Cold-walled reactors are more commonly used in industry due to the higher sensitivity to secondary-flow effects and turbulences, however, they provide the greatest degree of control over the deposition. Since the deposition on the walls of the reactor does not take place, smaller amounts of precursor are required and therefore better deposition rates can be attained.

1.3 CHEMICAL BACKGROUND

Antimony has the electronic configuration $5s^2 5p^3$, therefore the more common oxidation states are +3 (III) and +5 (V). It belongs to Group 15, often referred to as the *Pnictogens* or *Pnictides*, and whereas nitrogen and phosphorus are typical non-metals, arsenic and antimony are described as metalloids or semi-metals, and bismuth has many properties associated with metallic behaviour.

Compared to nitrogen and phosphorus, antimony presents less extensive allotropy. The most stable crystalline forms for antimony are the *α-forms*, form I and form II. Form I is cubic wherein each antimony is surrounded octahedrally by six others and form II has a metallic hexagonal close-packed structure in which each antimony has twelve nearest neighbours. These two crystalline forms are both high pressure modifications.

Although there are several geometrical structures adopted by Sb(V), Sb(III) compounds are more structurally diverse as a result of the presence of a non-bonded or lone pair of electrons. On the basis of VSEPR theory, for three-, four- and five-coordination, the structures are generally trigonal pyramidal, SbB_3E, trigonal bipyramidal, SbB_4E, and square-based pyramidal, SbB_5E, where E represents the lone pair (Figure 1.5).

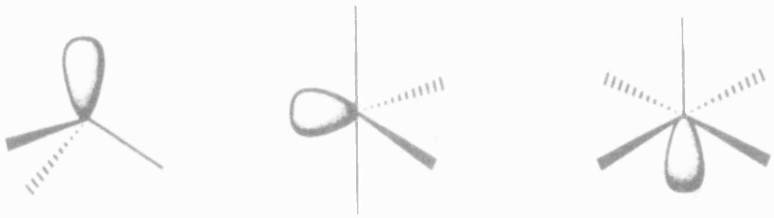

(a) (b) (c)

Figure 1.5 Structures for formulas: (a) SbB_3E, (b) SbB_4E and (c) SbB_5E.

For SbB_6E systems, which have seven electron pairs, there are a number of possible structures based on the octahedron which are quite close in energy, depending on which position is occupied by the lone pair (Figure 1.6).[8]

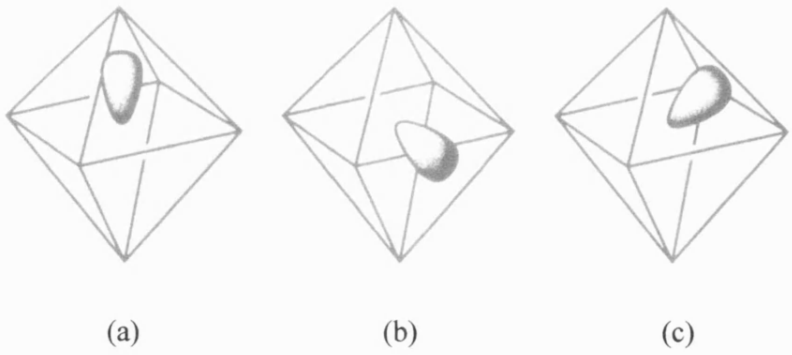

Figure 1.6 Lone pair stereochemical activity through (a) a vertex; (b) an edge; (c) a face of an octahedron.

1.3.1 Antimony Sulphide

The main form of antimony sulphide is Sb_2S_3, commonly known as *Stibnite* and it usually appears as dark grey masses with a metallic appearance, although artificial crystals may appear as greyish-black needles. The crystal structure (Figures 1.7 and 1.8) shows it to consist of infinite Sb_4S_6 chains parallel to the *b* axis and the chains are linked to form crumpled sheets at right angles to the *a* axis (Figure 1.8). These sheets are held together by weak Sb···Sb interactions in he range 3.37-3.64 Å, which is shorter that the sum of the van der Waals radii (4.05 Å).[9]

There is also a monoclinic variation on Sb_2S_3, which X-ray analysis showed to be $Sb_{10}S_{15}$, that is isostructural with $Pb_3S_8S_{13}$ (fuloppite) in which three Pb^{2+} are replaced by two Sb^{3+} to preserve charge neutrality. This unusual Sb(III) species is metastable at room temperature and when is allowed to cool slowly (12 h from 250 to 125 °C) gives Sb_2SO_2 as the only product.[10]

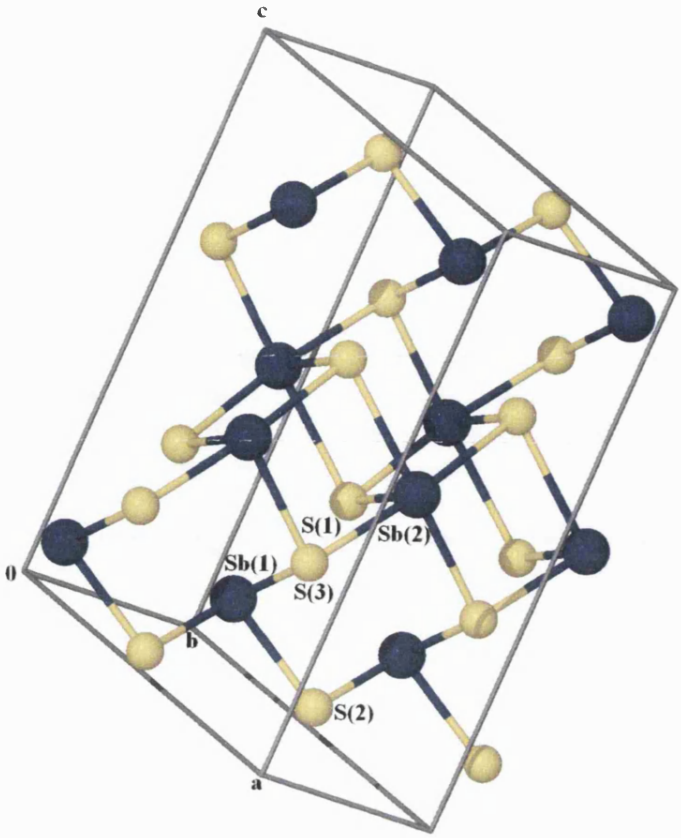

Figure 1.7 Crystal structure of the infinite chain of Sb_4S_6.[9]

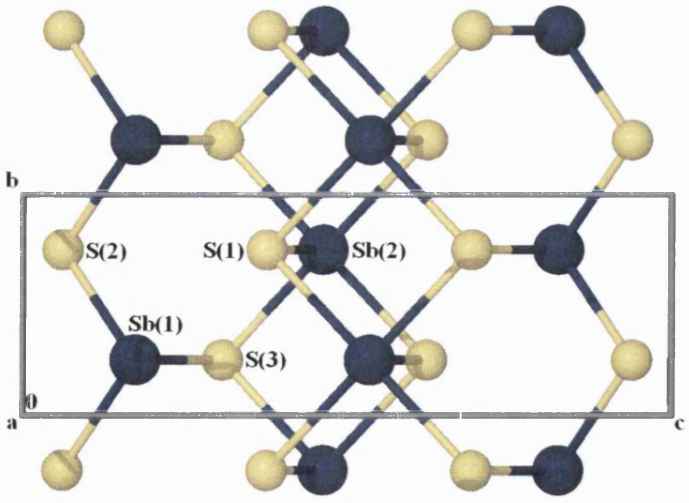

Figure 1.8 Crystal structure of the infinite chain of Sb_4S_6 [9] viewed along the *a* axis.

Amorphous antimony trisulphide has various colours; it may appear dark grey, reddish-brown, fiery red, carmine-red, orange-red and violet. The difference in the colours is probably related with the size of the grains and, as well, depends on the mode of preparation.[11] Thermogravimetric studies show that the transformation between the amorphous orange-carmine form and the crystalline black form takes place around 270 °C.[12]

Thin films studies of Sb_2S_3 are attracting wide attention due to the multiple applications of this material. Antimony trisulphide is a weakly polar, semiconducting ferroelectric which exhibits phase transitions with small structural changes in the coordination sphere of Sb atoms.[13] The band gap of Sb_2S_3, between 1.78 and 2.5 eV, covers the visible and near infrared ranges of the solar spectrum and therefore is a potential candidate for solar energy conversion.[14] Other important applications are as photoconducting cells, photovoltaic cells[15] and other electronic devices such as microwaves,[16] television cameras[17] and switching devices.[18]

Thermal and oxidative studies reported that when oxygen is present the stability of antimony sulphides may vary, therefore, antimony trisulphide is converted to the cubic form of antimony trioxide at temperatures around 400 °C and antimony tetraoxide at higher temperatures.[19]

1.3.1.1 Preparative Routes

During the last decade, a wide range of methods for the preparation of M_2S_3 (M = Sb and Bi) thin films has been reported; however, attempts to do it using CVD are poorly represented with only handful of examples documented. From the survey of literature only a few examples could be found where Bi_2S_3 thin films were obtained. Trindade and co-workers[20] recently reported one of the first examples of the chemical vapour deposition of Bi_2S_3 from bismuth (III) dithiocarbamato complexes, $Bi(S_2CNRR')_3$ using LPCVD. Also,

Bochmann *et al*,[21] have demonstrated similar results using bulky thiolate complexes leading to films contaminated with elemental bismuth.

To the best of our knowledge, there are no references where Sb_2S_3 has been deposited by CVD and, therefore, this will be one of the main goals of this thesis. In order to explore the conditions of formation and properties of Sb_2S_3, several *non*-CVD methods will be discussed further on in this section. The different approaches of synthetic routes to Sb_2S_3 can be classified depending if it has been prepared by deposition of Sb_2S_3 thin films by other *non*-CVD methods or as bulk material:

(a) Thin films by *non*-CVD methods

One of the main techniques used for the deposition of Sb_2S_3 thin films from aqueous media is by *Chemical Bath Deposition*. Although some of the conditions can be variable, the majority of the work reported used antimony trichloride as the source of antimony and a sulphur-containing salt as the sulphur source.

Selim *et al*[22] reported the reaction between a solution of $SbCl_3$ and a 1M solution of sodium thiosulphate at 283 K to give orange-yellow films on amorphous glass substrates. They show how different deposition times affect directly the particle size of the material deposited. X-ray diffraction revealed that the films obtained were amorphous in nature and that by annealing them at 473 K over an hour the films turned darker in colour and the crystallinity of the films was enhanced dramatically.

A variation on this method was reported by Lokhande *et al*[23] which involves the preparation of nanocrystalline Sb_2S_3 films from acidic medium by chemical bath deposition using thioacetamide as the sulphur source. In this case, the use of an acid such as HCl seems to be the key to optimise the quality of the films. The formation of Sb_2S_3 is represented by the following proposed mechanism (Equations 1.1 to 1.3).

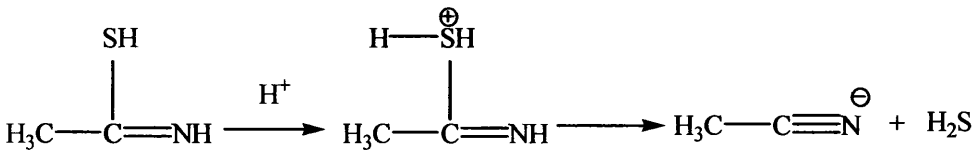

[1.1]

$$H_2S \longrightarrow H^+ + SH^- \longrightarrow H^+ + S^{2-} \qquad [1.2]$$

$$2Sb^{3+} + S^{2-} \longrightarrow Sb_2S_3 \qquad [1.3]$$

The Sb^{3+} and S^{2-} ions produced through reactions in the bath condense at the substrate to form a Sb_2S_3 thin film in an ion-by-ion condensation mechanism.

Other variations of this method have been reported with variations in solvents, deposition times and salts used as sulphur source, producing very similar Sb_2S_3 thin films in which the annealing of the amorphous films produce much more crystalline films.[15, 24]

Another usual technique used for the deposition of Sb_2S_3 thin films is *Spray Pyrolysis*. Bhosale *et al*[25] reported the preparation of Sb_2S_3 thin films on a glass substrate from non-aqueous medium by spraying a mixture of $SbCl_3$ and thiourea dissolved in glacial acetic acid onto hot glass substrates kept at 250 °C. They produced well adherent Sb_2S_3 thin films which were crystalline in nature. Such films were found to be semiconducting and photoactive.

In comparison, Rajpure and co-workers[26] reported the same results than the ones published by Bhosale but by using an aqueous medium. The studies revealed that the films prepared from the latter are amorphous while those obtained from non-aqueous media are polycrystalline. Although optical absorption studies proved both films to be photoactive, there is a significant variation of the optical band gap between both films, tending to be approximately 0.7 eV higher in the films obtained by non-aqueous medium.

Some other methods have been reported such as *Vacuum Evaporation*,[27] showing similar properties of the Sb_2S_3 thin films obtained.

(b) Bulk antimony trisulphide

The methods cited above deal with the production of Sb_2S_3 thin films, however, there are other studies where the production of Sb_2S_3 single crystals and nanorods are also reported.

In the 1970s, Hanafi and co-workers[28] studied the different colours displayed by antimony sulphide. Chemical and thermogravimetric analysis showed that the orange form of Sb_2S_3 contains an excess of sulphur and X-ray diffraction studies indicate that this form is amorphous but contains small amounts of crystalline Sb_2S_3. They also state that the optimum temperature for the transformation of the orange form into the black crystalline form is approximately 270 °C.

Another interesting study is the one reported by Li and co-workers[29] where by using an autoclave filled with distilled water they prepare Sb_2S_3 bulk prismatic single crystals using $SbCl_3$ and sulphur as the raw materials in the presence of a weak reducing agent. The main advantage of this method is the high purity and quality of the crystals obtained and the use of relatively low temperatures (180 °C) during the process. Nonetheless, the main disadvantage is the extremely long reaction time required to produce this material (around 7 days) and the difficulty of adapting it to the thin film area.

The use of a single-source precursor for the formation of Sb_2S_3 is not limited only to CVD purposes and as an example, Qian and co-workers[30] produced crystalline Sb_2S_3 rods by thermolysis of antimony(III) diethyldithiocarbamate. By refluxing the precursor in ethylene glycol at 290 °C for 90 min and allowing the flask to cool down to room temperature they collected a black crystalline precipitate which by XRD was confirmed to be Stibnite, Sb_2S_3. The morphology of the Sb_2S_3 obtained was described as flower-like

bunches of rods and straw-shaped rod bundles. This represents an easy method for the production of bulk Sb_2S_3 in high yields, using simple reaction apparatus and low temperatures.

Other examples in the literature have reported the synthesis of microcrystallites[31] and Sb_2S_3 nanowires[32] by *Solvothermal growth*, with very similar features to the ones described above.

1.3.2 Antimony Sulpho-iodide

Antimony sulpho-iodide, SbSI, has been extensively studied in single crystal form since its discovery,[33] primarily due to its many interesting properties as a ferroelectric material.[34]

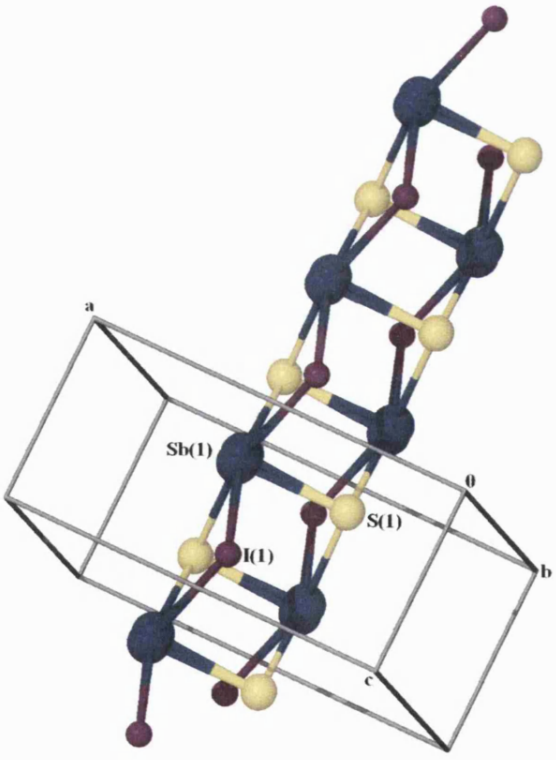

Figure 1.9 Crystal structure of the double chains of $Sb_2S_2I_2$.[35]

SbSI crystallises in orthorhombic symmetry with the lattice constants of a = 8.49 Å, b = 10.10 Å, c (needle axis) = 4.16 Å. The crystal structure of SbSI (Figure 1.9) consists of $Sb_2S_2I_2$ double chains.[34] The chain is formed by intramolecular covalent bonds and the neighbouring chains are stabilised by weak intermolecular van der Waals interactions.

1.3.1.2 Preparative Routes

There are no reports about deposition of thin films containing M(S)I by CVD and hence the synthesis of complexes that can be potentially used as single-source precursors is vital. Only a couple of references from the early 90s showed the preparation of copper iodide and silver iodide by laser-assisted molecular beam deposition[36] and vapour phase electrolytic deposition[37], respectively.

In particular, ferroelectric SbSI has been synthesised by a relatively large number of routes which again, as with Sb_2S_3, can be classified depending if it has been prepared by deposition of SbSI thin films by other *non*-CVD methods or as bulk material:

(a) Thin films by *non*-CVD methods

One of the first studies on the preparation of SbSI thin films was reported by Yoshida and co-workers,[38] whereby an *Electron Beam Evaporation* method and subsequent heat treatment they produced *c*-axis oriented SbSI thin films. They reported several technical difficulties on the preparation of the films due to the large difference of vapour pressure of Sb, S and I and in the alignment of the crystal orientation on the substrate. Nevertheless, this last method was reported to be the most successful one for the preparation of thin films. The films obtained exhibited metallic appearance and were dark red in colour and confirmed to be SbSI by X-ray diffraction. They suggested the annealing of the films seems to be crucial for the orientation of the film along the *c*-axis that can be considered perpendicular to the substrate surface.

In the 1980s, Mansingh[39] reported similar results to the ones published by Yoshida using *Flash Evaporation* of uniformly powdered SbSI crystals as the deposition technique. They also remark on the importance of the annealing of the films to produce highly oriented films along the *c*-axis and in addition, by performing the annealing under a sulphur atmosphere at a 100 °C the stoichiometry and crystallinity of the films was considerably improved.

Another method of preparation of SbSI thin films reported recently by Solayappan *et al.*[40] is *Physical Vapour Transport* (PVT). By this method, stoichiometric, crystalline deep red in colour thin films of SbSI were deposited on platinized silicon substrates over annealed Sb_2S_3 buffer layers at different conditions. The films were produced by the reaction of the Sb_2S_3 buffer layer with a SbI_3 vapour in an ampoule according to the chemical reaction shown by Equation 1.4:

$$Sb_2S_3\ (s) + SbI_3\ (v) \longrightarrow 3\ SbSI\ (s) \qquad \textbf{[1.4]}$$

(b) Bulk SbSI

Since SbSI was first discovered by Dönges[33] in 1960, several techniques have been used to produce SbSI crystals. Melting growth routes[41] and vapour phase under vacuum techniques[42] to produce millimetre size SbSI crystals had been reported during the 1960s. The above procedures require high temperatures (450-600 °C) and long reaction times (1-3 days).

Recently, *Hydrothermal* methods have been the most successful route for the synthesis of bulk SbSI, not only due to the relatively low temperatures required (200 °C) but also the short reaction times needed (20-40 hours). Representative examples of this technique have been reported by Qian and co-workers where by reacting $SbCl_3$, thiourea and a source of iodine (usually NaI) in an autoclave they have achieved an easy route for the synthesis of SbSI nanocrystals. By changing the concentration of the reactants,

temperature and reaction time in the autoclave they reported control of the morphology of the SbSI crystals such as nanorods[43] or rodlike crystals with studded pyramids.[44]

1.3.3 What is a Ferroelectric Material?

In physics, the *ferroelectric effect* is an electrical phenomenon whereby certain materials may exhibit a spontaneous dipole moment, which can be reversed by the application of an electric field. The term ferroelectricity is used in analogy to ferromagnetism, in which a material exhibits a permanent magnetic moment. There are two main types of ferroelectrics:[45]

(a) Displacive ferroelectric: The effect is due to a polarization catastrophe, in which, if an ion is displaced from equilibrium slightly, the force from the local electric fields due to the ions in the crystal increase faster than the elastic restoring forces. This leads to an asymmetrical shift in the equilibrium ion positions and hence to a permanent dipole moment. An example of displacive ferroelectric is barium titanate ($BaTiO_3$) where the Ti atom is slightly too small to come into bonding contact with the surrounding oxygen atoms, and can "slip" so that it touched only three of them, creating a net dipole.

(b) Order-disorder ferroelectric: There is a dipole moment in each unit cell, but at high temperatures they are pointing in random directions. Upon lowering the temperature and going through the phase transition, the dipoles order, all pointing in the same direction within a domain.

A crystal is said to be *ferroelectric* when in the absence of an electric field it has two or more orientational states and that by applying an external electric field it can be shifted from one to another of these states.[46]

Both Sb_2S_3 and SbSI are displacive ferroelectric species where the transition between orientational states is relatively easy to achieve due to their low Curie temperatures (the temperature above which the material loses its spontaneous polarization and piezoelectric characteristics) which are close to room temperature.[34]

The most sensitive species to ferroelectricity is SbSI and this feature is directly related with its molecular structure. In the paraelectric phase, the chains of atoms are oriented along the polar *c*-axis forming square-pyramidal SbS_3I_2 groups with the Sb ion in the centre of the pyramid base. In this high symmetry phase all atoms lie on mirror planes normal to the *c*-axis. On passage into the polar phase, the Sb and S chains move along the *c*-axis with respect to the iodine sites removing the mirror-plane symmetry giving rise to a polar phase with spontaneous polarization along the *c*-axis.

1.3.4 Other Sulphide Materials

The CVD of metal chalcogenides, especially metal sulphides, is the focus of a great interest mainly in the materials area due to their optoelectronic properties, including semiconductivity, photoconductivity and luminescence. They are, however, far less well studied in general than the analogous metal oxides.

Transition metal sulphides are a major theme within this area as precursors for 12-16 sulphide semiconductor materials. The direct nature of the band gaps makes them suitable for use in devices, such as blue/green laser diodes, which could lead to high-density optical storage systems. Binary compounds such as MS films (M = Zn, Cd and Hg) have been deposited through different routes. In the original work in this area, 12-16 sulphide films were prepared employing separate metal and chalcogen sources such as $Cd(CH_3)_2$ and H_2S,[47] however these dual-source MOCVD processes are hazardous, therefore, recent single-source precursors for 12-16 materials have been developed such as

dithiocarbamates[48] and, more recently, using bulky silicon-based chalcogens ligands, i.e. $[\{MESi(SiCH_3)_3\}_2]$ (M = Zn, Cd and Hg; E = S, Se or Te).[49]

Also, sulphides such as TiS_2 have aroused great interest mainly because of their use as cathodes in rechargeable lithium batteries and therefore it has been deposited though different routes such as titanium thiolates[50, 51] or mixtures between $TiCl_4$ and H_2S yielding titanium (IV) sulphide films at a range of temperatures between 100-600 °C.[52]

Other transition metal sulphides reported in the literature that have been deposited as thin films include MoS_2,[50] NbS_2,[53, 54] CoS,[55, 56] MnS[55, 56] and WS_2.[57]

From the late 1980s the attention on transition metal sulphides has been focussed on the development of Cu_xS thin films, primarily for their use as photovoltaics. This has lead to the development of new single-source precursors for MOCVD, such as thiolates,[58] diketonates[59] or dithiocarbamates[60-62] which produced high-quality Cu_xS thin films.

Interest in Group 13 metal sulphides is mainly dominated by gallium sulphide, as GaS or Ga_2S_3, which have potential application in the passivation of GaAs and have been deposited as thin films from a number of reliable single-source precursors.[63-66] Although O'Brien *et al.* reported some work on the deposition of In_2S_3 from different dithiocarbamates,[67, 68] the main focus has been as a component of ternary compounds with general formula $MM'E_2$ (M = Ag, Cu; M'= Ga, In; E= S, Se) due to their applications in solar cells, photolithiography, optical memory devices, photoconductors and thermoelectric generators and coolers.

The deposition of these ternary materials by MOCVD from precursors e.g, $(PPh_3)_2CuIn(SEt)_4$ for the deposition of $CuInS_2$ films, and interest in the synthesis of new precursors capable of producing these chalcopyrite materials has increased considerably. The molecular structure of these ternary compounds was first described by Hirpo *et* al. in 1993[69] and since then, an extensive number of references had been published achieving the efficient deposition of different ternary compounds from various precursors such as

thiolates, selenolates and tricarboxylates.[70-80] Figure 1.10 shows the molecular structure of $(PPh_3)_2CuIn(SEt)_4$.[69]

Also, a wide area of research has been the deposition of Group 14 sulphides, specially of tin(II) and (IV) sulphides (SnS, Sn_2S_3 and SnS_2) using single-source precursors such as dithiocarbamates[81] and thiolates[81-83] due to the semiconductor properties of these materials. However, a large number of other methods have been successful on the formation of crystalline thin films such as chemical[84] and physical vapour transport,[85] thermal evaporation[86] and electrochemical methods.[87]

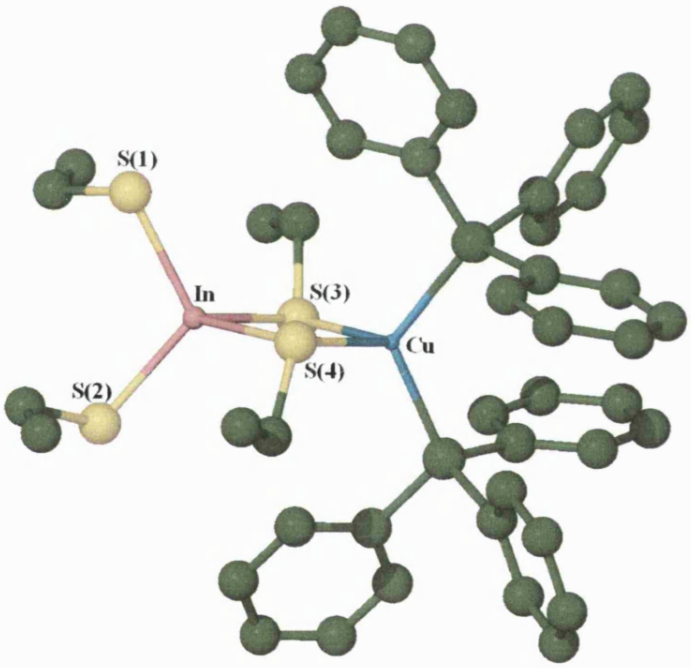

Figure 1.10 Molecular structure of $(PPh_3)_2CuIn(SEt)_4$.[69]

1.4 PRECURSORS

Metal-organic CVD processes use as many element sources as there are elements making up the material that is to be deposited. For several reasons that will be discussed later, only *single-source precursors* (SSP) will be reported throughout this thesis. A single-source precursor uses a single molecule that contains all the elements to be deposited into a film to produce the desire material. The precursor can be designed in such a way as to be specific for the target material, so decomposition takes place to produce the desired film with loss of unwanted organic ligands.

The choice of a particular source molecule for CVD is controlled by several complex factors and depends on the application being considered. One example is the high-purity dense metal films with smooth surfaces deposited at relatively low temperatures (<500 °C) and high deposition rates are required for microelectronic applications. The multilayer stacks require low temperature deposition in order to avoid mixing of layers.

Some of the most important requirements for a CVD precursor are: [4, 5]

(i) *Highly volatile, with high vapour pressure, for high transport rates (mainly for APCVD and LPCVD).*

(ii) *Solubility in most of the common solvents (important for AACVD).*

(iii) *Clean decomposition pathways, for high purity films, e.g. the use of ^{t}Butyl groups benefits the β-elimination mechanism which cleaves the metal-carbon bond, as discussed in Section 1.4.*

(iv) *Good thermal stability during its evaporation and transport in the gas phase.*

(v) *Easy to handle and cheap to manufacture (for industry use), commonly by the use of adducts. e.g. Me_3In which is pyrophoric is usually replaced by $Me_3In{\cdot}NMe_3$.*[2]

One of the main requirements for the precursor in APCVD and LPCVD is having a relatively high vapour pressure in order to provide adequate concentration of the species in the vapour phase and therefore, a suitable deposition rate may be attained. Enhancement of the volatility requires a minimisation of the polarisability, dipoles and interactions between molecules of the precursor in the condensed state, e.g. suppression of covalent intermolecular interactions. The high volatility in a precursor molecule can be achieved chemically by controlling the molecular weight and minimising[88] intermolecular interactions by:

(a) *Employing bulky substituents.* For example, in the case of $M(OR)_n$, by the use of bulky R groups, the tendency to form dimers, trimers etc. by the coordination to M by the oxygen lone pair can be minimised and consequently will give only the monomer.

(b) *Employing fluorinated* ligands. The substitution of fluorine for hydrogen increases the volatility due to the diminished number of hydrogen bonds and the difficulty to polarise fluorides due to the minimising of dipole-dipole interactions between molecules. For example, using $M(OCH_2CF_3)_2$ instead of $M(OCH_2CH_3)_2$.

(c) *The saturation of the coordination sphere of the metal.* e.g. using glymes. This method is basically used in CVD of Group II elements (Ca^{II}, Sr^{II} and Ba^{II}) which present problems for MOCVD being plagued by poor reproducible stoichiometries, poor thermal stability and low volatility due to the small charge-to-radius ratio and lability of the alkaline metals leading to variable growth rates and compositions.[89] The large coordination spheres of these elements allow oligomerisation to take place, so the coordination sphere has to be saturated.[90] The low oxidation state prevents coordinating further β-diketoneate ligands on the metal centre so neutral ligands are required. One of the neutral ligands used to saturate the coordination sphere are the polyethers, which are called glymes and consist of the OCH_2CH_2 repeat unit, providing additional donor atoms. When glymes are coordinated to the elements, this leads complexes with lower melting points and much more air and moisture stability and hence, easier to handle. Figure 1.11 shows a Sr complex

bonded to two molecules of diglyme. The coordination sphere of the Sr is saturated and therefore the complex is more stable.

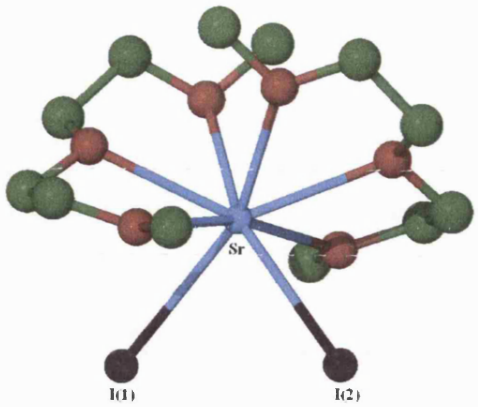

Figure 1.11 Molecular structure of *cis*-$[SrI_2(diglyme)_2]$.[91]

An extensive area has been developed to grow metal sulphides, especially for 12-16 materials such as ZnS and CdS, by the use of adducts of the metal alkyls of zinc and cadmium as precursors of the growth of wide-band-gap semiconductors by MOCVD. Adducts like dioxane, trioxane, triethylamine and triazine, of dimethylzinc increase the stability of the complexes by saturating the coordination sphere of the metal like glyme adducts. However, the purpose of using these adducts is to increase volatility and at the same time successfully inhibit homogeneous pre-reaction in the growth of $[ZnS]_n$ and related alloys by MOCVD.

Some of the potential advantages of the use of such adducts are: [2]

- The vapour pressure of the metal alkyl is effectively reduced; therefore there is no need to cool bubblers containing dimethylzinc.
- Reaction occurs before the precursors reach the hot zone of the reactor, thus the "homogeneous pre-reaction" may be considerably limited.
- Layers may have improved electrical properties due to the purification of the alkyl during the preparation of the adduct.

Despite the increasing use of these species in MOCVD, very little is known about the mechanism of the reaction in the gas-phase in the reactor. Figure 1.12 show one of the adducts of dimethylzinc and triazine.[92]

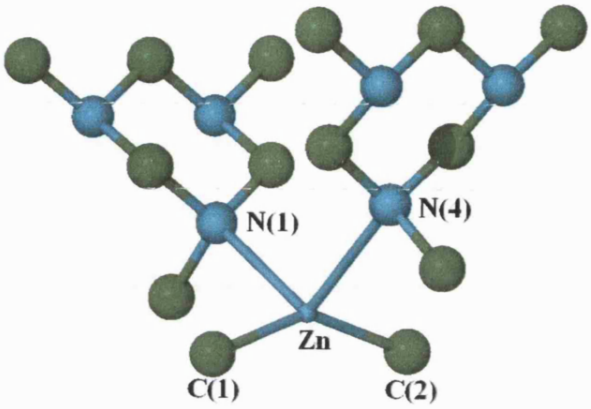

Figure 1.12 The triazine adduct of dimethylzinc.[92]

1.4.1 Single-Source Precursors

The design of the precursor needs to be done thoughtfully; a molecule comprising *m* number of A elements and *n* number of B elements will not necessarily deposit the material having the formula A_mB_n. The result will depend on a fragile balance between the energy of the bonds that must be broken and those that should be maintained, and on possible reactions according to whether the ligands are decomposed into reactive fragments or cleanly stripped off in the vapour phase.

The use of single-source precursors presents several advantages over dual or multi-source precursors. Firstly, the installations are simpler and easier to handle in respect of flow and temperature controls and secondly it can be a much safer route, if it eliminates the use of highly toxic or oxygen/moisture sensitive substances are required such as H_2S, NH_3, PH_3, SiH_4 and AsH_3.[93]

Chemistry of Group 15 elements, especially arsenic, antimony and bismuth compounds derived from xanthates, dithiocarbamates and phosphorous based acids have been an active area of research for more than four decades.[94-96] However, whereas CVD of arsenic and bismuth sulphides films have been studied extensively,[20, 96-99] nothing has been reported about CVD of antimony sulphides films. Chemical Vapour Deposition of antimony compounds has been usually centred on the deposition of antimony oxides although not very much has been reported. The first film deposited by CVD was Sb_2O_5 by aerosol-assisted AACVD via hydrolysis of $SbCl_5$ and H_2O[100, 101] and after some work has been undertaken using metal-organic MOCVD depositing Sb_2O_3 films using different single-source precursors such as alkoxides and N,N-dialkylcarbamates.[82, 102, 103]

1.4.1.1 Dithiocarbamates and Xanthates

During the last decades, a wide range of metal dithiocarbamates and xanthates has been reported, not only from a structural point of view but also for their applications as single-source precursors for the CVD of metal sulphides. Various thermochemical studies have been reported[104] in order to understand the thermal decomposition pathways of these complexes that will also be discussed in following chapters.

The molecular structure of both dithiocarbamates and xanthates is similar and so are their thermochemistry, hence their study is often linked together.

One of the first examples using dithiocarbamates to produce metal sulphide films by MOCVD was reported by Saunders *et al.*[105] where they use diethyldithiocarbamates to grow ZnS thin films in a low-pressure reactor. However, since then, many others have improved the quality of the films produced specially by using asymmetrically substituted dithiocarbamates. O'Brien and co-workers have reported the deposition of many metal sulphides from various sources such as dithiocarbamates; one example of these complexes is $[Zn(S_2CNMePr^i)_2]_2$[106] which consists of discrete dimers and is illustrated by Figure 1.13.

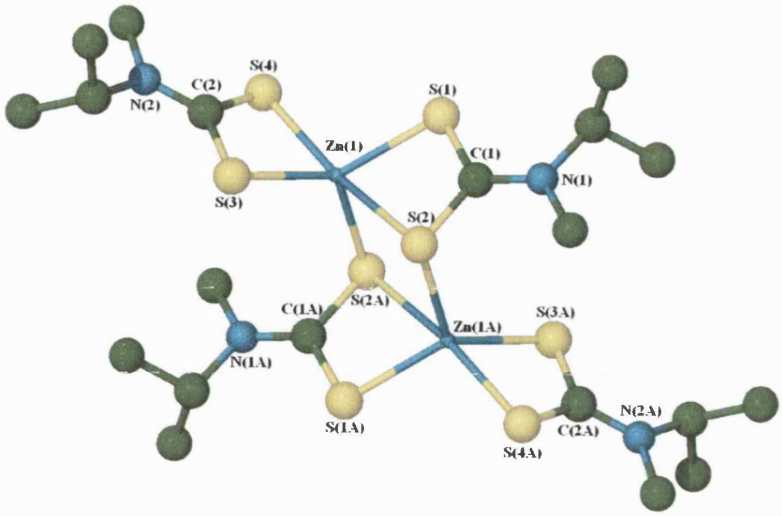

Figure 1.13 Molecular Structure of $[Zn(S_2CNMePr^i)_2]_2$.[106]

There are several other references using both dithiocarbamates and xanthates as ideal candidates for the deposition of transition metal sulphide thin films. O'Brien *et al.* also had reported the deposition of CdS from another asymmetrically substituted dithiocarbamates such as $Cd(S_2CNMeBu^n)_2$[107] and ZnS from $[Zn(S_2CNMeBu^n)_2]_2$.[106] By comparing the quality of the material deposited by both symmetrical and asymmetrically substituted dithiocarbamates, they conclude by proving that the asymmetrical dithiocarbamates gives better results over the symmetrical dithiocarbamates due to their higher volatility and lower melting temperatures.

Other transition metal complexes tested as CVD precursors which produced the correspondent transition metal sulphides thin films include CdS from cadmium O-alkylxanthates such as $Cd(S_2COEt)_2$ and $Cd(S_2COPr^i)_2$ [108] or CuS from asymmetrically substituted dithiocarbamates such as $Cu(S_2CNMeHex)_2$ [61] by LP and AACVD.

There also a number of Main Group dithiocarbamates and xanthates used to produce their parent metal sulphide thin films. Group 14 metal sulphides had been deposited from several single-source precursors, nonetheless the vast majority of them come from the

deposition of tin sulphides, SnS and SnS_2 due to their potential applications as photovoltaic holographic recording systems and solar control devices.[109] Molloy *et al.* reported the synthesis of a series of tin(IV) asymmetric dithiocarbamates derivatives, such as $Ph_3Sn(S_2CNMeBu^n)$ [110] which by APCVD did not function as single-source precursors to produce tin sulphide thin films and where a secondary source of sulphur such as H_2S was required. In addition to this, they also reported a series of homoleptic tin(IV) dithiocarbamates and heteroleptic tin(IV) species containing both thiolates and dithiocarbamates which produced SnS_2 and SnS thin films, respectively, with thermal control of film composition.[81] An example of one of these heteroleptic species, $Sn(SC_6H_{11})_2(S_2CNEt_2)_2$, is illustrated by Figure 1.14.

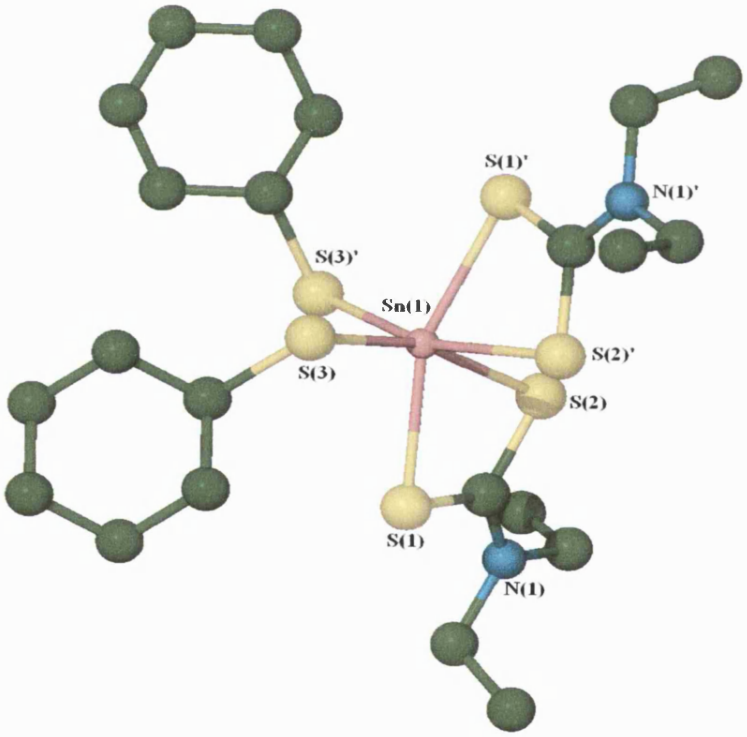

Figure 1.14 Molecular structure of $Sn(SC_6H_{11})_2(S_2CNEt_2)_2$.[81]

Deposition of Group 13 metal chalcogenolates using dithiocarbamates is mainly dominated by the growth of indium sulphide thin films. The majority of the work on this filed was carried out by O'Brien and co-workers, where In_2S_3 thin films were grown from alkyl metal dithiocarbamates[68] and dialkyldichalcogenocarbamates[111] such as $EtIn(S_2CNEt_2)$. The composition of the films grown was highly dependant on the temperature at which the deposition takes place and the nature of the precursor used. Different crystalline forms of indium sulphide were obtained, such as β-In_2S_3, In_6S_7, or InS and the presence of hydrogen atoms in the β position of the alkyl group plays a key role for the where a β-H elimination process is proposed for the decomposition pathway.

1.3.1.2 Thiols

Organothiolate anions (RS^-) are a widly known type of ligand that together with the homologous organoselenolates (RSe^-), alkoxides (RO^-) and aryloxides (ArO^-) anions, could be classified as a pseudohalides, comparable as a ligand with Cl^-, Br^- and I^-. The coordination chemistry of thiols is potentially more variable than that for other ligands mainly because the substituent R group can be manipulated powerfully and adjusted delicately to effect steric and electronic control of ligation ability.[112]

Although thiols mainly act as monodentate ligands, they also have a reputation for bridging metal atoms, a reputation engendered by the insolubility of the familiar metal thiolates with formula $[M(SR)_n]_p$, frequently formed when both thiolate ions and metal ions are mixed in protic media. However, over the years many monomeric structures, $M(SR)_n$, had been published with can be used for a broad number of applications.

One of the potential applications of metal thiolate complexes is their use as precursors for the CVD of metal sulphides and hence they will be used in this thesis. As for this purpose, several metal thiolates had been reported in the literature as single or dual-source precursors for the deposition of metal sulphide thin films.

Transition metal sulphides have been deposited from various different sources as mentioned earlier and one of them is metal thiolates. Cheon *et al.*[50] reported the deposition of both MoS_2 and TiS_2 thin films from metal thiolates with formula $M(SBu^t)_4$ in a low-pressure reactor. The films produced were suitable for the various characterisation techniques used such as X-ray powder diffraction or Auger electron spectroscopy (AES) and tended to be easily hydrolysed leading to the loss of sulphur and the incorporation of oxygen. The molecular structure of one of these precursor used, $Mo(SBu^t)_4$ was reported earlier by Otsuka and co-workers[113] and it is shown by Figure 1.15.

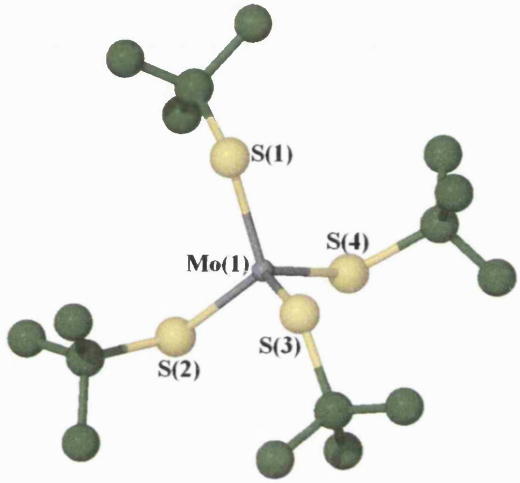

Figure 1.15 Molecular Structure of $Mo(SBu^t)_4$.[113]

It is important to remark that complementary to what Cheon *et al.*[50] published, Parkin and co-workers[114] reported the deposition of TiS_2 from a single-source precursor such as $Ti(SBu^t)_4$ under aerosol-assisted CVD conditions using various solvents. They reasoned that the influence of the solvent used for the deposition produced very different and unique morphologies in the films, and furthermore, this could potentially lead to improved properties.

In addition to this work, Parkin *et al.*[115] also reported the deposition of TiS_2 thin films, this time by a dual-source such as $Ti(NMe_2)_4$ and Bu^tSH under atmospheric pressure

conditions, leading to similar results in terms of film properties but enabling online coating in an industrial glass production.

Main Group metal sulphides deposited by CVD have been deposited from various sources such as dithiocarbamates (cited previously), however, from metal thiolates most of the examples reported is referred to Groups 13 and 14.

The majority of the work published in the literature about Group 14 is related to tin sulphides reported by Molloy and co-workers.[116, 117] They reported the deposition of tin sulphide, SnS_2, SnS and Sn_2S_3, from a series of homoleptic tin (IV) thiolates[117] typified by $Sn(SPh)_4$ and found that in the absence of a second source of sulphur (such as H_2S), only SnO_2 films were observed. Even by using H_2S as a co-reactant gas, film composition is strongly dependant on the temperature at which the decomposition takes place; at $T < 500$ °C thin films with predominantly SnS_2 were produced and at $T > 500$ °C only SnS thin films were obtained, both by AACVD.

They also reported the deposition of tin sulphide thin films by APCVD from various highly volatile tin(IV) thiolates[116] by the incorporation of fluoroalkyl substituents on the thiolate chain and found that again, H_2S is required as co-reagent for films formation. An example of one of the (fluoroalkylthiolates)tin(IV) precursors is illustrated below by Figure 1.16.

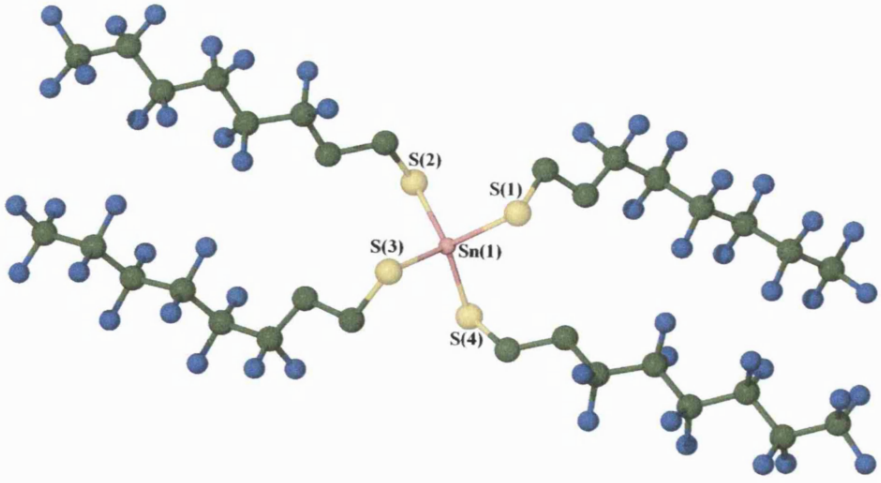

Figure 1.16 Molecular Structure of $Sn[SCH_2CH_2(CF_2)_5CF_3]_4$.[116]

Deposition of Group 13 metal sulphides had also been reported from single-source precursors from both Gallium and Indium thiolates. Gallium sulphide thin films have been grown from precursors such as $[(Bu^t)_2Ga(SBu^t)]_2$, $[(Bu^t)GaS]_4$ and $[(Bu^t)GaS]_7$.[118, 119] Films produced at 400 °C were consisted of stoichiometric GaS and at temperatures higher than 475 °C gave amorphous films with a Ga:S ratio of 2:3, consisted with Ga_2S_3. Some of the films were subsequently used for passivation coatings of GaAs purposes.

Likewise Gallium sulphide thin films, Indium sulphide films had been reported,[120, 121] partly driven by the desire to produce bimetallic materials such as $CuInS_2$ due to their potential applications in solar cells. Indium thiolates[120, 121] had been synthesised as single-source precursors for the deposition of both InS and In_2S_3 phases. Precursors like $[(Me)_2In(SBu^t)]_2$ and $(Bu^n)In(SPr^i)_2$ were used to produce indium sulphide films that were found to be highly dependant on the temperature at which the experimental process was carried out, conditioning consequently the microstructural features and chemical composition of the sulphide deposited.

The aim of this thesis is primarily to describe the synthesis of single-source precursors for the CVD of antimony sulphide, Sb_2S_3. A variety of sulphur-containing antimony(III) compounds such as dithiocarbamate, xanthates and thiolates, have been synthesised and fully characterised for this purpose. CVD experiments have been carried out in order to assess the viability of each precursor and to determine the composition of the deposited material.

The second and more ambitious part of the thesis describes the synthesis and characterisation of single-source precursors such as antimony(III) iodo-thiolates for the CVD of antimony sulpho-iodide, SbSI. The the challenge lies in keeping the linkage Sb-I unaltered, which under the harsh conditions of the CVD process is the bond more likely to be broken.

Chapter Two

Antimony(III) Dithiocarbamates

2.1 INTRODUCTION

Dithiocarbamates are extremely versatile ligands with wide number of applications. In the past decades they have been used as accelerators in vulcanization, as high-pressure lubricants and as fungicides and pesticides.[122] They have been found to act usually as uninegative bidentate ligands, coordinating to metal centres through both sulphur atoms, however they can also act as monodentate ligands. According to the criterion of Bonati and Ugo,[123] the presence of a solitary band in the 950-1050 cm^{-1} IR region is due to symmetrical bidentate coordination of the dithiocarbamato group while the splitting of this band within a narrow range of 20 cm^{-1} is due to the unsymmetrical monodentate nature of the dithiocarbamato group. Figure 2.1 illustrates an example of the different coordination modes of dithiocarbamate ligands to a metal centre.

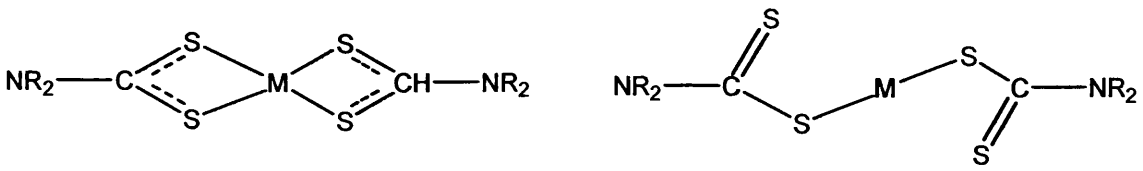

Figure 2.1 Representation of bi- and monodentate coordination of dithiocarbamate metal complex.

The chemistry of metal dithiocarbamates, especially of arsenic, antimony and bismuth complexes, has been an active area of research for more that four decades and a wide range of compounds with formula $M(S_2CNR_2)_3$ (M = As, Sb and Bi; R = Me, Et, ^{i}Pr, ^{n}Pr, CH_2CH_2OH, etc) are known.[98] Figure 2.2 shows the molecular structures of one of these arsenic (III) dithiocarbamates. There are several reasons that make these compounds interesting; firstly, they show a great structural diversity which ranges from monomeric to polymeric supramolecular assemblies, and secondly they present a remarkable number of potential applications.

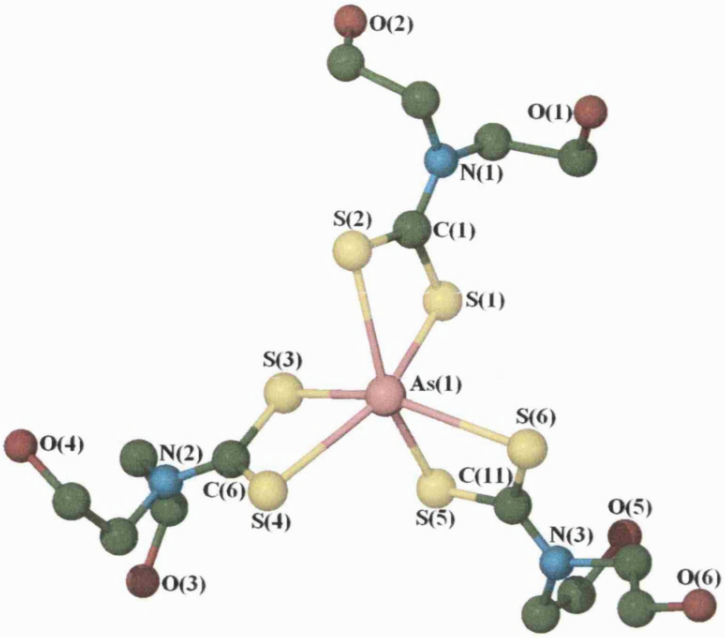

Figure 2.2 Molecular structure of $As[S_2CN(CH_2CH_2OH)_2]_3$.[98]

One of the potential applications of metal dithiocarbamate complexes which attracted our interest due to the nature of this thesis is the use of these compounds as molecular single-source precursors in CVD processes for the deposition of chalcogenide materials (e.g. Sb_2S_3). There is just one reference to date about the use of Group 15 metal dithiocarbamates as single-source precursors, reported by O'Brien and co-workers.[20] They used bismuth dithiocarbamates such as $Bi(S_2CNEt_2)_3$ and $Bi[S_2CN(Me)(Hex)]_3$ for the deposition of crystalline films consisting of well-defined Bi_2S_3 fibers. An example of the molecular structure of one of these precursors is illustrated by Figure 2.3.

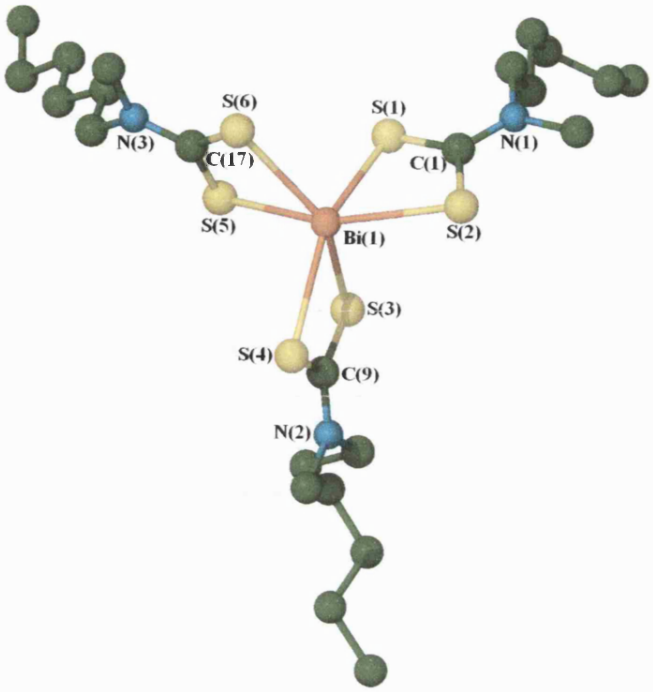

Figure 2.3 Molecular structure of $Bi[S_2CN(Me)(Hex)]_3$.[124]

Although there are no references reporting CVD studies from antimony(III) precursors up to date, there is an overwhelming number of structural data on tris dithiocarbamates, whether the amine is symmetrical or asymmetrically substituted, with coordination number 6 and with three strong and three weak Sb-S bonds. Variations of the R groups within the ligands lead to significant distortions from the ideal octahedral geometry and hence "secondary interactions", which play a key role in stabilising the crystal structures of main group elements compounds, might be affected creating an interesting field for crystal engineering.

Apart from these homoleptic complexes, a myriad of mixed ligand complexes have also been reported. This includes antimony(III) halodithiocarbamates with general formula $XSb(S_2CNR_2)_2$ [125-127] (X = Cl, Br and I). Also, several organometallic derivatives with alkyl/aryl groups such as $MeSb(S_2CNEt_2)_2$ have been structurally characterised.

The most common oxidation state for Group 15 elements is +3, however, there are a large number of pentavalent complexes dominated by antimony compounds for which both inorganic and organometallic compounds have been reported.[98] The reduction of antimony(V) compounds to antimony(III) is often quite facile when sulphur-containing ligands are present and the redox process becomes important. The structures of complexes such as $Me_3Sb(S_2CNMe_2)_2$, illustrated by Figure 2.4, have been established by single crystal X-ray diffraction methods showing that antimony acquires a distorted pentagonal bipyramidal configuration with a planar SbC_3 unit. The stabilization of the pentavalent state for antimony with a sulphur ligand comes from σ-electron donating methyl groups.[128]

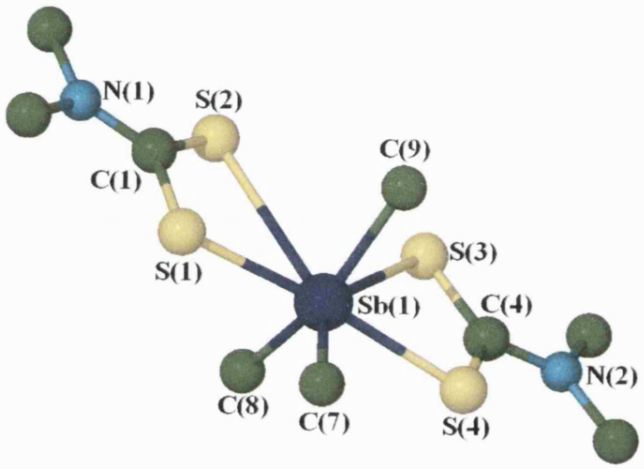

Figure 2.4 Molecular structure of $Me_3Sb(S_2CNMe_2)_2$.[128]

Some of the structurally characterised examples of antimony(III) dithiocarbamates reported in the literature, together with coordination number, geometry and significant bond distances are summarised in Table 2.1. There are three main geometries described for antimony(III) dithiocarbamates (shown in Table 2.1), and an example of each of these geometries is illustrated by Figures 2.5 to 2.7. This classification is based on the differences in the antimony atom coordination geometry, depending on the Sb-S bond angles and the planes defined by the coordinated sulphur atoms.

Table 2.1 Coordination Geometries Exhibited by Antimony (III) Dithiocarbamates

Coordination Number	Geometry	Example	Range of Sb-S (Å)	Ref.
6	Distorted Pentagonal Bipyramidal	$Sb[S_2CN(CH_2)_5]_3$	2.524(9)-3.001(8)	129
6	Distorted Pentagonal Bipyramidal	$Sb[S_2CN(CH_2)_6]_3$	2.507(14)-3.009(18)	129
6	Distorted Pentagonal Bipyramidal	$Sb[S_2CN(CH_2Ph)_2]_3$	2.534(7)-2.947(8)	129
6	Distorted Octahedron	$Sb(S_2CNEt_2)_3$	2.487(4)-2.965(4)	130
6	Distorted Octahedron	$Sb(S_2CNPr^n_2)_3$	2.465(4)-2.822(5)	131
6	Distorted Trigonal Prism	$Sb[S_2CN(Me)Ph]_3$	2.528(2)-3.000(3)	132

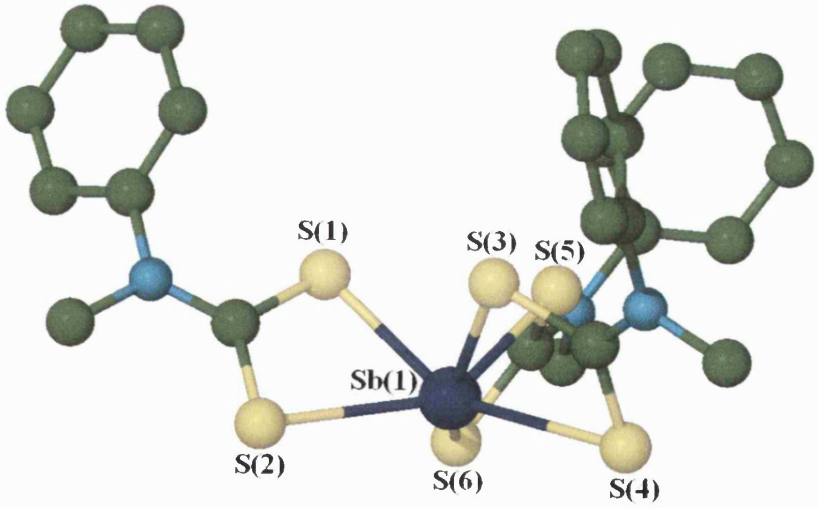

Figure 2.5 Molecular structure of $Sb[S_2CN(Me)Ph]_3$ [132]described as distorted trigonal prism.

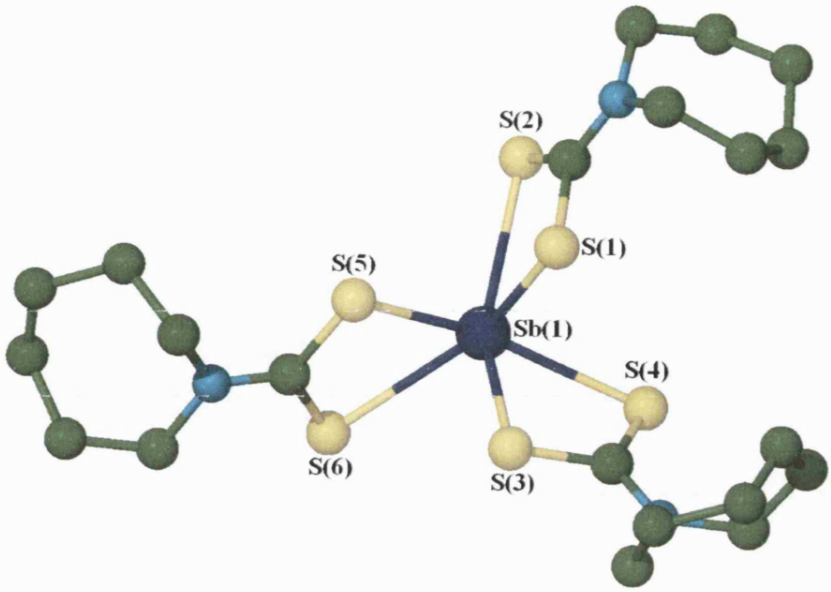

Figure 2.6 Molecular structure of $Sb[S_2CN(CH_2)_6]_3$ [129] described as distorted pentagonal bipyramidal.

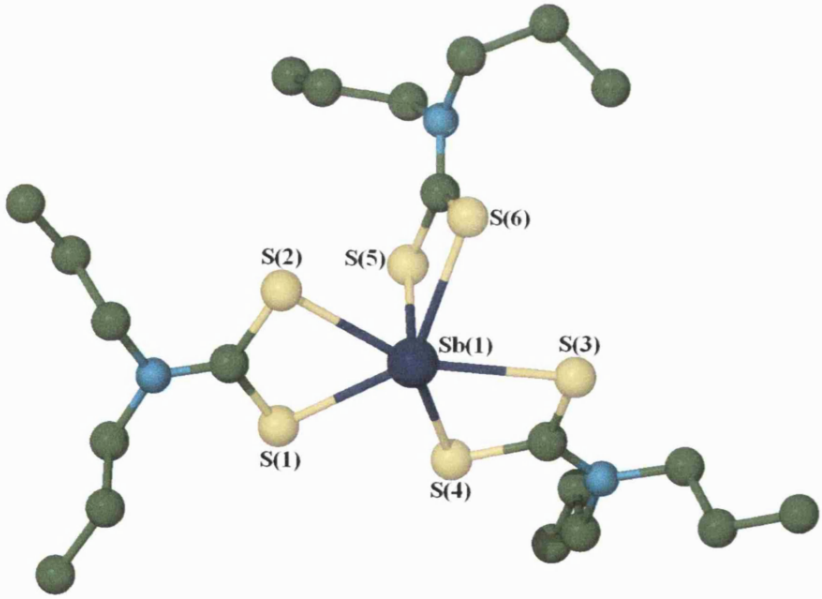

Figure 2.7 Molecular structure of $Sb(S_2CNPr^n_2)_3$ [131] described as distorted octahedron.

Deposition of thin films of Sb_2S_3 have received relatively little attention, in particular, chemical vapour deposition (CVD) routes have been neglected, from either dual-source or single-source precursors. Our interest in the deposition of metal sulphide thin films from single-source precursors has caused us to turn our attention to this area and we herein report in this chapter, the preparation, characterisation and properties of CVD candidates for Sb_2S_3 films are evaluated. Metal dithiocarbamates are attractive precursors for CVD processing, especially those with an asymmetrically substituted amine. This asymmetrical substitution in the amine leads to poor packing and weak molecular interaction between molecules and lowering the degree of association and thereby the volatility is increased.

2.2 RESULTS AND DISCUSSION

2.2.1 Synthetic Routes

The synthesis of metal dithiocarbamates is relatively easy to achieve and there are different methods available that mainly depend on the nature of the dithiocarbamate. Although some dithiocarbamate salts need to be kept under nitrogen atmosphere, the resulting metal complexes are generally air stable and soluble in most organic solvents, this being the case for the compounds described in this chapter.

Some dithiocarbamates are commercially available as a salt which are easy to handle, such as KS_2CNEt_2, and just by mixing it with the metal source (usually metal halides) the corresponding metal dithiocarbamate can be rapidly obtained. A representation of this route is illustrated by Equation 2.1. However, asymmetrically substituted derivatives are not commercially available and need to be prepared by deprotonation with a suitable

base (such as butyl lithium, sodium or potassium hydroxide) of the secondary amines and then reacted with carbon disulphide. This route is represented by Equations 2.2 and 2.3.

$$MCl_n + n\,KS_2CNR_2 \xrightarrow{\text{methanol}} M(S_2CNR_2)_n + n\,KCl \qquad [2.1]$$

$$HN(Me)R + BuLi \xrightarrow{\text{hexane}} LiN(Me)R \xrightarrow{CS_2} LiS_2CN(Me)R \qquad [2.2]$$

$$MCl_n + n\,LiS_2CN(Me)R \xrightarrow{\text{methanol}} M[S_2CN(Me)R]_n + n\,LiCl \qquad [2.3]$$

Some examples of metal dithiocarbamates reported in the literature together with information regarding the variations in the method used and brief comments concerning experimental conditions are summarised in Table 2.2.

A series of antimony(III) dithiocarbamates have been prepared in this work following the different synthetic strategies reported in the literature, previously mentioned. All precursors were obtained in high yields (*ca.* 60 %), soluble in most organic solvents and found to be air- and moisture-stable for long periods of time but with an intense sulphur odour.

A summary regarding the preparation of the precursors synthesised and reported in this chapter, including yields and physical properties, is represented in Table 2.3

Table 2.2 Synthetic Routes Used for the Preparation of Metal Dithiocarbamates

Compound	Synthesis [a]	Comments	Yield (%)	Ref.
$Pb(S_2CNEt_2)_2$	2.1	For the asymmetrical dithiocarbamates no base was added, PbO acted both as metal source and base.	93	133
$Pb(S_2CNEtPr^i)_2$	2.2 - 2.3		53	
$Pb(S_2CNMeBu^n)_2$	2.2 - 2.3		58	
$Pb(S_2CNBu^n{}_2)_2$	2.2 - 2.3		56	
$Pb(S_2CNBu^i{}_2)_2$	2.2 – 2.3		46	
$Pb[S_2CNMe(n\text{-}C_6H_{13})]_2$	2.2 – 2.3		76	
$Bi(S_2CNMeHex^n)_3$	2.2 – 2.3	For the asymmetrical dithiocarbamates no base was added, Bi_2O_3 acted both as metal source and base.	70	124
$Bi(S_2CNMeBu^n)_3$			91	
$Bi(S_2CNBu^n{}_2)_3$			56	
$Bi(S_2CNEt_2)_3$			45	
$Sb[S_2CN(CH_2)_5]_3$	2.2 – 2.3	KOH was used as a base. Products with high m.p (199-309 °C).	No Data provided	129
$Sb[S_2CN(CH_2)_6]_3$				
$Sb[S_2CN(CH_2Ph)_2]_3$				
$Cu(S_2CNBu^n{}_2)_2$	2.2 – 2.3	High yields.$LiOH{\cdot}H_2O$ was used as base. Very soluble black products and crystals suitable for X-ray diffraction were obtained from ether.	64	60
$Cu(S_2CNBu^i{}_2)_2$			91	
$Cu(S_2CNHex^c{}_2)_2$			75	
$Cu[S_2CN(CH_2Ph)_2]_2$			85	
$Cu(S_2CNEtBu^n)_2$			69	
$Cu(S_2CNPr^nBu^i)_2$			70	
$Cu(S_2CNPr^n{}_2)_2$			74	
$Cu(S_2CNPr^i{}_2)_2$			58	
$Cu[S_2CN(allyl)_2]_2$			86	

[a] Equation numbers cited in text.

Table 2.3 Preparation of Antimony(III) Dithiocarbamates and Selected Physical Properties

Precursor	Synthesis[a]	Yield (%)	Appearance	Melting Point
$Sb[S_2CN(Me)(Bu^n)]_3$ (**4**)	2.2 – 2.3	58	Yellow solid	m.p: 98-100 °C
$Sb[S_2CN(Me)(Bz)]_3$ (**5**)	2.2 – 2.3	82	Sticky brown solid	m.p: 56-58 °C
$Sb[S_2CN(Me)(Hex^n)]_3$ (**6**)	2.2 – 2.3	82	Yellow oil	-

[a] Equation numbers cited in text.

2.2.2 Crystal Structures

Crystallographic quality crystals of the two analogous compounds $Sb[S_2CN(Me)(Bu^n)]_3$ (**4**) and $Sb[S_2CN(Me)(Bz)]_3$ (**5**) were both obtained from slow evaporation of a saturated dichloromethane solution at room temperature. The crystals were found to be air-stable and data collection was carried out at 150 K. The molecular structures of precursors (**4**) and (**5**) are shown in Figures 2.8 and 2.9, respectively. Relevant bond distances and angles are summarized in Tables 2.4 and 2.5 respectively, with further data provided in Appendix 4.

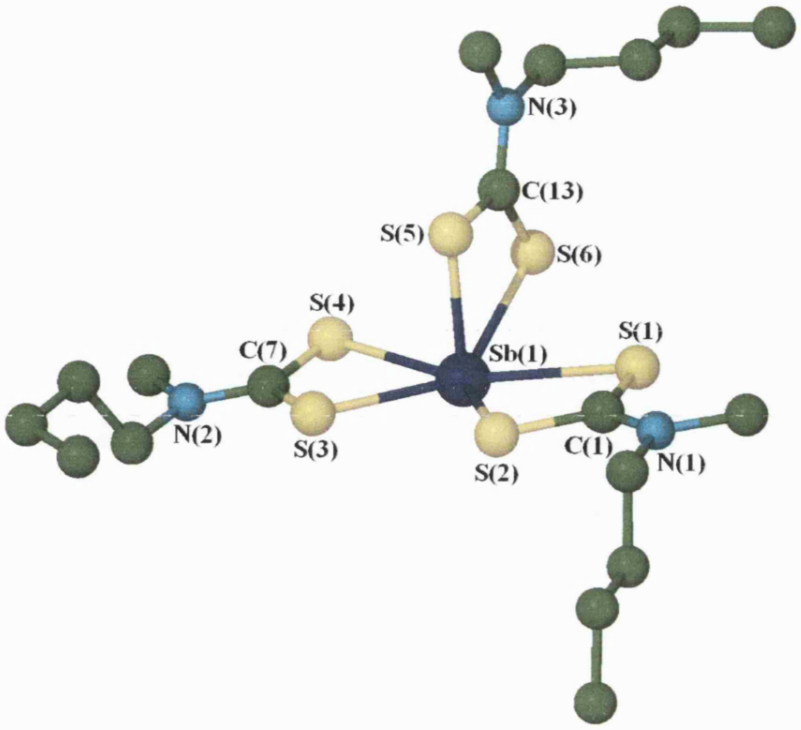

Figure 2.8 Molecular structure of $Sb[S_2CN(Me)(Bu^n)]_3$ (**4**).

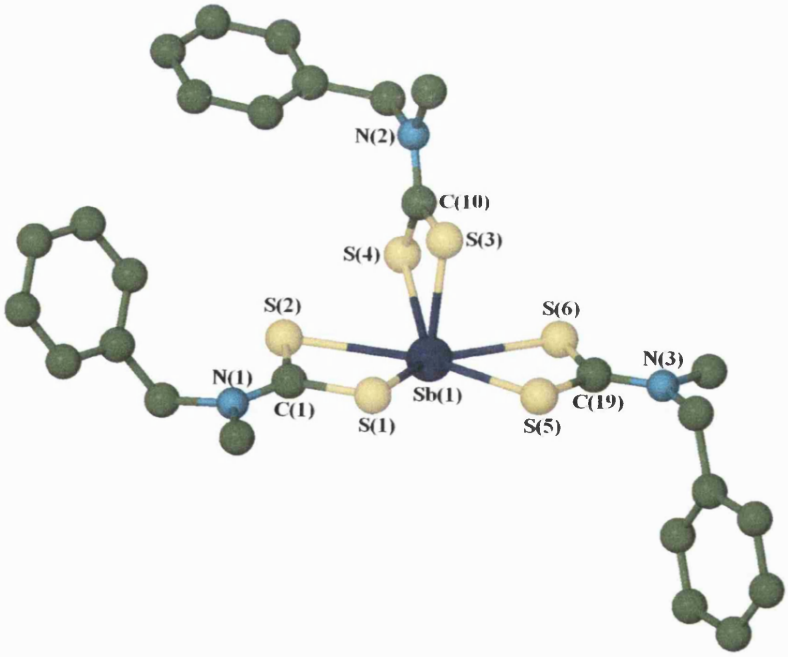

Figure 2.9 Molecular structure of $Sb[S_2CN(Me)(Bz)]_3$ (**5**).

Table 2.4 Selected Bond Distances (Å) for $Sb[S_2CN(Me)(Bu^n)]_3$ (**4**) and $Sb[S_2CN(Me)(Bz)]_3$(**5**)

	(4)		**(5)**
Sb(1)-S(1)	2.8848(13)	Sb(1)-S(1)	2.6853(10)
Sb(1)-S(2)	2.6536(13)	Sb(1)-S(2)	2.8076(10)
Sb(1)-S(3)	2.6388(12)	Sb(1)-S(3)	2.4787(9)
Sb(1)-S(4)	2.8187(13)	Sb(1)-S(4)	2.8518(9)
Sb(1)-S(5)	2.4948(12)	Sb(1)-S(5)	2.6718(9)
Sb(1)-S(6)	2.9098(12)	Sb(1)-S(6)	2.7907(10)
S(1)-C(1)	1.706(5)	S(1)-C(1)	1.730(4)
S(2)-C(1)	1.740(5)	S(2)-C(1)	1.719(4)
S(3)-C(7)	1.733(5)	S(3)-C(10)	1.748(4)
S(4)-C(7)	1.708(5)	S(4)-C(10)	1.696(4)
S(5)-C(13)	1.760(5)	S(5)-C(19)	1.732(4)
S(6)-C(13)	1.682(5)	S(6)-C(19)	1.704(4)
C(1)-N(1)	1.338(6)	C(1)-N(1)	1.332(5)
C(7)-N(2)	1.345(6)	C(10)-N(2)	1.327(4)
C(13)-N(1)	1.333(6)	C(19)-N(1)	1.336(5)

Table 2.5 Selected Bond Angles (°) for $Sb[S_2CN(Me)(Bu^n)]_3$ (**4**) and $Sb[S_2CN(Me)(Bz)]_3$ (**5**)

	(4)		(5)
S(1)-Sb(1)-S(2)	64.69(4)	S(1)-Sb(1)-S(2)	65.16(3)
S(3)-Sb(1)-S(4)	65.70(4)	S(3)-Sb(1)-S(4)	67.22(3)
S(5)-Sb(1)-S(6)	66.24(4)	S(5)-Sb(1)-S(6)	65.66(3)
S(1)-C(1)-S(2)	119.0(3)	S(1)-C(1)-S(2)	118.3(2)
S(3)-C(7)-S(4)	118.9(3)	S(3)-C(10)-S(4)	119.0(2)
S(5)-C(13)-S(6)	119.5(3)	S(5)-C(19)-S(6)	119.2(2)

The molecular structures of both precursors (**4**) and (**5**) present very similar structural characteristics. Both complexes are primarily monomeric in the solid state, presumably due to the steric effect of the bulky alkyl and aryl groups. In each molecule, the antimony atom is surrounded by six sulphur atoms from the three asymmetrically chelating dithiocarbamate ligands. Three of the sulphur atoms are more tightly coordinated to the antimony [2.4787(9)-2.6718(9) Å] and the other three sulphur atoms less tightly coordinated with longer Sb-S distances [2.7907(10)-2.9098(12) Å]. This asymmetric mode of coordination is reflected in the associated C-S distances of each dithiocarbamate group. Hence, a longer C-S distance [1.706(5)-1.740(5) Å] involves more tightly held sulphur atoms. This type of arrangement is unexceptional and similar characteristics had been reported for various metal dithiocarbamate complexes.[106, 129, 133, 134]

The geometry of both complexes can best be described as distorted octahedral, where the main cause of the distortion is the stereochemically active lone pair of the

antimony generating a *pseudo*-seven-coordinated arrangement. The structure of the core region of this type of molecules is minimally perturbed by the introduction of asymmetric amine substituents such as n-butyl or benzyl groups. The geometry of both precursors (**4**) and (**5**), described as distorted octahedral, is one of the geometries commonly adopted by antimony(III) dithiocarbamates (shown by Table 2.1). One of the main causes of the distorsion in the octahedral geometry is the different alignment of the sulphur atoms coordinated to the antimony atom. One dithiocarbamate group is generally occupying the position *trans* to the lone pair of the antimony and four sulphur atoms of the other two dithiocarbamate groups define the overall geometry of the molecule. These four sulphur atoms and the antimony atom in complexes (**4**) and (**5**) are coplanar, generating a more regular geometry, however in other antimony(III) dithiocarbamates, only the sulphur atoms *trans* to each other are coplanar with a torsion angle of 18 ° between the two planes (one formed by two sulphur atoms *trans* to each other and the antimony and the other plane formed by the other two sulphur atoms *trans* to each). An example of this is illustrated by Figures 2.10 and 2.11.

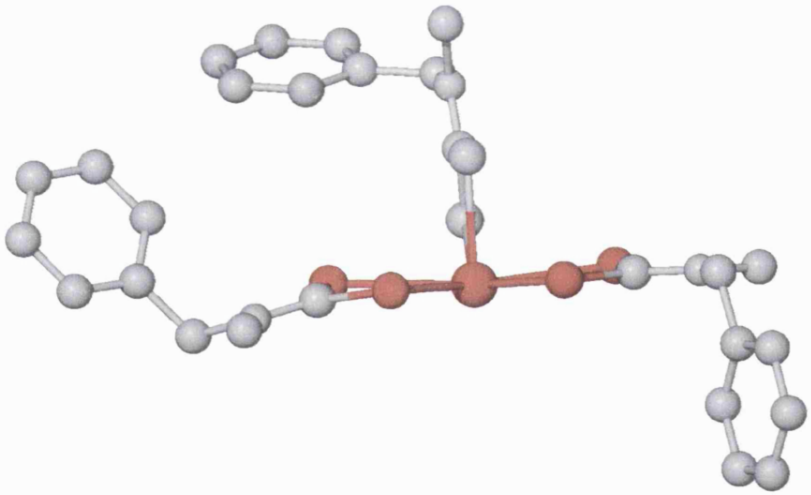

Figure 2.10 Molecular structure of $Sb[S_2CN(Me)(Bz)]_3$ (**5**) showing the plane formed by the antimony and sulphur atoms of two of the dithiocarbamate groups.

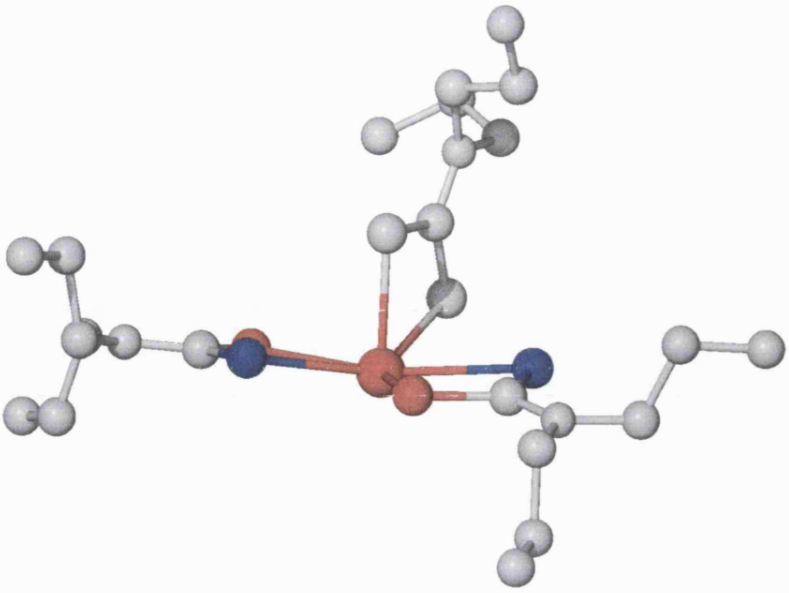

Figure 2.11 Molecular structure of $Sb(S_2CNPr^n_2)_3$ [131] showing the two planes formed by the antimony and sulphur atoms *trans* to each other.

It is important to remark that although bond distances and angles from both precursors (**4**) and (**5**) are in agreement with the ones reported for other antimony dithiocarbamates, the geometry differs from analogous Group 15 dithiocarbamates. Complexes such as $Sb[S_2CN(Me)Ph]_3$ [129] or $Bi[S_2CN(Me)(Hex^n)]_3$ [124] have been described as distorted triangular antiprisms. There are two triangular faces within the molecule, one of them is defined by three short M-S bonds and the other defined by the other three long M-S bonds. The face defined by the three long M-S bonds is deviated from the *pseudo*-3-fold axis where the stereochemically active lone pair of the metal is accommodated as a consequence of the electronic repulsion effects.

Another interesting feature observed in the structures of both precursors (**4**) and (**5**) is their nature to supramolecular association by adopting dimeric structures. Figures 2.12 and 2.13 show this dimeric association between molecules for both precursors $Sb[S_2CN(Me)(Bu^n)]_3$ (**4**) and $Sb[S_2CN(Me)(Bz)]_3$ (**5**). In precursor (**4**), the molecules associate quite strongly into dimers, with an Sb···Sb separation of 3.835 Å, supported by

intermolecular Sb(1)···S(1') interactions of 3.442 Å. To accommodate this, one dithiocarbamate is considerably less symmetrically chelated [Sb(1)-S(5) 2.4948(12), Sb(1)-S(6) 2.9098(12) Å] than the other pair. As a consequence, the corresponding S=C [S(6)-C(13) 1.682(5) Å] is shorter than the analogous S(1)-C(1) [1.706(5) Å] or S(4)-C(7) [1.708(5) Å]. Compound (**5**) adopts a similar dimeric structure, though the dimer is considerably less tightly bound [Sb···Sb 5.362; Sb(1)···S(6') 3.744 Å]. As can be seen in Figures 2.12 and 2.13, the monomer components are slipped with respect to each other. The reason why the Sb···Sb interaction occurs more strongly in precursor (**4**) is not obvious, nevertheless it might be due to steric factors, since the phenyl groups in precursor (**5**) are bulkier than the n-butyl groups in precursor (**4**). This type of intermolecular interaction has been reported for other Group 15 dithiocarbamates. Raston and co-workers[130] reported the crystal structure of $Bi(S_2CNEt_2)_3$ where the bismuth coordination sphere is completed by the close proximity of a sulphur atom from a neighbouring molecule at a distance of 3.210(5) Å, forming a dimer in the solid state.

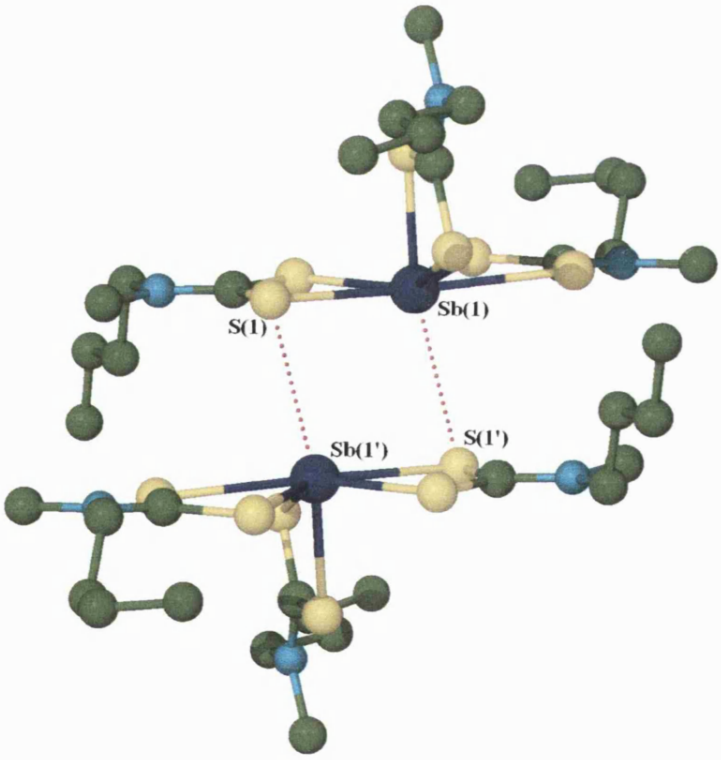

Figure 2.12 Molecular structure of $Sb[S_2CN(Me)(Bu^n)]_3$ (**4**) showing the dimeric association between molecules.

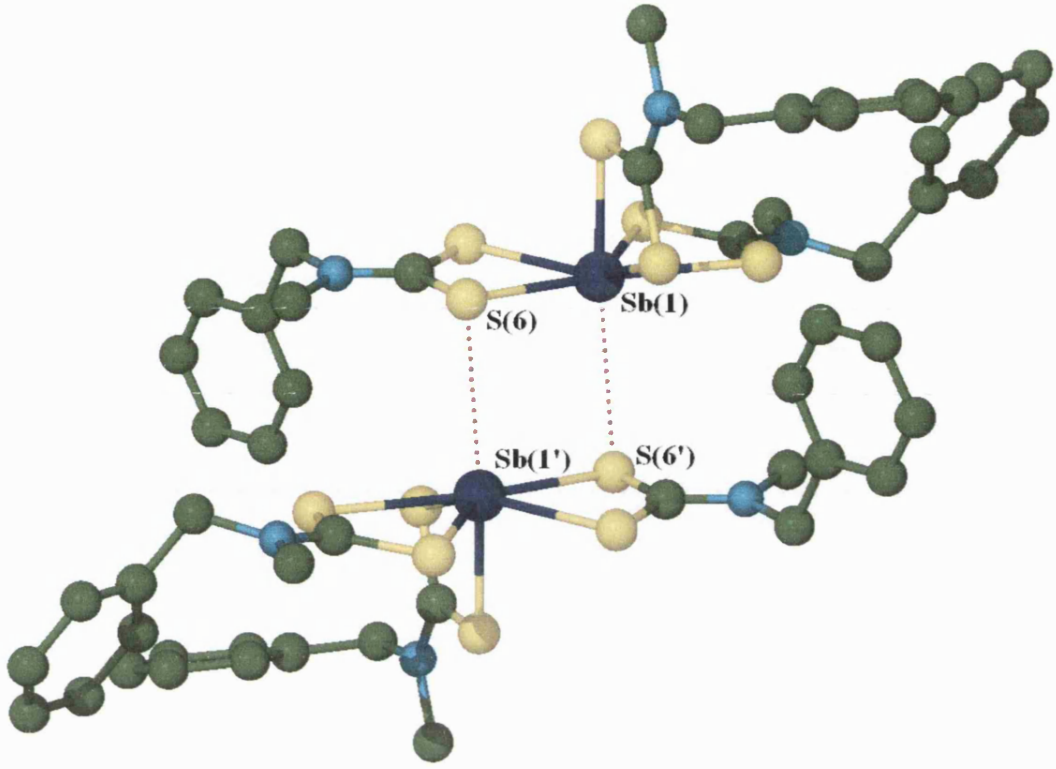

Figure 2.13 Molecular structure of $Sb[S_2CN(Me)(Bz)]_3$ (**5**) showing the dimeric association between molecules.

The structures of various antimony dithiocarbamates, symmetrical and asymmetrically substituted, and their intermolecular interactions have been recently reviewed by Tiekink *et al.*[129] , and both of the structural arrangements above have precedent, namely $Sb(S_2CNEt_2)_3$ and $Sb[S_2CN(CH_2)_5]_3$.

2.2.3 CVD Testing of Precursors

The precursors $Sb[S_2CN(Me)(Bu^n)]_3$ (**4**), $Sb[S_2CN(Me)(Bz)]_3$ (**5**) and $Sb[S_2CN(Me)(Hex^n)]_3$ (**6**) were tested as CVD precursors. Details of the apparatus are provided in Appendix 2.

All the precursors are air- and moisture-stable and soluble in most common organic solvents. Asymmetrically substituted R groups were chosen in order to decrease the melting point of the complexes and therefore increase their volatility due to the less dense packing of the molecules in the lattice. The increase in the volatility of the complexes should give a more suitable CVD precursor and hence better results in the film deposition.

This section gives details of the tests carried out on compounds (**4**), (**5**) and (**6**) by Thermogravimetric Analysis (TGA) in order to have an indication of the temperature at which decomposition might be expected to start and reach completion and to determine suitable conditions for the deposition of the film.

TGA of precursor (**4**) shows the decomposition to begin at approximately 220 °C and it is effectively over by 370 °C (Figure 2.14), where the residual weight observed corresponds to Sb_2S_3, 28.8 % (theoretical 27.9 %). Above 400 °C, weight loss matches with the transformation Sb_2S_3 to Sb_2O_3, 24.8 % (theoretical 23.9 %). Presence of Sb_2O_3 is also observed in the films, as it will be discussed later. This is in agreement with work reported in the literature about the thermal stability of antimony (III) sulphide. Thermal and oxidative studies reported that when oxygen is present the stability of antimony sulphides may vary, therefore, antimony trisulphide is converted to the cubic form of antimony trioxide (Sb_2O_3) at temperatures around 400 °C and antimony tetraoxide (Sb_2O_4) at higher temperatures.[135]

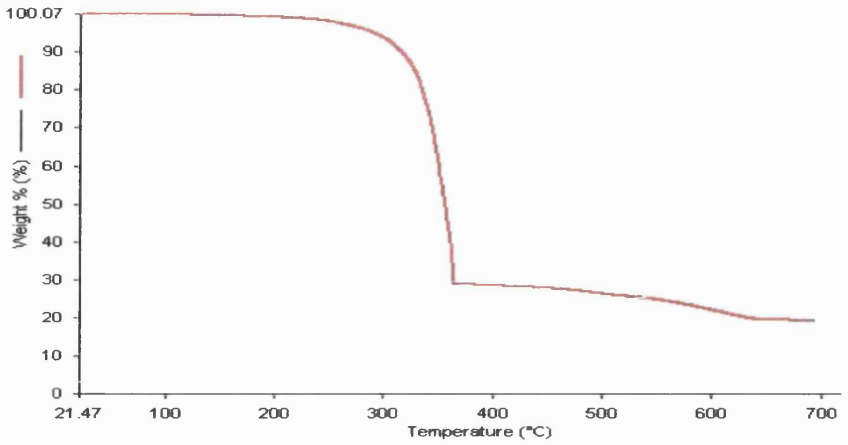

Figure 2.14 TGA of $Sb[S_2CN(Me)(Bu^n)]_3$ (**4**).

TGA of precursor (**5**), illustrated by Figure 2.15, present a similar shape to Fig. 2.12 and shows decomposition of the product starts at approximately 200 °C and it is effectively over by 370 °C where the residual weight observed corresponds to Sb_2S_3, 20.0 % (theoretical 19.4 %).

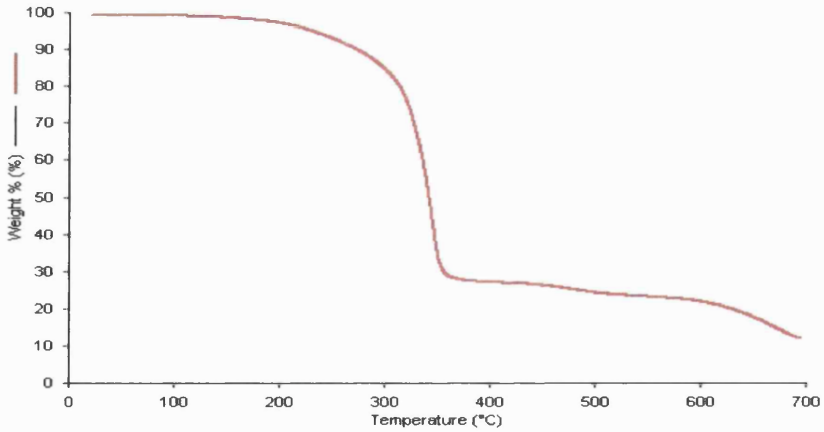

Figure 2.15 TGA of $Sb[S_2CN(Me)(Bz)]_3$ (**5**).

TGA of precursor (**6**), illustrated by Figure 2.16, also present similar shape than precursors (**4**) and (**5**) showing decomposition of the product starts at approximately 210 °C and it is effectively over by 380 °C were the residual weight observed corresponds to Sb_2S_3, 17.6 % (theoretical 21.0 %). Here the observed residual weight is lower than the theoretical; this loss could be associated with evaporation of the precursor, which is an oil..

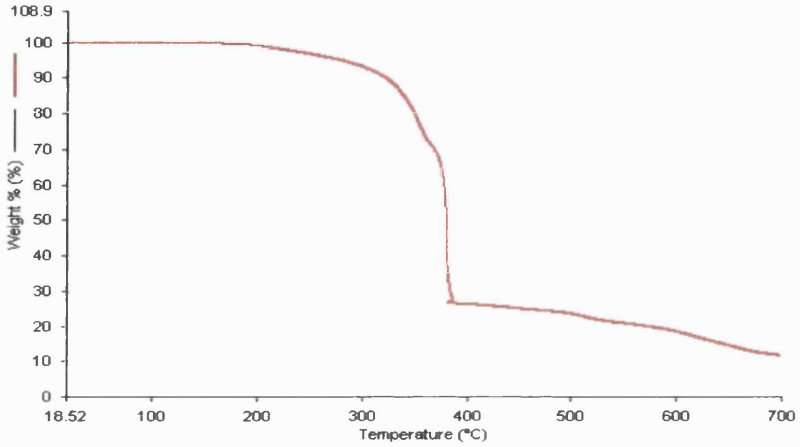

Figure 2.16 TGA of $Sb[S_2CN(Me)(Hex^n)]_3$ (**6**).

Despite their relatively low melting points, none of (**4**)-(**6**) proved a viable precursor for low pressure (LP) CVD. Carry over even at relatively elevated temperatures ($90 < T < 300^oC$) lead to poor substrate coverage and extensive decomposition of the precursor. It is plausible that the dimeric nature of these compounds, at least as far as (**4**) and (**5**) are concerned, is responsible for this lack of volatility.

Complete decomposition of both (**4**) and (**5**) at 400°C under dynamic vacuum generated black crystalline materials of needle morphology with an estimated length of 100 μm and 10 μm in width (Figure 2.17) which were identified as Sb_2S_3 (Stibnite) by their powder diffraction patterns (Figure 2.18) which matches that of stibnite, Sb_2S_3 (PDF 06-0474); the derived unit cell dimensions are identical to those reported by others (a = 3.84, b = 11.23, c = 11.31 Å, orthorhombic).[136] Quantitative EDAX analysis showed only minor signals due to carbon and oxygen and an Sb:S ratio of 1.55 giving the formula $Sb_2S_{3.1}$. Microanalysis of the black residue from (**4**) indicated the presence of 0.57% carbon, 0.03%

hydrogen and 0.00% nitrogen, though these values increased markedly for (**5**) (9.25, 1.24, 0.25%, respectively) for decomposition under the same conditions.

Figure 2.17 SEM of the residue after decomposition of (**5**) at 400°C under a dynamic vacuum. Red bar = 100 μm.

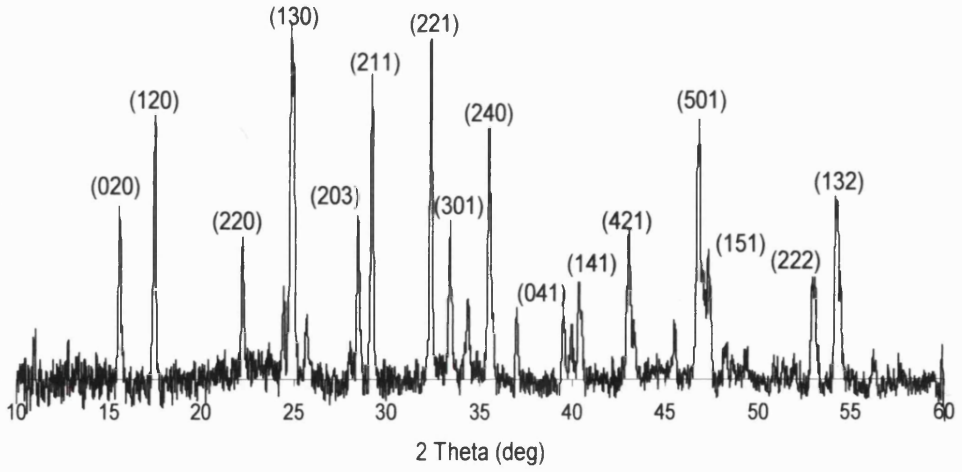

Figure 2.18 Glancing angle X-ray pattern for the black solid formed by the decomposition of (**4**) under vacuum at 400°C.

As a consequence of the lack of volatility but good solubility of each compound in common organic solvents, deposition was attempted *via* AACVD methods. All three precursors displayed broadly similar deposition characteristics which are strongly temperature dependent. Deposition conditions for the films analysed are displayed in Table 2.6.

Table 2.6 AACVD conditions for experiments using precursors (**4**) to (**6**).

Precursor	Reactor Temperature (°C)	Carrier Gas (Ar) Flow Rate(l/min)	Run Time (h)	Film Color
(**4**)	460 °C	0.8	2.5	Light Grey
(**4**)	395 °C	0.8	2.5	Dark Grey
(**5**)	395 °C	0.8	2.5	Light Brown
(**5**)	340 °C	0.8	2.5	Light Brown
(**6**)	400 °C	0.8	2.5	Light Grey
(**6**)	260 °C	0.8	3.0	Dark Grey

2.2.4 Film Analysis

Films were examined by visual inspection, Energy Dispersive X-ray Analysis (EDAX) and Scanning Electron Microscopy (SEM). Glancing Angle X-ray diffraction studies were also performed on the films to determine if they were crystalline, and then confirm the nature of the deposited film. It was possible to perform quantitative EDAX on all films due to the suitable size of the particles deposited on the surface of the film.

2.2.4.1 *Butylmethyldithiocarbamate Antimony (III) - $Sb[S_2CN(Me)(Bu^n)]_3$ (4)*

T = 460 °C: The films are grey and thin and show poor substrate coverage, precluding XRD analysis. SEM, represented in Figure 2.19, reveals the presence of both needle and octahedral deposits which qualitative EDAX indicates contain antimony but not sulphur; oxygen is also seen, but this is to be expected as the underlying glass substrate is also exposed to the X-rays. When the octahedral particles were analysed by quantitative EDAX only antimony metal was found.

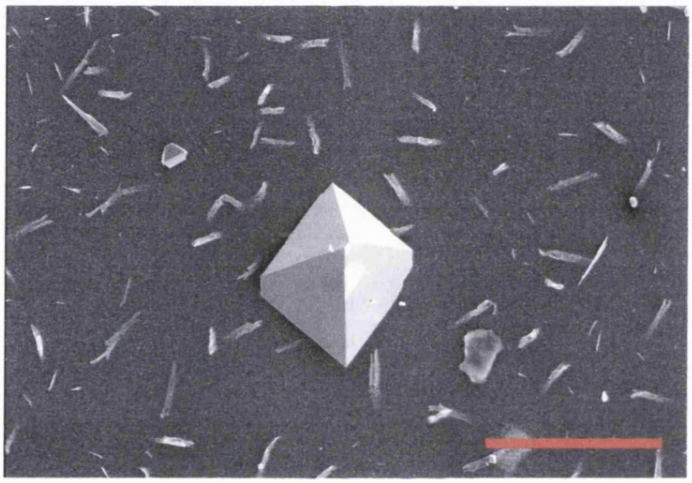

Figure 2.19 SEM of film grown from precursor (**4**) at 460 °C. Red bar = 100 μm.

T = 395 °C: A thin grey film was obtained, however, now cubic deposits were present in the film. EDAX of the film (Figure 2.20) show the presence of a large amount of oxygen and quantitative analysis reveals a relation between antimony and oxygen matching with the formula Sb_2O_3 (atomic %, Sb: 40.7; O: 59.2). SEM of the Sb_2O_3 found in the film is shown in Figure 2.21. We have noted in other studies that antimony metal has a similar prismatic appearance, so it is possible that these oxides are formed *via* Sb(0) as an intermediate.[137]

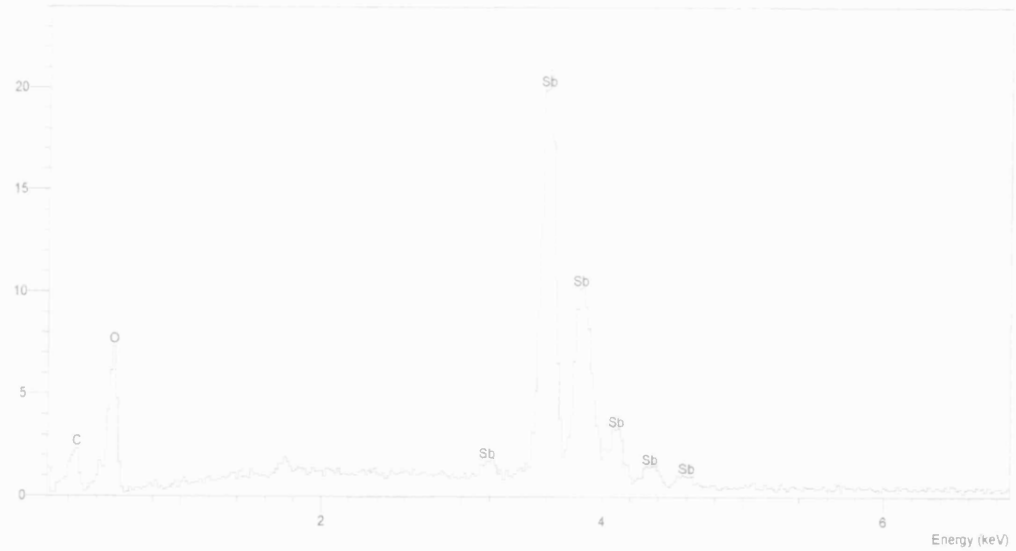

Figure 2.20 EDAX qualitative analysis of film grown from precursor from (**4**) at 460 °C.

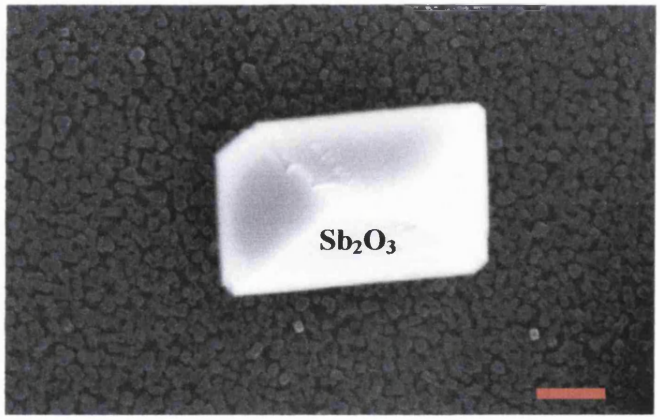

Figure 2.21 SEM of film grown from precursor (**4**) at 395 °C. Red bar = 1 μm.

2.2.4.2 *Benzylmethyldithiocarbamate Antimony (III) - $Sb[S_2CN(Me)(Bz)]_3$ (5)*

Experiments were carried out at 395 and 340 °C. Basically two main crystalline morphologies were found when the films were investigated by SEM. One sharp needle-like

growth, with an estimated length of 30 μm, corresponding by quantitative analysis with the oxysulphide species Sb_2OS_2, *Kermesite*, (atomic %, Sb: 38.9; O: 21.2; S: 39.8) and a smaller and prismatic one corresponding with Sb_2O_3 (atomic %, Sb: 41.4; O: 58.5). At both temperatures, the same types of species were found, however, more round-shape particles corresponding to Sb_2O_3 were found at 395 °C. SEM image of the film obtained at 395 °C is shown in Figure 2.22.

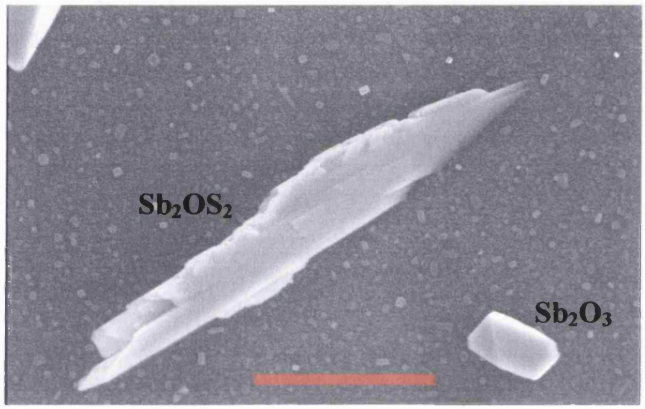

Figure 2.22 SEM of film grown from precursor (**5**) at 395 °C. Red bar = 10 μm.

EDAX of the film grown at 345 °C in which the antimony, oxygen and sulphur peaks are labelled is shown in Figure 2.23.

Figure 2.23 EDAX qualitative analysis of film grown from precursor from (**5**) at 345 °C.

The XRD pattern of the film grown from precursor (**5**) at 395 °C is shown by Figure 2.24. While the pattern is more complex than that for the bulk decomposition products identified as Sb_2S_3, several lines are indexable to this phase though the match is not as precise as for the bulk material. Additional weaker lines imply that the film is not phase-pure, though no additional components can be identified with any certainty. Of the diffraction lines that are clearly not due to Sb_2S_3, the two most intense (d = 3.240, 5.148 Å) match antimony oxide (either [222] senarmonite d = 3.216, PDF 75-1565 or [111] Sb_2O_4 d = 3.241 Å, PDF 78-2067) and sodium antimony sulphide $Na_3Sb_2S_4$ ([110], d = 5.150 Å, PDF 35-1016), respectively, the latter a plausible product involving sodium from the glass substrate. Other, weaker lines (marked U in Figure 2.24) show some similarity to the cited pattern for KSb_5S_8, which, like $Na_3Sb_2S_4$, might arise from an interaction with the glass substrate.

There is no evidence in the XRD pattern of the film to suggest crystalline antimony oxy-sulphide is present, so oxygen incorporation into a Sb_2S_3 lattice seems more plausible. Such a scenario, but involving only trace amounts of oxygen, might also explain the minor deviation in observed d-spacing for the Sb_2S_3 component of the grey film.

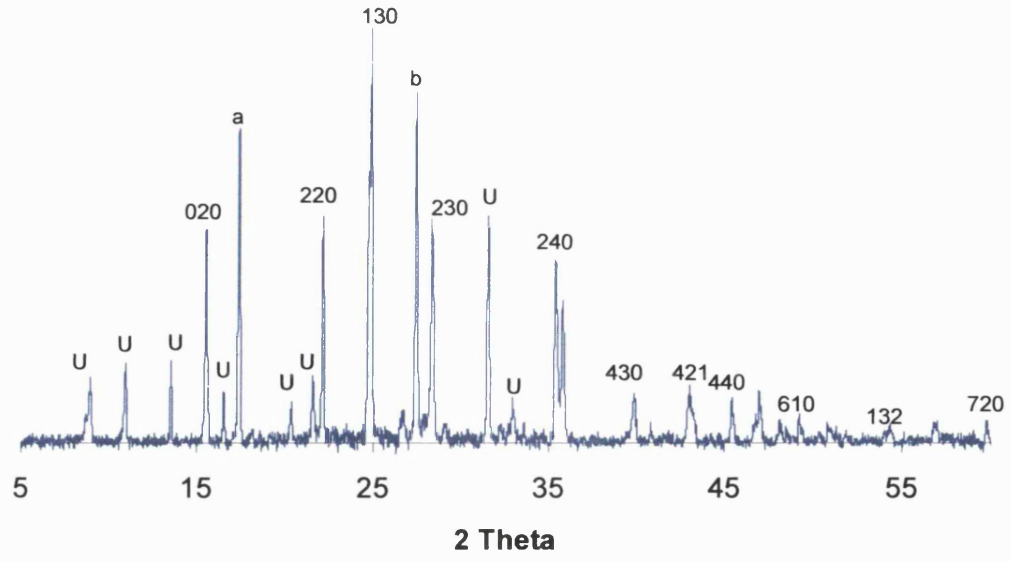

Figure 2.24 Glancing angle X-ray pattern of the film grown from (**5**) at 395°C. Peaks marked U could not be assigned.

2.2.4.3 *Hexylmethyldithiocarbamate Antimony (III) - $Sb[S_2CN(Me)(Hex^n)]_3$ (5)*

T = 400 °C: In general the substrate coverage was poor and the glass surface was covered with a discontinuous film (Figure 2.25), dominated by prisms (EDXS: Sb:O 1.06 – 1.23). The low Sb:O ratio here possibly implies the formation, and subsequent oxidation of Sb(0). Also it is observed a much smaller number of hollow tubes corresponding by quantitative analysis with the antimony trisulphide, Sb_2S_3 (atomic %, Sb: 37.3; S: 56.8).

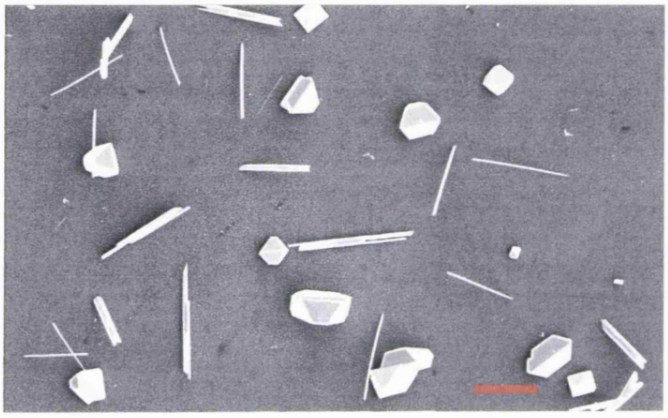

Figure 2.25 SEM of film grown from precursor (**6**) at 400 °C. Red bar = 10 μm.

260 °C: A thin grey film was deposited but now the hollow tubes (15 x 0.6 μm) dominate over the prisms, though the quantitative analysis of the two components remains broadly unchanged (tube: Sb:S average 1.30; prism Sb:O average 1.15). Figure 2.26 shows a SEM image of the fibers.

It would appear from this set of experiments that bulk decomposition of asymmetrically-substituted dithiocarbamates under dynamic vacuum yields phase-pure Sb_2S_3, and also that the precursors are insufficiently volatile to be used in LPCVD experiments but have sufficient solubility for AACVD. Furthermore, AACVD using these precursors can generate films which contain Sb_2S_3 but these are not phase-pure and become increasingly susceptible to oxidation as the deposition temperature increases, particularly on the substrate surface.

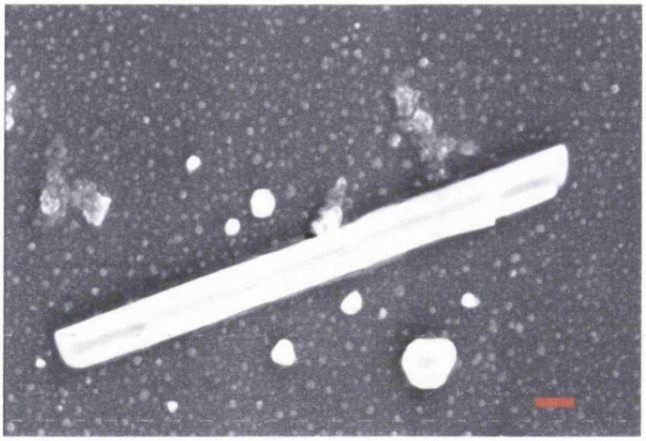

Figure 2.26 SEM of film grown from precursor (**6**) at 260 °C. Red bar = 1 μm.

This observation is in accord with an FT-IR study of the thermal stability of Sb_2S_3 under an N_2 flow (thus mirroring the AACVD conditions), which found that the sulphide was stable up to 275°C but is completely converted to Sb_2O_3 by 400°C and Sb_2O_4 at between 650 – 800°C.[135] The comment made by others that the optimum temperature for conversion of amorphous red Sb_2S_3 (with some crystalline material embedded) to fully crystalline black Sb_2S_3 is *ca.* 270°C is consistent with these findings.[28]

In conclusion, it would thus seems that any approach to obtaining high quality Sb_2S_3 films requires either a precursor which either decomposes cleanly at T < 300°C for use in AACVD, or is sufficiently volatile such that an LPCVD route is possible and where the decomposition temperature is less crucial. The origin of the oxygen in some of the films examined is debatable, but as this is absent when the precursors are decomposed under dynamic vacuum it would seem likely that it originates from the carrier gas and/or solvent unique to the AACVD experiments. Sb_2S_3 seems unusually susceptible to oxidation, at even modest temperatures as far as CVD is concerned, so LPCVD as a deposition technique would appear more attractive than AACVD in this case. We will report in Chapters three and four successful solutions using both these methods, employing antimony(III) xanthates and thiolates, respectively.

2.3 EXPERIMENTAL

Starting materials were commercially obtained (e.g. Aldrich) and were used without further purification unless otherwise stated. Standard Schlenck line techniques were employed where applicable. Further details about instrumentation used are given in Appendix 1.

2.3.1 Preparation of lithium butylmethyldithiocarbamate - $Li[S_2CN(Me)(Bu^n)]\cdot H_2O$ (1)

N,N-methylbutylamine (6.15 mL, 52 mmol) was added carefully under an atmosphere of nitrogen to a solution of BuLi (29.05 mL, 52 mmol) in anhydrous hexane (50 mL). After stirring for 30 min, carbon disulfide (2.95 mL, 52 mmol) was carefully added to this solution. The reaction was stirred for 12 hours and then the solvent was removed under vacuum. The residue was washed with hexane (2 x 50 mL) and dried under vacuum, producing 7.87 g (90%) of (**1**) as a yellow powder.

Microanalysis:

Found (calc.) for $C_6H_{14}NS_2OLi$ (**1**): C 40.47 (38.48)%; H 7.38 (7.53)%; N 7.68 (7.48)%.

^{1}H-NMR [δ (ppm), $CDCl_3$]:

4.90 (br s, H_20), 3.95 (2*H*, m, NCH_2), 3.40 (3H, s, NCH_3), 1.55 (2H, m, β-CH_2), 1.25 (2H, m, γ-CH_2), 0.85 (3H, t, CH_3).

^{13}C-NMR [δ (ppm), $CDCl_3$]:

49.0 (NCH_2), 33.3 (NCH_3), 28.5 (β-CH_2), 19.2 (γ-CH_2), 12.8 (CH_3).

2.3.2 Preparation of lithium benzylmethyldithiocarbamate - Li[S_2CN(Me)(Bz)] (2)

It was prepared by the same procedure as (**1**) using N,N-methylbenzylamine (6.72 mL, 52 mmol) and giving 9.60 g (91%) of a beige powder.

Microanalysis:

Found (calc.) for $C_9H_{10}NS_2Li$ (**2**): C 52.20 (53.18)%; H 5.41 (4.96)%; N 6.65 (6.89)%.

^{1}H-NMR [δ (ppm), THF-d_8]:

7.30-7.10 (5H, m, *H*-Ph), 5.40 (2H, s, NCH_2), 3.30 (3H, NCH_3).

^{13}C-NMR [δ (ppm),THF-d_8]:

214.3 (S_2*C*N), 138.2 (H_α-Ph), 127.5 (H_β-Ph), 127.2 (H_γ- Ph), 126.0 (Ph), 57.2 (N*C*H_2), 39.2 (N*C*H_3)

2.3.3 Preparation of lithium hexylmethyldithiocarbamate – Li[S_2CN(Me)(Hex^n)]·H_2O (3)

(**3**) was prepared by the same procedure as (**1**) and (**2**) using N,N-methylhexylamine (2.00 mL, 13.19 mmol) and a solution of BuLi (7.36 mL, 13.19 mmol) in anhydrous hexane (20 mL). 2.00 g (77%) of (**3**) as a pale yellow powder was obtained.

Microanalysis:

Found (calc.) for $C_8H_{18}NS_2OLi(H_2O)$ (**3**): C 45.60 (44.62)%; H 9.94 (8.42)%; N 6.64 (6.50)%.

^{1}H-NMR [δ (ppm), $CDCl_3$]:

4.90 (br s, *H*$_2$0), 3.90 (2H, m, NCH_2), 3.40 (3H, s, NCH_3), 1.60 (2H, m, β-CH_2), 1.20 (6H, m, γ-ε-CH_2), 0.80 (3H, t, CH_3).

^{13}C-NMR [δ (ppm), $CDCl_3$]:

206.3 (S_2*C*N), 33.3 (N*C*H_3), 30.6 (N*C*H_2), 25.8 (β-*C*H_2), 25.6 (γ-*C*H_2), 21.6 (δ-*C*H_2), 21.5 (ε-*C*H_2), 13.0 (*C*H_3).

2.3.4 Preparation of butylmethyldithiocarbamate antimony (III) – $Sb[S_2CN(Me)(Bu^n)]_3$ (4)

A solution of compound (**1**) (4.33 g, 25.7 mmol) in methanol (30 mL) was added dropwise to a solution of $SbCl_3$ (1.95 g, 8.6 mmol) in methanol (20 mL). After stirring overnight, a yellow solid appeared and the solvent was evaporated under vacuum. Then CH_2Cl_2 (40 mL) was added and the soluble material separated by cannula filtration. The solvent was evaporated and the resulting yellow powder recrystallised from toluene giving 3.00 g (58%) of (**4**) as bright yellow crystals. m.p: 98-100 °C.

Microanalysis:

Found (calc.) for $C_{18}H_{36}N_3S_6Sb$ (**4**): C 35.40 (35.50)%; H 5.74 (5.92)%; N 7.06 (6.92)%.

^{1}H-NMR [δ (ppm), $CDCl_3$]:

3.80 (2H, m, NCH_2), 3.35 (3H, s, NCH_3), 1.65 (2H, m, β-CH_2), 1.30 (2H, m, γ-CH_2), 0.90 (3H, t, CH_3).

^{13}C-NMR [δ (ppm), $CDCl_3$]:

198.92 (S_2CN), 55.2 (NCH_2), 40.6 (NCH_3), 28.0 (β-CH_2), 19.0 (γ-CH_2), 12.8 (CH_3).

2.3.5 Preparation of benzylmethyldithiocarbamate antimony (III) - $Sb[S_2CN(Me)(Bz)]_3$ (5)

(**5**) was prepared by the same procedure as (**4**), adding to a solution of $SbCl_3$ (1.20 g, 5.3 mmol) in methanol (15 mL), a solution of compound (**2**) (3.20 g, 15.8 mmol) in methanol (35 mL). Finally, 3.10 g (82%) of (**5**) as a very sticky solid was obtained. m.p: 56-58 °C.

Microanalysis:

Found (calc.) for $C_{27}H_{30}N_3S_6Sb$ (**5**): C 47.90 (45.60)%; H 5.91 (5.92)%; N 4.21 (4.22)%.

^{1}H-NMR [δ (ppm), $CDCl_3$]:

7.35-7.15 (5H, m, *H*-Ph), 5.05 (2H, s, NCH_2), 3.25 (3H, NCH_3).

^{13}C-NMR [δ (ppm), $CDCl_3$]:

135.0 (C_α-Ph), 129.3 (C_β-Ph), 128.6 (C_γ-Ph), 128.3 (C_δ-Ph), 59.6 (NCH_2), 41.3 (NCH_3).

2.3.6 Preparation of hexylmethyldithiocarbamate antimony (III) - $Sb[S_2CN(Me)(Hex^n)]_3$ (6)

To a solution of $SbCl_3$ (0.85 g, 3.73 mmol) in 10 mL of methanol, a solution of compound (**3**) (2.20 g, 11.2 mmol) in 35 mL of methanol was added dropwise. After stirring overnight, a yellow and sticky solid appears and the solvent was evaporated under vacuum. The solid was washed with hexane (2 x 30 mL) and the product extracted with CH_2Cl_2. The solvent was evaporated leaving 2.10 g (82%) of compound (**6**) as a very sticky yellow solid.

Microanalysis:

Found (calc.) for $C_{24}H_{48}N_3S_6Sb$ (**6**): C 40.90 (41.56)%; H 6.93 (6.93)%; N 5.86 (6.06)%.

^{1}H-NMR [δ (ppm), $CDCl_3$]:

3.75 (2H, m, NCH_2), 3.25 (3H, s, NCH_3), 1.60 (2H, m, β-CH_2), 1.25 (6H, m, γ-ε-CH_2), 0.80 (3H, t, CH_3).

^{13}C-NMR [δ (ppm), $CDCl_3$]:

200.3 (S_2CN), 56.8 (NCH_3), 42.0 (NCH_2), 31.8 (β-CH_2), 27.3 (γ-CH_2), 26.8 (δ-CH_2), 22.9 (ε-CH_2), 14.4 (CH_3).

Chapter Three

Antimony(III) Xanthates

3.1 INTRODUCTION

Xanthates were first discovered by Zeise[138] in 1822 and have been used since then by industry as flotation agents, reagents for the separation and quantitative determination of a large number of cations,[139] biocides, catalysis and additives for lubricants.[98]

These xanthate ligands are analogous to dithiocarbamates and therefore are expected to resemble them in their bonding mode. Although xanthates can act as monodentate ligands (a), they are more often found acting as isobidentate ligands (b) when coordinated to metal atoms. Other possible coordination modes of xanthates include: anisobidentate (c), additional metal-oxygen interaction (d), bimetallic bridging through sulphur atoms (e) and occasionally bimetallic bridging where the oxygen atom becomes involved (f). All these coordination patterns of xanthate ligands are illustrated by Figure 3.1. [140]

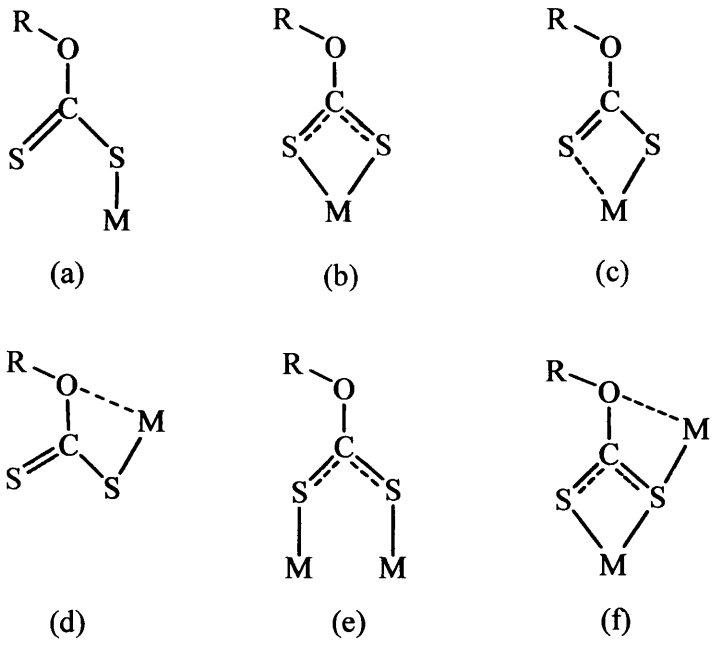

Figure 3.1 Coordination patterns of xanthate ligands.[140]

Surprisingly, despite the widespread study of the chemistry of metal xanthates during the last decades, Group 15 xanthates have received little attention as potential precursors for the deposition of sulphide material by CVD. In particular, to the best of our knowledge, nothing has been reported about the formation of Sb_2S_3 thin films by CVD from antimony xanthates.

Nevertheless, regardless of the lack of information of Group 15 xanthates in the CVD field, an extensive number of studies have been reported about the structural chemistry of these compounds. A wide range of Group 15 *tris*-xanthates with general formula $M(S_2COR)_3$ (M = As, Sb and Bi ; R = Me, Et, ^{i}Pr, ^{n}Pr, Bz, etc) have been reported previously.[98] Figures 3.2 and 3.3 show the molecular structures of some of these complexes.

The geometry of these *tris*-xanthates is generally distorted octahedral with coordination number 6 and with three strong and three weak M-S bonds. Variations of the R groups within the ligands lead to the formation of dimeric to polymeric structures by "secondary interactions" between the metal centre and the sulphur atoms of a neighbouring molecule, which plays a key role in stabilising the crystal structures (Figure 3.3).

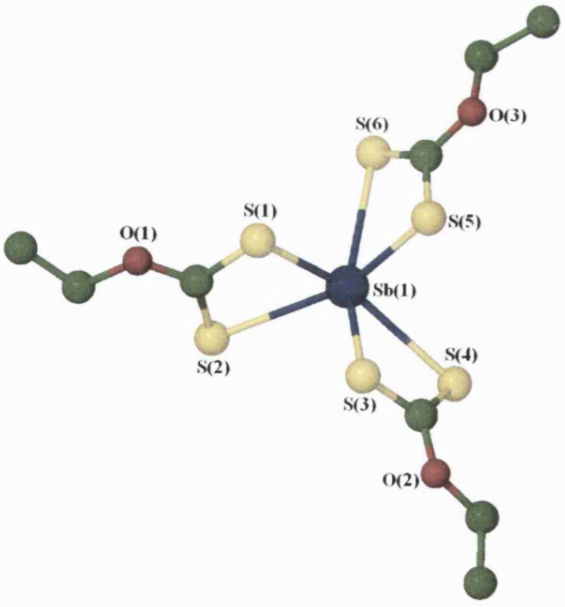

Figure 3.2 Molecular structure of $Sb(S_2COEt)_3$.[141]

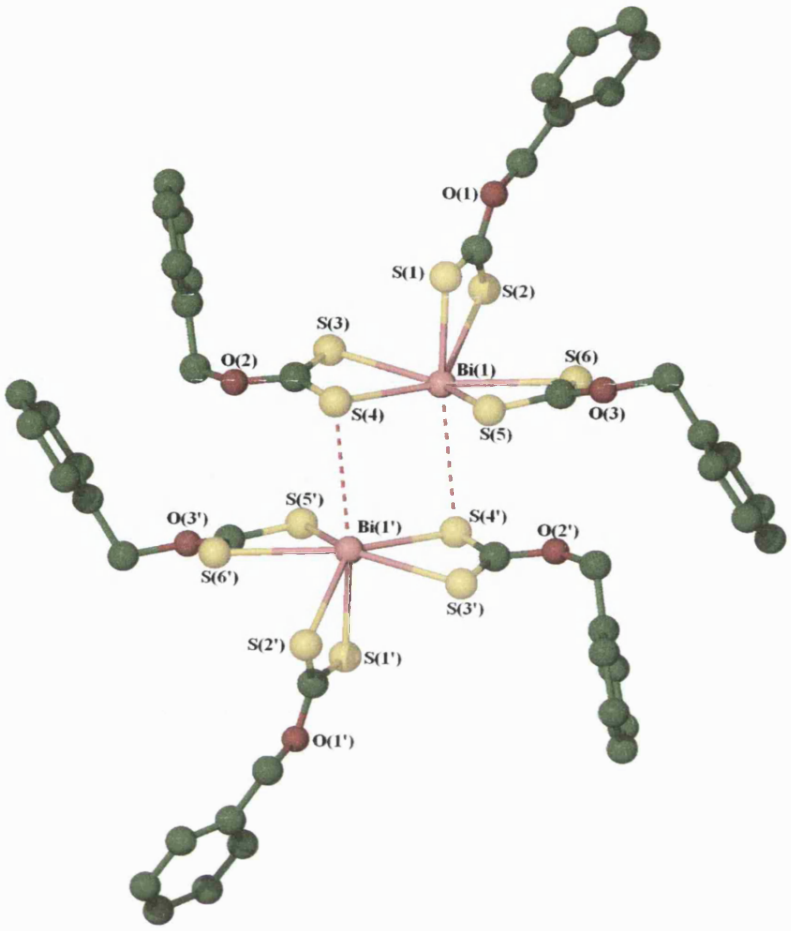

Figure 3.3 Molecular structure of $Bi(S_2COBz)_3$ [142] showing the dimeric association between molecules.

Besides this kind of homoleptic complex, an extensive number of mixed ligand complexes have also been reported. This includes haloantimony (III) xanthates with general formula $SbX(S_2COR)_2$ (X = Cl, Br and I).[143] Also, several organometallic derivatives with one or two alkyl/aryl groups with formula such as $RSb(S_2COR')_2$ and $R_2Sb(S_2COR')$ respectively have been structurally characterised. One of these species is illustrated by Figure 3. 4.[144]

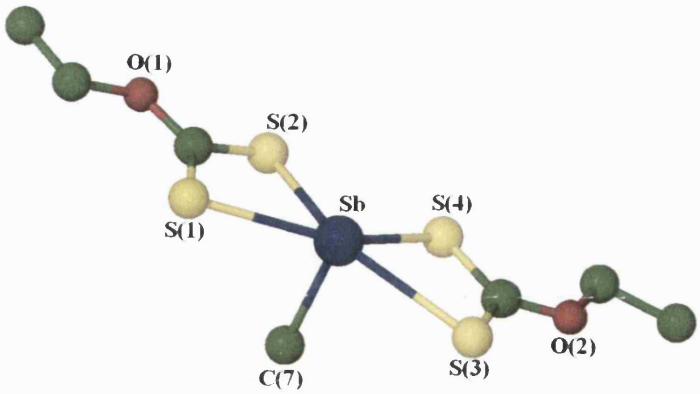

Figure 3.4 Molecular structure of $MeSb(S_2COEt)_2$ [144]

In contrast with the large number of antimony (III) xanthates reported in the literature, only a few examples of antimony (V) xanthates have been prepared i.e. $Me_3Sb(Xan)_2$, but without structural characterisation. These pentavalent complexes are stabilised by the σ-electron donation from the methyl groups. Some examples of these complexes include $Me_3Sb(S_2COBz)_2$ and $Me_3Sb(S_2CON\text{-pyrrolidine})_2$.[145]

Some of the structurally characterised examples of antimony (III) xanthates reported in the literature, together with coordination number, geometry and significant bond distances are summarised in Table 3.1.

In this chapter, the preparation, characterisation and properties of a series of antimony(III) xanthates and haloantimony(III) xanthates as CVD candidates for Sb_2S_3 and SbSI films are evaluated. Also, it is important to highlight that it has been reported that thermal gravimetric analysis reveals that metal xanthates, e.g. bismuth, exhibit lower decomposition temperatures (<150 °C) than dithiocarbamates.[146] This decrease in the decomposition temperature lowers the risk of oxygen incorporation by the conversion of antimony trisulphide to antimony trioxide (Sb_2O_3) at temperatures around 300 °C.[135]

Table 3.1 Coordination Geometries Exhibited by Antimony(III) Xanthates

Coordination Number	Geometry	Example	Range of Sb-S (Å)	Ref.
6	Distorted Octahedral	$Sb(S_2COEt)_3$	2.511(2)-3.002(3)	141
6	Distorted Octahedral	$Sb(S_2COPr^i)_3$	2.508(1)-3.006(1)	147
5	Pentagonal Bipyramidal	$MeSb(S_2COEt)_2$	2.580(7)-2.904(8)	144
5	Pseudopentagonal Bipyramidal	$PhSb(S_2COEt)_2$	2.4987(17)-2.5377(19)	148
6	Distorted Pseudo-octahedral	$Sb(S_2COEt)_2Br$	2.493(5)-2.993(4)	143
6	Pentagonal Bipyramidal	$Sb(oxine)_2(S_2COEt)$	3.059(2)-3.171(2)	141

3.2 RESULTS AND DISCUSSION

3.2.1 Synthetic Routes

The synthesis of metal *tris*-xanthates, like their analogous dithiocarbamates, is relatively easy to achieve and there are different methods available that mainly depend on the type of xanthate used. Generally, xanthate salts and their correspondent metal complexes are air- and moisture-stable and soluble in most organic solvents, this again being the case for the compounds described in this chapter.

There is one xanthate commercially available as a salt, KS_2COEt, which is easy to handle and just by mixing it with the metal source (usually metal halides) the corresponding

metal xanthate can be rapidly obtained (Equation 3.1). However, other derivatives are not commercially available and need to be prepared by deprotonation of the alcohol with a suitable base (usually potassium hydroxide) to form the corresponding alkoxide and then reaction with carbon disulphide. This route is represented by Equation 3.2.

$$MCl_n + n\,KS_2COEt \xrightarrow{\text{dichloromethane}} M(S_2COEt)_n + n\,KCl \qquad [3.1]$$

$$ROH + KOH \xrightarrow{-H_2O} RO^-K^+ \xrightarrow{CS_2} KS_2COR \qquad [3.2]$$

Haloxanthates complexes can be synthesized following three methods. The first two methods involve the reaction between the metal halide with either the already prepared xanthate ligand (Equation 3.3) or with the trisxanthate metal complex (Equation 3.4.) The third method consists in reacting the appropriate stoichiometric amount of the trisxanthate metal complex with the desired halide, illustrated by Equation 3.5.

$$MX_3 + 2\,KS_2COR \xrightarrow{\text{dichloromethane}} M(S_2COR)_2X + 2\,KX \qquad [3.3]$$

$$MX_3 + 2\,M(S_2COR)_3 \xrightarrow{\text{dichloromethane}} 3\,M(S_2COR)_2X \qquad [3.4]$$

$$2\,M(S_2COR)_3 + X_2 \xrightarrow{\text{dichloromethane}} 2\,M(S_2COR)_2X + ROC(=S)\text{-}S\text{-}S\text{-}C(=S)OR \qquad [3.5]$$

Although there are several Group 15 metal xanthate complexes reported, most of them are poorly characterised and the spectroscopic data do not appear entirely consistent. The characterisation techniques used are based primarily on elemental analysis and melting points, due to their thermal studies which had centred the attention since the 70's.

Examples of metal *tris*-xanthates and haloxanthates reported in the literature together with information regarding the variations in the method used for their synthesis and brief comments concerning experimental conditions are summarised in Table 3.2.

Table 3.2 Synthetic Routes Used for the Preparation of Metal Xanthates and Haloxanthates

Compound	Synthesis [a]	Comments	Yield (%)	Ref.
$Bi(S_2COMe)_3$ $Bi(S_2COEt)_3$ $Bi(S_2COPr^i)_3$	3.2	$Bi(NO_3)_3 \cdot 5H_2O$ was used as the metal source and reacted with HCl to form the metal halide.	71 69 60	146
$Sb(S_2COEt)_2Cl$ $Sb(S_2COEt)_2Br$ $Sb(S_2COEt)_2I$ $Bi(S_2COEt)_2Cl$ $Bi(S_2COEt)_2Br$	3.3 – 3.5	No characterisation data provided but elemental analysis.	No data provided.	143
$As(S_2COMe)_3$ $As(S_2COEt)_3$ $As(S_2COPr^i)_3$ $As(S_2COBu^n)_3$ $As(S_2COHex^c)_3$ $As(S_2COBz)_3$	3.2	No characterisation data provided but elemental analysis. Complexes volatilized completely under reduced pressure.	No data provided.	149
$Sb(S_2COMe)_3$ $Sb(S_2COEt)_3$ $Sb(S_2COPr^i)_3$ $Sb(S_2COBu^n)_3$ $Sb(S_2COHex^c)_3$	3.2	No characterisation data provided but elemental analysis.	No data provided.	149

[a] Equation numbers cited in text.

A series of antimony (III) xanthates and haloxanthates have been prepared in this work following the different synthetic strategies reported in the literature, previously mentioned. All precursors were obtained in high yields (> 60 %), soluble in most organic solvents and found to be air- and moisture-stable for long periods of time but with an intense sulphur odour.

A summary regarding the preparation of the precursors synthesised and reported in this chapter, including yields and physical properties, is represented in Table 3.3.

Table 3.3 Preparation of Antimony (III) Xanthates and Haloxanthates and Selected Physical Properties

Precursor	Synthesis[a]	Yield (%)	Appearance	Melting Point
$Sb(S_2COEt)_3$ [141] (**7**)	3.1	76	Yellow solid	m.p: 68-70 °C
$Sb(S_2COEt)_2I$ (**8**)	3.5	68	Yellow oil	-
$Sb(S_2COEt)_2Cl$ (**9**)	3.3	81	Pale yellow solid	-
$Sb(S_2COPr^i)_3$ [147] (**11**)	3.2	90	Yellow solid	m.p: 130-132 °C
$Sb(S_2COMe)_3$ [150] (**13**)	3.2	80	Pale yellow solid	120 °C dec.
$Sb(S_2COMe)_2I$ (**14**)	3.5	65	Yellow oil	-

[a] Equation numbers cited in text.

3.2.2 Crystal Structure

Crystallographic quality crystals of $Sb(S_2COEt)_2Cl$ (**9**) were obtained by slow evaporation of a saturated dichloromethane solution at room temperature. The crystals were found to be air- and moisture-stable and data collection was carried out at 150 K. The molecular structure of precursor (**9**) is shown in Figure 3.5. The relevant bond distances and angles of (**9**) together with data for the analoguous $Sb(S_2COEt)_2Br$ [143] for comparison, are summarized in Tables 3.4 and 3.5 with further data provided in Appendix 4.

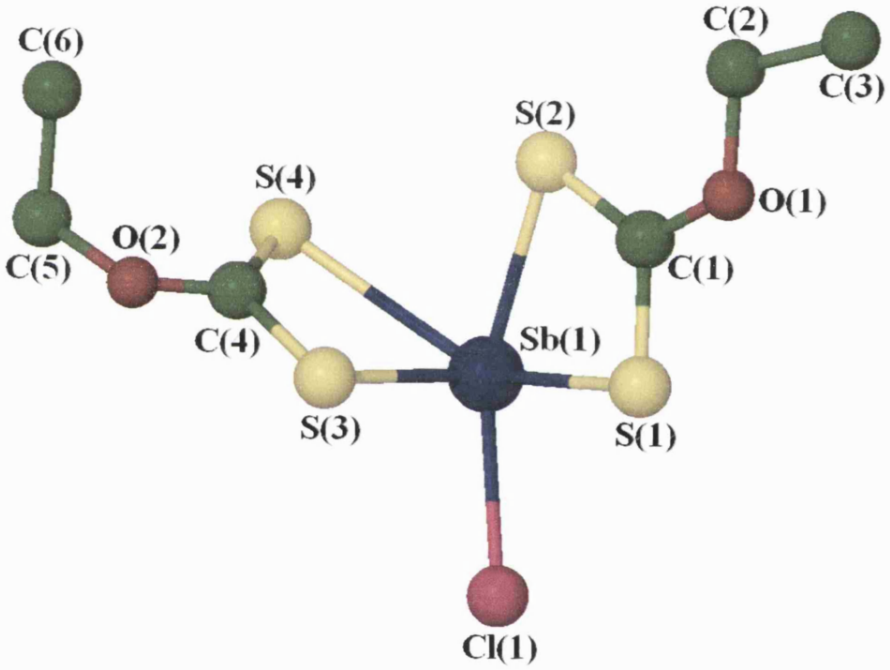

Figure 3.5 Molecular structure of $Sb(S_2COEt)_2Cl$ (**9**).

Table 3.4 Selected Bond Distances (Å) for $Sb(S_2COEt)_2Cl$ (**9**) and $Sb(S_2COEt)_2Br$[143]

	(9)	**$Sb(S_2COEt)_2Br$[143]**
Sb(1)-S(1)	2.5124(9)	2.513(5)
Sb(1)-S(2)	2.7143(8)	2.685(4)
Sb(1)-S(3)	2.4787(9)	2.493(5)
Sb(1)-S(4)	3.0255(9)	2.993(4)
Sb(1)-Cl(1)	2.6018(9)	
S(1)-C(1)	1.713(3)	1.732(16)
S(2)-C(1)	1.697(3)	1.678(15)
S(3)-C(4)	1.748(4)	1.719(15)
S(4)-C(4)	1.652(4)	1.683(16)
C(1)-O(1)	1.305(4)	1.284(18)
C(4)-O(2)	1.321(4)	1.291(18)
C(2)-O(1)	1.465(4)	1.493(22)
C(5)-O(2)	1.470(5)	1.483(18)
Sb(1)-Br(1)		2.780(2)

Table 3.5 Selected Bond Angles (°) for for $Sb(S_2COEt)_2Cl$ (**9**) and $Sb(S_2COEt)_2Br$[143]

	(9)	$Sb(S_2COEt)_2Br$[143]
S(1)-Sb(1)-S(2)	68.62(3)	68.7(1)
S(3)-Sb(1)-S(4)	65.32(3)	65.1(1)
S(1)-Sb(1)-Cl(1)	79.17(3)	
S(3)-Sb(1)-Cl(1)	86.57(3)	
S(1)-C(1)-S(2)	119.88(19)	118.8(9)
S(3)-C(4)-S(4)	124.3(2)	122.4(9)
C(1)-O(1)-C(2)	119.1(3)	199.0(1)
C(4)-O(2)-C(5)	119.7(3)	121.0(1)
S(1)-Sb(1)-Br(1)		78.3(1)
S(3)-Sb(1)-Br(1)		87.7(1)

The structure determination confirmed compound (**9**) as polymeric in the solid state where each antimony atom is six-coordinated surrounded by four sulphur atoms from the two asymmetrically chelating xanthate ligands and two chlorine atoms (one chlorine atom from a neighbouring molecule coordinated by intermolecular interaction). Two of the sulphur atoms are more tightly coordinated to the antimony [2.4787(9), 2.5124(9) Å] and the other two sulphur atoms less tightly coordinated with longer Sb-S distances [2.7143(8), 3.0255(9) Å]. This asymmetry is reflected in the associated C-S bond lengths of 1.748(4), 1.713(3) and 1.697(3), 1.652(4) Å, respectively. Thus, the geometry of complex (**9**) can best be described as distorted octahedral, with the chlorine atoms in *cis* conformation in the octahedral (Figure 3.6).

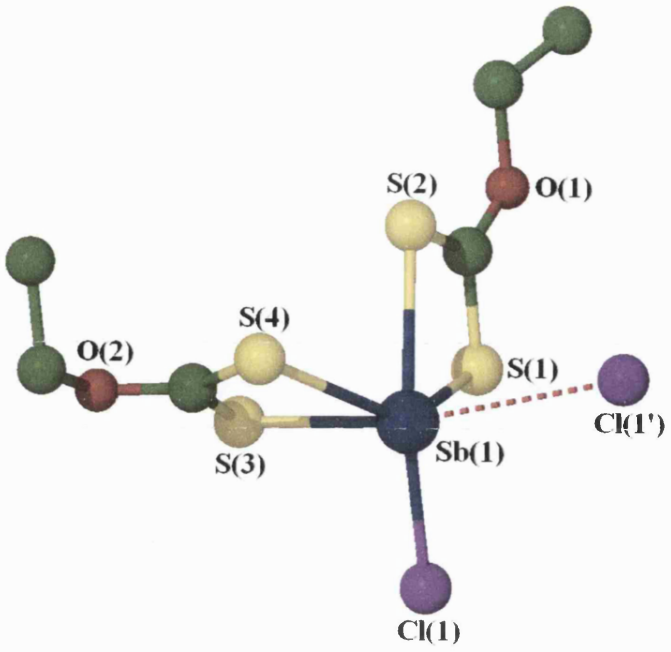

Figure 3.6 Molecular structure of $Sb(S_2COEt)_2Cl$ (**9**) showing the distorted octahedral geometry by intermolecular interaction with a chorine atom from a neighbouring molecule.

Bond distances and angles from complex (**9**) are in agreement with the ones reported for other antimony xanthates such as the related trisxanthate complex $Sb(S_2COEt)_3$ redetermined by Tiekink *et al.*[141] or its analogue $Sb(S_2COEt)_2Br$[143] (Tables 3.4 and 3.5).

Usually mono- and di-halo derivatives of both dithiocarbamate and xanthate complexes have associated structures with halogen bridges, although molecular weight measurements in $CHCl_3$ revealed they are monomeric in nature.[125] One clear example of this type of aggregation can be illustrated by the analogues complex $Sb(S_2COEt)_2Br$ reported by Tiekink and co-workers[143] which is to date the only monohaloxanthate antimony complex structurally characterized. The structure of $Sb(S_2COEt)_2Br$ (Figure 3.7) shows a zig-zag chain in which antimony atoms acquire hexa-coordination with bromine bridges. This aggregation of the molecules increases as one descends down in the group i.e. As<Sb<Bi. Hence bismuth complexes present higher tendency of aggregation like in

$Bi(S_2CNEt_2)_2I$[151] where the molecules are arranged in infinite polymeric chains stabilized by iodine bridges and therefore, each bismuth atom acquires an hexa-coordinated environment.

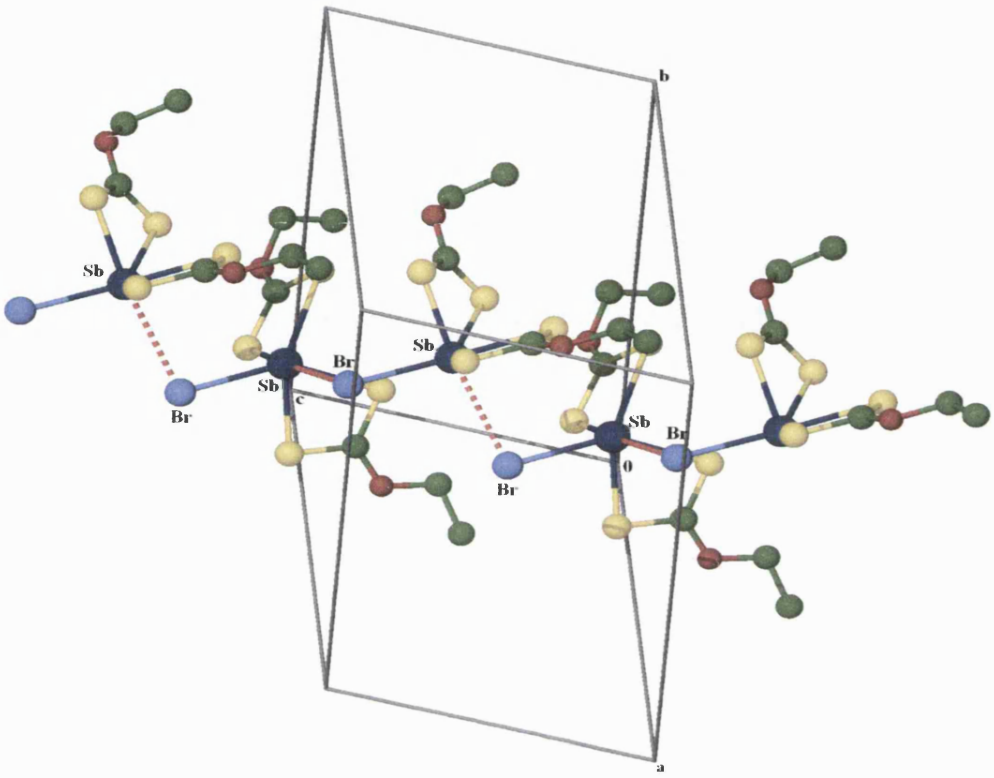

Figure 3.7 Molecular structure of $Sb(S_2COEt)_2Br$[143] showing the zig-zag chain in the polymer.

In case of compound (**9**), the polymer also forms a zig-zag chain of antimony atoms bridged by chlorine atoms (Figure 3.8). The distance between the antimony atom and the chlorine of the neighboring molecule in the chain is 3.214 (5) Å which is slightly shorter than the one between antimony atom and the bridging bromine in the analogue $Sb(S_2COEt)_2Br$[143] [3.269(2) Å]. This shortening in the interaction is unexceptional due to the smallest size of the chlorine atom and the higher electronegativity of the chlorine atom over the bromine within the molecule, which withdraws more electron density from the

antimony and hence, the interaction with the chlorine of the neighboring molecule is stronger.

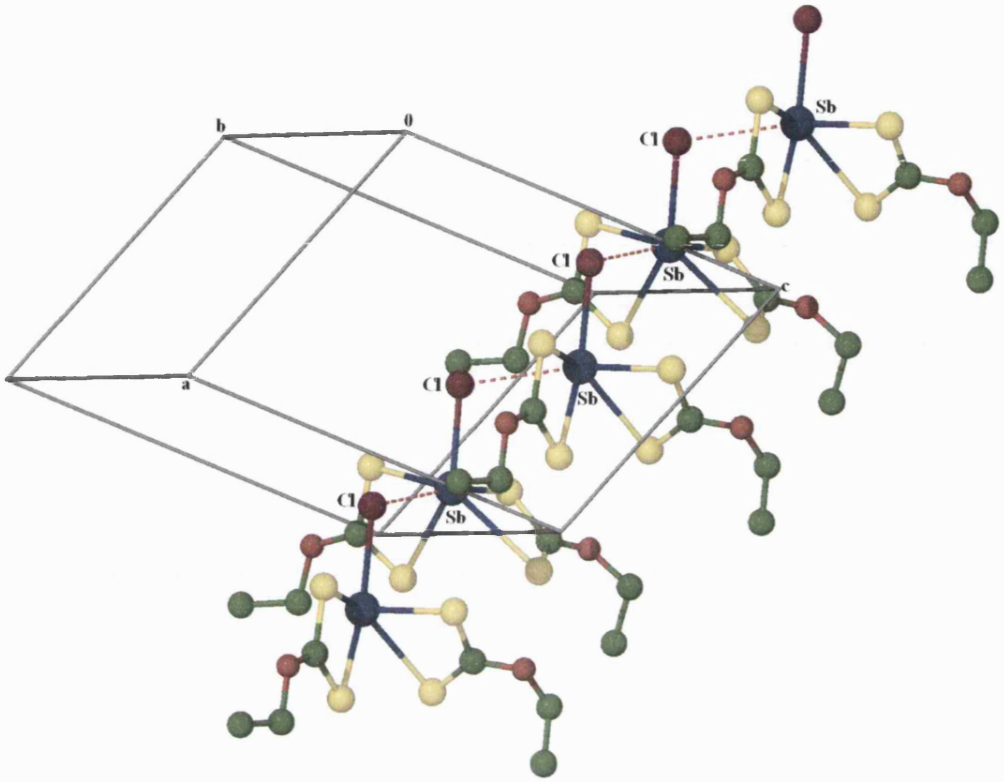

Figure 3.8 Molecular structure of $Sb(S_2COEt)_2Cl$ (**9**) showing the zig-zag chain in the polymer.

3.2.3 CVD Testing of Precursors

The precursors $Sb(S_2COEt)_3$ (**7**), $Sb(S_2COEt)_2I$ (**8**) and $Sb(S_2COPr^i)_3$ (**11**) were tested as CVD precursors. While precursors $Sb(S_2COEt)_3$ (**7**) and $Sb(S_2COPr^i)_3$ (**11**) were used as candidates for the deposition of Sb_2S_3 thin films, precursor $Sb(S_2COEt)_2I$ (**8**) was

used for the deposition of SbSI thin films. Details of the apparatus are provided in Appendix 2. Different substrates, 1.2 mm borosilicate glass slides and silicon wafers, were used for some experiments in order to study their influence on the film growth.

This section gives details of the tests carried out on compounds (**7**), (**8**) and (**11**) by Thermogravimetric Analysis (TGA) in order to have an indication of the temperature at which decomposition might be expected to start and reach completion, and to determine suitable conditions for the deposition of the film.

TGA of precursors (**7**) and (**11**) show very similar decomposition curves, both beginning at a relatively low temperatures, around 140 °C and 180 °C, respectively, and it is effectively over by 200 °C and 250 °C, respectively (Figures 3.9 and 3.10). For precursor (**7**), the weight remaining observed corresponds to Sb_2S_3, 36.5 % (theoretical 35.0 %). Above 400 °C, weight remaining matches with the transformation Sb_2S_3 to Sb_2O_3, 31.0 % (theoretical 29.2 %). As with the dithiocarbamates, this agrees with the results previously cited about the thermal stability of antimony trisulphide and its conversion into antimony trioxide.[135] As for precursor (**11**), the observed weight remaining corresponds to Sb_2S_3, 32.5 % (theoretical 32.2 %). Above 400 °C, like in previous compounds, weight remaining matches with the transformation Sb_2S_3 to Sb_2O_3, 27.0 % (theoretical 26.8 %).

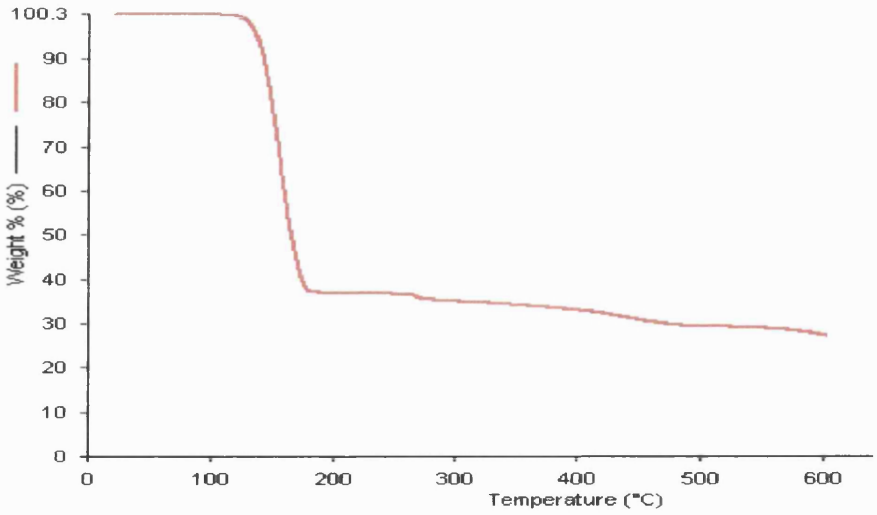

Figure 3.9 TGA of $Sb(S_2COEt)_3$ (**7**).

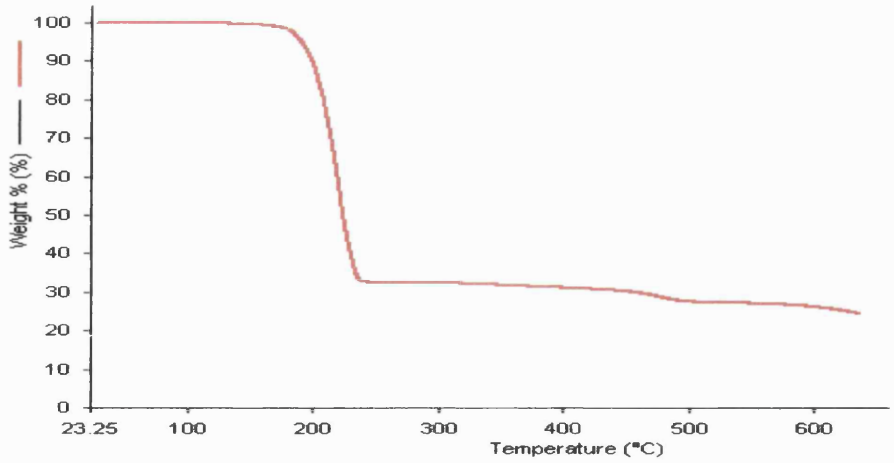

Figure 3.10 TGA of $Sb(S_2COPr^i)_3$ (**11**).

TGA for compound (**8**) is shown in Figure 3.11. The decomposition of the product starts at approximately 100 °C and it is effectively over by 250 °C, were the weight remaining observed corresponds to Sb_2S_3, 38.0 % (theoretical 35.0 %). Above 400 °C, the weight remaining again matches with the transformation Sb_2S_3 to Sb_2O_3, 31.0 % (theoretical 29.7 %), as it has been observed previously.

The aim of the use of haloxanthates is the deposition of Sb(S)I and looking at the TGA, the weight remaining for Sb(S)I (57 %) occurs at around 180 °C. Hence, deposition experiments need to be carried out at temperatures between 140 and 200 °C where the Sb-I linkage still remains unaltered, before decomposition reaches Sb_2S_3 and Sb_2O_3.

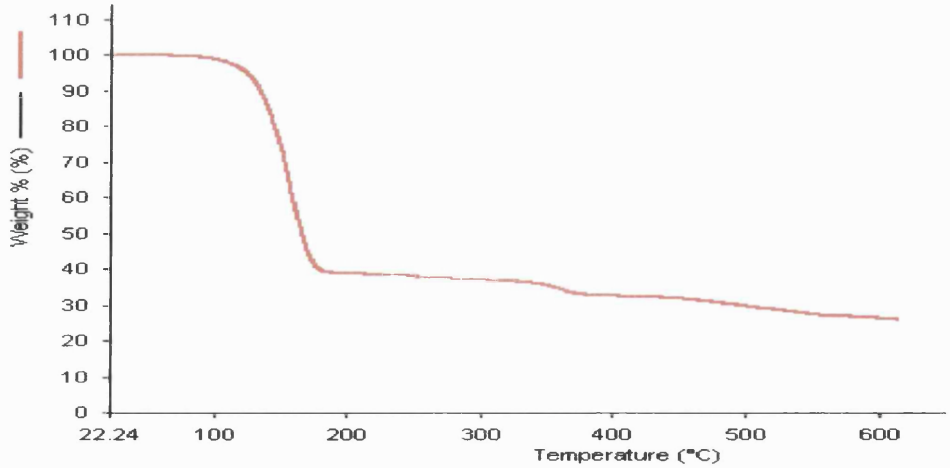

Figure 3.11 TGA of $Sb(S_2COEt)_2I$ (**8**).

In the case of the metal xanthates, a comprehensive study, with an extended range of metals and terminal alkyl substituents - with some emphasis on fluorinated alkyl substituents (usually C_6F_5) - has been carried out regarding their thermal stability and the resulting influence in the volatility on these complexes.[152] Most of these complexes decompose to the corresponding stoichiometric metal sulphides. Also, it was observed that the thermal stability increases as the chain length of the terminal alkyl group of the xanthato ligand increases.[152]

Figure 3.12 represents the thermogravimetric curves for antimony (III) xanthate complexes. Usually, if the chain length of the terminal alkyl group of the xanthato ligand is short, the complex starts decomposing at lower temperatures, leading to complete decomposition giving antimony trisulphide.[149] From Figure 3.12 it could be observed the exception of antimony (III) methylxanthate which starts decomposing at higher temperature that its analogue antimony (III) ethylxanthate despite the alkyl chain length. This anomalous behaviour could be explained as a consequence of a different decomposition mechanism (absence of β hydrogen atoms) that will be discussed in section 3.2.5. The TGA analysis of precursors (**7**) and (**11**) agrees with this data reported in the literature and illustrated by Figure 3.12.

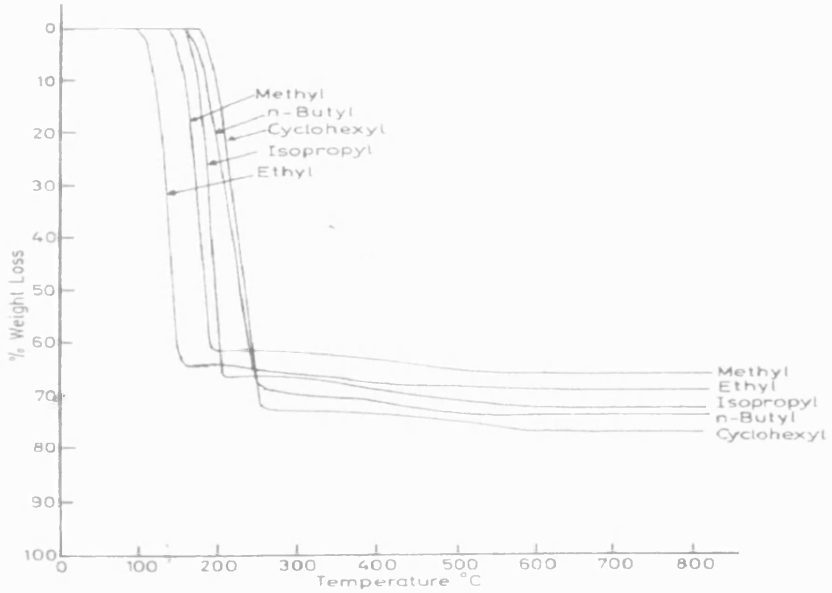

Figure 3.12 Thermogravimetric curves for antimony (III) xanthate complexes.[149]

Despite the low melting point of the xanthates, LPCVD studies across a range of temperatures from 90-200 °C gave very poor coverage of the substrates, which were unable to be characterised. Again, like the antimony (III) dithiocarbamates from Chapter 1, antimony (III) xanthates exhibited extremely low volatility.

As a consequence of the lack of volatility but good solubility of each compound in common organic solvents, as with the previous dithiocarbamates, deposition was attempted *via* AACVD methods. All three precursors displayed broadly similar deposition characteristics and their deposition conditions for the films analysed are displayed in Table 3.6. Despite the good solubility of precursors $Sb(S_2COMe)_3$ (**13**) and $Sb(S_2COMe)_2I$ (**14**) in most organic solvents, extremely poor films were obtained when they were used as precursors for AACVD. As mentioned before, this anomalous behaviour of methylxanthates might be related to their decomposition mechanism and will be discussed in section 3.2.5

Table 3.6 AACVD conditions for experiments using precursors (**7**), (**8**) and (**11**).

Precursor	Reactor Temperature (°C)	Carrier Gas (Ar) Flow Rate(l/min)	Run Time (h)	Substrate Used	Film Colour
(**7**)	200 °C	0.8	2	Glass	Orange-Yellow
(**8**)	190 °C	0.8	2.5	Glass	Orange
(**11**)	240 °C	0.8	1.5	Glass	Orange
(**11**)	240 °C	0.8	1.5	Silicon	Orange

3.2.4 Film Analysis

Films were examined by visual inspection, Energy Dispersive X-ray Analysis (EDAX) and Scanning Electron Microscopy (SEM). It was possible to perform quantitative EDAX on some of the films due to the suitable size of the particles deposited on the surface of the film.

Precursors used for the CVD of Sb_2S_3 thin films:

3.2.4.1 *Tris(ethylxanthate) Antimony (III) – $Sb(S_2COEt)_3$ (7)*

Several runs were performed from 220 to 190 °C in order to determine the best conditions to achieve deposition of Sb_2S_3, however only suitable films were obtained at 200 °C. A yellow film was produced which, although by visual inspection the film appeared to be thick, EDAX analysis shows a very thin film where together with the antimony and sulphur peaks, a very intense silicon peak is observed due to the breakthrough to the underlying glass substrate. Figure 3.13 shows the EDAX of the film grown at 200 °C. Comparing the difference in the peak heights in the EDAX, it can be observed that the estimated ratio between Sb and S is close to that shown previously in other films, which quantitative EDAX has shown to be Sb_2S_3.

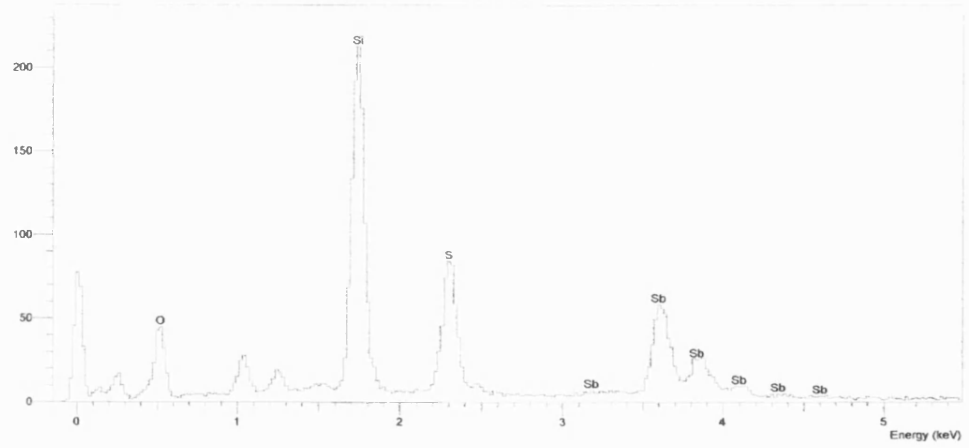

Figure 3.13 EDAX qualitative analysis of film grown from precursor from (**7**) at 200 °C.

SEM image of the film obtained from (7) at 200 °C is shown in Figure 3.14. The deposited Sb_2S_3 particles of about 3 μm in width appear to be randomly deposited over the film and are formed at the same time from smaller microspheres. From Figure 3.16 it can be observed that each microsphere is of approximately 0.8 μm. This is a completely different morphology to that obtained using dithiocarbamates as precursors, where Sb_2S_3 presented a needle-like shape.

Due to the low thickness of the films it was not possible to achieve further accurate compositional analysis.

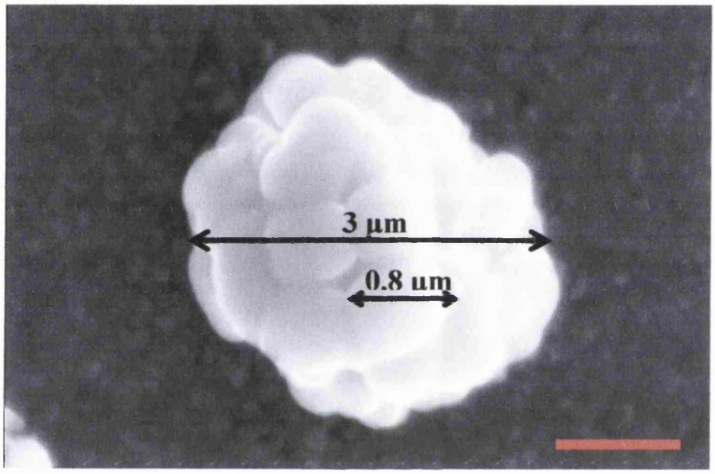

Figure 3.14 SEM of film grown from precursor (7) at 200 °C. Red bar = 1 μm.

Although the composition of the film could not be determined by quantitative analysis it is in agreement with the results reported by Cao and co-workers[153] where they obtained exactly the same Sb_2S_3 of sphere-like morphology by solvothermal methods. They reported the preparation of hollow Sb_2S_3 microspheres, where the dimensions of the particles matches entirely with the ones deposited in our films by AACVD. These hollow microspheres were analysed by X-ray diffraction and transmission electron microscopy (TEM) and revealed to be amorphous Sb_2S_3.

3.2.4.2 *Tris(isopropylxanthate) Antimony (III) – $Sb(S_2COPr^i)_3$ (11)*

After several runs in the temperature range between 200-250 °C, it was found that 240 °C was the ideal temperature to produce thick orange films suitable to perform characterisation analysis. Initial films were deposited on glass slides where by qualitative EDAX (Figure 3.15) it could be observed that mainly antimony and sulphur peaks appeared in the spectra with only traces of the underlying glass substrate, giving an idea of the good thickness of the film. Quantitative EDAX showed Sb:S ratio of 1.44 matching with the formula Sb_2S_3.

SEM image of the film obtained from (**11**) at 240 °C on glass slides is shown in Figure 3.16. It can be observed the Sb_2S_3 deposited consisting in spherical particles, very similar to those deposited from precursor (**7**), joined together forming a uniform film. Some bigger particles with a fiber-like shape with an estimated width of 2.5 μm and 12 μm length can also be observed, randomly deposited on top of the film. Quantitative analysis showed both the spherical and fiber-like particles to be Sb_2S_3.

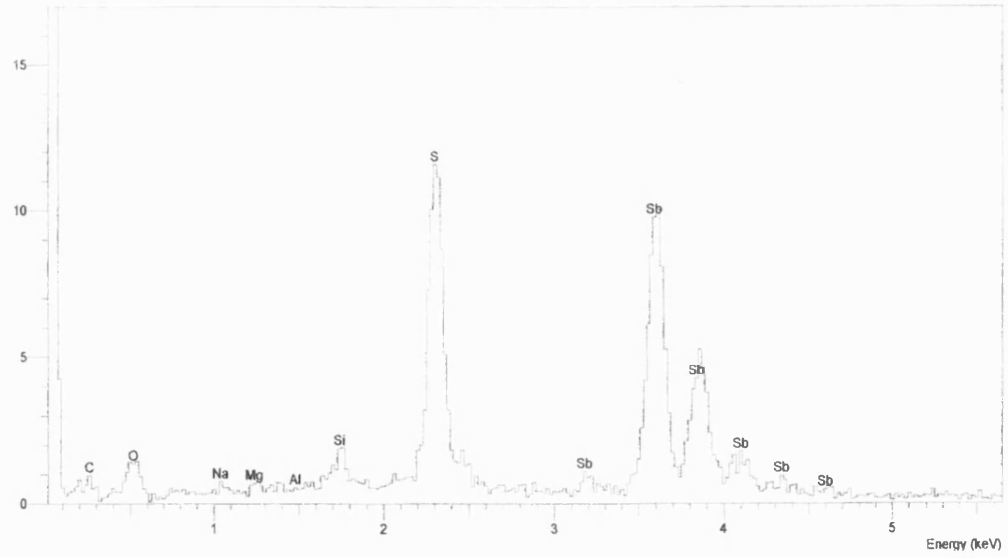

Figure 3.15 EDAX qualitative analysis of film grown from precursor from (**11**) at 240 °C on glass slides.

For the first time thick and homogeneous films of Sb_2S_3 had been produced and therefore, studies of the effect on the morphology were carried out by using different substrates, such as silicon wafers.

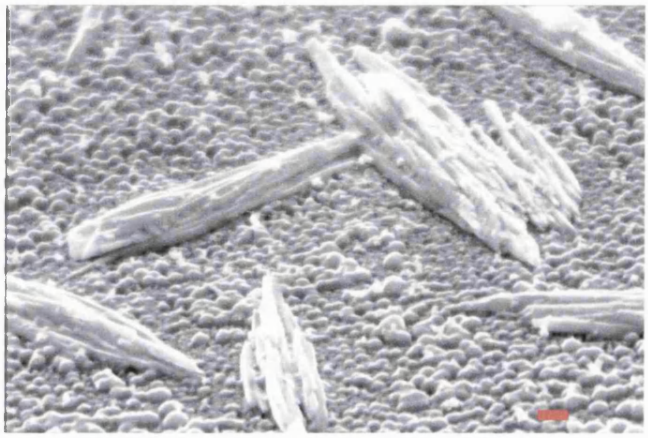

Figure 3.16 60° tilt SEM of film grown from precursor (**11**) at 240 °C on glass slides. Red bar = 1 μm.

The same temperature, 240 °C, used to produce the films on glass slides was found be the ideal temperature to produce new films, this time over silicon slides. The orange films obtained looked thick enough for the characterisation analysis. Qualitative EDAX (Figure 3.17) shows antimony and sulphur peaks and a minor silicon peak from the underlying substrate, which indicates good thickness.

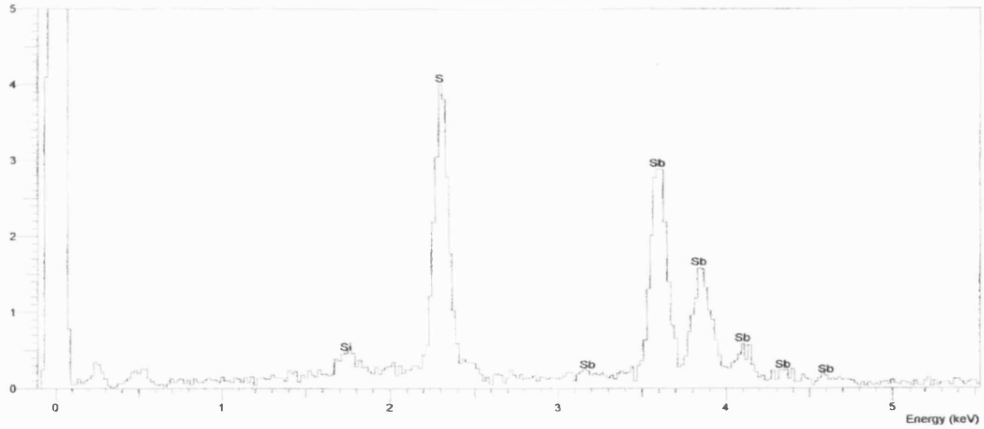

Figure 3.17 EDAX qualitative analysis of film grown from precursor from (**11**) at 240 °C on silicon slides.

Figure 3.18 shows the SEM image the film obtained from (**11**) at 240 °C on silicon slides. The morphology of the deposited material has changed dramatically, now tending to grow as oriented fibers. The fibers are approximately of 0.5 μm in width and 10 μm in length. It can be observed that these fibers look very similar to those deposited on top of the film using glass slides (Figure 3.16) and also how small spherical particles appear on the tip of the fibers (similar to those one that formed the homogeneous film deposited on glass slides). Figure 3.19 shows the SEM image of these spherical particles adhered to the fibers at higher magnification. As expected, the films deposited on silicon wafers are more oriented due to the more ordered surface of the silicon wafers than the glass ones.

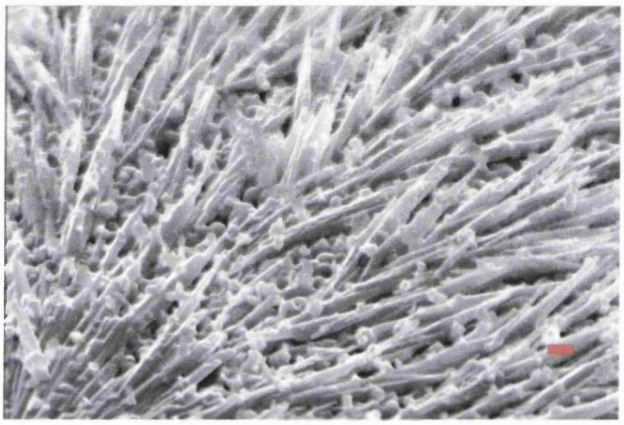

Figure 3.18 SEM of film grown from precursor (**11**) at 240 °C on silicon slides. Red bar = 1 μm.

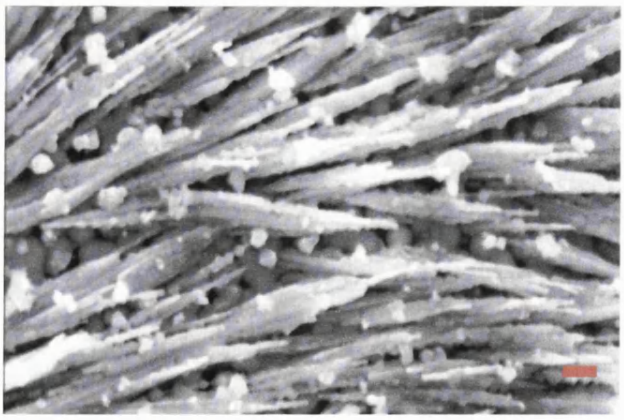

Figure 3.19 SEM of film grown from precursor (**11**) at 240 °C on silicon slides at higher magnification. Red bar = 1 μm.

In order to study the crystallinity of the films, XRD was performed in the films on both glass and silicon substrates. All the films were crystalline and the diffraction patterns could be compared to those standard antimony sulphides from the data base. Figures 3.20 and 3.21 show the glancing angle X-ray patterns of the films grown from precursor (**11**) using glass and silicon substrates, respectively. In the XRD of the film grown from precursor (**11**) on glass slides (Figure 3.20) most of the peaks could be indexed, excepting the two marked with (*) which could not be assigned. The majority of the peaks, marked in black, matches to that of Stibnite, Sb_2S_3 (orthorhombic, PDF 06-0474), however, three peaks, marked in blue, matches with $Sb_{10}S_{15}$ (PDF 39-0211), which is a monoclinic variation on Sb_2S_3, isostructural with $Pb_3Sb_8S_{15}$ (fuloppite) in which three Pb^{2+} replace two Sb^{3+}.

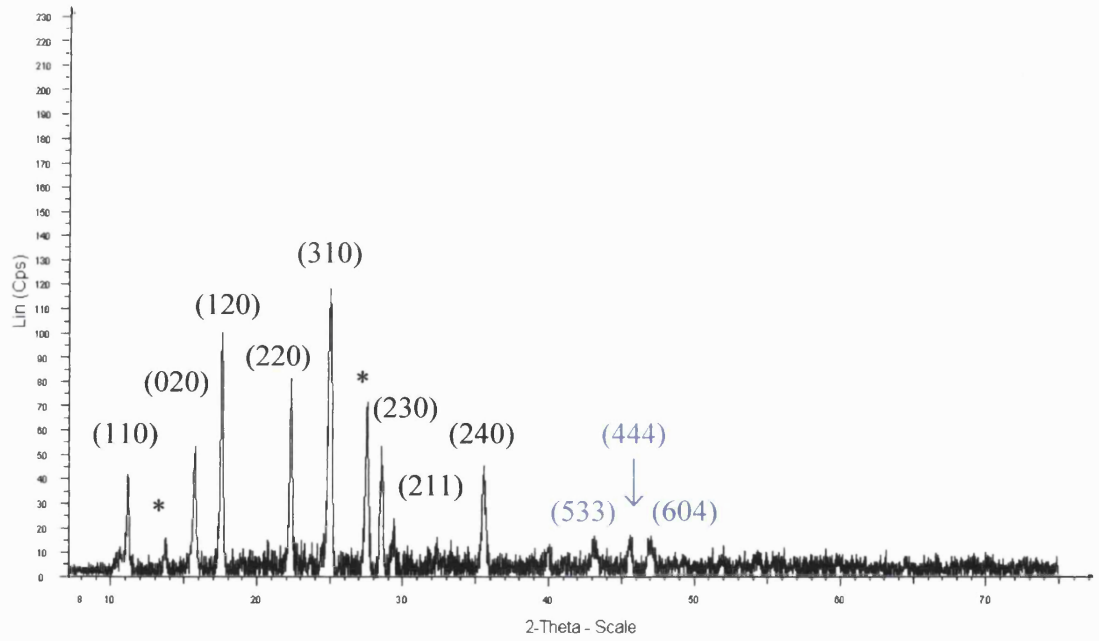

Figure 3.20 Glancing angle X-ray pattern of film grown from precursor (**11**) on glass slides. Peaks marked in black match to that of Stibnite, Sb_2S_3 (orthorhombic, PDF 06-0474) and peaks marked in blue match with reflexions from $Sb_{10}S_{15}$ (PDF 39-0211). Peaks marked with (*) which could not be assigned.

The XRD of the film grown from precursor (**11**) on silicon slides (Figure 3.23) shows a highly oriented film, with only three reflexions, of which reflexion (244) seems to be the preferred orientation. All three peaks could be indexed matching again with $Sb_{10}S_{15}$ (PDF 39-0211).

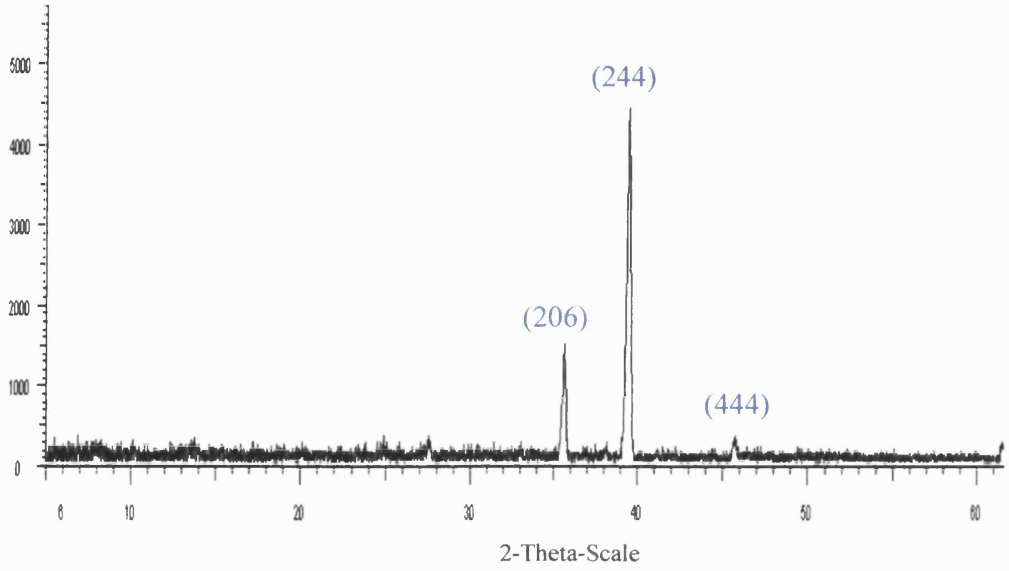

Figure 3.21 Glancing angle X-ray pattern of film grown from precursor (**11**) on silicon slides.

It is also important to notice how the width of each reflexion has increased compared with the reflexion curves on the XRD from the film grown on glass slides. This fact is directly related with the size of the crystal analysed. Both magnitudes, the width of the reflexion curve (know as *B*) and the width of the crystal, are inversely proportional to each other according to *Scherrer's* formula:[154]

$$t = \frac{0.9\lambda}{\sqrt{B^2_M - B^2_S} \cdot Cos\theta}$$

where t is the crystallite thickness, λ the X-ray wavelength, θ the Bragg angle (half the measured diffraction angle) and B_M and B_S are the width in radians of diffraction peaks of the sample and a standard at half height.

This variation in the increase in the width of the reflexion is in agreement with the size of the particles deposited on both glass and silicon substrates, where the fibers grown on silicon wafers are considerably smaller (0.5 μm) than those grown on glass slides (2.5 μm).

Precursor used for the CVD of SbSI thin films:

3.2.4.3 *Iodobis(ethylxanthate) Antimony (III) – $Sb(S_2COEt)_2I$ (8)*

At 190 °C suitable orange films were obtained where the EDAX (Figure 3.22) shows antimony, sulphur and iodine peaks, together with an intense silicon peak due to the poor thickness of the film.

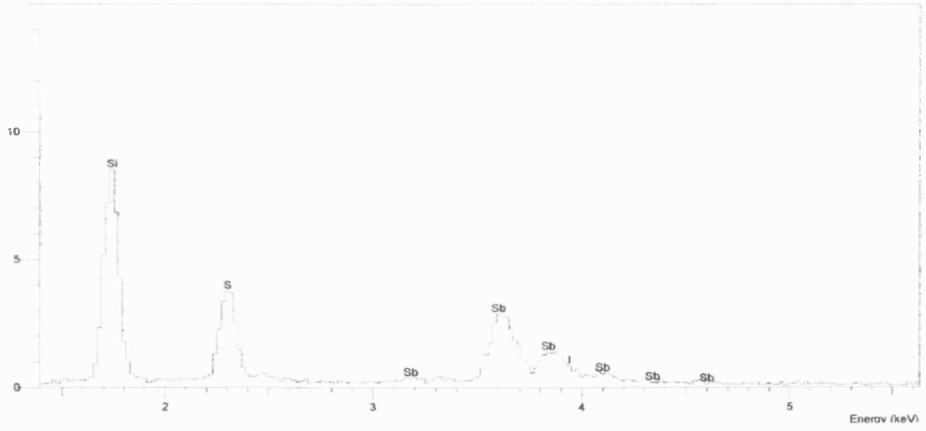

Figure 3.22 EDAX qualitative analysis of film grown from precursor from (**8**) at 190 °C.

Antimony and iodine peaks are very close together in the EDAX spectrum and therefore, by Wavelength Dispersive Spectroscopy (WDS) a particular region of the spectrum was possible to be selected (Figure 3.23) in order to be able to separate the set of peaks corresponding to antimony from those corresponding to iodine and be sure both elements are present in the film.

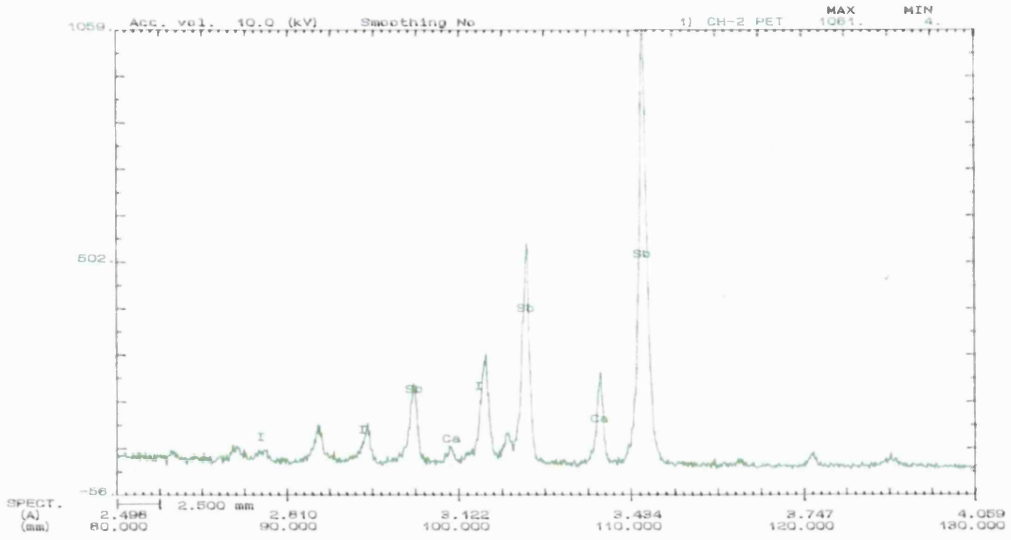

Figure 3.23 WDS analysis of film grown from precursor from (**8**) at 190 °C.

SEM image of the film obtained from (**8**) at 190 °C is shown in Figure 3.24. It could be observed from the film an underlying layer consisting of small particles that were unable to be characterised due to their poor thickness, and bigger particles with a fibrous appearance of approximately 10 μm in length randomly deposited on top of the underlying film. Figure 3.25 shows the SEM image of the film grown from precursor (**8**) at 190 °C at higher magnification.

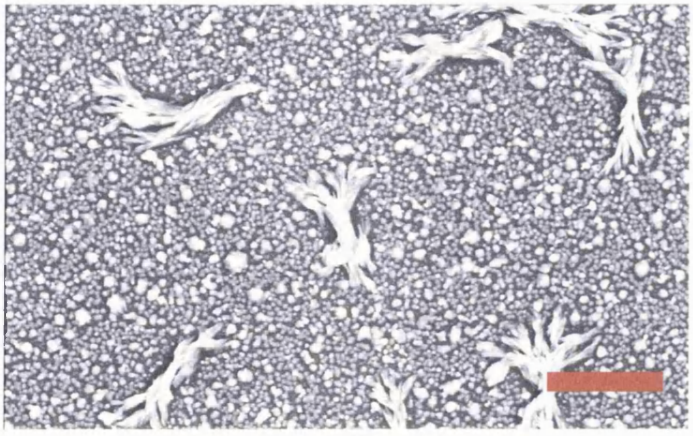

Figure 3.24 SEM of film grown from precursor (**8**) at 190 °C. Red bar = 10 μm.

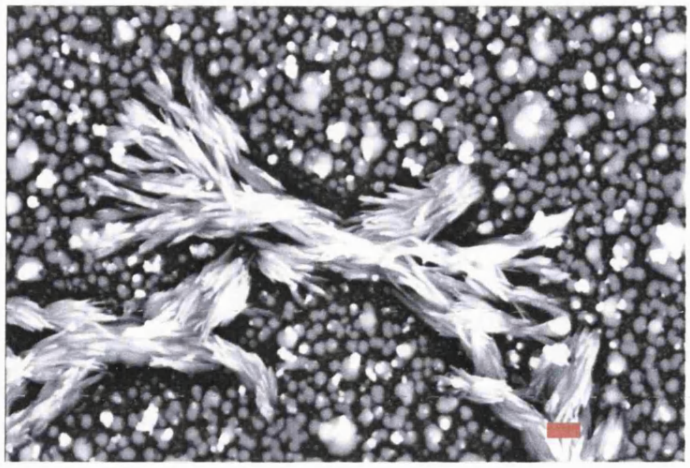

Figure 3.25 SEM of film grown from precursor (**8**) at 190 °C at higher magnification. Red bar = 1 μm.

Despite the poor thickness of the films and therefore the lack of quantitative data, the qualitative analysis shows that iodine is incorporated in the film and this represents an extraordinary achievement not reported to date in the literature.

3.2.5 Decomposition Mechanisms

One of the main interests of the metal dithiocarbamate and xanthate complexes is their thermochemistry. Insufficient systematic investigations have been reported to be able to predict the thermal decomposition mechanisms of these complexes. In most cases, the volatile decomposition products and the pseudo-stable solid-state intermediates have not been characterized and therefore the relevant decomposition mechanisms have not been well defined.

Several decomposition studies have been carried out using xanthates with different metals and different R groups and, generally, a two stage decomposition is apparent with the intermediate formation of the metal sulphide and final formation of the metal. Usually the last stage of the decomposition is accompanied with the transformation at higher temperatures to the metal oxide as residue.[152] Figure 3.26 illustrates the pathway of the decomposition.

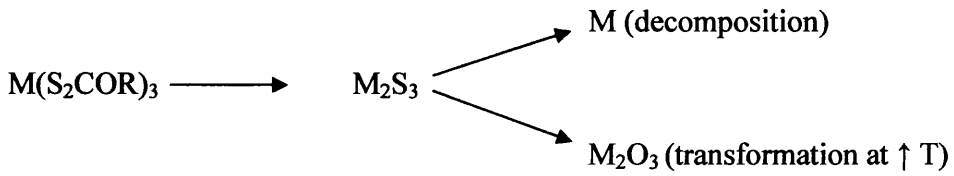

Figure 3.26 Decomposition Pathway for a metal xanthate.

Although some studies on the thermal decomposition for metal dithiocarbamates and xanthates have been reported, it is not possible to predict their corresponding decomposition mechanism. The decomposition mechanisms appear to be controlled primarily by the structure of the ligand and by the coordination sphere and oxidation state of the coordinated metal. Furthermore, since intermolecular factors clearly affect the volatility of the complexes they also influence the mechanisms of the decomposition.

In order to explore and understand the decomposition mechanisms of antimony (III) xanthates, the mass spectrum of precursor $Sb(S_2COPr^i)_3$ (**11**) has been recorded in this work. The formation of common structure ions and their fragmentation pattern is discussed but unfortunately pure pyrolytic results had not been achieved.

The ionisation method employed for the mass spectrum of precursor $Sb(S_2COPr^i)_3$ (**11**) was *Electron Impact* (EI), which although is a harsh technique, represents more accurately the CVD process which the precursor is subjected to. The main peaks found in the EI-MS spectrum of precursor $Sb(S_2COPr^i)_3$ (**11**) are shown by Table 3.7. Peaks are assigned in Table 3.7 according to whether or not they present the antimony isotopic

pattern, consisting of two peaks with intensities of 57 and 43 corresponding to the isotopes ^{121}Sb and ^{123}Sb, respectively. A representation of the antimony isotopic pattern is shown by Figure 3.27.

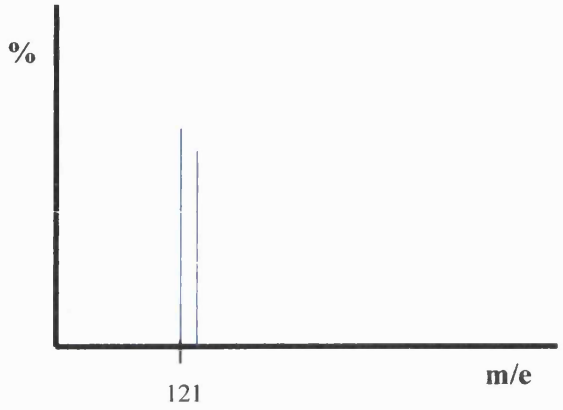

Figure 3.27 Isotopic pattern of antimony.

Table 3.7 Peaks found in the EI-MS spectrum of precursor $Sb(S_2COPr^i)_3$ (**11**)

m/e [a]	Ion	Sb Isotopic Pattern
391 (a)	$[Sb(S_2COPr^i)_2]^+$	Yes
349 (b)	$[Sb(S_2COPr^i)(SCOSH)]^+$	Yes
307 (c)	$[Sb(SCOSH)_2]^+$	Yes
196 (d)	?	No
153 (e)	$[SbS]^+$	No
76 (f)	$[CS_2]^+$	No
60 (g)	$[COS]^+$	No
42 (h)	$[C_3H_6]^+$	No

[a] Based on ^{121}Sb

The molecular ion of precursor (**11**) was not detected in the spectra when the Electron Impact technique was used, probably due to the instability of the odd electron species $[Sb(S_2COPr^i)_3]^{+\bullet}$ which will tend to lose one dithiocarbamate group $(S_2COPr^i)^\bullet$ as a radical, becoming stable as an even electron species, $[Sb(S_2COPr^i)_2]^+$. The highest mass number ion observed, which appear as a consequence of the fragmentation of the molecular ion mentioned, is the ion $[Sb(S_2COPr^i)_2]^+$ (a). Besides ion (a) there are two other intense ions (b) and (c) which also shows the isotopic pattern of antimony. The m/e differences between the first three peaks is *c.a.* m/e 42 which matches with the molecular formula of propene (C_3H_6) which can be formed by internal elimination following the mechanism of the *Chugaev* type reaction.

The Chugaev reaction is an important class of elimination reaction that involves the elimination of water from primary alcohols, *via* xanthate as intermediate, to produce terminal alkenes. In the first step of the reaction, the alkoxide is formed from the deprotonation of the primary alcohol, followed by the xanthate formation by insertion of CS_2 and addition of iodomethane (Scheme 1).

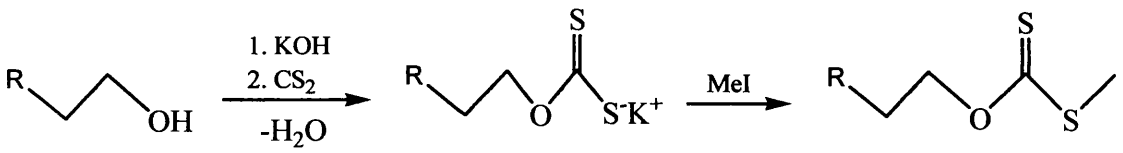

Scheme 1. Formation of the xanthate intermediate.

At about 200 °C, the alkene is formed by a *syn*-elimination of the β-hydrogen atom. In a 6-membered cyclic transition state the hydrogen atom is moved from the β-C-atom to the sulfur and giving carbonyl sulphide (OCS) and methanethiol as side products (Scheme 2). This second step in the Chugaev reaction is the key step in the decomposition of the metal xanthate complexes.

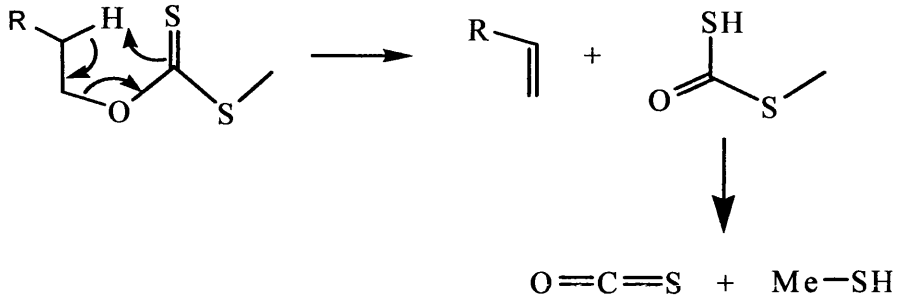

Scheme 2. Formation of the alkene by *syn*-elimination.

A similar mechanism pathway must occur for the decomposition of precursor (**11**) since one of the most prominent peaks appears at m/e 60 in the spectra due to the ion $[COS]^+$ which characterises the fragmentation mode of the precursor. Also another prominent peak appears at m/e 76, almost certainly due to the ion $[CS_2]^+$ from fragmentation of other ions, e.g. (S_2COPr^i).

As mentioned before, the difference between the three main peaks containing isotopic pattern of antimony (peaks a, b and c) is 42, matching with the exact mass of propene. Also peak (e) which also contains antimony at m/e 153 matches with the loss of the two COS groups leaving behind the antimony sulphide species $[SbS]^+$. No other significant peaks appeared in the spectra, however, with the peaks showed it is feasible to establish a mechanism for the decomposition of precursor (**11**) illustrated by Scheme 3.

A very similar mechanism had been proposed by Efrima and co-workers[155] for the decomposition of cadmium xanthates to give cadmium sulphide nanoparticles. They reported that the release of COS in the decomposition, as in the classical Chugaev reaction, drives irreversibly the reaction to completion. However, the pathway to produce cadmium sulphide is by colloidal methods rather than by CVD, nonetheless the use of alkylamine solvents seems to have a central role in the synthesis of the nanoparticles, not only by lowering the decomposition temperature of the metal xanthates (acting as a Lewis base

activating the O-C-S_2M group by moving charge density from the C-S bond toward the S-M bond) but also by acting as catalyst of the reaction.

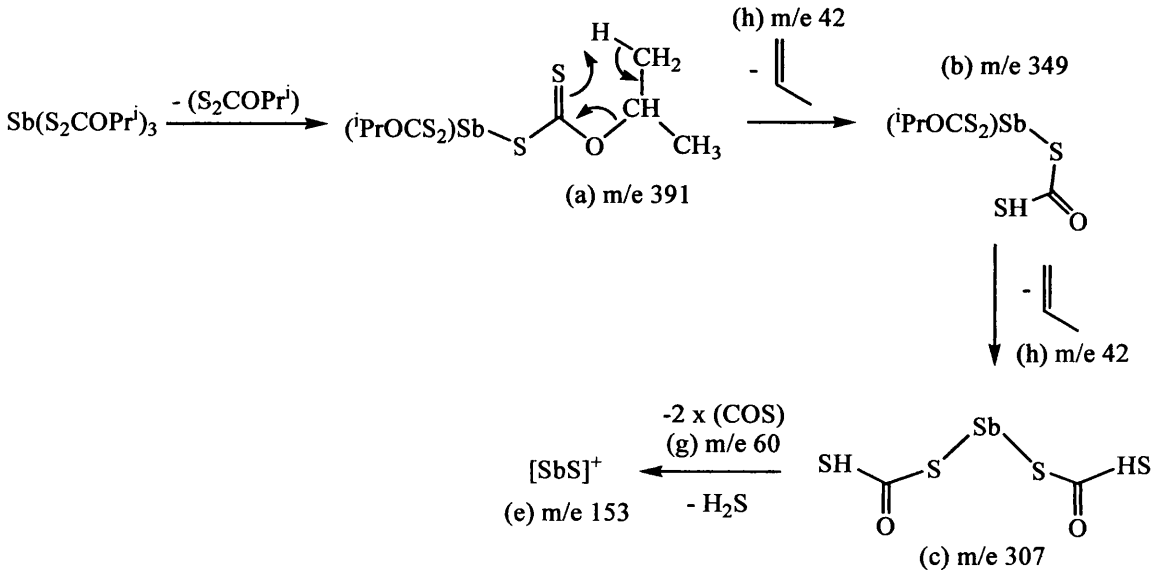

Scheme 3. Proposed decomposition mechanism of precursor $Sb(S_2COPr^i)_3$ (**11**).

This mechanism, based on a *syn*-elimination of the β-hydrogen atom, will not occur with precursors $Sb(S_2COMe)_3$ (**13**) and $Sb(S_2COMe)_2I$ (**14**) due to the lack of β-hydrogen atoms in the molecule and will explain why very thin films with poor coverage were obtained when using them as CVD precursors [even though precursor $Sb(S_2COMe)_3$ (**13**) presents lower decomposition temperature than, for instance, precursor $Sb(S_2COPr^i)_3$ (**11**)]. The lack of β-hydrogen atoms in the molecule might also explain the anomalous behaviour on the decomposition temperature of precursors $Sb(S_2COMe)_3$ (**13**) and $Sb(S_2COMe)_2I$ (**14**), which in case of precursor $Sb(S_2COMe)_3$ (**13**), the alkyl chain is shorter than its analogue antimony (III) ethylxanthate but starts decomposing at higher temperature, indicating that another decomposition mechanism might take place.

As a comparison between the decomposition mechanisms of antimony (III) dithiocarbamates and xanthates, the mass spectrum of one of the dithiocarbamate complexes synthesised in this thesis, $Sb[S_2CN(Me)(Hex^n)]_3$ (**6**), was recorded.

The ionisation method employed for the mass spectrum of precursor $Sb[S_2CN(Me)(Hex^n)]_3$ (**6**) was also *Electron Impact* (EI). The main peaks found in the EI-MS spectrum of precursor $Sb[S_2CN(Me)(Hex^n)]_3$ (**6**) are shown by Table 3.8.

Table 3.8 Peaks found in the EI-MS spectrum of precursor $Sb[S_2CN(Me)(Hex^n)]_3$ (**6**)

m/e	Ion	Sb Isotopic Pattern
272 (a)	$\{SC[N(Me)(Hex^n)]_2\}^+$	No
158 (b)	$\{SC[N(Me)(Hex^n)]\}^+$	No
126 (c)	$\{H_2C[N(Me)(Hex^n)]\}^+$	No
114 (d)	$[N(Me)(Hex^n)]^+$	No
76 (e)	CS_2	No

In contrast with metal xanthates, there is no formation of alkene in metal dithiocarbamates, mainly due to the lack of oxygen in the molecule and therefore no COS release occurs, which is the main feature of Chugaev-type reactions. This fact is in agreement with the data provided by the spectra, where alkene peaks are not observed. It is important to remark that also no peaks containing isotopic pattern of antimony are observed, however, it is possible to establish a mechanism following the fragmentation mode for the decomposition of precursor (**6**), illustrated by Scheme 4.

The peaks shown in the spectrum and hence the fragmentation mode proposed are in agreement with the ones reported in the literature by Manoussakis *et al.*[156] for their

studies of the decomposition mechanisms of Group 15 dithiocarbamates. As in the mass spectra of precursor (**11**), the molecular ion of precursor (**6**) is not detected when the Electron Impact technique was used. In the paper reported by Manoussakis,[156] the molecular ions are not detected either and the peaks corresponding to polynuclear compounds with general formula M_nS_m (where M = As, Sb, Bi) are only noticeable for arsenic and bismuth, observing only traces for some of the ones containing antimony, which is in agreement with the absence of these type of peaks in the spectra of precursor (**6**).

It is also important to remark that different peaks positions and therefore different fragmentation modes are found for dithiocarbamates with cyclic amines than those with N-dialkyl substituted amines, because it is possible to have one or two alkyl groups detached in the latter compounds.[156]

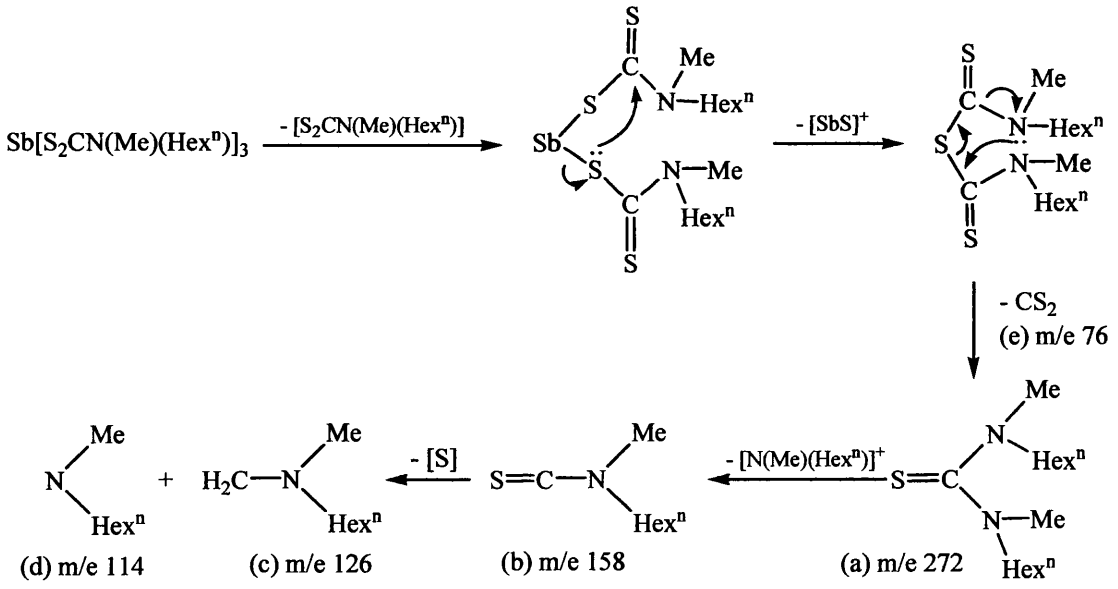

Scheme 4. Proposed decomposition mechanism of precursor $Sb[S_2CN(Me)(Hex^n)]_3$ (**6**).

Overall, it is possible to establish different decomposition routes for antimony (III) dithiocarbamates and xanthates by the study of their mass spectra. Antimony (III) dithiocarbamates follows a selective fragmentation mode, depending of the substituents in the amine, whereas antimony (III) xanthates tend to decompose following a Chugaev-type reaction with the release of COS as the driving force of the reaction. The formation of either CS_2 or COS seems to be key for the decomposition mechanism of these compounds. Due to the stronger nature of the bond C=O over the C=S bond, COS is a more stable species than CS_2 and hence xanthates complexes tend to decompose at lower temperatures than dithiocarbamates.

It is important to highlight the lower decomposition temperatures of xanthates complexes over dithiocarbamates. Thermogravimetric analysis revealed that metal xanthates exhibited a decomposition temperature (<150 °C) lower that of dithiocarbamate analogous (>250 °C).[146] The reason for this is hitherto unknown, although it has been suggested that it is related to the degree of supramolecular aggregation.

In conclusion, although antimony (III) xanthates are not volatile enough for LPCVD studies, their high solubility makes them ideal candidates as precursors for AACVD. Their relatively low decomposition temperature (140 °C) compared with the analogous dithiocarbamates, allows efficient deposition of pure Sb_2S_3 thin films with excellent coverage, in case of precursor $Sb(S_2COPr^i)_3$, what without oxygen contamination.

Also, for the first time from a single-source precursor, $Sb(S_2COEt)_2I$ (**8**), the incorporation of iodine on thin films has been demonstrated, showing that the Sb-I bond, prone to be lost at relatively high temperatures due to its weak nature, it still unaltered. Further studies of iodine incorporation on thin films using different single-source precursors will be described in Chapter 5.

3.3 EXPERIMENTAL

Starting materials were commercially obtained (e.g. Aldrich) and were used without further purification unless otherwise stated. Standard Schlenck line techniques were employed where applicable. Further details about instrumentation used are given in Appendix One.

3.3.1 Preparation of Tris(ethylxanthate) Antimony (III) - $Sb[S_2COEt]_3$ (7) [141]

A solution of $SbCl_3$ (2.00 g, 8.8 mmol) in dichloromethane (20 mL) was added to a suspension of KS_2COEt (4.21 g, 26.3 mmol) in dichloromethane (80 mL). After stirring overnight, a yellow solution and a creamy solid appeared. The solid was filtered off and the filtrate dried by the addition of $MgSO_4$ anhydrous. The solution was filtered and the solvent was evaporated giving a yellow solid. The solid was washed with hexane (2 x 25 mL) and dried under vacuum producing 3.25 g (76%) of (7). m.p: 68-70 °C.

Microanalysis:
Found (calc.) for $C_9H_{15}O_3S_6Sb$ (7): C 22.20 (22.27)%; H 3.07 (3.11)%.
^{1}H-NMR [δ (ppm), $CDCl_3$]:
4.55 (2H, c, CH_2), 1.40 (3H, t, CH_3).
^{13}C-NMR [δ (ppm), $CDCl_3$]:
221.4 (S_2C), 71.0 (CH_2), 12.4 (CH_3).

3.3.2 Preparation of Iodobis(ethylxanthate) Antimony (III)) - $Sb[S_2COEt]_2I$ (8)

0.5 equivalents of I_2 (0.26 g, 1.05 mmol) in dichloromethane (40 mL) was added to a solution of compound (7) (1.00 g, 2.10 mmol) in dichloromethane (40 mL). An orange solution is formed. After leaving it stirring overnight, the solution turns to a bright yellow

solution. The solvent was evaporated remaining a sticky material. The sticky material was washed with hexane (2 x 25 mL) and dried under vacuum, giving 0.35 g (68%) of (**8**) as a yellow oil.

Microanalysis:

Found (calc.) for $C_6H_{10}O_2S_4ISb$ (**8**): C 14.96 (14.67)%; H 2.11 (2.05)%.

^{1}H-NMR [δ (ppm), $CDCl_3$]:

4.60 (2H, c, C*H*$_2$), 1.40 (3H, t, C*H*$_3$).

^{13}C-NMR [δ (ppm), $CDCl_3$]:

221.0 (S_2C), 71.9 (*C*H$_2$), 12.9 (*C*H$_3$).

3.3.3 Preparation of Chlorobis(ethylxanthate) Antimony (III)) - $Sb[S_2COEt]_2Cl$ (9)

A solution of $SbCl_3$ (1.50 g, 6.6 mmol) in dichloromethane (20 mL) was added to a suspension of KS_2COEt (2.11 g, 13.1 mmol) in dichloromethane (60 mL). After stirring over night, a yellow solution and a creamy solid appeared. The solid was filtered off and the filtrate dried by the addition of $MgSO_4$ anhydrous. The solution was filtered and the solvent was evaporated giving a yellow solid. The solid was washed with hexane (2 x 25 mL) and dried under vacuum producing 2.12 g (81%) of (**9**).

Microanalysis:

Found (calc.) for $C_6H_{10}O_2S_4ClSb$ (**9**): C 18.30 (18.03)%; H 2.63 (2.52)%.

^{1}H-NMR [δ (ppm), $CDCl_3$]:

4.60 (4H, c, C*H*$_2$), 1.40 (6H, t, C*H*$_3$).

^{13}C-NMR [δ (ppm), $CDCl_3$]:

221.7 (S_2C), 73.1 (*C*H$_2$), 14.2 (*C*H$_3$).

3.3.4 Preparation of Potassium Isopropylxanthate - $K[S_2COCH(CH_3)_2]$ (10)

In a 100 mL round-bottomed flask, potassium hydroxide (2.00 g, 35.6 mmol) was reacted with isopropanol (25 mL, 0.62 mol) and heated under reflux for 1 hour. The solution was allowed to cool and the liquid decanted from the residual solid into another flask. Carbon disulphide (2.14 mL, 35.6 mmol) was added slowly and with constant shaking. After 1 hour the alcoholic solution was evaporated. The creamy-yellow solid formed was washed ether (2 x 25 mL) and dried under vacuum giving 5.00 g (81%) of (**10**).

Microanalysis:

Found (calc.) for $C_4H_7OS_2K$ (***10***): C 27.80 (27.55)%; H 4.01 (4.04)%.

^{1}H-NMR [δ (ppm), DMSO-d_6]:

5.50 (1H, sep, C*H*), 1.20 (6H, d, CH_3).

^{13}C-NMR [δ (ppm), DMSO-d_6]:

229.7 (S_2C), 72.3 (*C*H), 22.3 (*C*H_3).

3.3.5 Preparation of Tris(Isopropylxanthate) Antimony (III) - $Sb[S_2CO^iPr]_3$ (11)

A solution of $SbCl_3$ (2.07 g, 9.1 mmol) in dichloromethane (20 mL) was added to a suspension of KS_2CO^iPr (4.75 g, 27.3 mmol) in dichloromethane (80 mL). After stirring over night, a yellow solution and a creamy solid appeared. The solid was filtered off and the solvent was evaporated giving a yellow solid. The solid was washed with hexane (2 x 25 mL) and dried under vacuum producing 4.30 g (90%) of (**11**). m.p: 130-132 °C.

Microanalysis:

Found (calc.) for $C_{12}H_{21}O_3S_6Sb$ (**11**): C 27.10 (27.32)%; H 3.98 (4.01)%.

^{1}H-NMR [δ (ppm), $CDCl_3$]:

5.50 (1H, sep, C*H*), 1.35 (6H, d, CH_3).

^{13}C-NMR [δ (ppm), $CDCl_3$]:

222.2 (S_2C), 81.4 (*C*H), 22.1 (*C*H_3).

3.3.6 Preparation of Potassium Methylxanthate- K[S_2COMe] (12)

It was prepared by the same procedure as (**9**) but refluxing absolute methanol (1.44 mL, 35.5 mmol) and potassium hydroxide (2.00 g, 35.6 mmol). After washing with ether, the reaction yield 4.63 g (89%) of (**12**) as a pale yellow solid.

Microanalysis:

Found (calc.) for $C_2H_3OS_2K$ (**12**): C 17.42 (18.10)%; H 2.06 (2.36)%.

^{1}H-NMR [δ (ppm), DMSO-d_6]:

3.70 (3H, s, C*H*$_3$).

^{13}C-NMR [δ (ppm), DMSO-d_6]:

230.3(S_2C), 57.7 (*C*H$_3$).

3.3.7 Preparation of Tris(Methylxanthate) Antimony (III) - Sb[S_2COMe]$_3$ (13)

It was prepared by the same procedure as (**11**) but stirring a solution of $SbCl_3$ (2.41 g, 10.6 mmol) in dichloromethane (20 mL) with a suspension of KS_2COMe (4.65 g, 31.8 mmol) in dichloromethane (60 mL). Remaining 3.75 g (80%) of (**13**) as a pale yellow solid. (m.p: decompose to grey solid at 120°C)

Microanalysis:

Found (calc.) for $C_6H_9O_3S_6Sb$ (**13**): C 16.28 (16.25)%; H 2.02 (2.04)%.

^{1}H-NMR [δ (ppm), $CDCl_3$]:

4.15 (9H, s, C*H*$_3$).

^{13}C-NMR [δ (ppm), $CDCl_3$]:

223.7 (S_2C), 62.1 (*C*H$_3$).

3.3.8 Preparation of Iodobis(methylxanthate) Antimony (III) - $SbI[S_2COMe]_2I$ (14)

To a solution of compound (**13**) (0.50 g, 1.10 mmol) in dichloromethane (20 mL), 0.5 equivalents of I_2 (0.14 g, 0.55mmol) in dichloromethane (40 mL) was added and yellow solution was formed. After leaving it stirring overnight the solvent was evaporated remaining a sticky material. The sticky material was washed with hexane (4 x 25 mL) and dried under vacuum, giving 0.33 g (65%) of (**14**) as a yellow oil.

Microanalysis:

Found (calc.) for $C_4H_6O_2S_4ISb$ (**13**): C 9.46 (10.37)%; H 1.33 (1.30)%.

^{1}H-NMR [δ (ppm), $CDCl_3$]:

4.15 (6H, s, CH_3).

^{13}C-NMR [δ (ppm), $CDCl_3$]:

222.0 (S_2C), 61.1 (CH_3).

Chapter Four

Antimony(III) Thiolates

4.1 INTRODUCTION

The coordination and structural chemistry of transition metal thiolates have witnessed a dramatic increase in the reported literature during the past two decades, mainly because thiolate coordination occurs for many metal ions in metallo-enzymes.[157] In contrast, thiolate chemistry of the main group metals remains less developed. Although some metal thiolate complexes of groups 13 and 15 metals with general composition $M(SR)_3$ have been described,[51, 116, 117, 157-160] there is a scarcity of structural data on this kind of complexes due to their generally poor solubility and hydrolytic instability in solution.

There are numerous descriptions of molecular structure types for the different metal thiolates depending mainly on the coordination number of the metal.[112] However, concentrating on the bonding of the SR group there are mainly two types of coordination to the metal centre:

- *Monodentate* thiolates, where the sulphur is bonded to one metal centre by a single covalent bond:

  $M\text{-}(SR)_n$

- *Bridging* thiolates, where the thiolate is bonded to two metal centres, by a single covalent bond and a dative bond using one of the lone pairs from the sulphur:

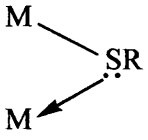

The structural chemistry of Group 15 metal thiolates has acquired considerable interest due to the tendency of these metal centres to adopt high coordination numbers, the presence of the sterically ambivalent lone pairs and the tendency to adopt oligomeric structures.[151]

The preferred geometry for antimony(III) thiolates, with coordination number 3, is *trigonal pyramidal* and a representative example is the complex *tris*(phenylthiolate) antimony reported by Peters *et al*[51], shown in Figure 4.1 .

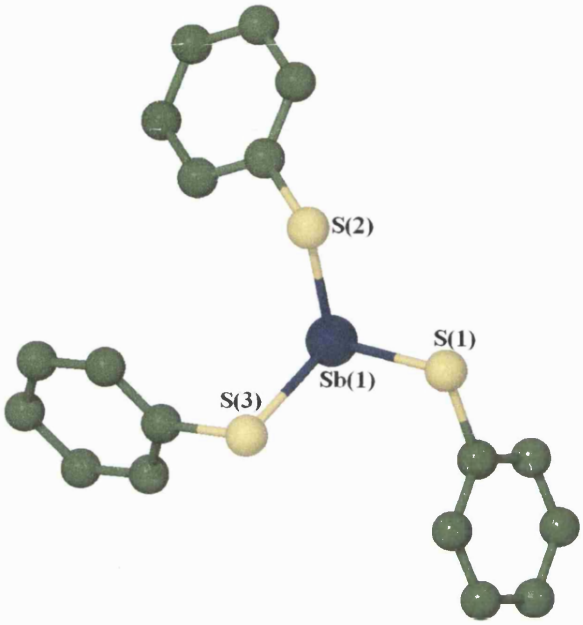

Figure 4.1 Molecular structure of $Sb(SPh)_3$.[51]

When the coordination number increases to 6, one of the possible geometries adopted by antimony (III) thiolates is *capped octahedral* and a clear example of it, Sb(2-$SC_5H_4N)_3$, was reported by Block *et al*[157] shown in Figure 4.2. The molecular structure of Sb(2-$SC_5H_4N)_3$ shows the antimony with a six-coordinate environment and distorted from octahedral geometry by the presence of the chelating ligands with sulphur and nitrogen donors and the stereochemically active lone pair.

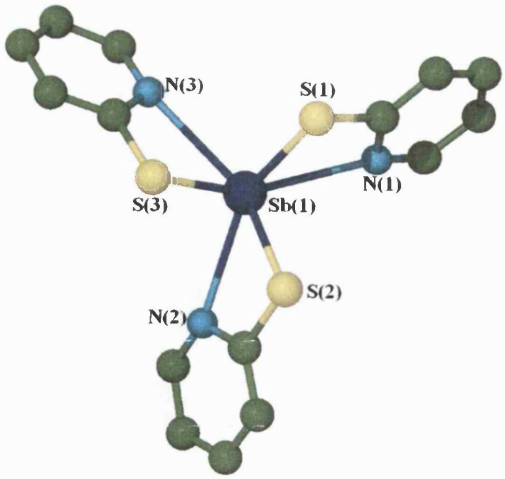

Figure 4.2 Molecular Structure of $Sb(2\text{-}SC_5H_4N)_3$.[157]

There are only a few structurally characterised examples of antimony(III) thiolates reported in the literature, some of them together with coordination number, geometry and significant bond distances are summarised in Table 4.1.

Table 4.1 Coordination Geometries Exhibited by Antimony (III) Thiolates

Coordination Number	Geometry	Example	Bond Distances Sb-S (Å)	Ref.
3	Trigonal Pyramidal	$Sb(SPh)_3$	2.423(2)	51
3	Trigonal Pyramidal	$Sb(SC_6H_3Me_2\text{-}3,5)_3$	2.437(2)	161
6	Capped Octahedral	$Sb(2\text{-}SC_5H_4N)_3$	2.470(1)	157
6	Capped Octahedral	$Sb(2\text{-}SC_5H_3N\text{-}3\text{-}SiMe_3)_3$	2.487(1)	157
3	Distorted Octahedral	$SbPh(EDT\text{-}TTFS_2)$	2.454(2)	162
3	Trigonal Pyramidal	$Sb(SC_6H_2Pr^i_3\text{-}2,4,6)_3$	2.425(2)	21
3	Distorted Octahedral	SbPh(dddt)	2.466(2)	162
3	Trigonal-Pyramidal	$Sb(SC_6H_4Me\text{-}4)_3$	2.433(7)	161

Although the main oxidation state for antimony is (III), there are also a relatively large number of antimony(V) complexes reported with ligands such as halides and oxygen donor ligands, where the coordination numbers encountered are most commonly four, five and six.[8] In contrast, there are not many antimony(V) thiolates reported, where only ionic antimony(V) thiolates have been structurally characterised and no neutral complexes $Sb(SR)_5$ had been found. Complexes with general formula $[NEt_4]$ $[Ar_2Sb(dithiolene)_2]$ have been reported by various sources[163-165] and were found to present similar geometries in which the antimony atom is six-coordinated. These ionic antimony(V) dithiolenes present in the solid state a distorted octahedral geometry determined by a combination of steric factors and ligand bite. Nonetheless, Sb-S bond distances are on average very similar (2.477(7) Å) to the ones shown in analogous complexes of antimony(III).

During the last decade, thiolates have been one of the most relevant groups for their use as precursors to produce metal sulphides. Although there are several references about different precursors for metal sulphides,[112, 157, 159, 160, 162, 166-168] only a few of them have been used as single-source precursors for CVD.[50, 114-117, 169]

Most of the metal thiolates reported as precursors for CVD are centred on the deposition of transition-metal sulphides with general formula MS_2 (M = Co,[55, 56] Cu,[58] Mn,[55, 56] Mo,[50] Nb[169] and Ti[50, 114, 115]) due to their wide range of electronic properties. Main group sulphides are much less well studied and the majority of the references come from CVD of tin sulphides in Group 14 reported by Molloy *et al*[81, 116, 117, 170] and from gallium sulphide, as GaS or Ga_2S_3, in Group 13 which has been deposited as thin films from a number of reliable single-source precursors.[63-66, 171] There are no references to date about CVD of antimony(III) sulphide and that is why the study of antimony thiolates becomes extremely relevant.

Metal thiolate decomposition can be most of the time controlled by using the right temperature range, presenting them as ideal candidates from a CVD point of view. Also, an important advantage of using metal thiolates as single-source precursors is to obviate the need to use toxic H_2S as co-reactant; hence it provides a much safer route.

One essential property, that of enhancing volatility, can be achieved by the incorporation of fluorine into the alkane chain in the thiol group. Although fluorine incorporation benefited CVD conditions, it has been found to cause fluorine contamination into the resultant film when trying to deposit metal oxides. It also had been observed by incorporation of fluorine in the alkyl chain that, instead of obtaining the expected metal oxides from precursors like $[NaOCH(CF_3)_2]_4$ and $Zr[OCH(CF_3)_2]_4$,[172] metal fluorides are produced exclusively, such as NaF or ZrF_4, respectively. This is due to the short M•••F contacts which can be present in fluorinated alkoxides arrangements.

Also, it is well-known that chelation within a complex increases its stability, and therefore by substitution of the thiolate (monodentate) with aminothiolate ligands (bidentate) will not only introduce extra stability but also will enable the possible incorporation of another metal complex by chelation through the lone pair of the nitrogen of the aminothiolate to another metal centre. There are several examples of these kinds of compound in the literature and one of these is illustrated in Figure 4.3 where cadmium is coordinated to two aminothiolate ligands in a distorted tetrahedral arrangement.[173]

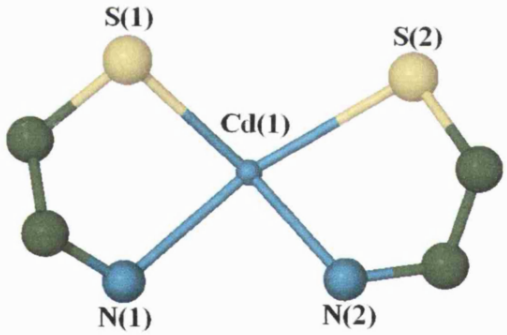

Figure 4.3 Molecular Structure of $Cd(SCH_2CH_2NH_2)_2$.[173]

In this chapter, the preparation, characterisation and properties of some further CVD candidates for Sb_2S_3 films are evaluated. Metal thiolates are attractive precursors for CVD processing due to their higher volatility compared with other analogous single-source precursors, such as metal dithiocarbamates and xanthates, and their thermal decomposition to produce metal sulphides takes place at moderately low temperatures (120-200 °C).[174]

Metal thiolates not only present higher volatility but also a clean decomposition pathway to give metal sulphides and organic molecules (usually recovering the thiols and/or alkenes) as by-products.[50, 175-177]

4.2 RESULTS AND DISCUSSION

4.2.1 Synthetic Routes

The synthesis of metal thiolates is relatively easy to achieve and there are different methods available that mainly depend on the nature of the thiolate. Thiols are commercially available either as protonated species, or deprotonated as a salt which are much less malodorous and easier and less uncomfortable to handle. Although some thiols need to be kept under nitrogen atmosphere, the resulting metal complexes are air stable and soluble in most organic solvents, this being the case for the compounds described in this chapter.

A common method of preparation of antimony(III) thiolates is by using the thiolate salt, whether it is commercially available or easily obtained by reduction of the parent thiol. The reaction is produced by stirring the metal halide and a stoichiometric amount of thiolate salt in methanol to give the desired product together with the inorganic halide. The desired product can be easily removed by extraction in a less polar solvent such as diethyl ether.[157] A representation of this route is given by Equation 4.1:

$$MCl_n + n\,NaSR \xrightarrow{MeOH} M(SR)_n + n\,NaCl \qquad [4.1]$$

However, when there is no thiolate salt available and only the thiol can be used, it has been reported the reaction between the antimony(III) halide and the thiol refluxing in toluene[161] or by using a base such as triethylamine[157] also forms $Sb(SR)_3$. A representation of this method is illustrated by Equation 4.2:

$$MCl_n + n\,HSCH_2R \xrightarrow[\text{toluene}]{\text{reflux}} M(SCH_2R)_n + n\,HCl \qquad \textbf{[4.2]}$$

However, this method it not suitable for some thiols and metal amides are necessary as starting material rather than metal halides. Thus, by protonolysis of metal amides with the corresponding chalcogenols if is feasible to produce the desired metal thiolates, yielding pure compounds free of ionic impurities under very mild conditions. A representation of this method is illustrated by Equation 4.3:

$$M[N(SiMe_3)_2]_3 + 3\,HSR \longrightarrow M(SR)_3 + 3\,NH(SiMe_3)_2 \qquad \textbf{[4.3]}$$

A variation of Equation 4.2 which involves the use of ammonia as a base rather than triethylamine had been reported by Molloy and co-workers.[116] This method involved the reaction between the reactants by passing dry ammonia to ensure completion of the reaction and followed by filtration of the ammonium chloride produced in the reaction, shown by Equation 4.4:

$$MCl_n + n\,HSCH_2R \xrightarrow[\text{toluene}]{NH_3} M(SCH_2R)_n + n\,NH_4Cl \qquad \textbf{[4.4]}$$

Routes for the synthesis of metal aminothiolate complexes have been reported previously.[173, 178-180] These methods involved either the direct reaction of the metal halide with the aminothiolate in a range of different solvents or by prior deprotonation and neutralisation of the ligand (often commercially available as hydrochloride salt) and the addition of the metal halide. A representation of this last variation is shown by Equation 4.4:

$$n\ Me_2NCH_2CH_2SH.HCl \xrightarrow[2)\ MCl_n]{1)\ 2n\ NaOH\ /\ methanol} M(SCH_2CH_2NMe_2)_n + 2n\ NaCl \quad \textbf{[4.4]}$$

Information regarding the methods used, compounds produced and brief comments concerning experimental conditions for previously reported species, are summarised in Table 4.2.

Table 4.2 Synthetic Routes Used for the Preparation of Metal Thiolates

Compound	Synthesis [(a)]	Comments	Yield (%)	Ref.
$Sb(SC_6H_3Me_2\text{-}3,5)_3$ $Sb(SC_6H_4Me\text{-}4)_3$	4.1	Reliable reaction involving Celite for separation of by-products.	65 51	161
$Sb(2\text{-}SC_5H_4N)_3$ $Sb(2\text{-}SC_5H_3N\text{-}3\text{-}SiMe_3)_3$	4.1	Good method. Easy handling.	70 50	157
$Sb(SC_6H_2Me_3\text{-}2,4,6)_3$ $Sb(SC_6H_2Pr^i_3\text{-}2,4,6)_3$ $Sb(SC_6H_2Bu^t_3\text{-}2,4,6)_3$	4.2	High yields. Pure products free of ionic impurities.	75 89 82	21
$Sn[SCH_2CH_2(CF_2)_5CF_3]_4$ $Sn[S\text{-}p\text{-}F\text{-}C_6H_4)_4$ $Sn(SCH_2CF_3)_4$	4.3	Simple, fast and efficient method.	92 69 84	116
$Bi(SCH_2CH_2NMe_2)_3$ $Cd(SCH_2CH_2NMe_2)_2$	4.4	Slow reaction and low yields.	38 47	180 173

[(a)] Equation numbers cited in text.

A series of antimony(III) thiolates have been prepared in this study following the different synthetic strategies reported in the literature, previously mentioned. Regarding the nature and availability of the thiols needed to produce the desired precursors, different methods were used in order to achieve the highest yields due to the volume of material required for CVD purposes. All precursors were obtained in high yields (> 60 %) and the majority of them were found to be air- and moisture-stable (excepting the fluorinated precursor which decomposed after a few days exposed to the air) with a pungent odour.

A summary regarding the preparation of the precursors synthesised and reported in this chapter, including preparative route used, yields and physical properties is represented in Table 4.3

Table 4.3 Synthetic Routes Used for the Preparation of Antimony (III) Thiolates

Precursor		Synthesis[a]	Yield (%)	Appearance	Solubility
$Sb(SBu^t)_3$	**(15)**	4.1	70	Off-white solid m.p: 150 °C	Most organic solvents
$Sb(SCH_2CF_3)_3$	**(16)**	4.3	70	Clear oil	Most organic solvents
$Sb(SCH_2Ph)_3$	**(17)**	4.3	90	Clear oil	Most organic solvents
$Sb(SCH_2CH_2NMe_2)_3$	**(18)**	4.4	68	Off-white solid m.p: 98-100 °C	Most organic solvents

[a] Equation numbers cited in text.

4.2.2 Crystal Structures

Crystallographic quality crystals of the two contrasting compounds $Sb(SBu^t)_3$ (**15**) and $Sb(SCH_2CH_2NMe_2)_3$ (**18**) were obtained by slow vacuum sublimation onto a cold finger and by slow diffusion of a saturated solution in dichloromethane layered with hexane, respectively. The crystals were found to be air stable and data collection was carried out at 150 K. The molecular structures are shown in Figures 4.4 - 4.8 from different perspectives. Relevant bond distances and angles are summarized in Tables 4.4 and 4.5 respectively, with further data provided in Appendix 4.

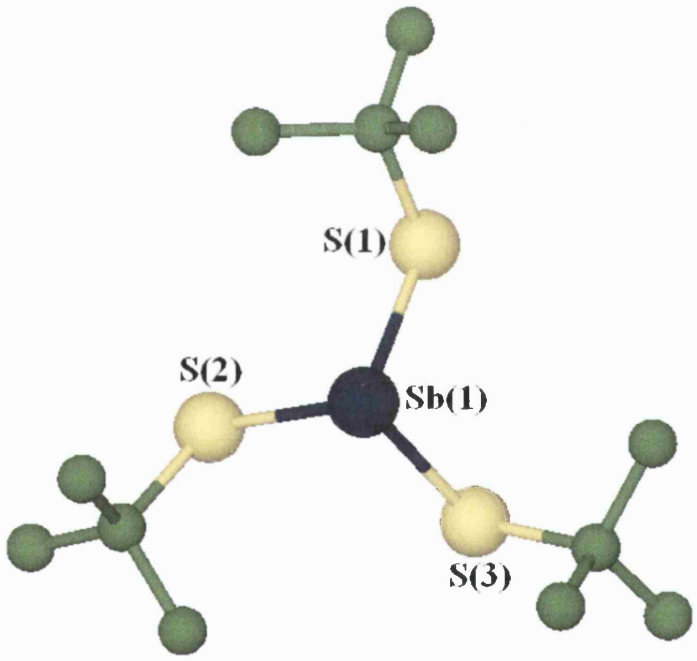

Figure 4.4 Molecular Structure of $Sb(SBu^t)_3$ (**15**) showing the trigonal nature of the compound.

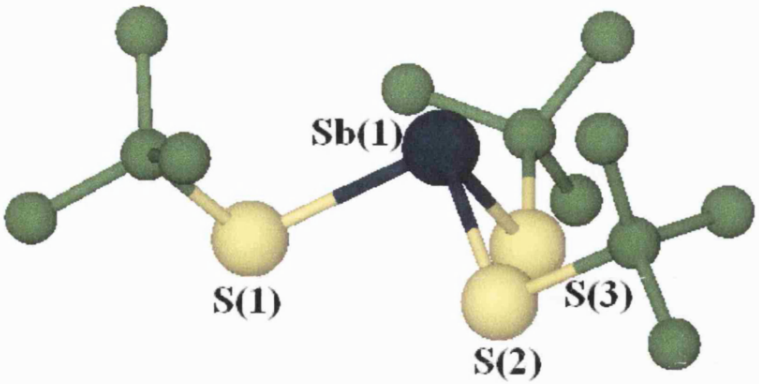

Figure 4.5 Molecular Structure of $Sb(SBu^t)_3$ (**15**) showing the pyramidal geometry of the compound so the lone pair of electrons of the antimony can be accommodated

Table 4.4 Selected Bond Distances (Å) for $Sb(SBu^t)_3$ (**15**) and $Sb(SCH_2CH_2NMe_2)_3$ (**18**)

	(15)	**(18)**
Sb(1)-S(1)	2.4248(14)	2.4870(5)
Sb(1)-S(2)	2.4248(14)	2.4854(5)
Sb(1)-S(3)	2.4248(14)	2.4851(5)
S(1)-C(1)	1.852(6)	1.823(2)
S(2)-C(5)	1.852(6)	1.828(2)
S(3)-C(9)	1.852(6)	1.824(2)
Sb(1)-N(1)		2.8440(5)
Sb(1)-N(2)		2.8480(5)
Sb(1)-N(3)		2.8380(5)

Table 4.5 Selected Bond Angles (°) for $Sb(SBu^t)_3$ **(15)** and $Sb(SCH_2CH_2NMe_2)_3$ **(18)**

	(15)	**(18)**
S(1)-Sb(1)-S(2)	92.12(6)	87.109(19)
S(2)-Sb(1)-S(3)	92.12(6)	87.291(19)
S(1)-Sb(1)-S(3)	92.12(6)	86.683(18)
S(1)-Sb(1)-N(1)		74.81(5)
S(2)-Sb(1)-N(2)		75.25(5)
S(1)-Sb(1)-N(3)		74.71(5)

The molecular structure of **(15)** was found to consist of a monomer in which antimony is bonded to three *tert*-butyl groups arranged in a propeller-like fashion forming the expected trigonal-pyramidal geometry. The asymmetric unit contains 1/3 of a molecule with the central Sb atom located on a 3-fold rotation axis and hence only one Sb-S bond is unique generating the other two bonds by symmetry. Figures 4.4 and 4.5 shows the molecular structure of **(15)** from different perspectives. The average Sb-S bond distances is 2.427 (14) Å and bond angles of 92.12(6) ° are very similar to other $Sb(SR)_3$ complexes reported in the literature[161]. Figure 4.6 shows the three-dimensional arrangement in the crystal viewed along the *c* axis.

There are only a few reported structures for antimony thiolates with formula $Sb(SR)_3$, only one of which involves SBu^t thiolate group. This was reported by Jones *et al*[181] where the $Sb(SBu^t)_3$ unit is present acting as a ligand to an organotransition-metal centre, $[W(CO)_5\{S(Bu^t)Sb(SBu^t)_2\}]$. In this adduct, there are two different values for Sb-S distances, a longer distance of 2.492(1) Å for the Sb-S where the sulphur is also bonding to the tungsten and two shorter ones of 2.395(2) and 2.397(2) Å for the other two pendant *tert*-

butyl groups. The coordination to the tungsten weakens one Sb-S bond distance and this consequently strengthens the other two. The Sb-S bond distance in precursor (**15**) is 2.4248(14) which is closer to the corresponding values for the terminal Sb-S distances in the adduct with a difference of 0.03 Å whereas the difference with the coordinated SBu^t to the tungsten is 0.06 Å. The three S-Sb-S bond angles in precursor (**15**) are all 92.63(6)° typical for a trigonal pyramidal geometry, however in the Sb-W adduct due to the coordination of one of the SBu^t groups to the tungsten the S-Sb-S bond angle increases up to 102.44(6)° reducing the other two terminal SBu^t angles S-Sb-S to 90.75(6) and 90.95(6)°, presenting a distorted trigonal pyramidal geometry. This is suggested to be due to some degree of steric repulsion between the tungsten centre and the Bu^t groups bonded to the sulphur.

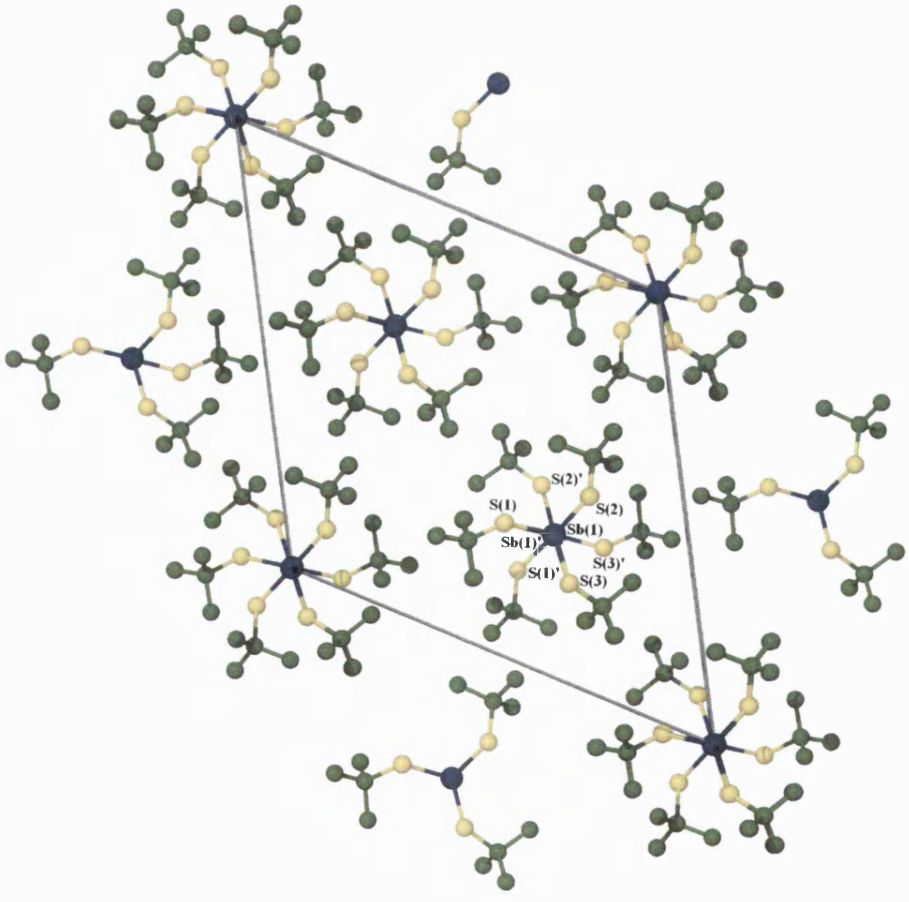

Figure 4.6 The structure of (**15**) in the crystal viewed along the *c* axis.

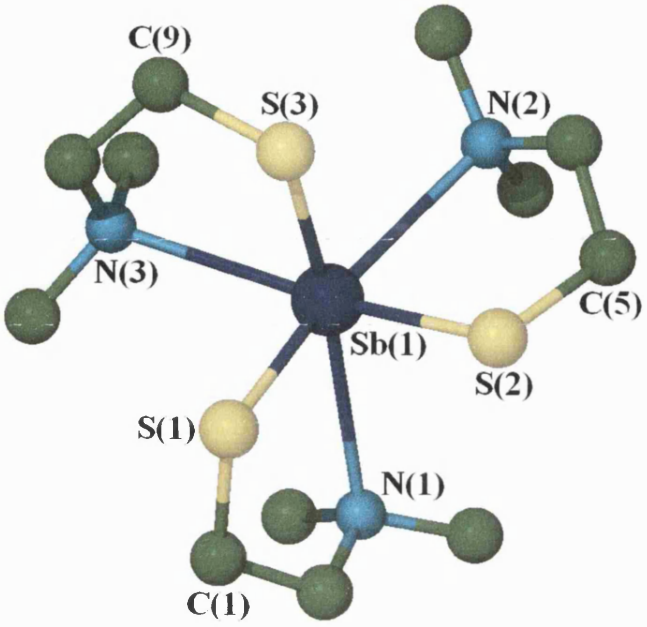

Figure 4.7 Molecular structure of $Sb(SCH_2CH_2NMe_2)_3$ (**18**).

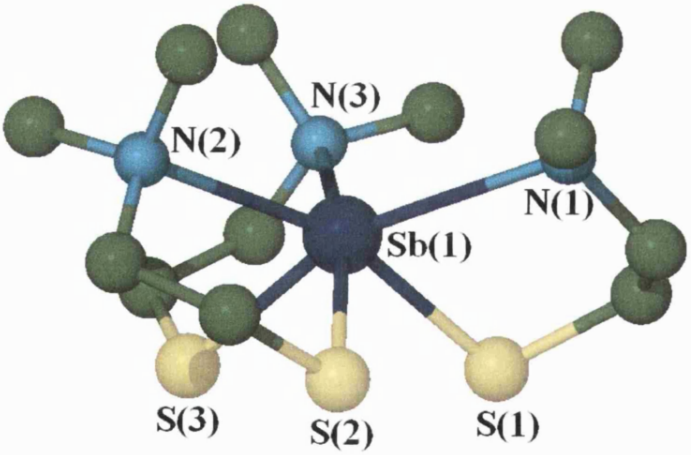

Figure 4.8 Molecular structure of $Sb(SCH_2CH_2NMe_2)_3$ (**18**) showing the distorted trigonal prism arrangement of the compound so the lone pair of electrons of the antimony can be accommodated.

The molecular structure of (**18**) was found to be monomeric in nature with coordination number of 6, where the antimony is surrounded by three sulfur and three nitrogen atoms in a distorted trigonal prism arrangement. The interaction between the antimony and the three nitrogen atoms forces the coordination to be considerably splayed in order to accommodate the lone pair, directed along the *c* axis.

The Sb-S bond distances are in the range between 2.4851(5) and 2.4870(5) Å and on average of 2.4858(5) Å, consisted with the ones reported for other antimony(III) thiolates.[21, 157, 162]

The bond angles reported for other group 15 thiolates[21, 157, 161] adopting a trigonal-pyramidal coordination geometry, on average for S-Sb-S, are *ca.* 94° with a sum of angles of 280° compared to compound (**18**) were the average for S-Sb-S bond angles are 87.028(18) °and the sum of angles is *ca.* 261°. This angular distortion might be associated with the intramolecular interaction between the Lewis acidity of the antimony centre and the nitrogen of the pendant amine narrowing the angle.

From main group elements, Briand and co-workers reported the synthesis and characterization of a series of different bismuth aminoethanethiolates.[180] One example of these compounds is $Bi(SCH_2CH_2NH_2)_3$, where the molecular structure presents a distorted pentagonal pyramidal geometry. In surprising contrast, the Bi-S bond distances in the bismuth aminoethanethiolates are longer [2.567(5)-2.748(7) Å] and the Bi-N bond distances shorter [2.64(2)-2.81(2) Å] than in compound (**18**). These structural differences in bond distances can be rationalized in terms of the bigger size of the bismuth over the antimony and therefore the Bi-S bond will be longer and also due to the more electropositive character of the bismuth over the antimony atom the Bi-N bond will be stronger (and consequently shorter) than the Sb-S bond.

Other aminoethanethiolate complexes with transition metals, such as cadmium and mercury, have been reported.[173, 178, 179] The majority of them form dimers and polymers due to the intermolecular interaction between the metal centre and the sulfur of the adjacent

molecule. One example of these dimers was reported by Atwood *et al.*[173] where the complex $[Cd(SCH_2CH_2NH_2)_2]_2$ consists of discrete molecules associated as a dimer linked through intermolecular hydrogen bonds between the sulphur and the metal centre of the adjacent molecule.

The molecular structure of $Me_2Al(SCH_2CH_2NMe_2)$ (**19**), shown in Figure 4.9, was isolated as a by-product from the unexpected ligand exchange reaction between $Sb(SCH_2CH_2NMe_2)_3$ (**18**) and $AlMe_3$ in an attempt to obtain the bimetallic adduct $Sb(SCH_2CH_2NMe_2)_3 \cdot AlMe_3$.

The crystals were obtained by slow diffusion of a saturated solution in toluene layered with hexane and found to be air- and moisture-sensitive. The data collection was carried out at 150 K. The relevant bond distances and angles of compound (**19**) together with the analogous structures of $^tBu_2Al(SCH_2CH_2NMe_2)$[182] and $^tBu_2Al(SCH_2CH_2NEt_2)$[182] for comparison, are summarized in Tables 4.6 and 4.7 with further data provided in Appendix 4.

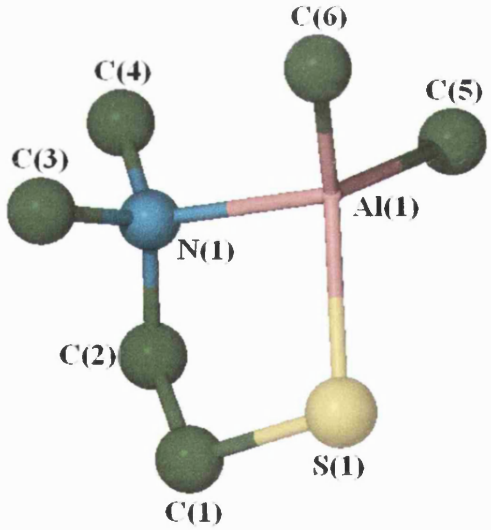

Figure 4.9 Molecular structure of $Me_2Al(SCH_2CH_2NMe_2)$ (**19**).

The crystal structure was found to consist of discrete monomers with the aminothiolate acting as a chelating ligand. The complex presents a distorted tetrahedral

geometry due to the reduced bite angle of the aminothiolate ligand, and the five-membered cycle formed within the molecule possesses an envelope conformation with the carbon adjacent to the amine nitrogen twisted out the plane, forming a dihedral angle, of *ca.* 50.1°.

Table 4.6 Selected Bond Distances (Å) for $Me_2Al(SCH_2CH_2NMe_2)$ (**19**) and $^tBu_2Al(SCH_2CH_2NMe_2)$[182] and $^tBu_2Al(SCH_2CH_2NEt_2)$[182]

	(19)	**$^tBu_2Al(SCH_2CH_2NMe_2)$[182]**	**$^tBu_2Al(SCH_2CH_2NEt_2)$[182]**
Al(1)-S(1)	2.2725(5)	2.262(2)	2.272(4)
Al(1)-N(1)	2.0100 (11)	2.044(4)	2.061(7)
S(1)-C(1)	1.8321(15)	1.804(2)	1.804(2)
N(1)-C(2)	1.4927(16)	1.492(2)	1.495(2)
C(1)-C(2)	1.516(2)	1.511(2)	1.513(2)

Table 4.7 Selected Bond Angles (°) for $Me_2Al(SCH_2CH_2NMe_2)$ (**19**) and $^tBu_2Al(SCH_2CH_2NMe_2)$[182] and $^tBu_2Al(SCH_2CH_2NEt_2)$[182]

	(19)	**$^tBu_2Al(SCH_2CH_2NMe_2)$[182]**	**$^tBu_2Al(SCH_2CH_2NEt_2)$[182]**
N(1)-Al(1)-S(1)	90.88(3)	90.10(1)	90.20(3)
C(1)-S(1)-Al(1)	95.00(5)	96.36(1)	96.26(1)
C(2)-N(1)-Al(1)	104.92(7)	104.65(1)	104.90(1)
N(1)-C(2)-C(1)	111.35(11)	112.25(1)	111.92(1)
C(5)-Al(1)-C(6)	115.63(7)	116.65(1)	117.09(1)
C(3)-N(1)-C(4)	108.38(10)	107.55(1)	110.97(1)

The compound $Me_2Al(SCH_2CH_2NMe_2)$ (**19**) has been previously reported by Beachley *et al* [183] where they suggested it to be monomeric by solution molecular weight measurements, however the crystal structure was not reported.

The analogous structures, $^tBu_2Al(SCH_2CH_2NMe_2)$ and $^tBu_2Al(SCH_2CH_2NEt_2)$,[182] have also been described but obtained through a completely different synthetic route by the reaction between the aluminium alkyl with the parent thiol. An example of these structures is the compound $^tBu_2Al(SCH_2CH_2NMe_2)$ reported by McMahon *et al*[182] which is illustrated in Figure 4.10.

The Al-N and Al-S bond distances (2.0100(11) Å and 2.2725(5) Å, respectively) and N-Al-C and N-Al-S bond angles (115.63(7)° and 90.88(3)°, respectively) in compound (**19**) are almost exactly the ones reported for analogous complexes $^tBu_2Al(SCH_2CH_2NMe_2)$ or $^tBu_2Al(SCH_2CH_2NEt_2)$,[182] where the Al-N and the Al-S distances are 2.044(4), 2.061(7) and 2.262(2), 2.272(4), respectively and with N-Al-C and N-Al-S angles of 116.6(2)° and 90.1(1)°, respectively. The dihedral angles that define the envelope conformation of the cycle formed within the molecule in $^tBu_2Al(SCH_2CH_2NMe_2)$ and $^tBu_2Al(SCH_2CH_2NEt_2)$ are *ca.* 48.1 and 49.7°, respectively, out of the plane, again in agreement with the values shown for compound (**19**).

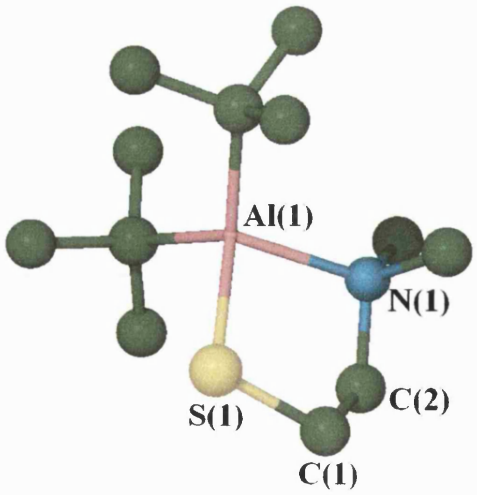

Figure 4.10 Molecular Structure of $^tBu_2Al(SCH_2CH_2NMe_2)$.[182]

4.2.3 CVD Testing of Precursors

The precursors $Sb(SBu^t)_3$ (**15**) and $Sb(SCH_2CF_3)_3$ (**16**) were both tested as CVD precursors, with the testing carried out on a purpose-built low pressure CVD reactor. Details of the apparatus are provided in Appendix 2. Different substrates, 1.2 mm borosilicate glass slides and silicon wafers, were used in order to study their influence on the film growth.

This section gives details of the tests carried out on compounds (**15**) and (**16**) to establish their volatility and to determine the suitable conditions for the deposition of the films. Due to the excellent yields obtained from both precursors, several runs were possible before establishing the ideal conditions for the deposition.

Figure 4.11 shows the Thermogravimetric Analysis (TGA) for precursor (**15**). The analysis shows a shoulder (~150 °C) corresponding to the onset of sublimation. The total residual mass (~25 %) is lower than that for Sb_2S_3 (theoretical: 44 %), again reflecting the volatility of $Sb(SBu^t)_3$ and mass loss due to sublimation. Low pressure CVD studies were consequently carried out above 100 °C were the precursor starts to sublime. The furnace temperature was set up at 150 °C where the precursor starts to decompose and the substrate temperature at 300 °C where the precursor has completely decomposed to produce the desired Sb_2S_3.

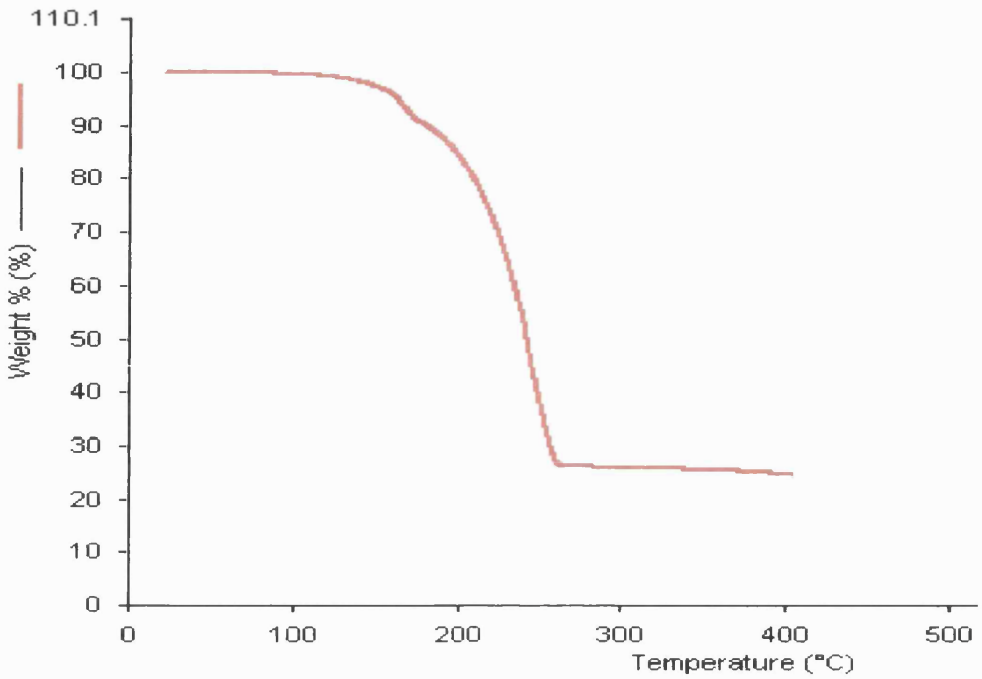

Figure 4.11 Thermogravimetric analysis for $Sb(SBu^t)_3$ (**15**).

The different deposition conditions used for each precursor are summarized in Table 4.8 together with the substrate used and description of the films obtained.

Table 4.8 Conditions for the CVD of Sb_2S_3 using Antimony (III) Thiolates

Precursor	Furnace Temperature (°C)	Substrate Temperature (°C)	Run Time (h)	Substrate Slides	Film Colour
(15)	130 °C	300 °C	2	Glass	Black
(15)	130 °C	300 °C	1	Silicon	Dark Grey
(16)	150 °C	450 °C	0.5	Glass	Light Grey
(16)	150 °C	450 °C	0.5	Silicon	Light Grey

The conditions listed in Table 4.8 were found to produce the best coatings of the appropriate thickness in order to enable further analysis of the deposited material. Several runs needed to be performed so the coated area could be controlled and although by the appearance of the coating was possible to estimate quantitatively the film thickness, completely uniform and homogeneous coatings were impossible to achieve. However, all films adhered well to the substrates and could not be easily removed without scratching.

Due to the high volatility of both (**15**) and (**16**) precursors at low pressure, low temperatures were required to volatise the precursors in the furnace (130-150 °C). For precursor (**16**), in order to ensure maximum decomposition and not simply pump the precursors from the reaction chamber, high temperatures in the substrate were necessary (>400 °C). Nonetheless, undecomposed precursor still condensed in the cold zones of the reaction tube.

4.2.4 Film Analysis

Films were examined by visual inspection, Energy Dispersive X-ray Analysis (EDAX) and Scanning Electron Microscopy (SEM). Glancing Angle X-ray diffraction studies were also performed on the films to determine if they were crystalline, and then confirm the nature of the deposited film. SEM showed the surface of the films to consist of different morphologies depending not only on the precursor used but also on substrate where the deposition took place. It was possible to perform quantitative EDAX on all films due to the good coverage and thickness.

All the films obtained from both precursors (**15**) and (**16**) present identical EDAX analysis, displaying antimony and sulphur peaks with high intensity and only showing minimal peaks corresponding to elements from the substrate (e.g. silicon, sodium or

oxygen) indicating that the film has been coated with suitable thickness. Figures 4.12 and 4.13 show the EDAX of the film grown from precursor (**15**) using glass slides and silicon wafers as substrate.

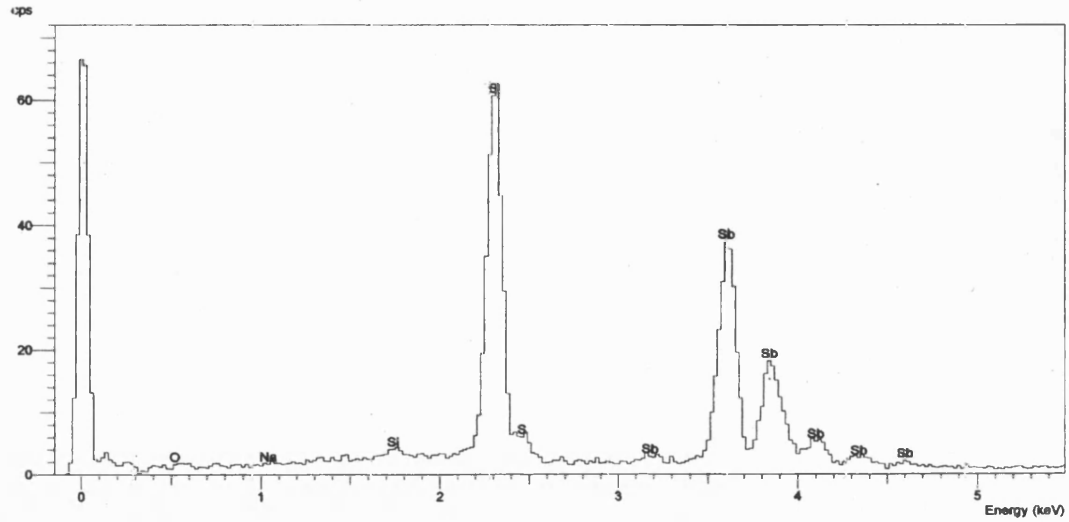

Figure 4.12 EDAX qualitative analysis of film grown from precursor (**15**) on glass slides.

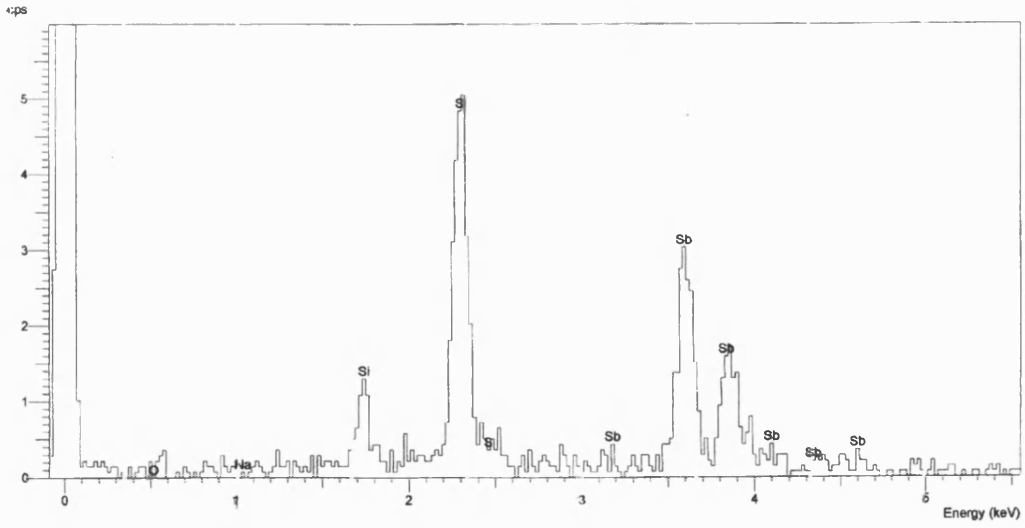

Figure 4.13 EDAX qualitative analysis of film grown from precursor (**15**) on silicon wafers.

Figures 4.14 and 4.15 show the EDAX of the film grown from precursor (**16**) using glass slides and silicon wafers as substrate, respectively. It could be observed that there are only minimal peaks corresponding to elements from the substrate (e.g. silicon, sodium or oxygen) and that no fluorine peaks are observed which indicates the clean decomposition of the precursor. In Figure 4.15 no silicon peaks are observed proving the good coverage of the silicon wafer.

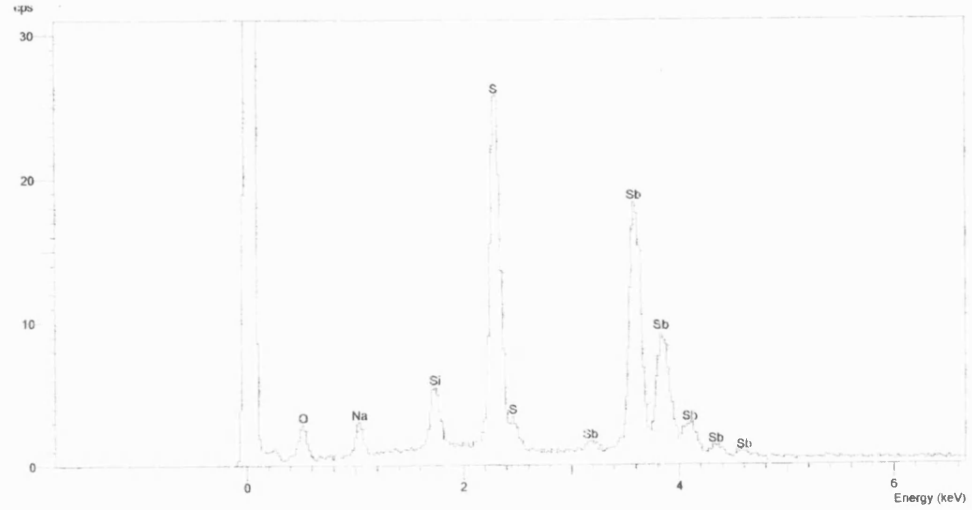

Figure 4.14 EDAX qualitative analysis of film grown from precursor (**16**) on glass slides.

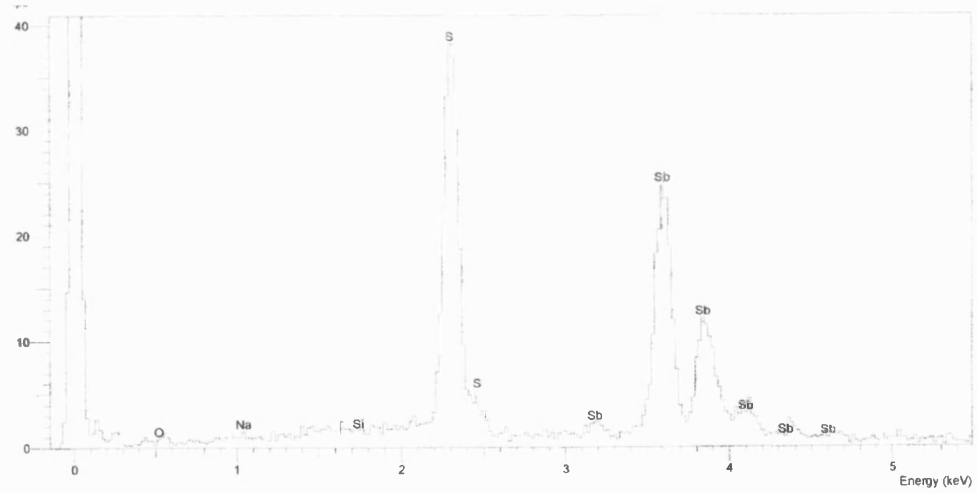

Figure 4.15 EDAX qualitative analysis of film grown from precursor (**16**) on silicon wafers.

All the films were crystalline and the diffraction patterns could be compared to standard Sb_2S_3 Stibnite (orthorhombic, PDF 06-0474). Figures 4.16 and 4.17 show the glancing angle X-ray patterns of the films grown from precursor (**15**) using glass and silicon substrates, respectively. All peaks could be fully indexed, however, the most intense reflexions found in the films do not entirely match with the most intense peaks shown in the random orientation from the standard Sb_2S_3 Stibnite found in the data base. The most intense peak in the film corresponds to the reflexion (310) in the films grown on glass sides and the reflexion (120) in the ones grown on silicon wafers. It is interesting the fact that although the most intense peak in the films grown on silicon substrates is the one corresponding to the reflexion (120), the reflexion (310) still is a very intensive peak, almost as intensive as the (120) reflexion. In the random orientation the most intense peak is the one for the reflexion (221). The rest of the main peaks in the random orientation are also the main peaks as in the deposited films, nonetheless, the intensities are different. It can be observed how the intensity for some of the main peaks varies when the film is grown on different surfaces. Neither of the films deposited on glass slides or silicon wafers show any significant preferred orientation, however, the orientations are not totally random. The differences in the intensities between patterns might indicate differing mixtures of oriented particles. Marginally, fewer reflections on the film deposited on silicon wafers is consistent with a more ordered substrate.

SEM images of the films obtained from precursor (**15**) showed uniform coverage consisting in fairly uniform small particles (*ca.* 3 μm) with plate shape. Films deposited using both glass and silicon slides as substrates present similar morphology with slight change on the alignment of the particles grown (Figures 4.18 to 4.21). Quantitative EDAX in the films deposited in both glass and silicon substrates revealed that the ratio between antimony and sulphur Sb:S is 1.39, consisted with the formula Sb_2S_3.

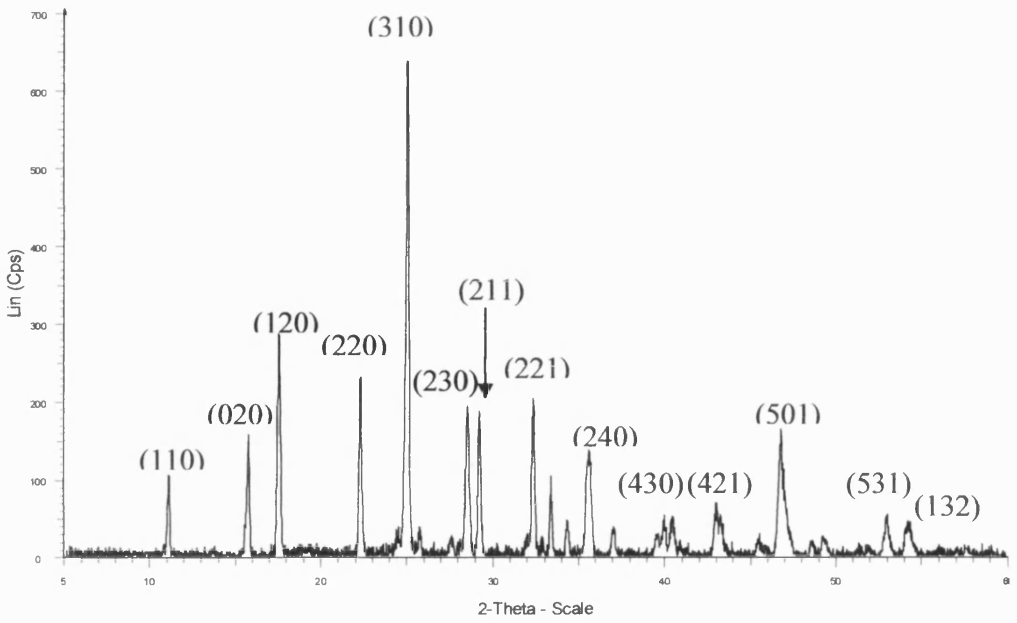

Figure 4.16 Glancing angle X-ray pattern of film grown from precursor (**15**) on glass slides.

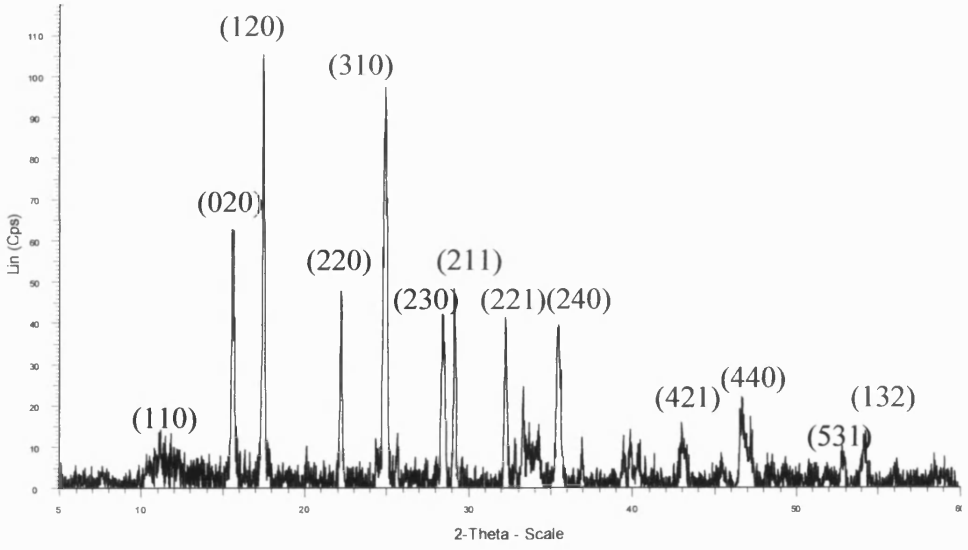

Figure 4.17 Glancing angle X-ray pattern of film grown from precursor (**15**) on silicon wafers.

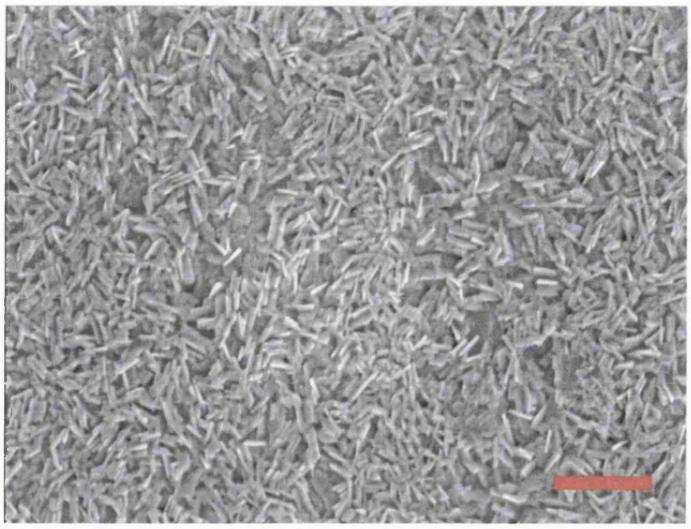

Figure 4.18 SEM of film grown from precursor (**15**) at 300 °C on glass slides. Red bar = 10 μm.

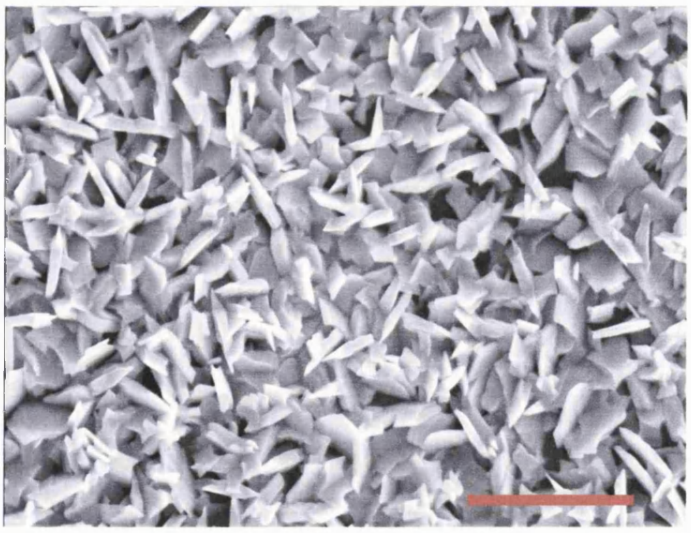

Figure 4.19 SEM of film grown from precursor (**15**) at 300 °C on glass slides at higher magnification. Red bar = 10 μm.

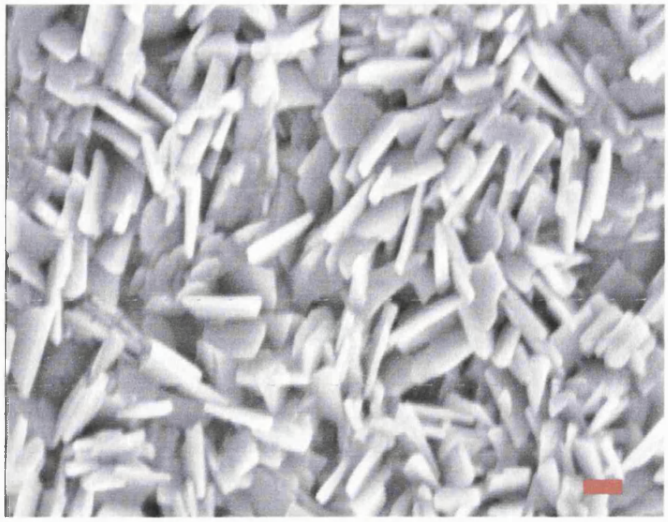

Figure 4.20 SEM of film grown from precursor (**15**) at 300 °C on silicon wafers. Red bar = 1 μm.

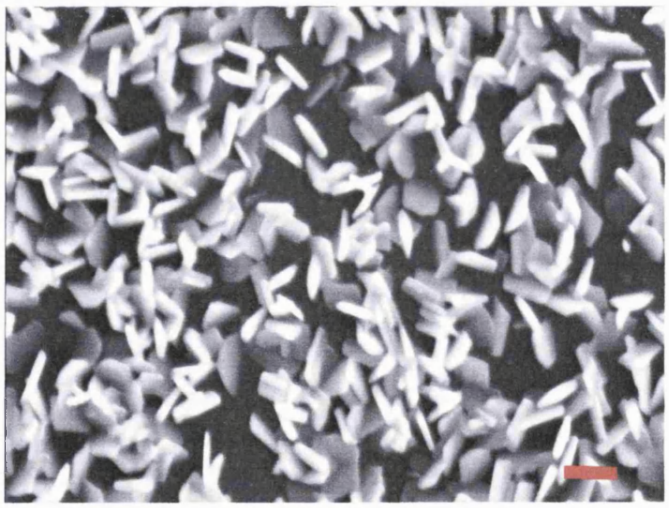

Figure 4.21 SEM of film grown from precursor (**15**) at 300 °C on silicon wafers. Red bar = 1 μm.

Figures 4.22 and 4.23 show the glancing angle X-ray patterns of the films grown from precursor (**16**) using glass and silicon substrates, respectively. The samples were crystalline and the diffraction patterns could be compared to standard Sb_2S_3 Stibnite (orthorhombic, PDF 06-0474) like the ones obtained from precursor (**15**). All peaks could be fully indexed and now the most intense peak corresponds to the reflexion (211) in the films grown on both glass sides and silicon wafers. As it happened before in the films obtained from precursor (**15**), in the films grown on silicon wafers from precursor (**16**) there is a second reflexion almost as intense as the (211) reflexion that corresponds to the reflexion (221), which is the most intense peak in the random orientation from the standard Sb_2S_3 Stibnite found in the data base. Overall, the films grown on silicon wafers again presents marginally fewer reflections, consistent with a more ordered substrate as expected due to the more ordered surface of the silicon wafers than in glass ones, likewise the films grown from precursor (**15**).

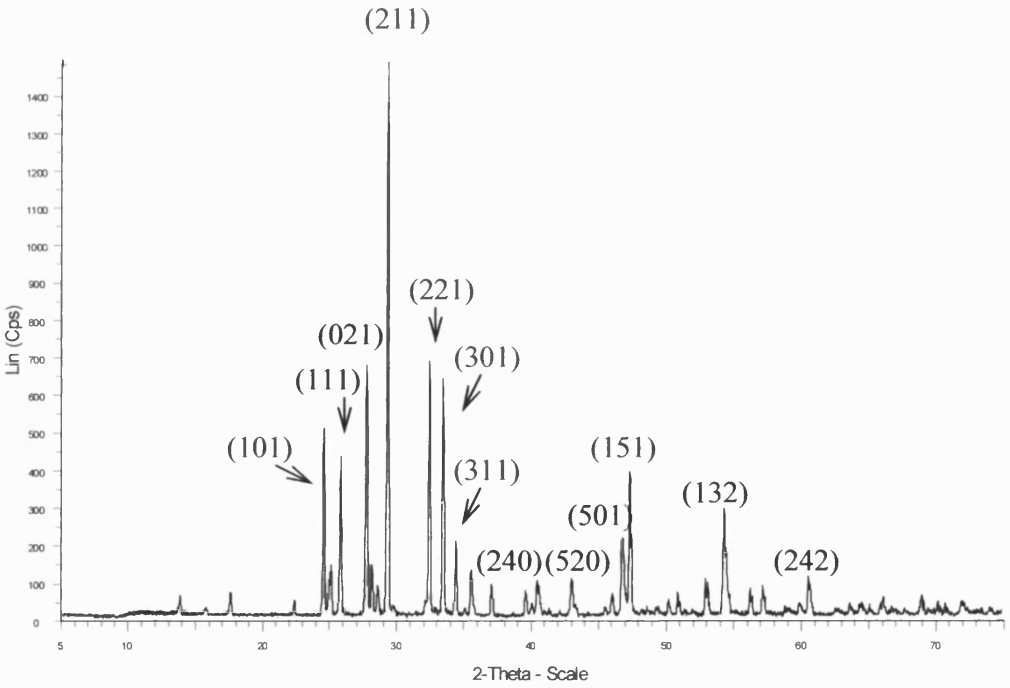

Figure 4.22 Glancing angle X-ray pattern of film grown from precursor (**16**) on glass slides.

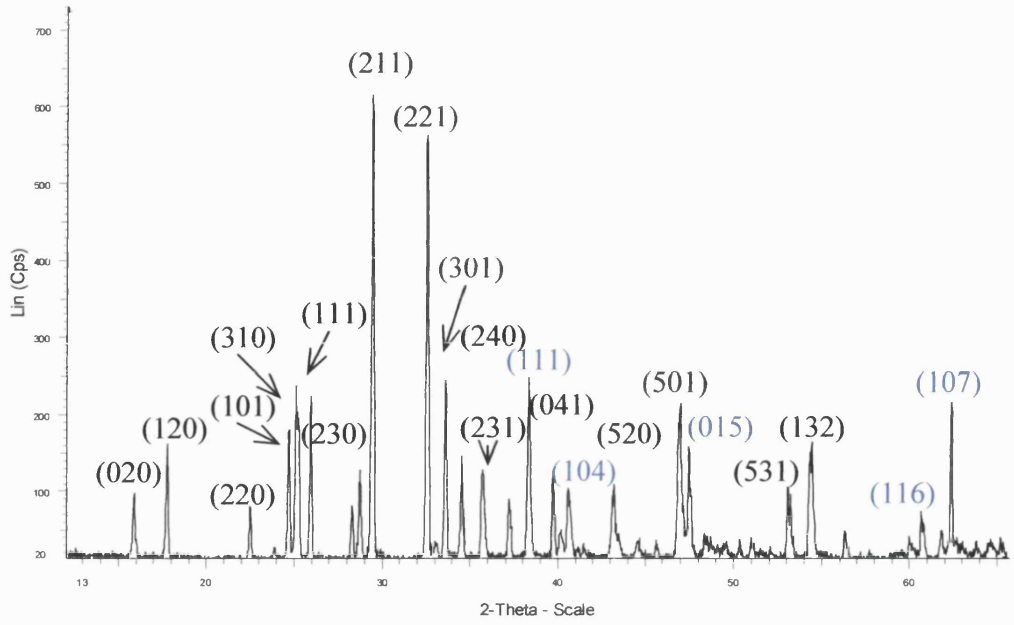

Figure 4.23 Glancing angle X-ray pattern of film grown from precursor (**16**) on silicon wafers. Blue peaks match with reflexions from crystalline antimony (rhombohedral, PDF 05-0562).

It is relevant to remark that some of the peaks in the films grown on silicon wafers (blue peaks) do not match with any of the reflexions of the random orientation from Sb_2S_3 Stibnite, however the can be easily assigned with reflexions from the random orientation of crystalline antimony (rhombohedral, PDF 05-0562). This result is in agreement with the fact that due to the relatively high temperatures used during the deposition process, some octahedral particles of antimony metal might appear in the surface of the film (Figure 4.26).

SEM images of the films obtained from the fluorinated precursor (**16**) showed uniform coverage and excellent thickness, using both glass and silicon substrates. In contrast to precursor (**15**), the morphology of the films changes dramatically when changing the substrate. For the films grown on glass, the material deposited consisted of various size crystallites (Figures 4.24 - 4.26) with non-uniform coverage, however in the films grown on glass slides, due to relatively high temperatures used (450 °C) some

octahedral particles appeared in the surface (Figure 4.26) which quantitative analysis proved to be antimony metal. The formation of antimony particles has been reported previously when high temperatures (>500 °C) were used in the deposition of antimony oxide from antimony alkoxides as precursors.[102] Figure 4.25 show the deposited film from precursor (**16**) at 450 °C tilted 73° where the thickness can be estimated to be 25μm and which quantitative analysis reveals that the ratio between antimony and sulphur Sb:S is 1.48, matching with the formula Sb_2S_3.

A completely different morphology appeared when precursor (**16**) is grown on silicon wafers as the substrate. The composition of the films can be described as divided in two main layers. The underlying layer presents a uniform coverage (Figure 4.27) with a very similar morphology that the one shown in the films grown on glass substrate (see comparison with Figure 4.26). The top layer is dominated by a rod-like material of different dimensions. It could be observed at higher magnification how these rod-like particles are also formed at the same time from smaller plates (Figures 4.29 and 4.30). Looking at Figures 4.28 and 4.29 that the rods have an estimated width of 115 μm where each stratum is *ca.* 10 μm in thickness. At a higher magnification of the rods (Figure 4.30) it is possible to distinguish between the different layers that form the rod, where the smallest plates vary in size and can be estimated to be of approximately 0.8 to 1.8 μm.

Figure 4.24 73° tilt SEM of film grown from precursor (**16**) at 450 °C on glass slides. Red bar = 10 μm.

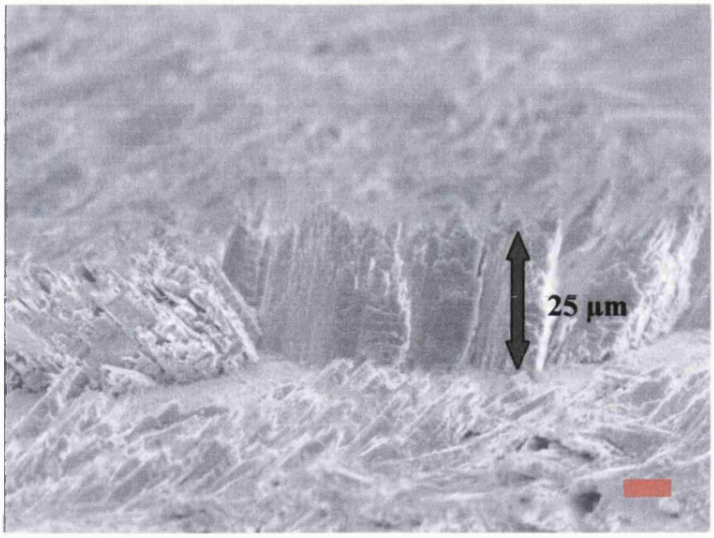

Figure 4.25 73° tilt SEM of film grown from precursor (**16**) at 450 °C on glass slides. Red bar = 10 µm.

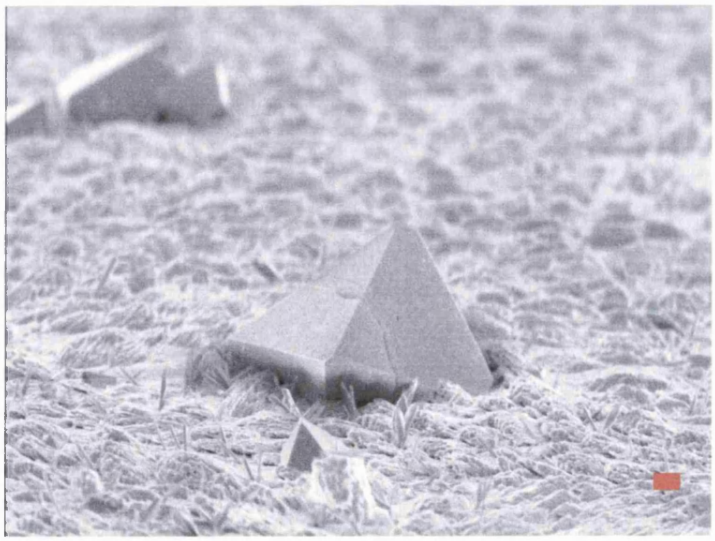

Figure 4.26 73° tilt SEM of film grown from precursor (**16**) at 450 °C on glass slides. Red bar = 10 µm.

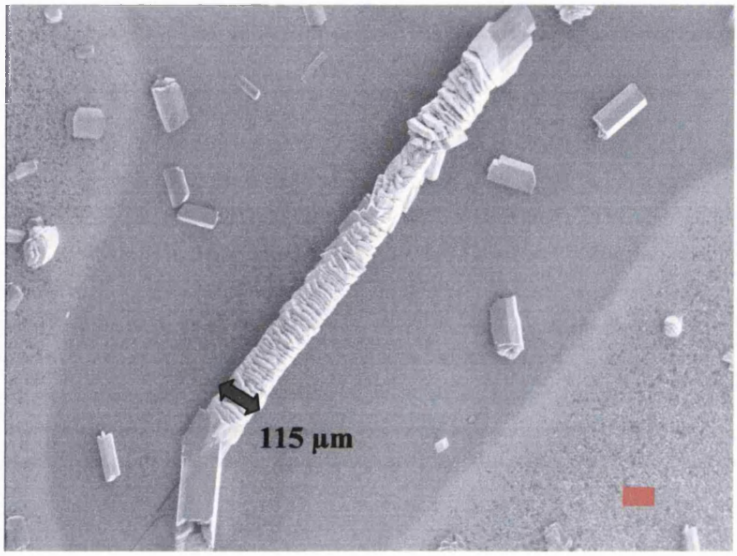

Figure 4.27 68° tilt SEM of film grown from precursor (**16**) at 450 °C on silicon wafers. Red bar = 20 µm.

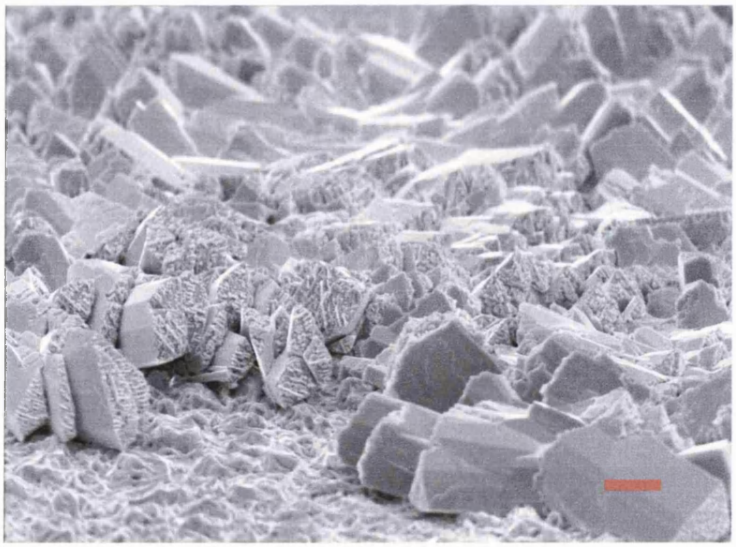

Figure 4.28 SEM of film grown from precursor (**16**) at 450 °C on silicon wafers. Red bar = 100 µm.

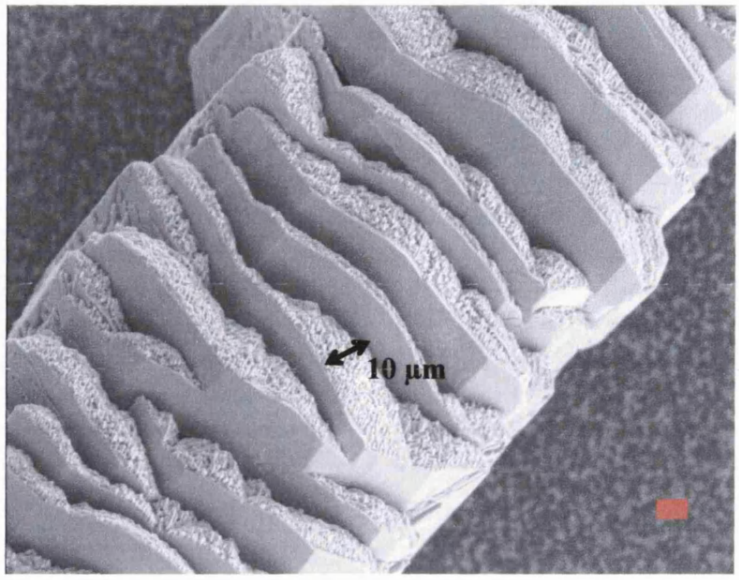

Figure 4.29 SEM of film grown from precursor (**16**) at 450 °C on silicon wafers at higher magnification. Red bar = 10 µm.

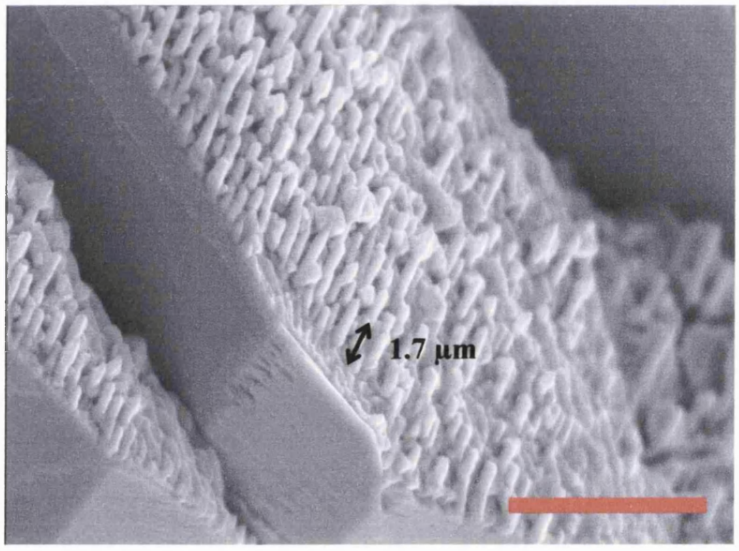

Figure 4.30 SEM of film grown from precursor (**16**) at 450 °C on silicon wafers at higher magnification. Red bar = 10 µm.

Again, like in the films deposited from precursor (**15**), quantitative analysis revealed that the ratio between antimony and sulphur Sb:S is 1.55, consisting with the formula Sb_2S_3.

In summary, the material deposited in films grown from precursor (**16**) was found to be Sb_2S_3 showing different morphologies depending on the substrate used. Also, due to the relatively high temperatures used during the deposition (>450 °C), some antimony metal with octahedral shape started to appear on the surface. Surprisingly, the antimony particles could be visually appreciated in films grown on glass slides by SEM but were not detectable by the powder diffraction analysis. On the contrary, these particles were not visually observed by SEM in the films grown on silicon wafers but detected by powder diffraction measurements. This fact can only be explained based on the random choice of the various portions of the films subjected to the different analysis. The selectivity of the areas analyzed by SEM did not entirely match with the areas covered by powder diffraction.

The mechanism for the deposition process was not investigated, however, other metal sulphides have been previously laid down by LPCVD from $M(SBu^t)_4$ (M= Mo, Ti)[50]. For these precursors, the major by-products found were *iso*-butene and *tert*-butylthiol together with some H_2S as a minor product. The formation of the main by-products in the deposition of MS_2 can be explained by a series of reactions initiated by a β-hydrogen abstraction and the consequently C-S bond cleavage producing *iso*-butene (Equation 4.5) and followed by proton-transfer reaction of the thiol hydrogen atom to an adjacent *tert*-butylthiolate ligand to give *tert*-butylthiol (Equation 4.6). This mechanism will take place twice to give the desired MS_2 and an overall of 2 equivalents of both *iso*-butene and *tert*-butylthiol. Alternatively (and competitively) the transfer of the thiol hydrogen atom to a neighboring thiol group would generate hydrogen sulphide (Equation 4.7). Both mechanisms are well accepted because both easily explain the presence of the different by-products. Equation 4.7 would be suitable for those precursors where H_2S was detected as a by-product.

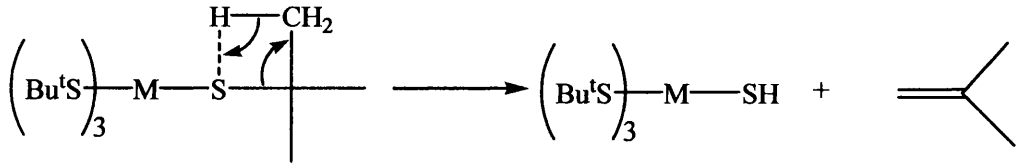

[4.5]

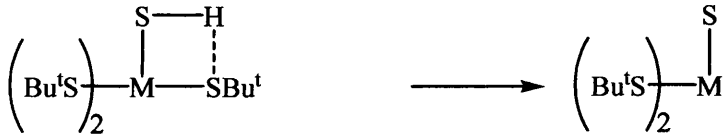

[4.6]

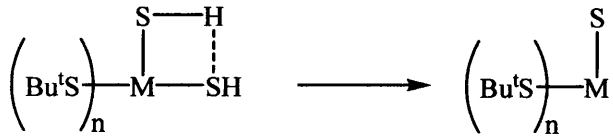

[4.7]

Very similar mechanisms have been also proposed with the analogous metal *tert*-butoxide compounds (oxygen analogue to the *tert*-butylthiol).[175-177]

In conclusion, films produced from antimony(III) thiolates were of high quality with good surface coverage and without contamination (no carbon or oxygen contamination was found, within the detection limit of the instrument). Compounds (**15**) and (**16**) have shown being extremely successful not only from a synthetic perspective but also for the CVD of Sb_2S_3 and the encouraging results of the films grown from them indicate that this group of compounds has a large potential for use as single-source precursors.

Compared with previous precursors tested, such as antimony(III) dithiocarbamates and xanthates, antimony(III) thiolates present much higher volatility and therefore, LPCVD studies were possible to perform at lower temperatures, avoiding the risk of oxygen incorporation by the conversion of antimony trisulphide to antimony trioxide (Sb_2O_3) at temperatures around 300 °C.[135]

4.3 EXPERIMENTAL

Starting materials were commercially obtained (e.g. Aldrich) and were used without further purification unless otherwise stated. Standard Schlenck line techniques were employed where applicable. Further details about instrumentation used are given in Appendix 1.

4.3.1 Preparation of tris(t-butylthiolato) antimony (III) – $Sb(SBu^t)_3$ (15)

A solution of sodium *tert*-butylthiolate (0.74 g, 6.6 mmol) in methanol (30 mL) was added to a solution of $SbCl_3$ (0.50 g, 2.2 mmol) in methanol (20 mL) which resulted in an immediate formation of a white suspension. The mixture was allowed to stir overnight after which time all volatiles were removed under vacuum. The crude reaction product was redissolved in diethyl ether (60 mL) and filtered through Celite resulting in a pale yellow solution. The solvent was evaporated and the remaining solid was washed with hexane (2 x 25 mL) and dried under vacuum, giving 0.60 g (70%) of (**15**) as a white solid. m.p: 150 °C (sublimes).

Microanalysis:

Found (calc.) for $C_{12}H_{27}S_3Sb$ (**15**): C 37.90 (37.02)%; H 6.45 (6.99)%.

^{1}H-NMR [δ (ppm), C_6D_6]:

1.40 (27H, s, CH_3).

^{13}C-NMR [δ (ppm), C_6D_6]:

47.0 [$C(CH_3)_3$], 35.9 [$C(CH_3)_3$].

4.3.2 Preparation of tris(2,2,2-trifluoroethanethiolato) antimony (III) – $Sb(SCH_2CF_3)_3$ (16)

2,2,2-trifluotoethanethiol (1.17 mL, 13.2 mmol) was added dropwise to a solution of $SbCl_3$ (1.00 g, 4.4 mmol) in toluene (60 mL) resulting a colourless solution. Ammonia was slowly bubbled through the reaction mixture, causing a white precipitate of NH_4Cl. This bubbling was continued until no more precipitate was formed (*ca.* 1.5 h). The soluble material was removed by cannula filtration, and the toluene removed under vacuum to leave 1.44 g (70%) of (**16**) as a clear oil.

Microanalysis:

Found (calc.) for $C_6H_6F_9S_3Sb$ (**16**): C 16.00 (15.42)%; H 1.37 (1.29)%

^{1}H-NMR [δ (ppm), $CDCl_3$]:

3.40 (6H, q, CH_2).

^{13}C-NMR [δ (ppm), $CDCl_3$]:

126.0 (q, $^1J_{C\text{-}F}$= 276 Hz, CF_3CH_2), 32.3 (q, $^2J_{C\text{-}F}$= 33.9 Hz, CF_3CH_2).

^{19}F-NMR [δ (ppm), $CDCl_3$]:

- 66.8 (t, $^3J_{H\text{-}F}$= 9.8 Hz, CF_3).

4.3.3 Preparation of tris(benzylthiolato) antimony (III) – $Sb(SBz)_3$ (17)

(**17**) was prepared by the same methodology as (**16**), using 4.4 mmol of $SbCl_3$ and benzyl mercaptan (1.54 mL, 13.2 mmol) to give 1.95 g (90%) of (**17**) as a clear oil which decomposes after a couple of days exposed to air.

Microanalysis:

Found (calc.) for $C_{21}H_{21}S_3Sb$ (**17**): C 52.00 (51.33)%; H 4.47 (4.31)%.

^{1}H-NMR [δ (ppm), $CDCl_3$]:

7.25-7.15 (5H, m, *H*-Ph), 3.90 (6H, s, CH_2).

^{13}C-NMR [δ (ppm), $CDCl_3$]:

140.1 (C_α-Ph), 129.1 (C_β, C_γ -Ph), 127.7 (C_δ-Ph), 34.6 (SCH_2).

4.3.4 Preparation of tris(dimethylaminoethanethiolato) antimony (III) – $Sb(SCH_2CH_2NMe_2)_3$ (18)

A solution of dimethylaminoethanethiol hydrochloride (3.72 g, 26.3 mmol) in methanol (50 mL) was treated with potassium hydroxide (2.95 g, 52.6 mmol) resulting a white suspension. The mixture was allowed to stir over 3 hours after which time a solution of $SbCl_3$ (2.00 g, 8.8 mmol) in methanol (25 mL) was added dropwise. The mixture was allowed to stir overnight followed by filtration giving a colourless solution. All volatiles were removed under vacuum resulting in a pale yellow solid. The crude product was then redissolved in chloroform (80 mL) and washed with water (50 mL) and anhydrous sodium hydrogenocarbonate until no more bubbling was evident. The chloroform layer was then isolated and dried with magnesium sulphate. After filtration the solvent was removed under vacuum to leave 2.40 g (68%) of (**18**) as a fine white solid. m.p: 98-100 °C.

Microanalysis:

Found (calc.) for $C_{12}H_{30}N_3S_3Sb$ (**18**): C 33.10 (33.18)%; H 7.06 (6.96)%; N 9.42 (9.67)%.

^{1}H-NMR [δ (ppm), $CDCl_3$]:

2.25 (18H, s, NCH_3), 2.65 (6H, s, CH_2N), 2.90 (6H, m, SCH_2).

^{13}C-NMR [δ (ppm), $CDCl_3$]:

62.80 (SCH_2), 45.3 (NCH_3), 27.8 (CH_2N).

4.3.5 Preparation of dimethyl(dimethylaminoethanethiolato) Aluminum (III)– $Me_2Al(SCH_2CH_2NMe_2)$ (19)

$AlMe_3$ (1.03 mL, 2.07 mmol) was added dropwise to a cooled suspension of $Sb(SCH_2CH_2NMe_2)_3$ (0.3 g, 0.69 mmol) in hexane (20 mL) under vigorous stirring over 3 hours. The mixture was allowed to warm up at room temperature giving a white suspension. The solvent was removed under vacuum to give a white solid that was dissolved in toluene (10 mL) and layered with hexane (10 mL). After 16 h at 4 °C air sensitive colourless crystals were obtained which were identified as (**19**) by X-ray crystallography.

Chapter Five

Antimony(III) Iodo-thiolates

5.1 INTRODUCTION

Antimony sulpho-iodide, SbSI, as mentioned in Chapter 1, has been extensively studied in single crystal form due to its many interesting properties as a ferroelectric material.[34] It has been synthesised by a relatively large number of routes such as Hydrothermal methods[43] or Electron Beam Evaporation.[38]

Nonetheless, due to its similarity to CVD, it is appropiate to refer again to the work published by Solayappan and co-workers[40] where they reported the growth of SbSI films with and without Sb_2S_3 buffer layers using the Physical Vapour Technique (PVT). For the growth of SbSI films without Sb_2S_3 buffer layers, a charge consisting of a *non*-stoichiometric mixture of 90% Sb_2S_3 and 10% of SbI_3 was used. The charge was loaded in a two-zone furnace ampoule sealed under vacuum together with the substrate perpendicularly mounted and kept at a different temperature. The typical temperatures used for the experimental process are 350 °C for the charge and 200 °C for the substrate. They found that the substrate temperature, charge composition and the ramp rate were vital parameters for the film deposition. Initial experiments produced large grained deep red discontinuous films consisting in crystalline and stoichiometric SbSI, characterised by XRD and Wavelength Dispersive Spectroscopy (WDS).

Solayappan also reported the liquid condensation of SbI_3 on the surface of the Sb_2S_3 substrate prior to the film formation of SbSI. The condensed liquid appeared either forming a continuous film or disintegrated into droplets. They reported that the appearance of condensed SbI_3 can be explained by premature volatilisation of the charge prior to the reaction with Sb_2S_3 and by decomposition of the SbSI formed during the experimental process when heated under vacuum according to the inverse reaction for the formation of SbSI illustrated by the following reaction:

$$3\ SbSI\ (s) \longrightarrow Sb_2S_3\ (s) + SbI_3\ (v)$$

The fact that SbSI has been produced by various methods at relatively low temperatures (around 200 °C) and that it is feasible to deposit it on films makes extremely interesting and challenging the search of single-source precursors from which SbSI can be deposited by CVD. Thus, the single-source candidate ought to have antimony, sulphur-based ligands and iodine present in its composition.

During the last decades, the structural chemistry of Group 15 metal thiolates has received considerable attention due to the tendency of these metal centres to adopt high coordination numbers and to adopt oligomeric structures.[151] However, the incorporation of a halogen atom to the metal centre to give halo-thiolate metal complexes is still a relatively unexplored field. To the best of our knowledge, there are no reports of iodo-thiolate metal complexes used as single-source precursors for the CVD of metal sulpho-iodide thin films.

Although there are a few examples in the literature of Group 15 halo-thiolates using monodentate thiolates, such as $SbI(SC_6H_2Me_3\text{-}2,4,6)_2$[51] (Figure 5.1), the majority of the complexes reported include bidentate thiolates such as 1,2-dithianes ($HSCH_2CH_2SH$) and thiolates containing 2-mercaptoethyl sulfide [$HS(CH_2)_2S(CH_2)_2SH$] as the backbone of the structure.

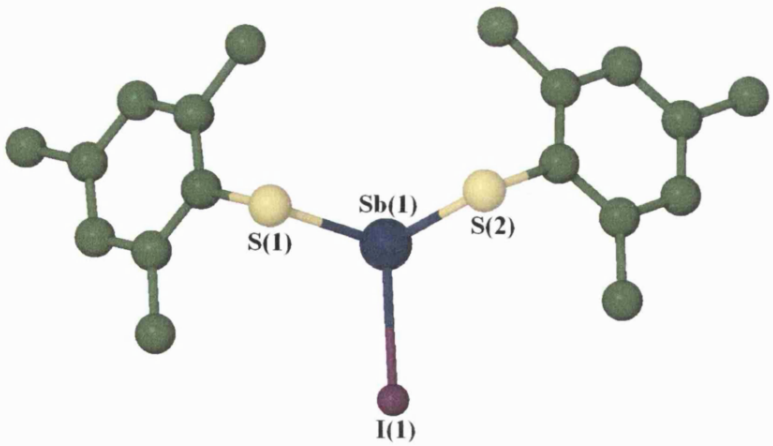

Figure 5.1 Molecular structure of $SbI(SC_6H_2Me_3\text{-}2,4,6)_2$.[51]

The first complex structurally characterised was reported by Bush and co-workers[184] in 1967 and contained 1,2-dithiane as the thiolate, $(CH_2S)_2SbCl$, and since then its analogues with arsenic[185] and bismuth[186] have also been reported. The common feature of these compounds is that only the chlorine derivative had been characterised and it presents coordination number 3 where the geometry around the antimony atom can be described as a distorted pseudo-tetrahedron considering the lone pair of electrons of the antimony atom.

Group 15 metal halo-thiolates containing 2-mercaptoethyl sulfide, $(SCH_2CH_2)_2SMX$ (M = As, Sb or Bi; X = Cl, Br or I), had been studied during the last decades in order to understand the hypervalency of Group15 elements. These complexes, also known as "metallocanes", are very interesting from a structural point of view due to their tendency to form eight-membered rings and the formation of a transannular secondary bonding within the molecules. Figure 5.2 shows the molecular structure of one of these arsenic metallocanes.[187]

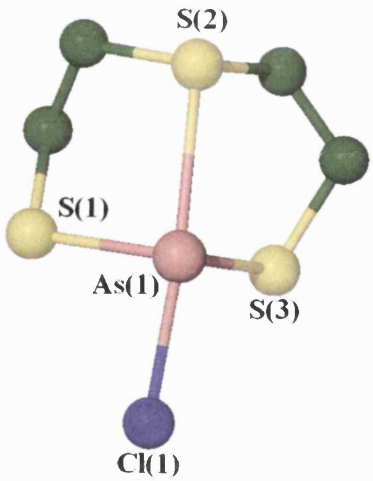

Figure 5.2 Molecular Structure of $(SCH_2CH_2)_2SAsCl$.[187]

An extensive study on a variation of these metallocanes, with formula $S(C_6H_4S)_2MX$ (M = As or Sb; X = Cl, Br or I), is the one reported by Alvarado-Rodriguez

et al.[188, 189] The different conformations of the eight-membered ring formed in these dibenzoarsocines and dibenzostibocines due to the transannular interaction were analysed. Figure 5.3 shows the molecular structure of one of the monohalogenated dibenzostibocines.[188]

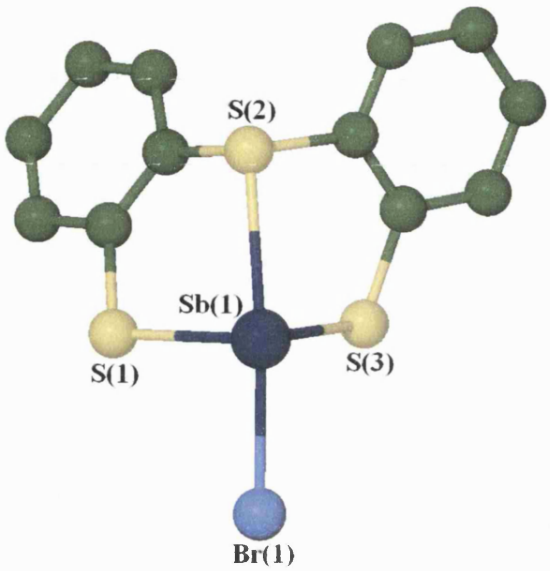

Figure 5.3 Molecular structure of $S(C_6H_4S)_2SbBr$.[188]

In these dibenzoheterocycles, the metal centre expands its coordination number to 4 through the transannular interaction by acting as a Lewis acceptor toward a sulphur atom. The geometry of these types of complexes, when the lone pair of the antimony atom is considered according to the VSEPR model, is described as distorted *pseudo*-trigonal bipyramidal.

In contrast with other antimony complexes, such as antimony thiolates, a survey in the literature reveals there are no antimony(V) halo-thiolates reported to date.

Some of the structurally characterised complexes of Group 15 halo-thiolates reported in the literature, together with coordination number, geometry and significant bond distances are summarised in Table 5.1.

Table 5.1 Coordination Geometries Exhibited by Group 15 Halo-thiolates

Coordination Number	Geometry	Example	Bond Distances Sb-S (Å)	Ref.
3	Distorted Tetrahedron	$(CH_2S)_2AsCl$	2.194(9), 2.225(1)	185
3	Distorted Tetrahedron	$(CH_2S)_2SbCl$	2.401(1), 2.412(1)	184
3	Distorted Tetrahedron	$(CH_2S)_2BiCl$	2.541(1), 2.848(1)	186
4	Distorted Ψ-Trigonal Bipyramidal	$S(SCH_2CH_2)_2AsCl$	2.248(1)-2.260(1)	187
4	Distorted Ψ-Trigonal Bipyramidal	$S(SCH_2CH_2)_2SbCl$	2.435 (2)-2.455(2)	190
4	Distorted Ψ-Trigonal Bipyramidal	$S(SCH_2CH_2)_2BiCl$	2.541(6)-2.849(5)	186
4	Distorted Ψ-Trigonal Bipyramidal	$S(C_6H_4S)_2SbBr$	2.4575(14)-2.4637(14)	188
4	Distorted Ψ-Trigonal Bipyramidal	$S(C_6H_4S)_2AsI$	2.283(1)-2.283(1)	189

In this chapter, the preparation, characterisation and properties of some further CVD candidates for SbSI films are evaluated. As with metal thiolates, an important advantage of using precursors containing thiolates as single-source precursors is to obviate the need to use toxic H_2S as co-reactant; hence it provides a much safer route. From a CVD point of view no one has reported the formation/deposition of SbSI from a single-source precursor and the challenge lies in keeping the relatively weak Sb-I linkage unaltered, which under the harsh conditions of the CVD process is the bond more likely to be broken.

5.2 RESULTS AND DISCUSSION

5.2.1 Synthetic Routes

The synthesis of metal iodo-thiolates is straightforward and relatively easy to achieve. Although some thiols need to be kept under nitrogen atmosphere, most of the resulting metal complexes are air stable and soluble in most organic solvents, this not being the case however, for the compounds described in this chapter which exhibited low solubility.

The most common method for the preparation of Group 15 halo-thiolates is by a two-step reaction, where in the first step the chlorinated derivative is obtained by direct reaction of the metal trichloride and a stoichiometric amount of the chosen thiol in toluene, to give the desired product together with hydrogen chloride.[188, 189] The product can be consequently isolated by precipitation on cooling the solution and suction filtration. A representation of this route is given by Equation 5.1:

$$MCl_3 + HSRSH \xrightarrow[\text{toluene}]{\text{reflux}} M(S_2R)Cl + HCl \qquad \textbf{[5.1]}$$

The second step of the reaction involves the reaction between the chlorinated derivative with one equivalent of the potassium halide salt (often excess is required to force the reaction to completion) in hot toluene. Depending on the solubility of the final product, the product is isolated by either precipitation on cooling or by reducing the volume of the solution. A representation of this method is illustrated by Equation 5.2:

$$M(S_2R)Cl + KX \xrightarrow[\text{toluene}]{\text{reflux}} M(S_2R)X + KCl \qquad \textbf{[5.2]}$$

Variations on this method, such as different selections of the solvent, have been reported depending primarily on the solubility of the final product.

Information regarding the methods used, compounds produced and brief comments concerning experimental conditions for previously reported species, are summarised in Table 5.2.

Table 5.2 Synthetic Routes Used for the Preparation of Group 15 Halo-thiolates

Compound	Synthesis [a]	Comments	Yield (%)	Ref.
$(CH_2S)_2AsCl$	5.1	CCl_4 is used as the solvent. Low m.p. product (39 °C).	87	185
$(CH_2S)_2SbCl$	5.1	HCl_{cc} is used as the solvent.	93	184
$(CH_2S)_2BiCl$	5.1	HCl_{cc} is used as the solvent.	82	191
$(SCH_2CH_2)_2SBiCl$	5.1	Insoluble product. DMSO used for recrystallisation.	87	186
$S(C_6H_4S)_2AsCl$	5.1	Column of Celite and Na_2SO_4 was required for isolation.	80	189
$S(C_6H_4S)_2AsBr$	5.2		71	
$S(C_6H_4S)_2AsI$	5.2		80	
$S(C_6H_4S)_2SbCl$	5.1	HBr/Tol mixture was required to obtain $S(C_6H_4S)_2SbBr$.	84	188
$S(C_6H_4S)_2SbBr$	5.2		62	
$S(C_6H_4S)_2SbI$	5.2		40	

[a] Equation numbers cited in text.

Two new antimony(III) iodo-thiolates have been prepared in this study following the common synthetic strategy reported in the literature, previously mentioned. All precursors were obtained in moderate yields (> 35 %) and the majority of them were found to be air- and moisture-stable with a pungent odour. Both iodo-derivatives were prepared from the known chlorine analogues ($S[SCH_2CH_2]_2SbCl$[190] and $[CH_2S]_2SbCl$[184]), whose formation was checked by X-ray crystallography.

A summary regarding the preparation of the precursors synthesised and reported in this chapter, including preparative route used, yields and physical properties is represented in Table 5.3.

Table 5.3 Synthetic Routes Used for the Preparation of Antimony(III) Iodo-thiolates

Precursor	Synthesis[(a)]	Yield (%)	Appearance	Solubility
$S(SCH_2CH_2)_2SbI$ **(20)**	5.1, 5.2	36	Pale Yellow solid m.p: 190 °C dec.	Slightly Soluble in DMSO
$(CH_2S)_2SbI$ **(21)**	5.1, 5.2	40	Bright Yellow Solid m.p: 195 °C dec.	Slightly Soluble in DCM

[(a)] Equation numbers cited in text.

5.2.2 Crystal Structures

Crystallographic quality crystals of the two analogous compounds $S(SCH_2CH_2)_2SbI$ (**20**) and $(CH_2S)_2SbI$ (**21**) were obtained by obtained from slow evaporation of saturated DMSO and dichloromethane solutions, respectively, at room temperature. The crystals were found to be air-stable and data collection was carried out at 150 K. The molecular structures of precursors (**20**) and (**21**) are shown in Figures 5.4 and 5.5, respectively. Relevant bond distances and angles are summarized in Tables 5.4 and 5.5 respectively, with further data provided in Appendix 4.

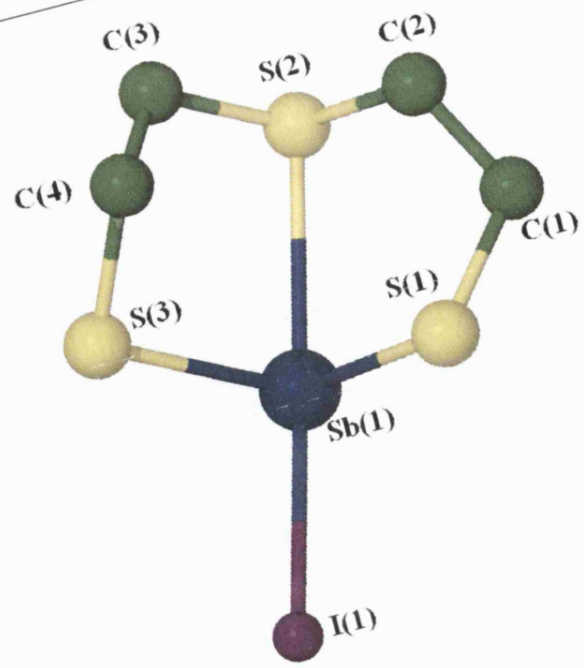

Figure 5.4 Molecular structure of $S(SCH_2CH_2)_2SbI$ **(20)**

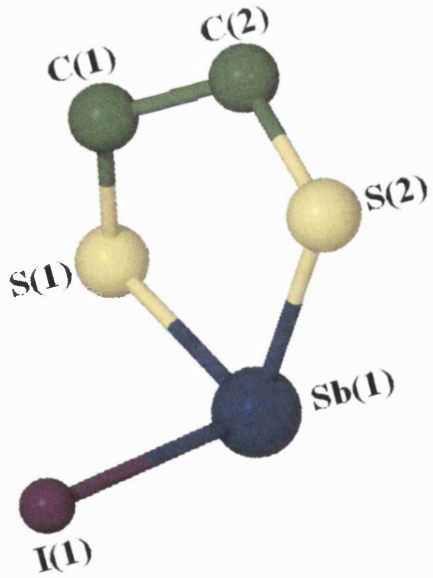

Figure 5.5 Molecular structure of $(CH_2S)_2SbI$ **(21)**

Table 5.4 Selected Bond Distances (Å) for $S(SCH_2CH_2)_2SbI$ (**20**) and $(CH_2S)_2SbI$ (**21**)

	(20)	**(21)**
Sb(1)-S(1)	2.4403(15)	2.4104(9)
Sb(1)-S(2)	2.8436(15)	2.4327(10)
Sb(1)-S(3)	2.4735(15)	
Sb(1)-I(1)	2.8962(6)	2.8219(3)
S(1)-C(1)	1.817(6)	1.829(4)
C(1)-C(2)	1.527(9)	1.510(6)
C(2)-S(2)	1.829(6)	1.831(4)
S(2)-C(3)	1.816(7)	
C(3)-C(4)	1.511(8)	
C(4)-S(3)	1.827(6)	

Table 5.5 Selected Bond Angles (°) for $S(SCH_2CH_2)_2SbI$ (**20**) and $(CH_2S)_2SbI$ (**21**)

	(20)	**(21)**
S(1)-Sb(1)-S(2)	80.70(5)	89.08(3)
S(1)-Sb(1)-S(3)	100.95(5)	
S(2)-Sb(1)-S(3)	80.64(5)	
S(1)-C(1)-C(2)	113.5(4)	112.0(3)
C(1)-C(2)-S(2)	111.0(4)	112.3(3)
S(1)-Sb(1)-I(1)	85.34(4)	96.53(3)
S(2)-Sb(1)-I(1)	160.96(3)	94.93(3)
S(3)-Sb(1)-I(1)	89.44(4)	
C(1)-S(1)-Sb(1)	100.8(2)	98.31(13)
C(2)-S(2)-Sb(1)	98.9(2)	99.35(13)
C(3)-S(2)-C(2)	102.1(3)	
C(3)-S(2)-Sb(1)	98.7(2)	
C(4)-S(3)-Sb(1)	101.81(19)	
C(4)-C(3)-S(2)	113.1(4)	
C(3)-C(4)-S(3)	113.3(4)	

The molecular structures of both precursors (**20**) and (**21**) in the solid state are monomeric, where the antimony atom is coordinated to one iodine atom and two sulphur atoms from the thiolate groups for precursor (**21**) and an additional intramolecular coordination site through a sulphur donor atom appears in precursor (**20**).

Precursor (**20**) can be viewed as an eight-membered heterocycle with a cross-ring 2,6-intramolecular interaction, involving a coordinative donation from sulphur to antimony, which is a well known structural arrangement for many *non*-metal elements.[189, 192] According to this bonding arrangement, the two related heterocyclic Sb-S bonds [2.4403(15), 2.4735(15) Å] are significantly shorter than the cross-ring Sb-S bond [2.8436(15) Å]. These values are in agreement with the ones reported for the chlorine analogue.[190] The geometry of these types of complexes has been described as a distorted Ψ-trigonal bipyramidal, where the thioether-like sulphur atom and the iodine are in the axial positions, the thiolate-like sulphur atoms occupy two equatorial positions and the stereochemically active lone pair of the antimony (III) atom in the third equatorial position.[188]

It can be observed in precursor (**20**) that the molecule exhibits a boat-chair conformation of the eight-membered ring (Figure 5.6) and also contains an approximate mirror plane with minor deviations for C(1) and C(4). This ring conformation has also been observed in penta-coordinated tin(IV) complexes such as $I(Me)Sn(SCH_2CH_2)_2S$,[192] where similar bond distances and angles to those in precursor (**20**) have been reported.

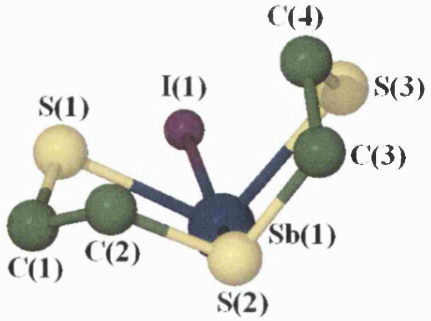

Figure 5.6 Molecular structure of $(SCH_2CH_2)_2SbI$ (**20**) showing the boat-chair conformation of the eight-membered ring.

Although the molecular structure of precursor (**20**) is essentially monomeric in nature, there are considerably strong intermolecular interactions between monomers, illustrated by Figure 5.7, similar to the intermolecular interactions formed between the antimony(III) dithiocarbamate monomers $Sb[S_2CN(Me)(Bu^n)]_3$ from Chapter 2 where the distance between the antimony atom and the sulphur from a neighbouring molecule, Sb(1)-S(1'), was 3.442 Å. Three intermolecular contacts, from the iodine (3.939 Å) and the two thiolate-like sulphur atoms (3.696 and 3.702 Å), to the antimony atom of a neighbouring molecule impose a seven-coordinate environment around each antimony atom in precursor (**20**). These bond distances are in agreement with the ones reported for the bismuth chloride analogue,[186] although they are shorter [3.534(7) and 3.285(6) Å for the Sb(1')-S and Sb(1')-I(1), respectively] than in precursor (**20**) probably due to the bigger size of the iodine atom compared with the chlorine. In the analoguous chlorinated antimony derivative, $S(SCH_2CH_2)_2SbCl$,[190] the three intermolecular contacts distances, one from the chlorine (4.047 Å) and the two thiolate-like sulphur atoms (3.852 and 4.013 Å) to the antimony atom of a neighbouring molecule, are longer that the ones in precursor (**20**) and this is in agreement with what has been also observed in analogous metallocanes such as $S(C_6H_4S)_2SbX$ (X = Cl, Br or I) where the shortest interactions corresponded to the iodo complex.[188]

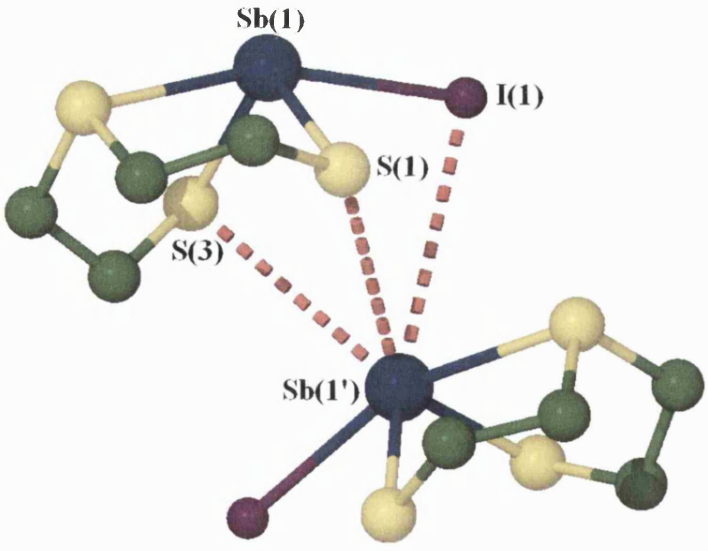

Figure 5.7 Molecular structure of $S(SCH_2CH_2)_2SbI$ (**20**) showing intermolecular contacts between molecules.

The molecular structure of precursor (**21**), shown by Figure 5.5, can be perhaps more easily considered in relation to the plane formed by S(1)-Sb-S(2), where Sb-S(1) and Sb-S(2) bond distances are 2.4104(9) and 2.4327(10) Å, respectively. These distances are slightly shorter than the ones in precursor (**20**) between the antimony and the thiolate-like sulphur atoms, probably due to the smaller size of the five-membered ring compared to the eight-membered ring of precursor (**20**) and the absence of a third cross-ring intramolecular interaction and the intermolecular interactions involving the antimony atom.

The five-membered ring formed in precursor (**21**) is *non*-planar so that the hydrogen atoms and the lone pair of electrons on the sulphur atoms are not eclipsed and presents a distorted envelope conformation. One of the carbon atoms [C(2)] is almost coplanar with the plane formed by S(1)-Sb-S(2) atoms, being only deviated by 0.25 Å and the other carbon atom [C(1)], departs from this plane as much as 0.55 Å (Figure 5.8) in the same direction as the Sb-I bond. These bond distances and deviations from the S(1)-Sb-S(2) plane are in agreement with the ones reported by Bush and co-workers in the chlorinated analogue.[184] Also, it is interesting to remark that despite the difference in volume between the iodine of precursor (**21**) and the chlorine in the structure reported by Bush *et al.*[184] the angle formed by the halogen and the S(1)-Sb-S(2) plane is very similar, where the values are 97 and 99°, respectively.

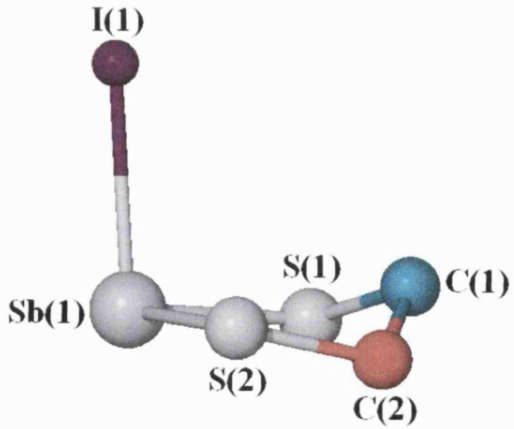

Figure 5.8 Molecular structure of $(CH_2S)_2SbI$ (**21**) showing deviations of the carbon atoms from the S(1)-Sb-S(2) plane.

The overall geometry of the molecular structure of precursor (**21**) around the antimony atom can be described as a slightly distorted pseudo-tetrahedron. This geometry can be elucidated taking into account that the bonds angles around the antimony atom indicate a trend towards orthogonality as compared with the idealised tetrahedral configuration and the bond angles are all close to 90°.

In the packing in the crystal structure of precursor (**21**) several intermolecular interactions occur between each pair of centrosymmetrically related molecules. The main intermolecular contacts (the ones with values *ca.* 3 Å) are hydrogen bonds formed between the iodine atom and the H(1B) and H(2A) of the neighbouring molecule with values of 3.452 and 3.559 Å, respectively. The bond angles C(2)-H(2A)-I(1') and C(1)-H(1B)-I(1') are 118.18(3)° and 131.44(3)°, respectively, which are deviated from the ideal linear angle of 180° due to the sp^3 hybridisation of the carbon atoms. These intermolecular contacts are illustrated by Figure 5.9. It is interesting the fact that, in contrast with precursor (**20**) where the intermolecular interactions are formed by direct interaction between the antimony atom and the iodine and thiolate-like sulphur atoms, in precursor (**21**) these contacts are formed by hydrogen bonding.

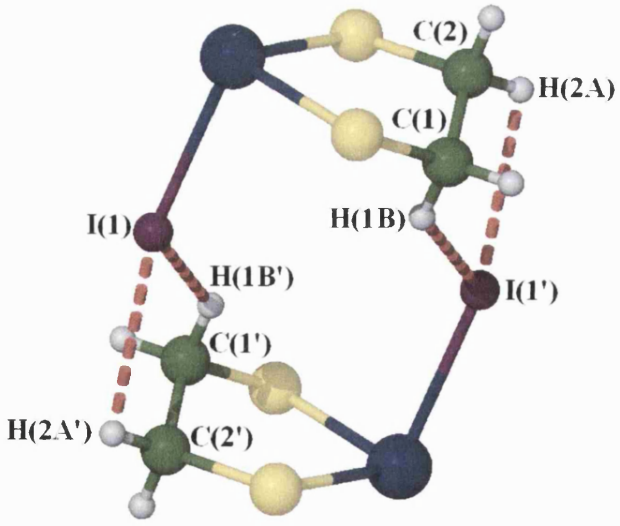

Figure 5.9 Molecular structure of $(CH_2S)_2SbI$ (**21**) showing intermolecular contacts between molecules.

In contrast to precursor (**21**), in the analogous molecular structure of compound $(CH_2S)_2SbCl$,[184] the intermolecular interactions between each pair of centrosymmetrically related molecules (illustrated by Figure 5.10) are formed between the two hydrogen atoms of the same carbon atom, H(1A) and H(1B), and the chlorine atom of the neighbouring molecule with values of 2.788 and 3.619 Å, respectively. The distance between the I(1') and H(2A) that formed a hydrogen bond precursor (**21**) are 3.559 Å, however in the analogous $(CH_2S)_2SbCl$[184] the Cl(1')-H(2A) distance is greater than 4.9 Å, moreover, the distance between I(1') and H(1A) in precursor (**21**) is 4.447 Å and no hydrogen bond is formed in contrast with the analogous $(CH_2S)_2SbCl$[184] where the hydrogen bond distance between Cl(1') and H(1A) is 2.788 Å. This different distribution of the intermolecular interactions in compound $(CH_2S)_2SbCl$[184] is due to the different arrangement of the molecules in the unit cell and one of them is considerably shorted (H[1A]-Cl[1'], 2.788 Å) as a result of the smaller size of the chlorine atom compared with the iodine atom.

The differences in the intermolecular interaction distances affect the bond angles, whereby the strongest interaction H(1A)-Cl(1') produces a decrease in the angle C(1)-H(1A)-Cl(1') from 118.18° shown in precursor (**21**) to 81.53° in $(CH_2S)_2SbCl$.[184] Consequently, the weakest interaction H(1B)-Cl(1') produces an increase in the angle C(1)-H(1B)-Cl(1') from 131.44° shown in precursor (**21**) to 134.10° in $(CH_2S)_2SbCl$.[184]

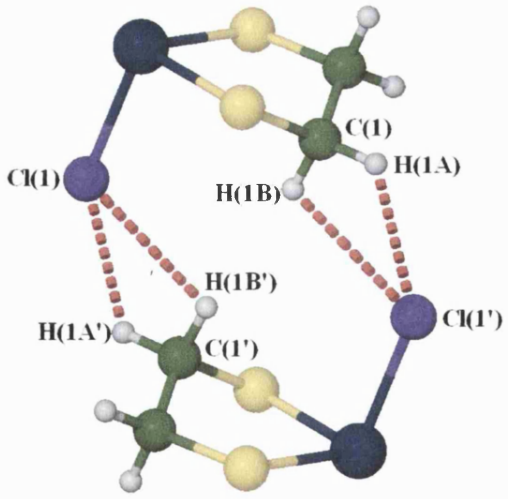

Figure 5.10 Molecular structure of $(CH_2S)_2SbCl$[184] showing intermolecular contacts between molecules.

5.2.3 CVD Testing of Precursors

The compounds $S(SCH_2CH_2)_2SbI$ (**20**) and $(CH_2S)_2SbI$ (**21**) were tested as CVD precursors. Details of the apparatus are provided in Appendix 2.

Both precursors are air- and moisture-stable and largely insoluble in most common organic solvents. Only precursor (**21**) showed low solubility in dichloromethane and chloroform.

This section gives details of the tests carried out on compounds (**20**) and (**21**) by Thermogravimetric Analysis (TGA) in order to have an indication of the temperature at which decomposition might be expected to start and reach completion and to determine suitable conditions for the deposition of the film.

TGA of precursor (**20**) and (**21**) present similar curves where the decomposition begins at approximately 220 °C for precursor (**20**) and at around 200 °C for precursor (**21**) and it is effectively over in both precursors by 400 °C (Figures 5.11 and 5.12).

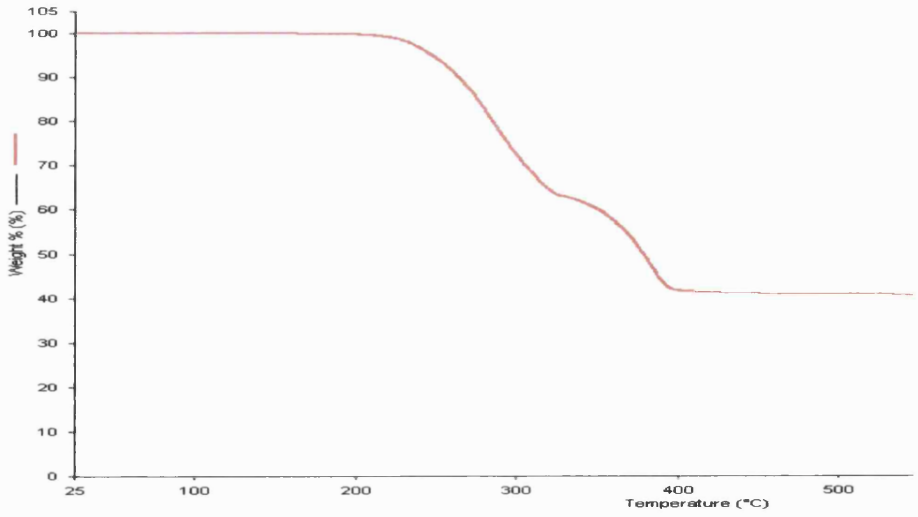

Figure 5.11 TGA of $S(SCH_2CH_2)_2SbI$ (**20**).

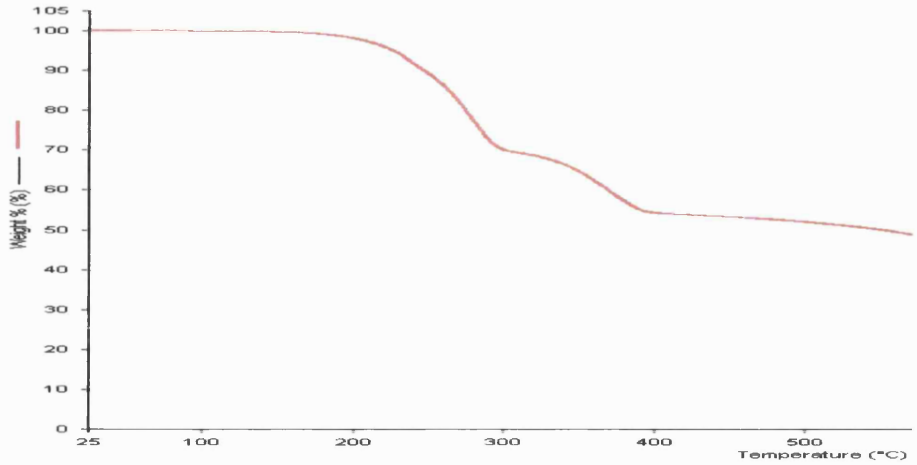

Figure 5.12 TGA of $(CH_2S)_2SbI$ (**21**).

5.2.4 Decomposition of Precursors

Both precursors (**20**) and (**21**) exhibited poor solubility in most organic solvents and therefore AACVD studies were not possible to be performed. Deposition was attempted *via* LPCVD methods by changing the temperature of both precursor and substrates but no consistent results were achieved. The decomposition temperature for the precursors was always kept around 200 °C where the TGA showed the decomposition started to take place and the substrate temperature was gradually increased from 200 to 400 °C during the different attempted runs. The experiments were carried out under both static and dynamic vacuum conditions.

During each set of decomposition experiments the same set up used for LPCVD runs was used keeping the substrate at room temperature for 1.5 hours. As a result of this, *three types of material* were obtained:

- Small colourless crystallites deposited on the coolest part of the reaction tube.
- Yellow film deposited on glass slides, held at room temperature.
- Purple residue remained in the precursor vial held in the furnace.

Decomposition products and films deposited were examined by visual inspection, Energy Dispersive X-ray Analysis (EDAX) and Scanning Electron Microscopy (SEM). Glancing Angle X-ray diffraction studies were also performed on the films to determine if they were crystalline, and then confirm the nature of the material formed.

At the coolest part of the tube, towards the opposite side of the furnace, *small colourless crystals* appeared when using both precursors (**20**) and (**21**). These crystals were characterised by X-ray diffraction and proved to be the known 1,4-dithiane reported in 1955 by Marsh.[193] The molecular structure of this six-membered ring is illustrated by Figure 5.13.

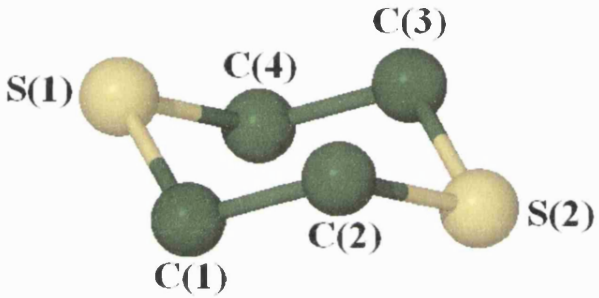

Figure 5.13 Molecular structure of 1,4-dithiane.[193]

The majority of the precursor used on each run during the course of each experiment remained in the vial used to place the precursors. After the experimental process, the precursor turned from a yellow amorphous powder into a *deep purple crystalline-like solid.* The appearance of a purple material is in agreement with that reported by Solayappan[40] where they identified and characterised the deep purple material deposited as SbSI using the Physical Vapour Technique (PVT). The same material was obtained when using both precursors (**20**) and (**21**). The solids were washed with CS_2 (in order to eliminate any possible sulphur traces produced during the decomposition) and diethyl ether, and then subsequently dried under vacuum. Elemental analysis on the solid obtained from precursor (**20**) showed only traces of carbon and hydrogen (C: 1.96 % and H: 0.10 %), proving its inorganic nature. Figures 5.14 and 5.15 show the SEM image of the purple solid obtained at 190 °C from precursor (**20**) at different magnifications.

Figure 5.16 shows the qualitative EDAX of the crystalline purple solid remained in the furnace from precursor (**21**). It could be observed that there are three main peaks corresponding to antimony, sulphur and iodine with similar intensities consisting with formation of SbSI.

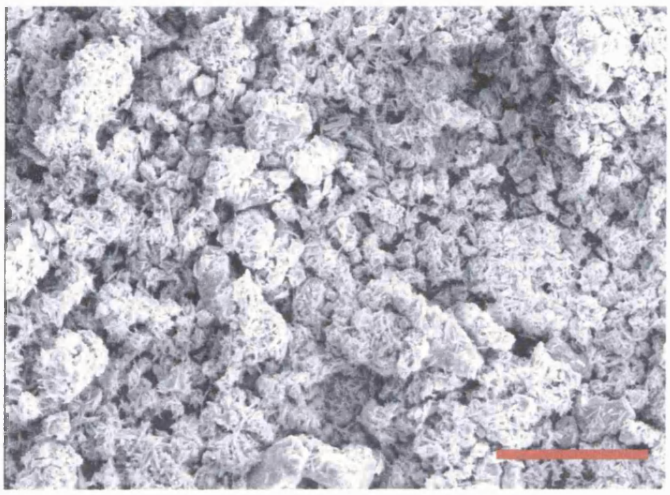

Figure 5.14 SEM of the solid obtained from precursor (**20**) at 190 °C. Red bar = 100 μm.

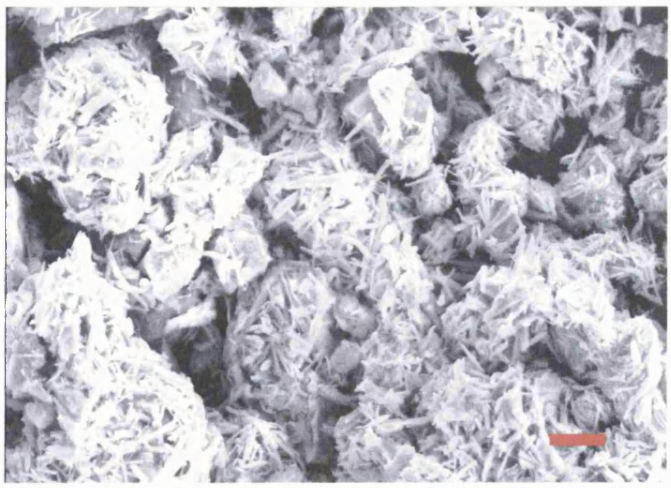

Figure 5.15 SEM at higher magnification of the solid obtained from precursor (**20**) at 190 °C. Red bar = 10 μm.

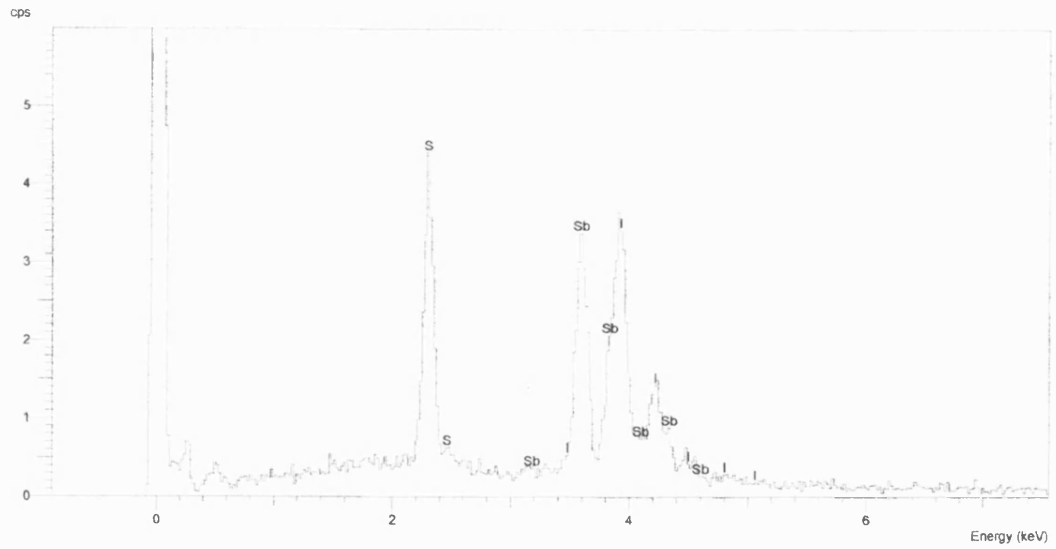

Figure 5.16 EDAX qualitative analysis of purple solid obtained from precursor (**21**).

The purple colour of the solid residue in the furnace is in agreement with the ones reported in the literature, where by hydrothermal methods,[43, 44] a crystalline purple to red solid was also obtained. Also, the three peaks with similar intensities from the qualitative EDAX (Figure 5.16) and the needle-shape of it shown by Figures 5.14 and 5.15 initially led us to believe that the material formed was indeed SbSI. However quantitative analysis could not be performed to confirm its composition due to the unsuitable morphology of the solid obtained. Despite the lack of confirmatory compositional analysis, it could be possible that Sb_2S_3 is embodied within the needles. In this respect, Ibanez *et al.*[194] reported that SbSI decomposes at 180 °C, and therefore, since the decomposition takes place at around 190 °C, it is plausible that some amorphous Sb_2S_3 is present in the bulk residue due to the decomposition of SbSI.

Also, when compound (**21**) was used as the precursor, a very similar purple solid was obtained. Figure 5.17 shows the SEM image of this material, where a resembling morphology to that obtained from precursor (**20**) can be observed.

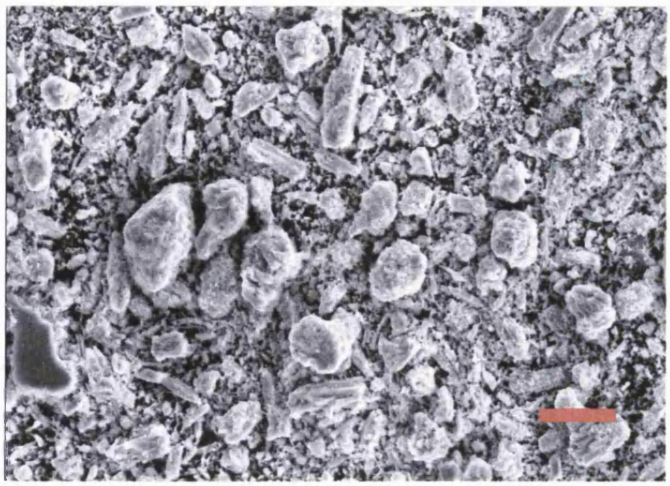

Figure 5.17 SEM of the solid obtained from precursor (**21**) at 190 °C. Red bar = 10 μm.

In order to establish the composition of these materials, XRD was performed on both solids, obtaining identical XRD patterns. Both materials were crystalline and the diffraction patterns could be compared to standard SbSI, antimony sulphide iodide (orthorhombic, PDF 88-2407). Figure 5.18 shows the XRD pattern of the solid obtained from precursor (**20**). All peaks could be fully indexed, where the most intense reflexion (121) found in the solid matches with the most intense peak shown in the random orientation from the standard SbSI antimony sulphide iodide found in the data base. With the XRD pattern we can confirm that the SbSI produced by decomposition of precursors (**20**) and (**21**) is the only crystalline product, however it is not possible to confirm whether or not other amorphous species, such as Sb_2S_3, are present in the solid together with the SbSI. The absence of Sb_2S_3 peaks is not surprising since the decomposition of precursors (**20**) and (**21**) takes place at 190 °C and it is known that Sb_2S_3 crystallises *ca.* 270°C, which is consistent with these findings.[28]

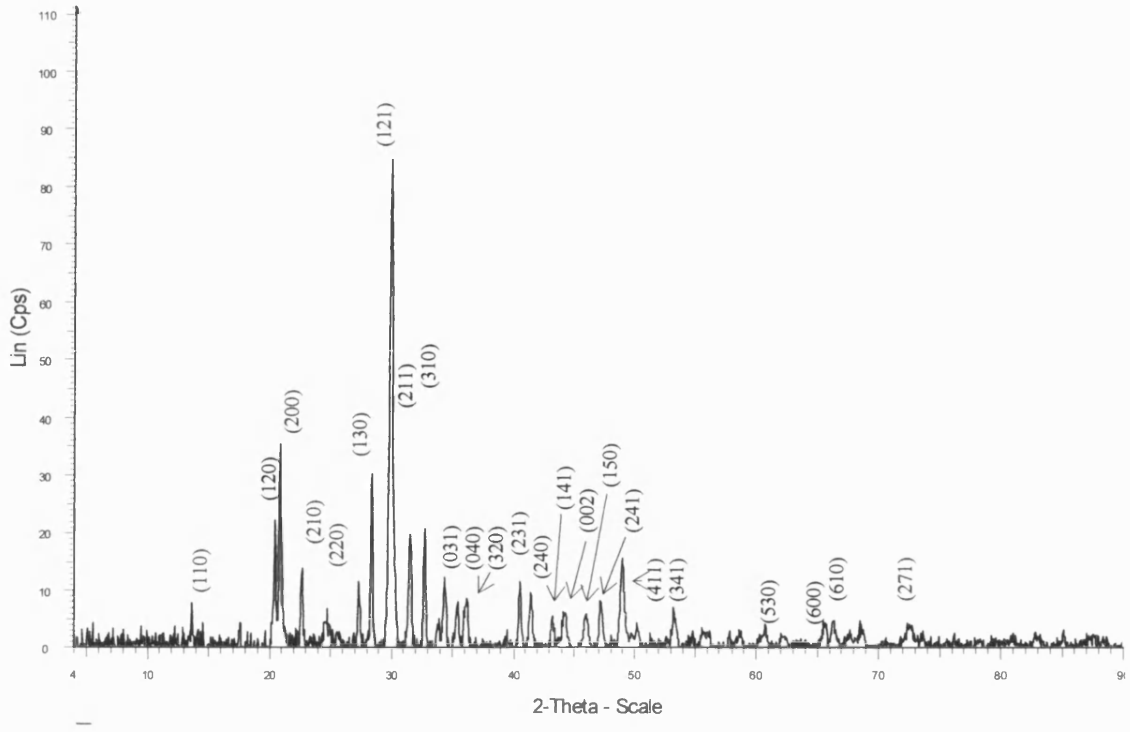

Figure 5.18 Glancing angle X-ray pattern of the solid obtained from precursor (**20**)

The third type of material appeared during the decomposition experiments was a *yellow film* with liquid appearance deposited on the glass substrate. The films looked relatively thick, showing better coverage when using precursor (**20**) rather than precursor (**21**). Both films had liquid appearance and were analysed by SEM. Figure 5.19 shows the SEM image of the film obtained from (**20**) at 190 °C where it can be observed the liquid nature of the material deposited. It seems the film consists of big droplets of material joined together forming a uniform film.

The film obtained from precursor (**20**) was thick enough for by qualitative EDAX (Figure 5.20) where it could be observed that mainly antimony, sulphur and iodine peaks appeared in the spectra with traces of the underlying glass substrate, giving an idea of the good thickness of the film.

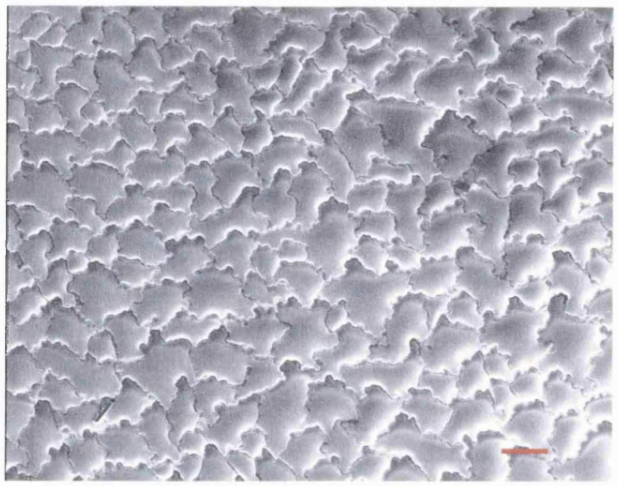

Figure 5.19 SEM of film deposited from precursor (**20**) at 190 °C. Red bar = 100 μm.

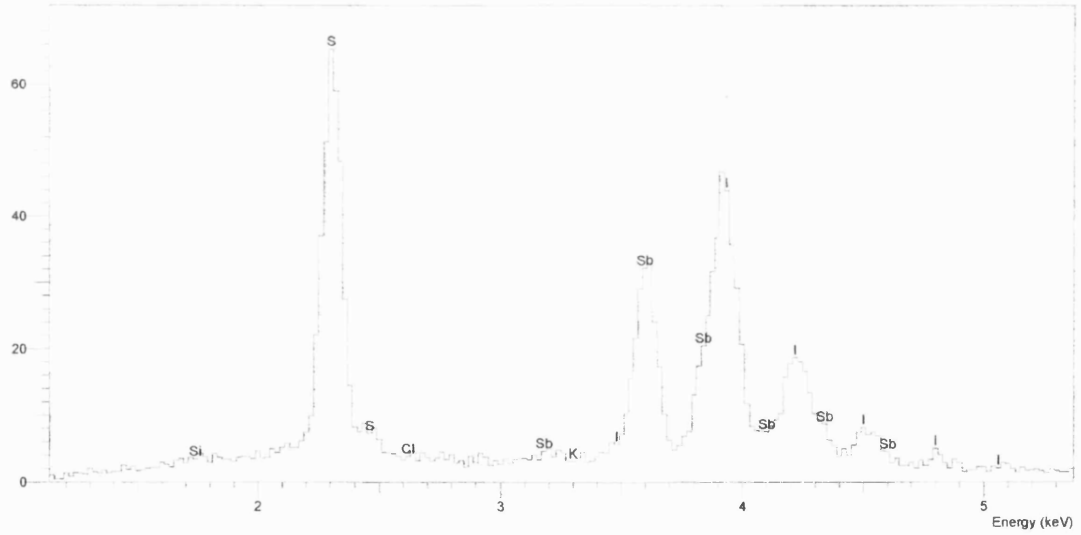

Figure 5.20 EDAX qualitative analysis of film deposited from precursor from (**20**) at 190 °C on glass slides.

Although the film was suitable for qualitative analysis, it was not possible to perform quantitative analysis on it due to the damage produced on the material deposited by the electron beam. SEM image of the damaged droplet after attempting to achieve quantitative analysis is shown by Figure 5.21.

When compound (**21**) was used as the precursor, very similar results were obtained. A yellow material was also deposited on the films at 190 °C, but this time the film looked considerably thinner than the one obtained from precursor (**20**). Figure 5.22 shows the SEM image of the film obtained from (**21**) at 190 °C where it can be observed again the liquid nature of the material deposited. In comparison with the film obtained from precursor (**20**), the droplets are more dispersed along the substrate producing a thinner film which it is reflected in the poor thickness shown by qualitative analysis.

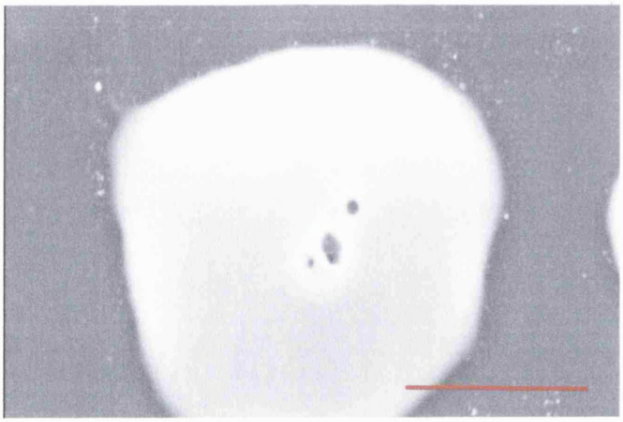

Figure 5.21 SEM of damaged film deposited from precursor (**20**) at 190 °C when trying to obtain quantitative analysis. Red bar = 10 μm.

Qualitative EDAX (Figure 5.23) shows sulphur, antimony and iodine peaks as the main peaks in the spectrum, however this time the ratio between the three of them has changed dramatically compared to those shown by the film deposited from precursor (**20**).

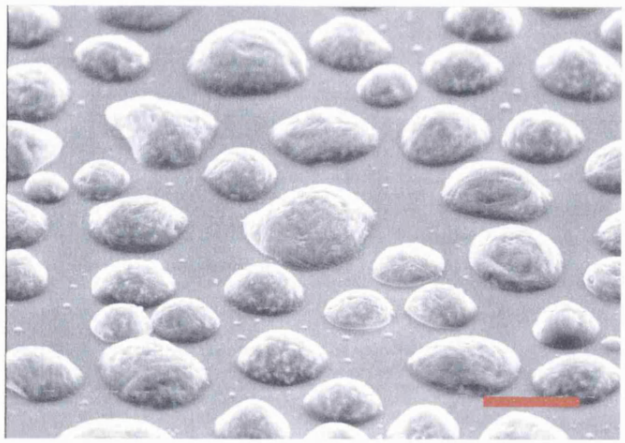

Figure 5.22 SEM of film deposited from precursor (**21**) at 190 °C. Red bar = 10 μm.

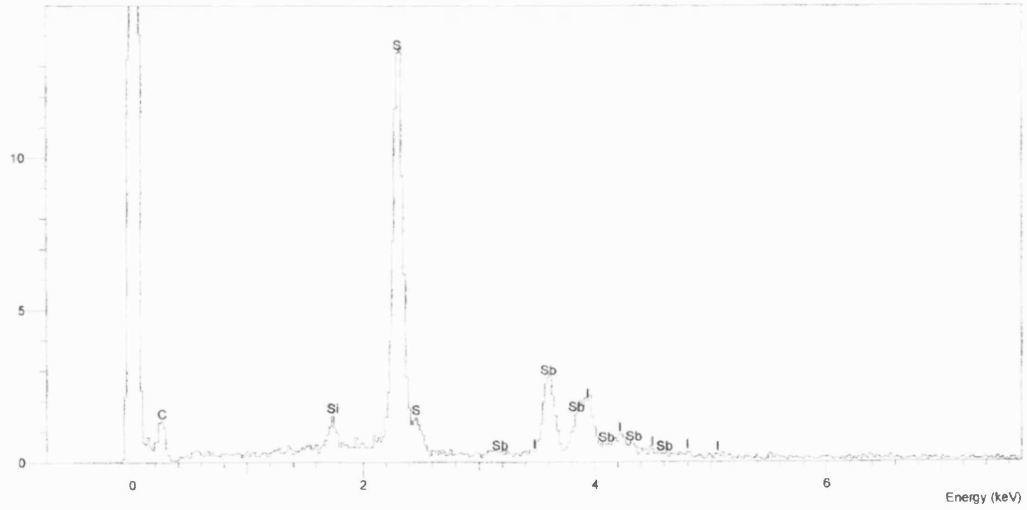

Figure 5.23 EDAX qualitative analysis of film deposited from precursor from (**21**) at 190 °C on glass slides.

This time the sulphur peak is considerably bigger than the antimony and iodine ones and also more noticeable peaks from the underlying glass substrate, such as silicon and carbon, appeared due to the poor thickness and low uniformity of the film. Once again, quantitative analysis was not possible to be performed on the films due to the irreversible damage caused by the electron beam at the surface of the film.

Looking at these results and bearing in mind the results reported by Solayappan *et al.*[40], we can now explain the appearance of the yellow material during the formation of SbSI from precursors (**20**) and (**21**). Although quantitative analysis were not possible to achieve, by the qualitative EDAX (Figures 5.20 and 5.23) it can be observed antimony, sulphur and iodine peaks in random distribution. We therefore suggest that the yellow layer consists of SbI_3, formed by decomposition of the SbSI produced during the experimental process. The origin of the intense sulphur peak, in both films obtained from precursors (**20**) and (**21**), could be explained by the following:

- It could come from traces of 1,4-dithiane ($C_4H_8S_2$), however a carbon peak should appear together with the sulphur peak in the EDAX spectra and the lack of it suggests this is probably not be the cause.

- The sulphur peak could appear also as a consequence of Sb_2S_3 embodied in the SbI_3 droplets; however this speculation is unlikely due to the low volatility of Sb_2S_3 and the lack of confirmatory quantitative analysis.

- A more reasonable explanation for the intense sulphur peaks in the EDAX spectra and the yellow coloration of the film suggests the presence of elemental sulphur as a result of the decomposition process. The majority of the yellow material is also insoluble in any solvent except in CS_2, strengthening the hypothesis that elemental sulphur is present in the material.

Overall, three type of species such as SbSI, SbI_3 and $C_4H_8S_2$, appeared as a consequence of the decomposition of precursors $S(SCH_2CH_2)_2SbI$ (**20**) and $(CH_2S)_2SbI$ (**21**), yet due to the lack of confirmatory quantitative analysis the purity of each species could not be achieved.

5.2.5 Decomposition Mechanisms

With all these collective set of experiments, we can propose a mechanism in the solid state for the decomposition of precursors (**20**) and (**21**) that will explain the appearance of the different species during the experimental process. Equation 5.4 shows the proposed intramolecular decomposition mechanism for precursor (**20**):

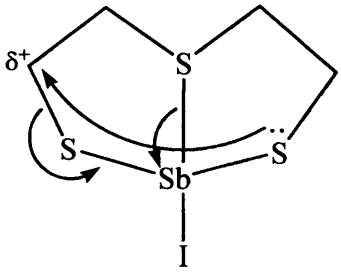

$S(SCH_2CH_2)_2SbI$ (**20**)

SbSI +

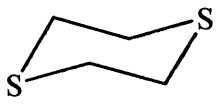

$C_2H_8S_2$

[5.4]

The distance between the thiolate-like sulphur atom and the opposite $C^{\delta+}$, which can look long in the above representation, is only of *ca.* 3.798 Å, facilitating the proposed mechanism. To the best of our knowlege, this represents a novel decomposition pathway for MOCVD, which are usually based on both α- and β-eliminations.

In the case of precursor (**21**), and in contrast to decomposition mechanism of precursor (**20**), an intermolecular decomposition mechanism will take place to allow two molecules to be involved in the process in order to give the six-membered ring ($C_2H_8S_2$) as the by-product of the reaction.

Subsequently, the SbSI produced will further start to decompose according to the reaction reported by Solayappan and co-workers[40] and confirmed by Ibanez and co-workers[194] to take place around 180 °C, illustrated by Equation 5.3, that will also justify the appearance of the species SbI_3 deposited on the glass substrate.

$$3\ SbSI\ (s) \longrightarrow Sb_2S_3\ (s) + SbI_3\ (v) \qquad [5.3]$$

With these collective set of results it is now possible to understand the TGA's of both precursors (**20**) and (**21**) illustrated by Figures 5.11 and 5.12. The decomposition is effectively over in both precursors by 400 °C and the residual weight observed corresponds to Sb_2S_3, 41.2 % (theoretical: 42.3 %) for precursor (**20**) and 53.2 % (theoretical: 50.1 %) for precursor (**21**). This is in agreement with the fact that SbSI decomposes at 180 °C to give Sb_2S_3, and hence it will be the ultimate decomposition species observed. An interesting feature is that both TGA present a shoulder in the curve at similar temperatures, at around 320 °C for precursor (**20**) and 310 °C for precursor (**21**). Although we cannot fully explain this, it is likely to be due to the decomposition of SbSI to give SbI_3 and Sb_2S_3, and hence the overall decomposition pathway is far from simple, involving decomposition of the precursors together with the decomposition of SbSI.

5.2.6 SbSI on deposited Sb_2S_3 buffer layer

In the previous section, details of the decomposition of precursors (**20**) and (**21**) were given; however, both precursors were not volatile enough to produce films by LPCVD. In addition, both precursors present extremely low solubility and hence AACVD studies were not possible either.

In the work from Solayappan and co-workers,[40] they also reported the growth of SbSI films using a buffer layer of annealed Sb_2S_3. This buffer layer seems to be crucial to improve the crystalline orientation of the SbSI thin films by promoting nucleation and improving nucleation density.

Although compounds (**20**) and (**21**) are not suitable for CVD purposes, the use of them as precursors for the growth of SbSI on a Sb_2S_3 buffer layer seems plausible. For the deposition of the buffer layer, *tris*(*t*-butylthiolato) antimony (III), precursor (**15**), was used under the conditions described in Chapter 4. Once the Sb_2S_3 thin film was deposited on a glass substrate, aliquots of a diluted solution of precursor (**21**) in dichloromethane were deposited on top of the film and left to dry in the air. Once the solvent was evaporated, the same procedure was repeated several times until a noticeable yellow film covered the underlying grey film. Subsequently, the film was placed in a furnace and heated at the rate of 1 °C/min up to 190 °C under a static nitrogen atmosphere. After 1.5 hours the film was allowed to cool down at exactly the same rate (1 °C/min) and a purple layer was now homogeneously covering the surface of the film.

The film looked thick enough for characterisation and by SEM (Figures 5.24 to 5.26) it can be observed that it is constituted by two different layers. Figures 5.24 and 5.25 show the SEM image of the film at different magnifications and it can be observed that the underlying films consist of small particles with a plate-like shape of about 3 μm in length that looks exactly like the ones obtained from precursor (**15**) that was confirmed to be Sb_2S_3 (Chapter 4, Figures 4.19 and 4.20). This is an unexceptional result taking into account that the same protocol that the one in Chapter Four was followed to produce Sb_2S_3, however it reassures the quality of the Sb_2S_3 buffer layer. Nonetheless, on top of the underlying Sb_2S_3 film, rod-like particles appeared which resembled very much to the SbSI reported by Solayappan.[40]

Figure 5.26 shows a SEM image tilted 78° where the two different layers can be observed, and where the top layer seems to be in-filling the underlaying layer. The film is fairly thick (about 50 μm) and it is clearly noticeable the underlying layer is formed by a homogeneous film of plate-like particles (Sb_2S_3) where a rod-like material (SbSI) starts to grow in between and above the Sb_2S_3 particles.

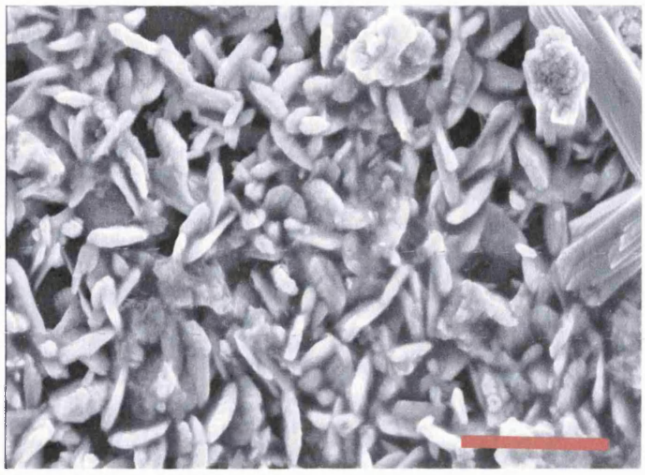

Figure 5.24 SEM of film deposited from precursor (**21**) over a Sb_2S_3 buffer layer at 190 °C. Red bar = 10 μm.

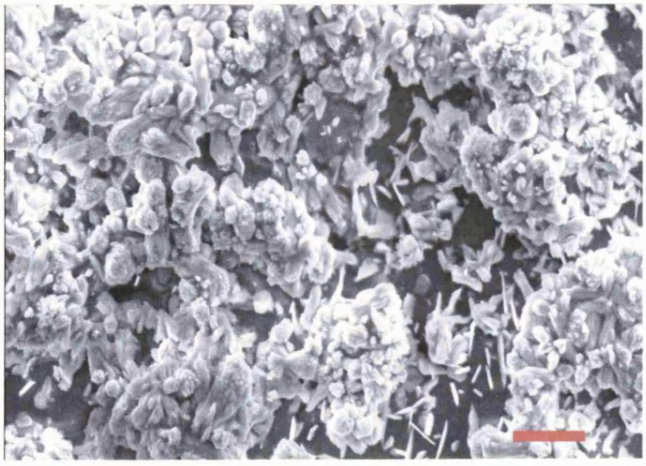

Figure 5.25 SEM of film deposited from precursor (**21**) over a Sb_2S_3 buffer layer at 190 °C at higher magnification. Red bar = 10 μm.

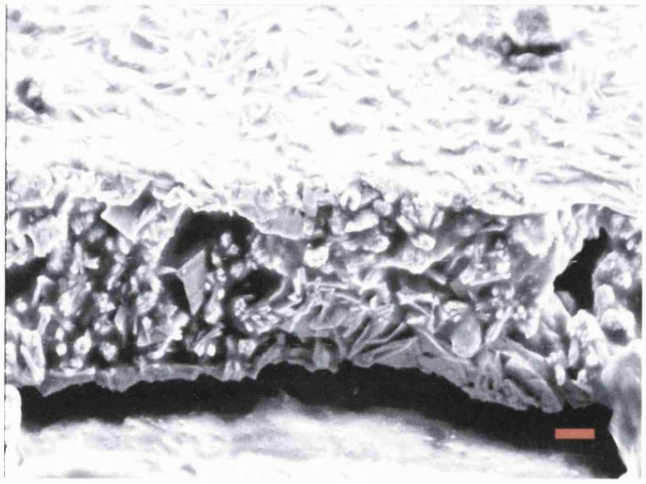

Figure 5.26 78 ° tilt SEM of film deposited from precursor (**21**) over a Sb_2S_3 buffer layer at 190 °C. Red bar = 10 μm.

When qualitative EDAX is performed on the films (Figure 5.27), three main peaks corresponding to antimony, sulphur and iodine appear in a very similar ratio. Unfortunately quantitative analysis did not give reliable results in the composition of the top layer to predict the exact ratio between the three elements mainly because the composition of the Sb_2S_3 buffer layer interfered in the analysis.

In order to study the crystallinity of the films, XRD was performed on different areas of the films such as a purple area where SbSI was grown and a grey area where mainly Sb_2S_3 seemed to dominate the film. Figure 5.28 shows the glancing angle X-ray pattern of the purple area of the films where SbSI was grown from precursor (**21**) on a Sb_2S_3 buffer layer. The films were crystalline and the majority of the peaks, marked in black, match to that of standard antimony sulphide iodide (SbSI, orthorhombic, PDF 88-2407), however, a few peaks, marked in blue, matches to that of standard *Stibnite* (Sb_2S_3, PDF 06-0474) as expected due to the Sb_2S_3 buffer layer.

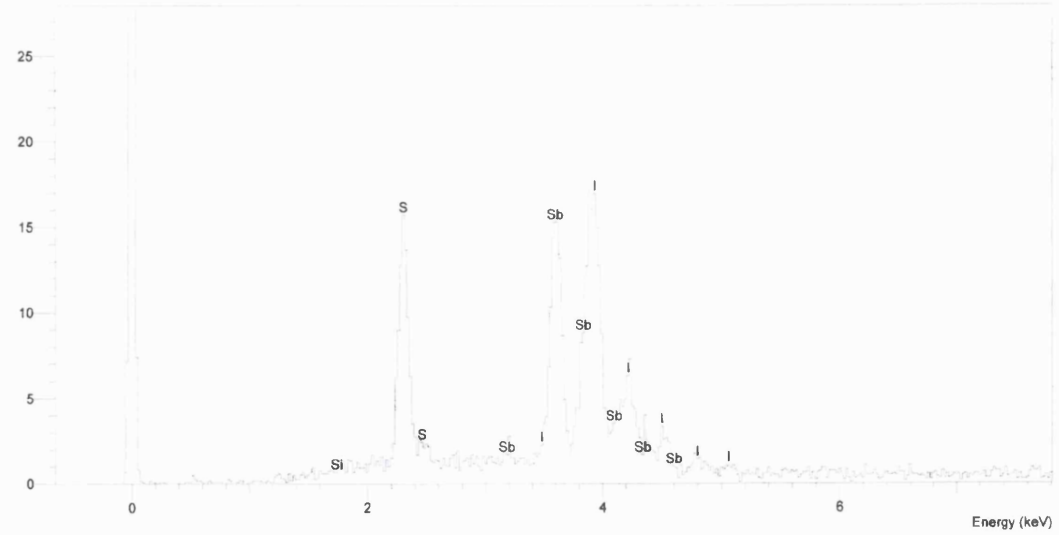

Figure 5.27 EDAX qualitative analysis of the film deposited from precursor (**21**) over a Sb_2S_3 buffer layer at 190 °C.

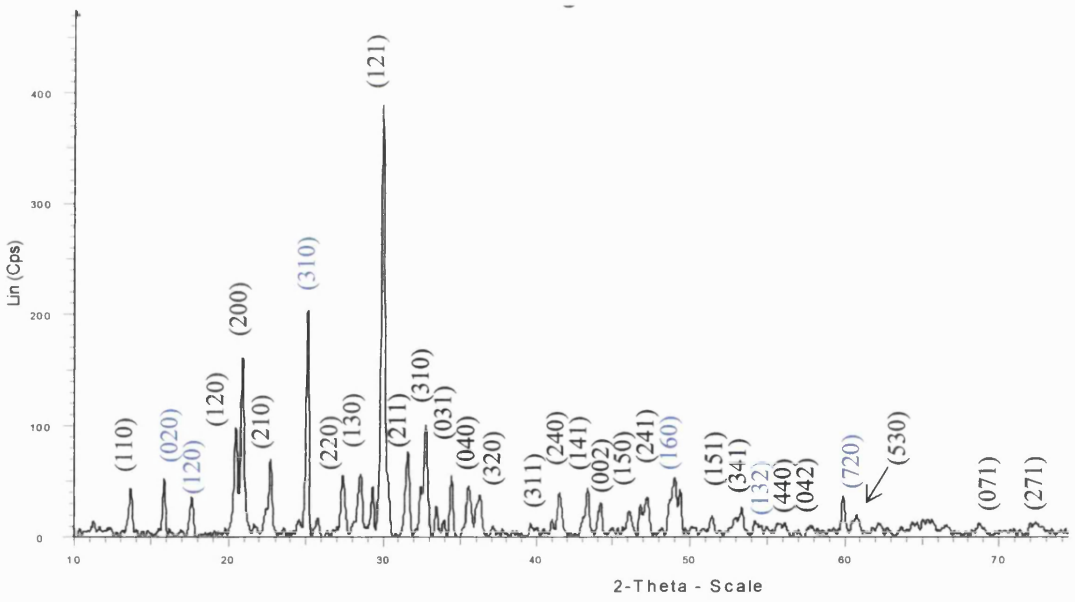

Figure 5.28 Glancing angle X-ray pattern of the purple area of the film deposited from precursor (**21**) over a Sb_2S_3 buffer layer at 190 °C. Black peaks match to that of standard SbSI (orthorhombic, PDF 88-2407). Blue peaks match to that of standard *Stibnite* (Sb_2S_3, PDF 06-0474)

Figure 5.29 shows the glancing angle X-ray pattern of the grey area of the films where SbSI was grown from precursor (**21**) on a Sb_2S_3 buffer layer. The films were again crystalline but this time the majority of the peaks, marked in blue, matches to that of standard *Stibnite* (Sb_2S_3, PDF 06-0474) as expected due to the grey colour of the film typical of the Sb_2S_3 buffer layer deposited prior to the growth of SbSI. On the contrary to that observed in the purple areas, a few peaks, marked in black, matches to that of standard antimony sulphide iodide (SbSI, orthorhombic, PDF 88-2407) due to the lower concentration of precursor (**21**) used. In addition, some new peaks, marked in red, can now be observed in the spectra that matches to that of standard *Fuloppite* ($Sb_{10}S_{15}$, PDF 39-0211), which has been observed previously in Chapter 3 when growing Sb_2S_3 films on glass slides from antimony(III) xanthates such as precursor $Sb(S_2COPr^i)_3$ (**11**).

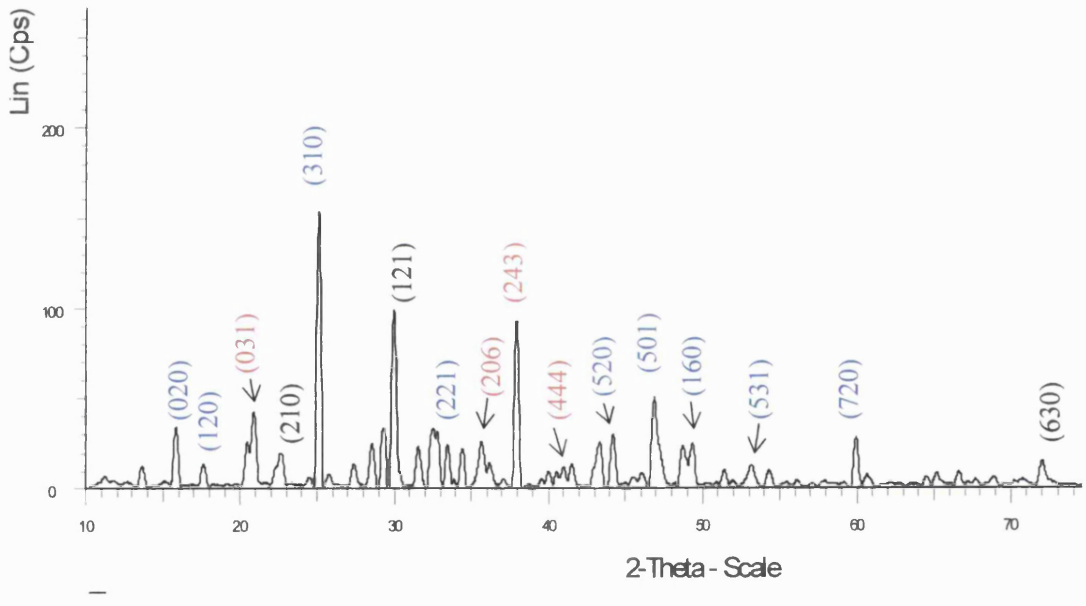

Figure 5.29 Glancing angle X-ray pattern of the grey area of the film deposited from precursor (**21**) over a Sb_2S_3 buffer layer at 190 °C. Blue peaks match to that of standard *Stibnite*, Sb_2S_3 (PDF 06-0474), black peaks match with standard SbSI (orthorhombic, PDF 88-2407) and red peaks match with standard *Fuloppite* ($Sb_{10}S_{15}$, PDF 39-0211).

and (**21**) is complex, where the decomposition of the precursors takes place at the same time that the decomposition of the produced SbSI to give a mixture of Sb_2S_3 and SbI_3.

5.3 EXPERIMENTAL

Starting materials were commercially obtained (e.g. Aldrich) and were used without further purification unless otherwise stated. Standard Schlenck line techniques were employed where applicable. Further details about instrumentation used are given in Appendix 1.

5.3.1 Preparation of Iodo(2-mercaptoethylsulphide) Antimony (III) – $S(SCH_2CH_2)_2SbI$ (20)

2-mercaptoethyl sulphide (0.28 mL, 2.2 mmol) was added dropwise to a solution of $SbCl_3$ (0.5 g, 2.2 mmol) in toluene (40 mL) and the mixture was heated at reflux for 5 hours. The solution was allowed to cool to room temperature and the resulting colourless crystals were separated by suction filtration and washed with hexane (2 x 30 mL) giving 0.60 g (88%) of $S(SCH_2CH_2)_2SbCl$ as white crystals. The spectroscopic properties were identical to those reported in the literature.[190]

A suspension of $S(SCH_2CH_2)_2SbCl$ (1.82 g, 5.9 mmol) and KI (1.95 g, 11.8 mmol) in toluene (60 mL) was heated at reflux for 16 hours resulting in a yellow suspension. The suspension was allowed to cool to room temperature and the yellow solid separated by suction filtration. The solid washed with ethanol (5 x 25 mL) and dried under vacuum to give 0.85 g (36%) of (**20**) as a pale yellow solid. m.p: 190 °C dec.

Microanalysis:

Found (calc.) for $C_4H_8S_3Sb$ (**20**): C 11.60 (11.98)%; H 1.91 (2.01)%.

^{1}H-NMR [δ (ppm), DMSO-d_6]:

3.35 (8H, m, CH_2).

^{13}C-NMR [δ (ppm), DMSO-d_6]:

31.35 (CH_2).

5.3.2 Preparation of Iodo(1,2-ethanedithiolate) Antimony (III) – $(CH_2S)_2SbI$ (21)

Precursor (**21**) was prepared by the same procedure as (**20**), by adding 1,2-ethanedithiol (0.36 mL, 4.38 mmol) to a solution of $SbCl_3$ (1.00 g, 4.38 mmol) in toluene (50 mL). Finally, 0.60 g (40%) of (**21**) were obtained as a bright yellow solid. m.p: 195 °C dec.

Microanalysis:

Found (calc.) for $C_2H_4S_2Sb$ (**21**): C 7.23 (7.04)%; H 1.20 (1.18)%.

^{1}H-NMR [δ (ppm), $CDCl_3$]:

3.75 (4H, s, CH_2).

^{13}C-NMR [δ (ppm), $CDCl_3$]:

41.85 (CH_2).

Conclusions

6. CONCLUSIONS

Two classes of compounds have been investigated as potential single-source precursors for the CVD of antimony sulphide, Sb_2S_3 and antimony sulpho-iodide, SbSI, respectively. All the compounds synthesised have been fully characterised and CVD deposition experiments have been conducted in order to assess their suitability. These conclusions aim to compare firstly the results obtained from the compounds prepared in Chapters Two to Four and highlight the major points discovered for the deposition of Sb_2S_3, and secondly to analyse the main breakthroughs for the formation of SbSI.

The CVD of Sb_2S_3 has been carried out from precursors such as antimony(III) dithiocarbamates, xanthates and thiolates. In terms of the ease of preparation, handling and yields obtained, all precursors were extremely favourable and the fact that the majority were air- and moisture-stable made the CVD process significantly facile.

Antimony(III) dithiocarbamates were insufficiently volatile to be used in LPCVD experiments but have sufficient solubility for AACVD. Moreover, deposition of Sb_2S_3 using these precursors by AACVD only takes place under 300 °C; at increasingly higher temperatures, Sb_2OS_2, Sb_2O_3 and Sb dominated the deposited film together with Sb_2S_3. The incorporation of oxygenated species is in agreement with reports that the sulphide is stable up to 275°C but is completely converted to Sb_2O_3 by 400°C.[135]

Overall, it seems that any approach to obtaining high quality Sb_2S_3 films requires either a precursor which either decomposes cleanly at $T < 300°C$ for use in AACVD, or is sufficiently volatile such that an LPCVD route is possible and where the decomposition temperature is less crucial due to the lack of any oxygen present in the system.

This led us to choose antimony(III) xanthates as single-source precursor which not only present similar structural features but also exhibit lower decomposition temperatures (by 150 °C lower) than dithiocarbamates.[146] This decrease in the decomposition

temperature lowers the risk of oxygen incorporation by the conversion of antimony trisulphide to antimony trioxide (Sb_2O_3) at temperatures around 300 °C.[135] However, although antimony(III) xanthates were also insufficiently volatile to be used in LPCVD experiments, due to their high solubility in most solvents, by AACVD pure Sb_2S_3 thin films were obtained without oxygen contamination. A significant discovery was that by mass spectroscopy of some of the precursors, it was possible to establish the decomposition mechanism, based on a Chugaev-type reaction, that will explain the lower decomposition temperatures exhibited by antimony(III) xanthates over their analogous dithiocarbamates.

In order to find single-source precursor that present sufficiently volatility to be used by LPCVD, antimony(III) thiolates were evaluated and found to produce highly pure Sb_2S_3 films with excellent surface coverage and without contamination. Growth studies using different substrates such as glass slides and silicon wafers established that although the films did not showed any significant preferred orientation, the orientations were not totally random, and marginally fewer reflections on the film deposited on silicon wafers is consistent with a more ordered substrate.

Future work regarding the deposition of Sb_2S_3 should concentrate in the development of new antimony(III) compounds with an all sulphur co-ordination sphere around the antimony in order to obtain an optimum proportion of sulphur relative to antimony for antimony sulphide film deposition. Antimony(III) dithiocarbamates require high decomposition temperatures increasing the risk of oxygen incorporation owing to the oxidation of Sb_2S_3 giving Sb_2O_3 and present extremely low volatility, therefore their use as CVD precursors is limited. Nonetheless, due to the encouraging results obtained from the antimony(III) xanthates and thiolates, a very interesting possibility will be the synthesis of similar complexes using bulkier and fluorinated substituents which will enhance volatility (for LPCVD) and solubility (for AACVD).

The second part of the project involved the formation or deposition of SbSI, for which two novel antimony(III) iodo-thiolates were synthesised. These precursors were not sufficiently volatile for LPCVD experiments and presented very low solubility making

them not suitable for AACVD studies. Nonetheless, decomposition studies showed that these novel precursors produced SbSI under mild conditions (190 °C, 1.5 hours) as a purple phase-pure crystalline material by an intramolecular (**20**), or intermolecular mechanism (**21**), releasing the organic fragment as a 1,4-dithiane which was characterised by x-ray crystallography. Notwithstanding, due to the decomposition of the SbSI species at 180 °C reported in the literature,[194] the decomposition pathway of precursors (**20**) and (**21**) is far more complex, where Sb_2S_3 and SbI_3 are also produced.

From a CVD point of view, this discovery represents a milestone in the deposition of SbSI from a single-source precursor since no references have been reported regarding this issue. The formation of SbSI has been reported in the literature, mainly from hydrothermal methods and there are no examples by CVD. The challenge lies in keeping the linkage Sb-I unaltered, which under the harsh conditions of the CVD process is the bond more likely to be broken.

Furthermore, these novel antimony(III) iodo-thiolates were used for the growth of SbSI films using Sb_2S_3 buffer layer deposited on glass slides from the precursor $Sb(SBu^t)_3$ (**15**). The Sb_2S_3 buffer layer was covered by a diluted solution of $(CH_2S)_2SbI$ (**21**) and subsequently heated under a static nitrogen atmosphere up to 200 °C producing relatively thick films which XRD analysis showed crystalline SbSI as the major component of the films together with some Sb_2S_3 from the buffer layer.

In this aspect, formation of SbSI from single-source precursors such as antimony(III) iodo-thiolates has been achieved and although the precursors exhibited low volatility and solubility, future work developing asymmetrically substituted antimony(III) iodo-thiolates will be a very interesting possibility in order to enhance the volatility of the precursors for LPCVD studies. In addition, it will be essential to keep the decomposition temperature of the precursors below 180 °C in order to avoid further decomposition of the SbSI species.

Another viable option would be the synthesis of antimony(III) iodo-thiolates with aromatic substituents, a feature that not only will enhance volatility due to the bulkier backbone of the molecules but also will increase their solubility, enabling AACVD studies as a promising approach for SbSI film deposition.[195]

Appendices

APPENDIX ONE

Instrumentation

Thermogravimetric Analysis (TGA).

TGA spectra have been recorded with a Perkin Elmer TGA 7 Thermogravimetric Analyser connected to a personal computer via TEC 7/DX Thermal Analysis Instrument controller. The TGA furnace allows operations from 30 to 1000 °C under a N_2 atmosphere. It is a small, platinum-wound micro furnace that allows rapid heating and cooling rates. A chromel-alumel thermocouple provides accurate sample temperature during analyses. Instrument and data have been elaborated with the Pyris software.

Microanalysis.

Carbon, hydrogen and nitrogen elemental analysis were performed using a Carlo-Erba Strumentazione E. A. mod. 1106 microanalyser operating at 500 °C. Results were calibrated against an acetanilide [$PhNHC(O)CH_3$] standard.

Nuclear Magnetic Resonance Spectroscopy.

^1H and $^{13}C\{^1H\}$ NMR spectra were recorded on a Bruker Avance 300 MHz Fourier Transform spectrometer using $SiMe_4$ as an internal reference. Values are quoted in ppm.

^{19}F NMR spectra were recorded on a Bruker Avance 400 MHz Fourier Transform spectrometer using $CFCl_3$ as an internal reference. Values are quoted in ppm. Coupling constants are quoted in Hz.

Mass Spectroscopy.

Mass spectra of the precursors were recorded at the University of Bath Mass Spectrometry Service in the EI-mode using a NOBA matrix using a FISONS Autosoec Mass Spectrometer.

Scanning Electron Microscopy (SEM).

SEM was carried out using a JEOL JSM T330 scanning electron microscope operating at an accelerating voltage ranging from 4 to 15 kV. Films were sputtered with carbon in order to avoid charging and to improve the secondary electron image quality.

Energy Dispersive X-Ray Analysis (EDAX).

Film thickness estimates using EDAX techniques were performed on a JEOL Superprobe instrument operating at an accelerating voltage of 5 kV or 15 kV with a beam current of $5x10^{-8}$ A or $5x10^{-9}$ A.

X-Ray Diffraction (XRD).

Data were collected on Nonius Kappa CCD diffractometer. Full matrix anisotropic refinement was implemented in the final least-squares cycles throughout. All data were collected from Lorentz and polarisation and some for extinction. Structure determination and refinement was achieved using a SHELX suite of programs and drawings were produced using Pov-Ray. Details of individual structure determination are given in Appendix 4.

APPENDIX TWO

CVD Reactors

The CVD apparatus used in this study has been assembled as a general screening rig for the use in this and other related projects. The system consists of a horizontal cold wall reactor with associated gas lines and electrical heater controls. The reactor contains two separate systems, a heated bubbler assembly (APCVD) and an ultrasonic nebuliser system (AACVD). For the purposes of this study only the ultrasonic nebuliser system (AACVD) was employed and hence will be discussed in detail. A schematic of the reactor system is shown in figure A2.1.

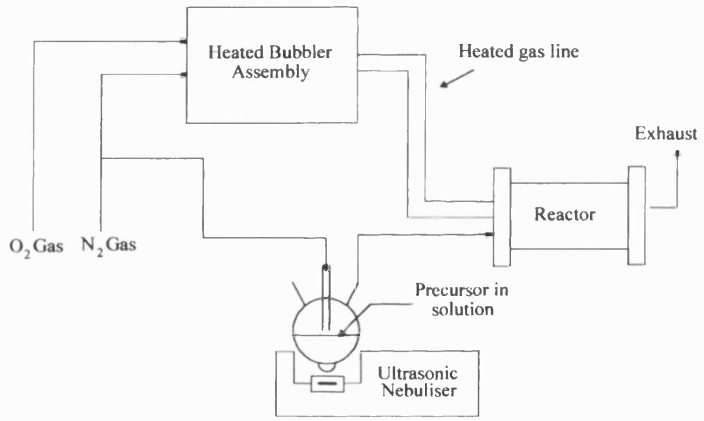

Figure A2.1 The CVD apparatus.

The nebuliser system used for AACVD is an ultrasonic humidifier from Pifco Health (model No 1077) bought from Argos (Figure A2.2). The piezoelectric transducer, situated in the reservoir containing water, transmits ultrasound through the water and the glass flask into the solution containing the precursor. The distance between the piezoelectric transducer and the flask is approximately 3-4 cm. The water in the reservoir is replaced every 30 minutes in order to cool the transducer.

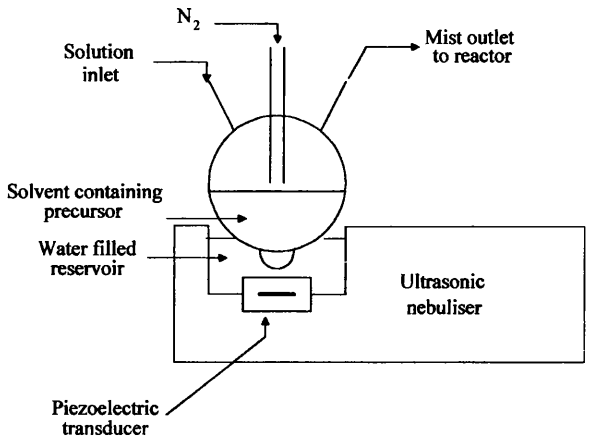

Figure A2.2 The ultrasonic nebuliser system.

The precursor solution is injected into the flask, which is under an inert atmosphere and placed on the nebulizer. The aerosol of fine droplets created (droplet size: 0.2–5 μm) can be controlled via two controls, the mist output (MO) and the humidity level (HL). The resulting aerosol is then swept out of the flask by a flow of argon and transported to the CVD reactor through a baffle to promote laminar flow.

The CVD reactor chamber where decomposition takes place is 8 mm high, 40 mm wide and 300 mm long. The ceiling tile and walls consist of quartz plates. The glass substrate is positioned on a large graphite susceptor, which is heated by three Watlow firerod cartridge heaters. The temperature of the graphite block is maintained by a Watlow series 965 controller, which monitors the temperature by means of thermocouples positioned inside the block. The graphite susceptor is held inside a large quartz tube (330 mm long, 100 mm diameter) suspended between stainless steel flanges upon which many of the electrical and gas line fittings are fixed. Air–tight seals are provided by 'Viton' O–rings. A schematic of the CVD reactor chamber is shown in Figure A2.3.

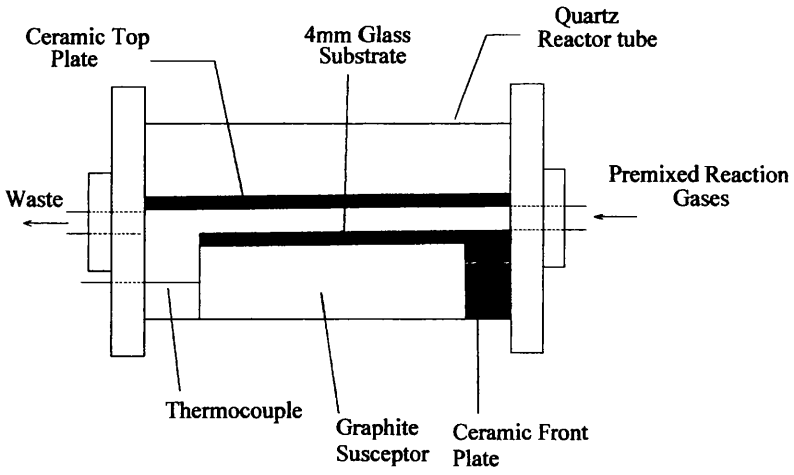

Figure A2.3 The CVD reactor chamber.

For the LPCVD experiments a different reactor was employed and a schematic of the apparatus is shown in Figure A2.4. The precursor sample to be decomposed is placed at the bottom end of the quartz tube reactor and the tube is then inserted in to the cylindrical heater, which heats the precursor. The quartz tube reactor also contains the glass substrate and a thermocouple.

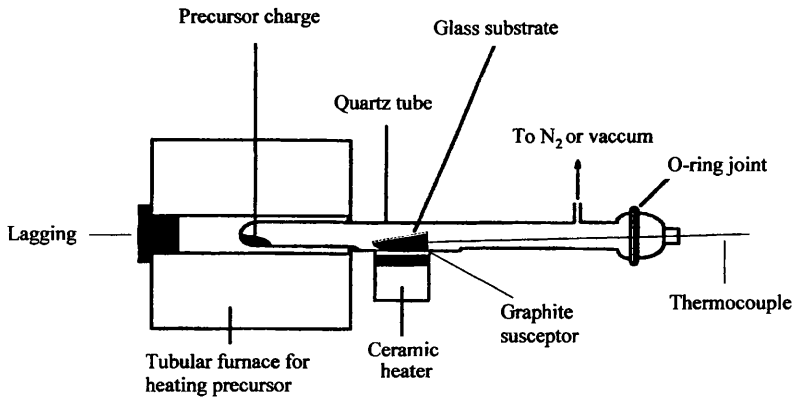

Figure A2.4 The Low-Pressure CVD reactor.

The glass substrate is positioned outside of the cylindrical heater, and heated conductively by a ceramic heater placed underneath. The temperature is monitored and controlled via a thermocouple and the whole reactor is connected to a Schlenk line to allow for the application of vacuum and backfill of argon.

Substrate Preparation Procedure

All glass substrates were cleaned in an identical manner prior to use. The cleaning routine was as follows:

a) The glass was washed thoroughly with water and detergent;
b) Then washed thoroughly with copious amounts of distilled water;
c) The substrate was finally washed with acetone and allowed to dry.

The glass substrate was always prepared prior to a deposition experiment and on completion of screening each precursor the nebuliser (AACVD), reactor tube (LPCVD) and any associated pipework were thoroughly cleaned in an Acid/Base bath followed by acetone to prevent unwanted contamination in films deposited from subsequent precursors.

The silicon wafers were only cleaned gently with cotton pads.

Deposition Conditions and SEM Methodology

After the films were grown they were sputtered with carbon in order to avoid charging and to improve the secondary electron image quality when examined by scanning electron microscopy (SEM).

Low-Pressure Chemical Vapour Deposition (LPCVD).

For each growth experiment approximately 0.3 g of the precursor was used. For these experiments the precursor was held at low pressure inside the quartz tube (ca. 0.1 mm Hg) and heated in a tube furnace until volatilization was complete (usually remaining some amorphous form of Sb_2S_3). At the same time, external to the furnace, the deposition substrate was independently heated by a ceramic infrared heater to the desired decomposition temperature. Any volatile material produced from heating the precursor was expected to decompose and deposit on the substrate and the possible by-products collected in the trap cooled with liquid nitrogen.

Aerosol-Assisted Chemical Vapour Deposition (AACVD).

For each growth experiment approximately 0.3 g of the precursor was used. Toluene was chosen as the solvent primarily because all precursors were very soluble in it. The precursors were dissolved in approximately 10 mL of freshly distilled toluene, however, more toluene (total volume of 50 mL) was often required during each experiment in order to prevent decomposition of the precursor as a consequence of solvent evaporation.

APPENDIX THREE

Numerical Index of Compounds Prepared in This Thesis

(1) $Li[S_2CN(Me)(Bu^n)]\cdot H_2O$

(2) $Li[S_2CN(Me)(Bz)]$

(3) $Li[S_2CN(Me)(Hex^n)]\cdot H_2O$

(4) $Sb[S_2CN(Me)(Bu^n)]_3$

(5) $Sb[S_2CN(Me)(Bz)]_3$

(6) $Sb[S_2CN(Me)(Hex^n)]_3$

(7) $Sb(S_2COEt)_3$

(8) $Sb(S_2COEt)_2I$

(9) $Sb(S_2COEt)_2Cl$

(10) $K(S_2COPr^i)$

(11) $Sb(S_2COPr^i)_3$

(12) $K(S_2COMe)$

(13) $Sb(S_2COMe)_3$

(14) $Sb(S_2COMe)_2I$

(15) $Sb(SBu^t)_3$

(16) $Sb(SCH_2CF_3)_3$

(17) $Sb(SBz)_3$

(18) $Sb(SCH_2CH_2NMe_2)_3$

(19) $Me_2Al(SCH_2CH_2NMe_2)$

(20) $S(SCH_2CH_2)_2SbI$

(21) $(CH_2S)_2SbI$

APPENDIX FOUR

Crystallographic Analysis and Structural Refinement for Compounds Synthesised in This Thesis

All crystallographic data are included in the CD attached at the end of this thesis.

CD Table of Contents:

(4) $Sb[S_2CN(Me)(Bu^n)]_3$	**h03kcm5**
(5) $Sb[S_2CN(Me)(Bz)]_3$	**h03kcm10**
(9) $Sb(S_2COEt)_2Cl$	**h05kcm30**
(15) $Sb(SBu^t)_3$	**h06kcm17**
(18) $Sb(SCH_2CH_2NMe_2)_3$	**k05kcm13**
(19) $Me_2Al(SCH_2CH_2NMe_2)$	**h05kcm19**
(20) $S(SCH_2CH_2)_2SbI$	**k05kcm20**
(21) $(CH_2S)_2SbI$	**h05kcm12**

References

REFERECES

1. K. K. Schuegraf, 'Handbook of Thin Film Deposition Processes and Techniques', Noyes Publications, 1988.
2. D. W. Bruce and D. O'Hare, 'Inorganic Materials', Wiley, 1997.
3. M. Hampden-Smith and T. Kodas, 'The Chemistry of Metal CVD', VCH, 1994.
4. K. D. Karlin, 'Progress in Inorganic Chemistry' 1994.
5. W. K. J. Vossen, 'Thin Film Processes', Academic Press, 1978.
6. H. W. Markstein, *EP&P*, 1977, **31**.
7. E. S. M. Langlet, J. L. Deschanvres, G. Delabouglise, F. Weiss, and J. C. Joubert, *J. Less Comm Met*, 1989, **151**, 399.
8. N. C. Norman, 'Chemistry of Arsenic, Antimony and Bismuth', Blackie Academic & Professional, 1998.
9. P. Bayliss and W. Nowacki, *Z Kristallogr Krist,* 1972, **135**, 308.
10. J. S. Swinnea, A. J. Tenorio, and H. Steinfink, *Am Mineral*, 1985, **70**, 1056.
11. J. W. Mellor, 'A Comprehensive Treatise on Inorganic and Theoretical Chemistry', Longsmans, 1929.
12. F. M. Ismail and Z. F. Hanafi, *Z. Phys Chem*, 1970, **244(3-4)**, 219.
13. C. H. Bhosale and K.Y. Rajpure, *Mater Chem Phys*, 2002, **73**, 6.
14. M. S. Selim and A.M. Salem, *J Phys D: Appl Phys*, 2001, **34**, 12.
15. O. Savadogo and K. C. Mandal, *Sol Energy Mater*, 1992, **26**, 117.
16. J. Grigas, J. Meshkauskas, and A. Orliukas, *Phys Status Solidi A*, 1976, **37**, K39.
17. J. George and M. K. Radhakrishnan, *Solid State Commun*, 1980, **33**, 987.
18. M. S. Ablova, A. A. Andreev, T. T. Dedegkaev, B. T. Melekh, A. B. Pevtsov, N. S. Shendel, and L. N. Shumilova, *Sov Phys Semicon+*, 1976, **10**, 629.
19. E. W. Pitzer, *Appl Spectrosc*, 1990, **44(9)**, 1498.
20. O. C. Monteiro, T. Trindade, J. H. Park, and P. O'Brien, *Chem Vap Dep*, 2000, **6**, 230.
21. M. Bochmann, X. J. Song, M. B. Hursthouse, and A. Karaulov, *J Chem Soc, Dalton Trans*, 1995, 1649.
22. A. M. Salem and M. S. Selim, *J Phys D: Appl Phys*, 2001, **34**, 12.

23. R. S. Mane and C. D. Lokhande, *Mater Chem Phys*, 2003, **82**, 347.
24. M. T. S. Nair, Y. Pena, J. Campos, V. M. Garcia, and P. K. Nair, *J Electrochem Soc*, 1998, **145**, 2113.
25. V. V. Killedar, K. Y. Rajpure, P. S. Patil, and C. H. Bhosale, *Mater Chem Phys*, 1999, **59**, 237.
26. K. Y. Rajpure and C. H. Bhosale, *Mater Chem Phys*, 2002, **73**, 6.
27. C. Ghosh and B. P. Varma, *Thin Solid Films*, 1979, **60**, 61.
28. Z. M. Hanafi and F. M. Ismail, *Z Phys Chem-Leipzig*, 1970, **244**, 219.
29. J. W. Wang and Y. D. Li, *Mater Chem Phys*, 2004, **87**, 420.
30. C. H. An, K. B. Tang, Q. Yang, and Y. T. Qian, *Inorg Chem*, 2003, **42**, 8081.
31. H. Hu, Z. Liu, B. Yang, M. Mo, Q. Li, W. Yu, and Y. Qian, *J Cryst Growth*, 2004, **262**, 375.
32. H. Hu, M. Mo, B. Yang, X. Zhang, Q. Li, W. Yu, and Y. Qian, *J Cryst Growth*, 2003, **258**, 106.
33. E. Doenges, *Z Anorg Chem*, 1960, **263**, 112.
34. E. Fatuzzo, G. Harbeke, W. J. Merz, R. Nitsche, H. Roetschi, and W. Ruppel, *Phys Rev*, 1962, **127**, 2036.
35. K. Itoh, H. Matsunaga, and E. Nakamura, *J Phys Soc Jpn*, 1976, **41**, 1679.
36. W. Wijekoon, M. Y. M. Lyktey, P. N. Prasad, and J. F. Garvey, *J Appl Phys*, 1993, **74**, 5767.
37. Y. Uchimoto, T. Okada, Z. Ogumi, and Z. Takehara, *J Chem Soc, Chem Comm*, 1994, 585.
38. M. Yoshida, K. Yamanaka, and Y. Hamakawa, *Jap J Appl Phys*, 1973, **12**, 1699.
39. A. Mansingh and T. S. Rao, *J Appl Phys*, 1985, **58**, 3530.
40. N. Solayappan, K. K. Raina, R. K. Pandey, and U. Varshney, *J Mater Res*, 1997, **12**, 825.
41. R. Nitsche and W. J. Merz, *J Phys Chem Solids*, 1960, **13**, 154.
42. R. Kern, *J Phys Chem Solids*, 1962, **23**, 249.
43. C. R. Wang, K. B. Tang, Q. Yang, B. Hai, G. Z. Shen, C. H. An, W. C. Yu, and Y. T. Qian, *Inorg Chem Comm*, 2001, **4**, 339.

44. Q. Yang, K. B. Tang, C. R. Wang, B. Hai, G. Z. Shen, C. H. An, C. J. Zhang, and Y. T. Qian, *J Cryst Growth*, 2001, **233**, 774.
45. S. Abrahams and K. Nassau, 'Encyclopedia of Materials Science and Engineering', Pergamon Press, 1986.
46. M. E. Lines and A. M. Glass, 'Principles and applications of ferroelectrics and related materials', Claredon Press, Oxford, 1977.
47. P. J. Wright and B. Cockayne, *J Cryst Growth*, 1984, **68**, 223.
48. J. R. Walsh, P. O'Brien, I.M. Watson, L. Hart, S.R.P. Silva, *J Cryst Growth*, 1996, **167**.
49. D. C. M. Afzaal, M. A. Malik, M. Montevalli, P. O'Brian, J. Park, J. D. Woollins, *Eur J Inorg Chem*, 2004, 171.
50. J. Cheon, J. E. Gozum, and G. S. Girolami, *Chem Mater*, 1997, **9**, 1847.
51. M. Peters, W. Saak, and S. Pohl, *Z Anorg Allg Chem*, 1996, **622**, 2119.
52. W. S. Rees, 'CVD of Nonmetals', VCH, 1996.
53. C. J. Carmalt, T. D. Manning, I. P. Parkin, E. S. Peters, and A. L. Hector, *J Mater Chem*, 2004, **14**, 290.
54. C. J. Carmalt, T. D. Manning, I. P. Parkin, E. S. Peters, and A. L. Hector, *Thin Solid Films*, 2004, **469-70**, 495.
55. F. Srouji, M. Afzaal, J. Waters, and P. O'Brien, *Chem Vap Dep*, 2005, **11**, 91.
56. J. P. Ge and Y. D. Li, *Chem Comm*, 2003, 2498.
57. T. T. Kodas and M. J. Hampden-smith, 'The Chemistry of Metal CVD', VCH, 1994.
58. S. Schneider, Y. Yang, and T. J. Marks, *Chem Mater*, 2005, **17**, 4286.
59. S. Schneider, J. A. S. Roberts, M. R. Salata, and T. J. Marks, *Angew Chem, Int Ed*, 2006, **45**, 1733.
60. S. C. Ngo, K. K. Banger, M. J. DelaRosa, P. J. Toscano, and J. T. Welch, *Polyhedron*, 2003, **22**, 1575.
61. M. Kemmler, M. Lazell, P. O'Brien, D. J. Otway, J. H. Park, and J. R. Walsh, *J Mater Sci-Mater El*, 2002, **13**, 531.
62. M. N. McCain, A. W. Metz, Y. Yang, C. L. Stern, and T. J. Marks, *Chem Vap Dep*, 2005, **11**, 291.
63. M. R. Lazell, P. O'Brien, D. J. Otway, and J. H. Park, *Chem Mater*, 1999, **11**, 3430.

64. G. A. Horley, M. R. Lazell, and P. O'Brien, *Chem Vap Dep*, 1999, **5**, 203.
65. S. Suh and D. M. Hoffman, *Chem Mater*, 2000, **12**, 2794.
66. A. Keys, S. G. Bott, and A. R. Barron, *Chem Mater*, 1999, **11**, 3578.
67. S. W. Haggata, M. A. Malik, M. Motevalli, and P. Obrien, *J Organomet Chem*, 1996, **511**, 199.
68. S. W. Haggata, M. A. Malik, M. Motevalli, P. Obrien, and J. C. Knowles, *Chem Mater*, 1995, **7**, 716.
69. W. Hirpo, S. Dhingra, A. C. Sutorik, and M. G. Kanatzidis, *J Am Chem Soc*, 1993, **115**, 1597.
70. T. C. Deivaraj, J. H. Park, M. Afzaal, P. O'Brien, and J. J. Vittal, *Chem Mater*, 2003, **15**, 2383.
71. K. K. Banger, M. H. C. Jin, J. D. Harris, P. E. Fanwick, and A. F. Hepp, *Inorg Chem*, 2003, **42**, 7713.
72. K. K. Banger, J. Cowen, and A. F. Hepp, *Chem Mater*, 2001, **13**, 3827.
73. Y. Rodriguez-Lazcano, M. T. S. Nair, and P. K. Nair, *J Cryst Growth*, 2001, **223**, 399.
74. S. L. Castro, S. G. Bailey, R. P. Raffaelle, K. K. Banger, and A. F. Hepp, *Chem Mater*, 2003, **15**, 3142.
75. M. Nanu, L. Reijnen, B. Meester, J. Schoonman, and A. Goossens, *Chem Vap Dep*, 2004, **10**, 45.
76. J. A. Hollingsworth, A. F. Hepp, and W. E. Buhro, *Chem Vap Dep*, 1999, **5**, 105.
77. J. H. Kim, D. Y. Chung, D. Bilc, S. Loo, J. Short, S. D. Mahanti, T. Hogan, and M. G. Kanatzidis, *Chem Mater*, 2005, **17**, 3606.
78. J. E. Cowen, A. T. Riga, A. F. Hepp, S. A. Duraj, K. Banger, and R. McClarnon, *J Therm Anal Calorim*, 2004, **75**, 929.
79. R. Ahlrichs, N. R. M. Crawford, A. Eichhofer, D. Fenske, O. Hampe, M. M. Kappes, and J. Olkowska-Oetzel, *Eur J Inorg Chem*, 2006, 345.
80. A. Assoud, K. M. Kleinke, and H. Kleinke, *Chem Mater*, 2006, **18**, 1041.
81. G. Barone, T. Chaplin, T. G. Hibbert, A. T. Kana, M. F. Mahon, K. C. Molloy, I. D. Worsley, I. P. Parkin, and L. S. Price, *J Chem Soc, Dalton Trans*, 2002, 1085.

82. G. A. Horley, M. F. Mahon, K. C. Molloy, P. W. Haycock, and C. P. Myers, *Inorg Chem*, 2002, **41**, 5052.

83. M. F. Mahon, T.G. Hibbert, K. C. Molloy, L. S. Price, I. P. Parkin, *J Mater Chem*, 2001, **11**, 469.

84. S. K. Arora, D. H. Patel, and M. K. Agarwal, *J Mater Sci*, 1994, **29**, 3979.

85. S. K. Arora, D. H. Patel, and M. K. Agarwal, *J Cryst Growth*, 1993, **131**, 268.

86. K. Deraman, S. Sakrani, B. B. Ismail, Y. Wahab, and R. D. Gould, *Inter J Electron*, 1994, **76**, 917.

87. S. A. Jodgudri, U. K. Mohite, K. M. Gadave, and C. D. Lokhande, *Indian J Pure Ap Phy*, 1994, **32**, 772.

88. P. C. Andrews, C. L. Raston, B. W. Skelton, and A. H. White, *Organometallics*, 1998, **17**, 779.

89. S. S. M. Hitchman, D. Gilliland, D. Cole-Hamilton, J. Nash, S. Thompson, S. Cook, *J Mater Chem*, 1995, **5**, 47.

90. P. A. W. Wojczak, M. Hampden-Smith, E. Duesler, *Inorg Chem*, 1996, **35**, 6995.

91. W. Maudez and K. M. Fromm, *Eur J Inorg Chem*, 2003, 3440.

92. M. B. Hursthouse, M. Motevalli, P. O'Brien, J. R. Walsh, and A. C. Jones, *Organometallics*, 1991, **10**, 3196.

93. A. N. Gleizes, *Chem Vap Dep*, 2000, **6**, 155.

94. V. K. Jain and S. S. Garje, *Coordination Chemistry Reviews*, 2003, **236**, 35.

95. N. Burford and G. G. Briand, *Chemica Reviews*, 1999, **99**, 2601.

96. A. Gupta, R. K. Sharma, R. Bohra, *J Organomet Chem*, 2003, **678**, 122.

97. S. S. Garje, V. K. Jain, and E. R. T. Tiekink, *J Organomet Chem*, 1997, **538**, 129.

98. S. S. Garje and V. K. Jain, *Coord Chem Rev*, 2003, **236**, 35.

99. H. I. S. Nogueira, O. C. Monteiroand T. Trindade, *Chem Mater*, 2001, **13**, 2103.

100. E. A. Eltaher and W. A. Badawy, *Thin Solid Films*, 1988, **158**, 277.

101. W. A. Badawy, *Thin Solid Films*, 1998, **186**, 59.

102. C. P. Myers, P. W. Haycock, M. Pichot, G. A. Horley, K. C. Molloy, S. A. Rushworth, and L. M. Smith, *Chem Vap Dep*, 2004, **10**, 35.

103. G. A. Horley, M. F. Mahon, K. C. Molloy, M. M. Venter, P. W. Haycock, and C. P. Myers, *Inorg Chem*, 2002, **41**, 1652.

104. J. O. Hill, Murray, J.P and Patil, K.C, *Rev Inorg Chem*, 1994, **14**, 363.

105. A. Saunders and A. Vecht, *J Electrochem Soc*, 1984, **131**, C93.

106. M. Motevalli, P. Obrien, J. R. Walsh, and I. M. Watson, *Polyhedron*, 1996, **15**, 2801.

107. P. Obrien, J. R. Walsh, I. M. Watson, L. Hart, and S. R. P. Silva, *J Cryst Growth*, 1996, **167**, 133.

108. D. Barreca, A. Gasparotto, C. Maragno, R. Seraglia, E. Tondello, A. Venzo, V. Krishnan, and H. Bertagnolli, *Appl Organomet Chem*, 2005, **19**, 59.

109. P. K. Nair and M. T. S. Nair, *J Phys D: Appl Phys*, 1991, **24**, 83.

110. A. T. Kana, T. G. Hibbert, M. F. Mahon, K. C. Molloy, I. P. Parkin, and L. S. Price, *Polyhedron*, 2001, **20**, 2989.

111. P. O'Brien, D. J. Otway, and J. R. Walsh, *Thin Solid Films*, 1998, **315**, 57.

112. I. G. Dance, *Polyhedron*, 1986, **5**, 1037.

113. S. Otsuka, M. Kamata, K. Hirotsu, and T. Higuchi, *J Am Chem Soc*, 1981, **103**, 3011.

114. C. J. Carmalt, S. A. O'Neill, I. P. Parkin, and E. S. Peters, *J Mater Chem*, 2004, **14**, 830.

115. E. S. Peters, C. J. Carmalt, and I. P. Parkin, *J Mater Chem*, 2004, **14**, 3474.

116. T. G. Hibbert, M. F. Mahon, K. C. Molloy, L. S. Price, and I. P. Parkin, *J Mater Chem*, 2001, **11**, 469.

117. G. Barone, T. G. Hibbert, M. F. Mahon, K. C. Molloy, L. S. Price, I. P. Parkin, A. M. E. Hardy, and M. N. Field, *J Mater Chem*, 2001, **11**, 464.

118. A. N. Macinnes, M. B. Power, and A. R. Barron, *Chem Mater*, 1993, **5**, 1344.

119. A. N. Macinnes, M. B. Power, and A. R. Barron, *Chem Mater*, 1992, **4**, 11.

120. H. Heral, L. Bernard, A. Rocher, C. Fontaine, and A. Munozyague, *J Appl Phys*, 1987, **61**, 2410.

121. R. Nomura, Y. Seki, K. Konishi, and H. Matsuda, *Appl Organomet Chem*, 1992, **6**, 685.

122. G. N. Kaludjerovic, V. M. Djinovic, S. R. Trifunovic, I. M. Hodzic, and T. J. Sabo, *J Serb Chem Soc*, 2002, **67**, 123.

123. F. Bonati and R. Ugo, *J Organomet Chem*, 1967, **10**, 257.

124. O. C. Monteiro, H. I. S. Nogueira, T. Trindade, and M. Motevalli, *Chem Mater*, 2001, **13**, 2103.

125. G. E. Manoussakis, C. A. Tsipis, and C. C. Hadjikostas, *Can J Chem*, 1975, **53**, 1530.

126. E. Kello, V. Kettmann, and J. Garaj, *Acta Crystallogr Sec C*, 1985, **41**, 520.

127. G. McKie, C. L. Raston, G. L. Rowbottom, and A. H. White, *J Chem Soc, Dalton Trans*, 1981, 1360.

128. J. A. Cras and J. Willemse, *Recl Trav Chim Pay B*, 1978, **97**, 28.

129. Y. Liu and R. T. Tiekink, *Crystengcomm*, 2005, **7**, 20.

130. C. L. Raston and A. H. White, *J Chem Soc, Dalton Trans*, 1976, 791.

131. C. A. Kavounis, S. C. Kokkou, P. J. Rentzeperis, and P. Karagiannidis, *Acta Crystallogr B*, 1982, **38**, 2686.

132. I. bin Baba, B. W. Skelton, and A. H. White, *Aust J Chem*, 2003, **56**, 27.

133. T. Trindade, P. Obrien, X. M. Zhang, and M. Motevalli, *J Mater Chem*, 1997, **7**, 1011.

134. V. Venkatachalam, K. Ramalingam, U. Casellato, and R. Graziani, *Polyhedron*, 1997, **16**, 1211.

135. E. W. Pitzer, *Appl Spectrosc*, 1990, **44**, 1498.

136. R. W. G. Wyckoff, in 'Crystal Structures, Vol. 2', New York, 1964.

137. C. P. Myers, P. W. Haycock, M. Pichot, G. A. Horley, K. C. Molloy, S. A. Rushworth, and L. M. Smith, *Chem Vap Dep*, 2004, **10**, 35.

138. W. C. Zeise, *Ann Pharm Fr*, 1835, **16**, 178.

139. A. A. Mohamed, I. Kani, A. O. Ramirez, and J. P. Fackler, *Inorg Chem*, 2004, **43**, 3833.

140. J. S. Casas, A. Castineiras, I. Haiduc, A. Sanchez, R. F. Semeniuc, and J. Sordo, *J Mol Struct*, 2003, **656**, 225.

141. B. F. Hoskins, E. R. T. Tiekink, and G. Winter, *Inorg Chim A-Art Let*, 1985, **97**, 217.

142. E. R. T. Tiekink, *J Crystallogr Spectrosc Res*, 1992, **22**, 231.

143. R. W. Gable, B. F. Hoskins, R. J. Steen, E. R. T. Tiekink, and G. Winter, *Inor Chim A-Art*, 1983, **74**, 15.

144. M. Wieber, D. Wirth, and C. Burschka, *Z Anorg Allg Chem*, 1983, **505**, 141.

145. A. Ouchi, M. Shimoi, F. Ebina, T. Uehiro, and Y. Yoshino, *Bull Chem Soc Jpn*, 1978, **51**, 3511.

146. Y. W. Koh, C. S. Lai, A. Y. Du, E. R. T. Tiekink, and K. P. Loh, *Chem Mater*, 2003, **15**, 4544.

147. B. F. Hoskins, E. R. T. Tiekink, and G. Winter, *Inorg Chim A-Art Let*, 1985, **99**, 177.

148. A. J. Blake, M. Pearson, D. B. Sowerby, and P. P. Woodhead, *Acta Crystallogr C*, 1997, **53**, 583.

149. M. A. Khwaja, T. J. Cardwell, and R. J. Magee, *Anal Chim Acta*, 1973, **64**, 9.

150. M. R. Snow and E. R. T. Tiekink, *Aust J Chem*, 1987, **40**, 743.

151. C. L. Raston, G. L. Rowbottom, and A. H. White, *J Chem Soc, Dalton Trans*, 1981, 1352.

152. J. P. M. J. O. Hill, K. C. Patil, *Rev Inorg Chem*, 1994, **14(5)**, 363.

153. X. B. Cao, L. Gu, L. Zhuge, W. J. Gao, W. C. Wang, and S. F. Wu, *Advanced Functional Materials*, 2006, **16**, 896.

154. B. D. Cullity, 'Elements of X-ray Diffraction', Addison-Wesley, 1978.

155. N. Pradhan, B. Katz, and S. Efrima, *J Phys Chem B*, 2003, **107**, 13843.

156. Manoussa.Ge, Micromas.Ed, and C. A. Tsipis, *Z Anorg Allg Chem*, 1974, **403**, 87.

157. E. Block, G. Oforiokai, H. K. Kang, J. Wu, and J. Zubieta, *Inorg Chem*, 1991, **30**, 4784.

158. R. C. Mehrotra, Gupta, V.D and Chatterjee, S, *Aust. J. Chem*, 1968, **21**, 2929.

159. A. F. Janzen, O. C. Vaidya, and C. J. Willis, *J Inorg Nucl Chem*, 1981, **43**, 1469.

160. J. P. H. Charmant, A. Jahan, N. C. Norman, and A. G. Orpen, *Inorg Chim Acta*, 2005, **358**, 1358.

161. W. Clegg, M. R. J. Elsegood, L. J. Farrugia, F. J. Lawlor, N. C. Norman, and A. J. Scott, *J Chem Soc, Dalton Trans*, 1995, 2129.

162. N. Avarvari, M. Fourmigue, and E. Canadell, *Eur J Inorg Chem*, 2004, 3409.

163. N. Avarvari and M. Fourmigue, *Organometallics*, 2003, **22**, 2042.

164. R. A. Howie, J. N. Low, G. M. Spencer, and J. L. Wardell, *Polyhedron*, 1997, **16**, 2563.

165. J. Wegener, K. Kirschbaum, and D. M. Giolando, *J Chem Soc, Dalton Trans*, 1994, 1213.

166. J. P. Fackler and W. J. Zegarski, *J Am Chem Soc*, 1973, **95**, 8566.

167. M. Li, A. Ellern, and J. H. Espenson, *Inorg Chem*, 2005, **44**, 3690.

168. L. M. Nguyen, M. E. Dellinger, J. T. Lee, R. A. Quinlan, A. L. Rheingold, and R. D. Pike, *Inorg Chim Acta*, 2005, **358**, 1331.

169. C. J. Carmalt, E. S. Peters, I. P. Parkin, T. D. Manning, and A. L. Hector, *Eur J Inorg Chem*, 2004, 4470.

170. G. Barone, T. Hibbert, M. F. Mahon, K. C. Molloy, I. P. Parkin, L. S. Price, and I. Silaghi-Dumitrescu, *J Chem Soc, Dalton Trans*, 2001, 3435.

171. C. J. Carmalt, E. S. Peters, S. J. King, J. D. Mileham, and D. A. Tocher, Modern Aspects of main Group Chemistry, Oxford University Press, 2006.

172. J. A. Samuels, W. C. Chiang, C. P. Yu, E. Apen, D. C. Smith, D. V. Baxter, and K. G. Caulton, *Chem Mater*, 1994, **6**, 1684.

173. M. S. Bharara, C. H. Kim, S. Parkin, and D. A. Atwood, *Polyhedron*, 2005, **24**, 865.

174. G. Carotenuto, B. Martorana, P. B. Perlo, and L. Nicolais, *J Mater Chem*, 2003, **13**, 2927.

175. M. Nandi, D. Rhubright, and A. Sen, *Inorg Chem*, 1990, **29**, 3065.

176. P. M. Jeffries, L. H. Dubois, and G. S. Girolami, *Chem Mater*, 1992, **4**, 1169.

177. A. N. Macinnes, M. B. Power, A. F. Hepp, and A. R. Barron, *J Organomet Chem*, 1993, **449**, 95.

178. M. S. Bharara, S. Parkin, and D. A. Atwood, *Inorg Chem*, 2006, **45**, 2112.

179. M. S. Bharara, T. H. Bui, S. Parkin, and D. A. Atwood, *Dalton Trans*, 2005, 3874.

180. G. G. Briand, N. Burford, T. S. Cameron, and W. Kwiatkowski, *J Am Chem Soc*, 1998, **120**, 11374.

181. A. M. Arif, D. J. Chandler, and R. A. Jones, *J Coord Chem*, 1987, **16**, 213.

182. C. N. McMahon, J. A. Francis, S. G. Bott, and A. R. Barron, *J Chem Soc, Dalton Trans*, 1999, 67.

183. O. T. Beachley and K. C. Racette, *Inorg Chem*, 1976, **15**, 2110.

184. M. A. Bush, P. F. Lindley, and P. Woodward, *J Chem Soc A*, 1967, 221.

185. N. Burford, T. M. Parks, B. W. Royan, B. Borecka, T. S. Cameron, J. F. Richardson, E. J. Gabe, and R. Hynes, *J Am Chem Soc*, 1992, **114**, 8147.

186. L. Agocs, N. Burford, T. S. Cameron, J. M. Curtis, J. F. Richardson, K. N. Robertson, and G. B. Yhard, *J Am Chem Soc*, 1996, **118**, 3225.

187. M. Drager, *Chem Ber*, 1974, **107**, 2601.

188. J. G. Alvarado-Rodriguez, N. Andrade-Lopez, S. Gonzalez-Montiel, G. Merino, and A. Vela, *Eur J Inorg Chem*, 2003, 3554.

189. S. Gonzalez-Montiel, N. Andrade-Lopez, and J. G. Alvarado-Rodriguez, *Eur J Inorg Chem*, 2006, 3762.

190. M. Drager, *Z Anorg Allg Chem*, 1974, **405**, 183.

191. P. Powell, *J Chem Soc A*, 1968, 2587.

192. U. Kolb, M. Beuter, M. Gerner, and M. Drager, *Organometallics*, 1994, **13**, 4413.

193. R. E. Marsh, *Acta Crystallogr*, 1955, **8**, 91.

194. A. Ibanez, J. C. Jumas, J. Olivierfourcade, and E. Philippot, *Revue De Chimie Minerale*, 1984, **21**, 344.

195. A. S. Batsanov, S. M. Cornet, K. B. Dillon, A. E. Goeta, P. Hazendonk, and A. L. Thompson, *J Chem Soc, Dalton Trans*, 2002, 4622.